2021

Flow and heat transfer characteristics of turbulent swirling impinging jets

Muhammad Ikhlaq
Edith Cowan University

Flow and Heat Transfer Characteristics of Turbulent Swirling Impinging Jets

This thesis presented in fulfilment for the degree of

Doctor of Philosophy

Muhammad Ikhlaq

MSc (Ozyegin University)
BE (NED University of Science and Technology)

School of Engineering
Edith Cowan University
Western Australia

2021

Use of Thesis

██. However the literary rights of the author must also be respected. If any passage from this thesis is quoted or closely paraphrased in a paper or written work prepared by the user, the source of the passage must be acknowledged in the work. If the user desires to publish a paper or written work containing passages copied or closely paraphrased from this thesis, which passages would in total constitute and infringing copy for the purpose of the Copyright Act, he or she must first obtain the written permission of the author to do so.

Abstract

Numerous industrial applications rely on impinging jets to impart convective heat and mass transfer in processes ranging from the cooling of electronic devices and gas turbine blades to drying of paper and food products. Conventionally, non-swirling impinging jets have been employed, but some studies have shown that inducing swirl allows better control of uniformity and improved convective fluxes. A better understanding of the underlying physical mechanisms that lead to such behaviour warrants deeper insights into the flow and heat transfer characteristics of impinging jets, both swirling and non-swirling. Whilst important to achieve, the flow field of an impinging jet is already quite complex even before the addition of swirl which, in free (not impinging) jets, induces vortex breakdown and other instability modes. The addition of swirl to impinging jets thus has the potential to affect the transient and steady-state convective behaviour, both of which are crucial in industrial applications.

This study features experimental and numerical investigations of incompressible turbulent impinging air jets that utilize aerodynamically generated swirl. The research focuses on the velocity field, upstream near the nozzle exit plane as well as further downstream, and the way in which it affects heat transfer at the impingement plane, both under transient and steady-state conditions. Boundary conditions at the nozzle exit were measured using Constant Temperature Anemometry. The surface temperature distribution of a thin foil heater, which forms the impingement surface cooled by the ambient temperature jet, was measured using infrared thermography for a range of Reynolds numbers (Re=11,600-35,000), swirl numbers (S=0-1.05), and impingement distances (H/D=2-6). The effects of different inflow conditions for non-swirling and weakly swirling impinging jets were also simulated (numerically) using ANSYS Fluent (version 16.2). Particle Image Velocity was utilized to resolve the flow field, over low (S=0.30) and higher (S=0.74) swirl over a range of Reynolds numbers (Re=11,600-35,000) and nozzle-to-plate distance (H/D=2 and 4).

Whilst the use of non-intrusive infrared thermography has been widely reported in studies of the steady-state heat transfer behaviour of impinging jets, an image processing methodology to resolve the time-dependant (transient) convective heat transfer behaviour was lacking. In this context, a MATLAB based method was developed to quantify the role of various impinging jet parameters on the time to reach steady-state. The effect of spatial discretization, image resolution, and the threshold value of time-dependent Nusselt number, on the time to reach steady-state, was also analysed.

The role of various operating (Re, S) and geometric conditions (H/D) on the temporal evolution of turbulent impinging jets was also resolved. By applying the innovative image processing methodology developed, results show that for non-swirling jets, transient heat transfer characteristics at some conditions (H/D=4) are distinct if compared to others (H/D=2 and 6) and that the heat transfer distribution over the impingement plate changes significantly over a small interval of time. For swirling jets, the peak Nusselt number shifts to the wall jet region as the intensity of the swirl increases. Two correlations (no-to-low swirl, moderate-to-high swirl) are proposed to predict the time needed to reach a steady-state for Re=35,000.

Computational Fluid Dynamics was then used to resolve the role of various (upstream) nozzle exist conditions (velocity profiles) on the emerging heat transfer characteristics at the impingement plane. Results showed that under some conditions (S=0.31, uniform velocity profile) a small recirculation zone, stabilised on the impingement plane, affects the heat transfer compared to other tested velocity profiles. This study also gave valuable insights on the impact of using (simple) geometric inserts to generate for swirl into impinging jets, a method widely used for its simplicity. Results showed that this can fundamentally perturb the results unlike the use of aerodynamic swirl which relies on tangential air ports.

For the experimentally measured flow field, vortex breakdown is observed for two of conditions (Re=11,600 and 24,600 at S=0.74) out of the six tested. Impingement affects the position, shape, and strength of the vortex breakdown. For Re=24,600, impingement significantly affects (shape and position) the recirculation bubble when compared to impingement at Re=11,600. Heat transfer characteristics at high swirl are compared with low swirling impinging jets. The vortex breakdown (at high swirl) affects the impingment heat transfer and showed comparatively uniform heat transfer distribution in contrast to low swirling impinging jets. Vortex breakdown significantly deteriorates stagnation zone heat transfer and the Nusselt number peak occurs in the wall jet region.

Benefits derived from this study include identifying impingement conditions that allow quicker stabilisation of heat transfer (shorter transients) as well as an improved understanding for the role of impingement on the upstream and downstream velocity field and heat transfer characteristics.

Keywords: Swirl, Impinging jets, Heat transfer, Flow-Field, Turbulence, Staedy-state, Transient, Infrared thermography, CFD, RANS, PIV, CTA, Image Processing.

Declaration

I certify that this thesis does not, to the best of my knowledge and belief:

(i)   Incorporate without acknowledgment any material previously submitted for a degree or diploma in any institution of higher education;

(ii)   Contain any material previously published or written by another person except where due reference is made in the text; or

(iii) Contain any defamatory material.

(iv)   I also grant permission for the Library at Edith Cowan University to make duplicate copies of my thesis as required

Muhammad Ikhlaq

Dated: 25.09.2020

Acknowledgments

Moreover, I thank ***The One Almighty*** for all these blessing and other

for it is to Him that I am indebted

List of Journal Papers Arising From This Candidature

- **Ikhlaq, M**., Al-Abdeli, Y. M., & Khiadani, M. (2020). Methodology for spatially resolved transient convection processes using infrared thermography. *Experimental Heat Transfer, 1-24*.
  DOI: 10.1080/08916152.2020.1749189
  This article is integrated in the Chapter 2 of this thesis.

- **Ikhlaq, M**., Al-Abdeli, Y. M., & Khiadani, M. (2019). Transient heat transfer characteristics of swirling and non-swirling turbulent impinging jets. *Experimental Thermal and Fluid Science*, *109*, 109917.
  https://doi.org/10.1016/j.expthermflusci.2019.109917
  This article is integrated in the Chapter 3 of this thesis.

- **Ikhlaq, M**., Al-Abdeli, Y. M., & Khiadani, M. (2020). Nozzle exit conditions and the heat transfer in non-swirling and weakly swirling turbulent impinging jets. *Heat and Mass Transfer*, *56*(1), 269-290.
  https://link.springer.com/article/10.1007/s00231-019-02710-1
  This article is integrated in the Chapter 4 of this thesis.

- **Ikhlaq, M**., Al-Abdeli, Y. M., & Khiadani, M. (2020). Flow and heat characteristics of turbulent swirling impinging jets (under review).
  This article is integrated in the Chapter 2 of this thesis.

Table of Content

List of Tables

List of Figures

List of Symbols, Nomenclature

A_p	Area of the jet exit plane or on the impingement surface (Experimental 0.06 m^2)
B	Measured data
$B'(i)$	Moving average of the measured data
c_p	Thin foil specific heat (500J/kg.K)
C_μ	Model constant (0.09)
C_p	Pressure coefficient
Cp	Fluid heat capacity(J/K)
D	Nozzle diameter at the exit plane (m)
D_L	Anisotropic dissipation (k_L)
D_T	Anisotropic dissipation (k_T)
E	Enthalpy (J/kg)
E	Residuals
$E'(i)$	Moving average of residuals
F	Filtered data
f_W	Inviscid near-wall damping function
f_ω	Boundary layer wake term damping function
H	Nozzle-to-plate distance (m)
H	Heat transfer coefficient (W/m^2.k)
K	Turbulent kinetic energy (m^2/s^2)
K_{eff}	Effective thermal conductivity
k_{foil}	Thermal conductivity of thin metallic foil (16.3W/m.K)
k_L	Laminar kinetic energy (m^2/s^2)
k_T	Turbulent kinetic energy(W/m^2.k)
L	Turbulent length scale (0.07D)
N	Data smoothing degree
N	Number of sample for error calculation
Nu(r)	Radially distributed Nusselt number
Nu_0	Stagnation point Nusselt number
Nu_A	Spatially averaged Nusselt number
Nu_{st-st}	Steady-state Nusselt number
Nu´´	d(Nu)/dt

M	Number of images for frame rate calculation
P	Pressure
$P\infty$	Ambient pressure
P_{KL}	Production of laminar kinetic energy by mean strain rate
P_{KT}	Production of turbulent kinetic energy by mean strain rate
Pr_t	Turbulent Prandtl number
Q	Volume flow rate (m^3/s)
$\dot{q}$	Heat flux (W/m^2)
r	Radial direction coordinate
R_{BP}	Bypass transition production term
Re	Reynolds number
R_{NAT}	Natural transition production term
S	Swirl number
T	Temperature (K)
t	Time (s)
T_{amb}	Ambient Temperature (K)
T_{ref}	Reference temperature (K)
T_w	Heat wall temperature (K)
$\langle u \rangle$	Time mean axial velocity (m/s)
U_b	Bulk axial velocity at the nozzle exit plane (m/s)
$\overline{U}$	Time-average mean axial velocity (m/s)
$\overline{u'^2}$	Axial velocity fluctuations (variance)
$u_{i,j}$	Axial, radial and azimuthal velocity component (m/s)
u'	Axial, radial and azimuthal velocity fluctuations (m/s)
$\overline{V}$	Time-average mean radial velocity (m/s)
$\overline{v'^2}$	Radial velocity fluctuations
W_b	Bulk tangential velocity at the nozzle exit plane (m/s)
$\langle w \rangle$	Time mean azimuthal velocity component (m/s)
w'	Azimuthal velocity fluctuations
x	Abscissa of impingement plate (m)
y	Ordinate of impingement plate (m)

Greek Letters

ρ	Density

μ	Dynamic viscosity
ν	Kinematic viscosity
λ	Thermal conductivity of the bulk air
δ_{ij}	Dirac's delta
ω	Specific rate of dissipation
ω_z	Vorticity in the direction of z-axis
$\in$	Rate of dissipation
ε	Error
σ_A	Standard deviation
α_T	Effective diffusivity for turbulence dependent variables

Abbreviations

CTA	Constant Temperature Anemometry
IR	Infrared
PIV	Particle Image Velocimetry
PP	Parabolic tangential velocity profile
SBR	Solid-body-rotation type tangential velocity profile
UP	Uniform (top-hat) tangential velocity profile
SST	Shear Stress Transport
RNG	Re-Normalisation Group
RANS	Reynolds-averaged Navier–Stokes
LES	Large Eddy Simulation
DNS	Direct Numerical Simulation

Chapter 1: Topical Introduction

This chapter will introduce the basic concepts of free/impinging jets, both non-swirling and swirling, with regards to their fluid flow and heat transfer characteristics.

1.1 INTRODUCTION

Impinging jets have been studied for more than two decades due to their many industrial applications, which include cooling stock and heat treatment in metal forming industries [1], cooling microelectronic devices, defogging (heating) of optical surfaces [2], as well as in the glass industry where they are used to quickly cool heated glass sheets (at 640^0C) [3]. Impinging jets can also be utilized for the cooling of different gas turbine sections, including a combustor (case/liner) and most importantly gas turbine blades [4,5] where they are used to enhance the convective heat transfer coefficient (1000-3000 W/m^{2}K equivalent to 1MW/m^2) [6]. In this context, material properties are a design limitation in modern turbines which is why cooling is one of the main processes that can keep turbines working safely. Impinging jets are also commonly used in the food and paper industry. The flow dynamics and impingement characteristics of impinging jets are also important in aircraft/satellite launch vehicles that employ short take-off and landing, where abrasion can occur over impingement surfaces [1,3,7].

A jet flow can be defined as a torrent of fluid entering its surrounding atmosphere, typically through a nozzle or orifice. Jet fluid can be similar or different to its corresponding environment [8]. The dissipation of jet momentum can occur very fast or slow, depending on operating conditions, geometry, and other factors.

The mass flow rate is represented by area under this Gaussian curve

Centreline velocity decay

Velocity increases by viscous diffusion

Shear layer

Initial velocity distribution determined by the nozzle geometry

Potential core

Axisymmetric axis
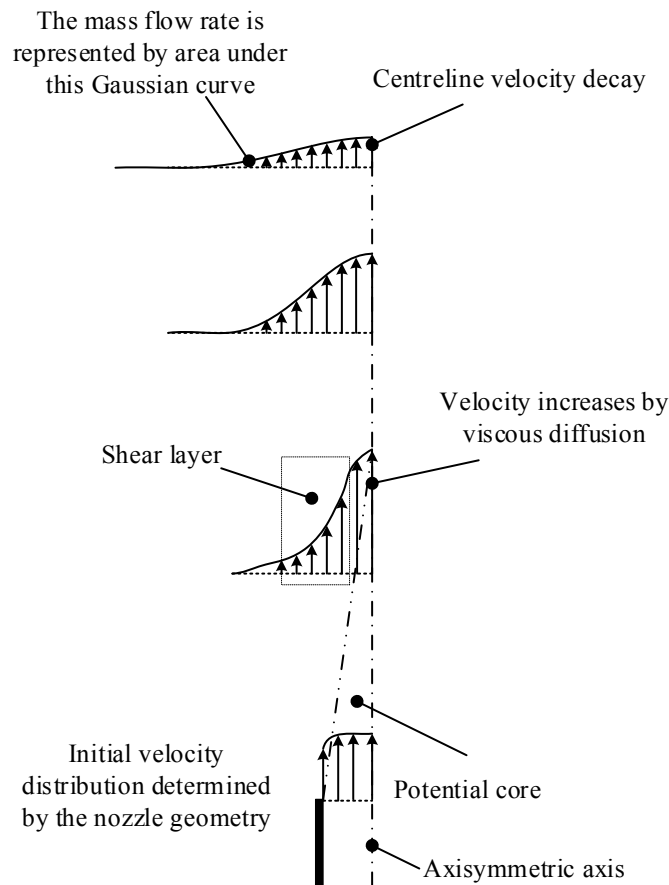
Figure 1.1: The flow field of a free jet.

Figure 1.1 shows jet development with respect to downstream distance for a free jet. Here momentum is transferred in a lateral direction (perpendicular to the jet flow) from the velocity gradient due to shearing at the jet edge. The inner region of the flow remains isolated and the spread of the shear layer does not interrupt it. The pressure at the centre of the jet core persists for a finite distance from the nozzle exit, before pressure and velocity decrease as the jet moves downstream. In regards to flow-through a pipe or circular nozzle, the developed flow appears like a parabolic/power-law profile and is axisymmetric. The velocity profile for a non-swirling and fully developed jet looks Gaussian, where the velocity becomes smaller and the distribution wider with distance from the nozzle exit plane. Martin [9] presented several equations for the prediction of jet velocity decay in free laminar jets. To date, many parameters have been used to characterize turbulent jets, some of them are entrainment, spread rate, and velocity decay. The spreading of jet fluid determines the effectiveness of jet mixing. Half jet width versus the axial distance is used to calculate jet spread (the distance between the centreline and the point where the local mean velocity is half of the local centreline mean velocity is known as half jet width). The turbulent jets can be characterised by evaluating the self-similarity solutions

velocity-decay constant of the jet [10]. Most of the turbulent free jets are self-similar with respect to dimensionless downstream distance. The centreline velocity of the jet decreases proportional to inverse distance (product with the decay-constant) from the nozzle.

1.1.1 Swirling Free Jets

Swirling flow can be generated either using geometrical insert/helical vanes as shown in Figure 1.2(a) or by introducing tangential flow into the mean flow path as presented in Figure 1.2(b). The latter method is known as an aerodynamically generated swirl.

(a)   (b)
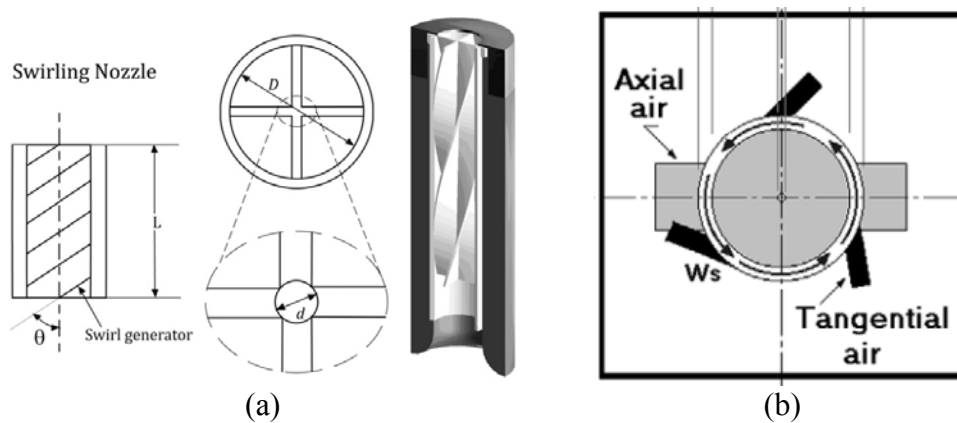
Figure 1.2: (a) Swirl generated by using insert/vanes [11] (b) Aerodynamically generated swirl [12].

As the tangential component of velocity in the flow increases, swirl intensity also increases, where the tangential component of velocity differentiates swirling and non-swirling jets. Swirling flows are applied in industrial burners and combustors, where flames can be stabilized by enhancing air and fuel mixing, whereby the swirl is applied to allow more entrainment of surrounding fluid at the shear layer. Swirl flows are also used in gas turbines [13–15], chemical reactors and cyclone separators. The swirl prevents the flame being extinguished in the gas turbine combustion chamber [16], while in chemical reactors and cyclone separators swirl enhances reactant mixing and extraction of solid particles from the gas, respectively [16–18].

Flow instabilities associated with a turbulent swirling jet affect the velocity field significantly, altering shear stresses and heat transfer characteristics at the impingement surface [19]. Swirling and non-swirling jet flow characteristics are quite different. Higher rates of shear layer entrainment and the introduction of tangential flow modify the velocity field significantly. Vortex breakdown, precessing vortex cores, and flow separation are complex phenomena that relate to turbulent swirling flow, which makes it difficult to understand and compare to non-swirling jets [20,21]. The spread of the jet core grows as the swirl number (defined chapter 2) increases, which leads to higher dissipation rates compared to lower degrees of swirl [22].

3

Vortex breakdown is a widely observed phenomenon that occurs in swirling flows when the swirl intensity reaches to a critical value for its corresponding Reynolds number (defined in Chapter 2). There is no universal critical value available where vortex breakdown can be observed due to the multitude definition of swirl number (details are provided in the Appendix D). In swirling jets, this appears to occur when the maximum rotational (azimuthal) velocity approaches its axial velocity. Vortex breakdown has several types, bubble, spiral, and double spiral [23]. A Precessing Vortex Core (PVC) is the highly unsteady and 3D time-dependent flow pattern, which is also usually asymmetric if it occurs within jet flows. PVCs have a helical structure and are produced by unstable bending flow modes. Typically, spiral vortex breakdown and first positive helical mode of PVC co-exist together [24]. This behaviour occurs in both flames [15,25] and non-reacting swirl jets [12].

1.1.2 Impinging Jets (Non-Swirling, Swirling)

For industrial applications, impinging jets can be used to actively enhance surface heat or mass transfer. As such, impinging jets have been investigated thus far in relation to their engineering and industrial applications.
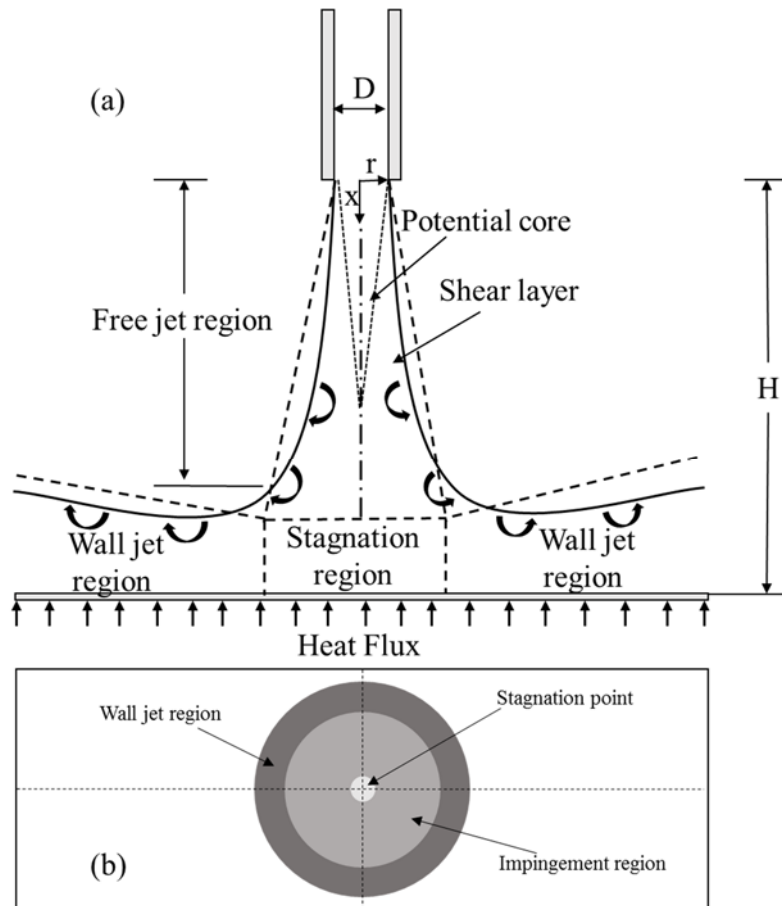
Figure 1.3: Regions for the unconfined axisymmetric impinging jet. (a) Downstream (axial) development (b) Lateral (radial) distribution at Impingement plane.

Velocity field: Figure 1.3(a) shows the fundamental structure of impinging jets. The unconfined impinging jet can be divided into three distinct regions named as the free jet region (I), impinging jet region (II) and wall jet region (III). Some characteristics of the impinging jets are similar to free jets. The free jet region also consists of a potential core and fully developed flow region and comprises the axial distance from the nozzle exit to the end of a developed velocity distribution [26]. Entrainment in the flow is similarly introduced at the shear layer from the surroundings. The properties of the jet at the exit of the nozzle depending on upstream conditions like velocity, turbulence characteristics, and temperature distributions. For large distances (beyond the potential core of the jet) the kinetic energy of the fluid progressively decays and can cause lower heat transfer rates. [2].

The jet impingement region forms upon jet impact and deflection on the surface, where heat transfer rates are higher nearer to the impingement region compared to other parts on the impingement plane. The rate of heat transfer reduces as the radial distance from the stagnation region (zero velocity at the surface) increases over an impingement plane [27,28]. The

5

entrainment of fresh air at the turbulent thermal boundary layer introduces fluid entrainment, which enhances heat transfer at the impingement surface [22,29]. Enhancement of heat transfer occurs through the mixing of fresh fluid into the thermal boundary layer carried by the breakup of large scale eddies into intermittent and smaller eddies. Following the impingement region, radial deceleration of the flow occurs over the surface as the wall jet region is formed. The entrainment of surrounding fluid is expected to experience significant interaction at the wall jet region, where the boundary layer develops in the wall jet region and; hence, reductions in heat transfer rates have been reported for axisymmetric impinging jets [30].

Heat Transfer Characteristics: Impinging jet performance can be characterized by the convective heat transfer coefficient (h) and Nusselt number (Nu), h and Nu are defined in Chapter 2. Typically conducting experiments to resolve the velocity field and temperature distribution over an impingement surface in turbulent swirling jets is much more complicated and demanding than those involving non-swirling flows. For impinging jets, the stagnation zone and the wall jet region hold distinct attributes. Non-swirling impinging jets hold maximum heat transfer at the stagnation zone due to the conversion of decelerating fluid velocity into the static pressure. The overall uniformity (distribution on target surface) of heat transfer for non-swirling jets is measured to be lower than the swirling jets [11]. Both the uniformity and magnitude of impingement heat transfer are dependant not only swirl number, but also the Reynolds number and impingement distance.

1.2 RESEARCH GAPS

Many industrial applications utilize impingement jet heat transfer, with different configurations including circular jets [31], slot jets [32], arrays of jets [33], and swirling jets [34]. Impingement heat transfer depends on numerous parameters whether jets are swirling or non-swirling; jet geometry; impingement surface to nozzle distance, and turbulence levels within the jet [9,31]. With the above in mind, there appears to be a number of gaps in the research undertaken thus far into turbulent impinging jets:

- Earlier studies have not presented methodologies to quantify the transient (convective) heat transfer characteristics of impinging jets when resolved using Infrared (IR) thermography.
- The temporal evolution of heat transfer in both swirling and non-swirling impinging jets has not been studied, particularly if using non-intrusive diagnostics when coupled with the (highly sensitive) heated thin foil technique.

6

- The effects of (upstream) nozzle exit conditions on impingement heat transfer, and their ability to induce (downstream) flow features at the impingement plane, has not been resolved previously.

- The effects of central blockages arising from geometric swirl generators on impingement heat transfer characteristics over a range of H/D have not been studied.

- The role of impingement in low and high swirling jets, in terms of the flow field, features it may induce and the subsequent effect of these features on impingement heat transfer has not been established over a range of operating (Re, S) and geometric (H/D) parameters.

1.2.1 Non-Swirling Impingement

For non-swirling jets, heat transfer is higher for near-field impingement distances (for small H/D), provided the impingement surface stays within the range of the potential core [2]. A localized small peak is observed in the radial distribution of heat transfer data if H/D extends beyond the potential core [35] but vanishes when turbulence promoters are used upstream (within the nozzle). Baughan and Shimizu have reported that for non-swirling jets, a maximum Nusselt number is observed at the stagnation point over the impingement plate when H/D≥6 where turbulence has relativity higher values and the potential core ends [27]. As the distance increases, eddy strength decreases and larger eddies occur, which prompts the thermal boundary layer to breakdown into smaller eddies. This process continues with a larger impingement distance, which leads to continuous degrading in heat transfer rates in the wall jet region [29]. The magnitude and the uniformity of the heat transfer at the target surface are important measurers to evaluate jet performance [36]. In the case of axisymmetric non-swirling jets, peak heat transfer is observed at the stagnation point for a nozzle-to-plate distance H/D=6 where typically the jet potential core ends and turbulence intensities become high. The development of the wall jet region (boundary layer) and velocity profiles leads to a decrease in heat transfer as radial distance increases from the stagnation point [27].

In impinging jet heat transfer, Reynolds number is one of the most influential parameters. In general, for non-swirling impinging jets, a higher Reynolds number leads to more intense heat transfer over the impingement surface for both single and multi-channel impinging jets and also the stagnation zone shrinks as the Reynolds number increases [28,37]. Accordingly, the position of the stagnation point is minimally affected by the Reynolds number. In non-swirling impinging jets, the first peak and second peak in the heat transfer distribution over the target

surface are found to be at 0.5D and 2D in the radial direction, these results are tested against the confined and semi-confined impinging jets (2<x/D<6) [35]. Few studies have found which investigated the conjugate transient heat transfer characteristics of non-swirling impinging jets (chapter 3 addresses them in detail) [38–41]. The current study differs from them due to the utilisation a thin foil heater. The thin foil heater has similar temperature distributions on its both sides due to its small thermal inertia. The temperatures at the front surface of the impingement plate are estimated using Inverse Heat Conduction Problem (IHCP) method, the temperature at the back of the target surface was measured using thermocouples. To the author's best knowledge, no study has utilised high-resolution IR thermography to look at the temporal evolution of transient heat transfer characteristics of swirling impinging jets.

1.2.2 Swirl Impingement

It is evident from the literature that the introduction of swirl alters impingement characteristics at the target surface. Almost all previous studies in this area have induced swirl either using insert or vanes (geometrical swirl). Different opinions were presented regarding impingement surface attributes for swirling jets since geometric swirl induced extra perturbation into the flow, which does not allow the effect of swirl to be measured independent to other parameters. When using helical vanes to generate swirl, Wen and Jang [39] have shown experimentally that a swirling flow has more heat transfer (Nusselt number) at the stagnation point. Many studies which have reported that swirl increases overall heat transfer for H/D>6, have not shown significant increment when the distance reached H/D>10. However, in most of these studies, geometrical inserts have been used to generate swirl [37,40–42]. Swirl generated by inserts or vanes gives less control over the degree of swirl, independent of Reynolds number, making it harder to facilitate a smooth transition from non-swirling to swirling jets compared to aerodynamically induced swirl (via tangential ports). Few studies have analyzed impingement heat transfer in aerodynamically generated swirling jets. Swirl number plays an important role in the flow field and heat transfer characteristics of turbulent swirling jets.

Ward and Mahmood [43] have studied the heat transfer of impinging jets with swirl reporting that the position of maximum Nusselt number shifts (1.5<x/D<2) radially outwards at higher swirl numbers. In non-swirling or low swirl number jets, heat transfer rates are at a maximum at the stagnation region and the small area around it, as shown in Figure 1.4. For a swirl number of 1.05 the maximum heat transfer region shifts radially outward from the stagnation point as shown in Figure 1.4(b). Relatively uniform heat transfer is observed over the impingement

surface for high swirl numbers because of vortices, stretching phenomenon of the jet core, and recirculation zones, which leads to uniform heat transfer rates over the impinging plate [22,43]. However, previous studies have largely utilized a low to moderate range of Reynolds numbers (4000-11500) for swirling jet investigations [43–46], with few studies utilizing high Reynolds numbers for the swirling jets [47].

(a)

(b)
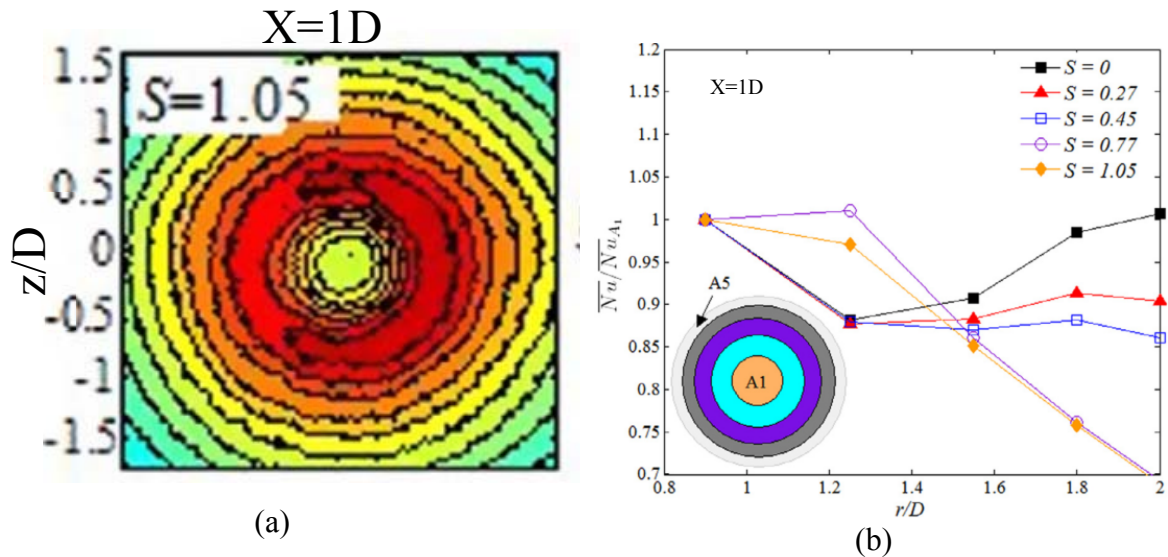
Figure 1.4: The effect of impingement distance (X) and swirl number (S) (at Re = 35,000) (a) Contour plot of Nusselt number (b) Heat transfer uniformity distribution at the impingement plate [47]**.**

Ianiro et al. [11,48] presented an experimental study of swirling impinging jets at a Reynolds number of 28,000, with five different swirl numbers from 0 to 0.8, and five nozzle-to-plate distances (from 2 to 10 nozzle diameters). The swirl was generated by helical vanes, there is zero-velocity zone at the centre of the nozzle due to the spine of the helical vane and adds extra perturbations and complex features into the flow. Infrared thermography and Particle Image Velocimetry was then used to measure surface temperature and flow field, where heat transfer data were averaged over the different areas of the heated plate to make an argument against the uniformity of heat transfer distribution for different operating conditions. Ianiro's [11,48] and Eiamsa-ard et al.'s [49] studies used geometrically generated swirl flow. Non-axisymmetric jet velocity profiles were also reflected in the reported heat transfer data, where these four-distinct regions present non-axisymmetric flow behaviour at the nozzle exit plane which can, therefore, lead to non-uniformity in heat transfer characteristics. Accordingly, there is a need to understand the effects of flow fields on heat transfer characteristics in axisymmetric turbulent swirling (and non-swirling) impinging jets**.**

In an experimental study by Ahmed et al. [47,50] measurements were made for the steady-state temperature distribution using a thin foil constant flux heater for Re=11,600-35,000, S=0-1.05 and H/D=1-6. Figure 1.4 shows the heat transfer intensity for the highest swirl number. Figure 1.4(a) and Figure 1.4(b) that the maximum heat transfer is not always necessarily in the stagnation region, but this depends on the swirl number. For small x/D ≤ 2, the heat transfer rate can be improved significantly from non-swirling to swirling. As mentioned in the literature, the heat transfer rate significantly reduces as the Reynolds number decreases, due to a lessening in overall mass flow rates. Ahmed et al. [47] utilized the same criteria to measure the uniformity of heat transfer over the impingement surface as Ianiro et al. [11]. Nusselt number was shown to vary over the impinging plate for all cases for 0.77<S<1.05 relatively flatter Nusselt number profile was observed compared to 0<S<0.77 noted by Ahmed et al. [47]. Introduction of swirl flow broadens the impinging area, which is why at high nozzle-to-plate distance relatively uniform heat transfer distribution is claimed; however, experimental validation is still needed to determine which flow features are involved.

Ahmed et al.'s [47] study has shown the change of swirl number and its effect on heat transfer distributions but did not address why this phenomenon is happening. Ianiro et al. [11] made flow field measurements try to correlate with heat transfer data, but the swirl was produced by geometrical inserts which can lead to uncertainty and also introduced non-uniformity in heat transfer results. No significant discussion has been found between the relation of heat transfer and flow features. Why is it that an increase in swirl number can lead to spatially uniform heat transfer over an impinging plate? No corroboration has thus far been made between flow field (flow features) and heat transfer; where the flow field measurements are needed to address this question.

Table 1.1: Numerical studies utilized different turbulence models.

Studies	Turbulence Model
Yen at al. [51]	Direct numerical simulation
Khelil et al. [52]	RSM
Wannassi and Monnoyer[53]	SST k-ω
Ahmed et al. [54]	RANS approach with RNG k-ε

Direct numerical simulation (DNS) has been conducted by Yan et al. [51] for free (non-impinging) swirling jets (Reynolds number of 5000) investigating vortex breakdown, anisotropic turbulent motion, and dissipation. For turbulent swirling impinging jets, there is a

high computational cost and so turbulence models (RANS) have been applied. In this context, Khelil et al.[52] carried out a numerical study for a swirling jet array with potential application in HVAC, noting the RSM turbulence model to be better than the standard k-ε in capturing mean flow behaviour. Vane type geometry has been previously used to introduce swirl where impingement has not been considered. Wannassi and Monnoyer [53] have performed experimental and numerical studies for swirling and non-swirling impinging jet array and note that the SST k-ω turbulence model showed fairly accurate results. Ahmed et al. [54] have utilized the velocity boundary conditions, measured at the nozzle exit, for the aerodynamically generated swirling flows. The results were validated against the literature for the non-swirling flow [55,56], where later an axisymmetric simulation was done using a commercial code comparing the flow field for different swirl numbers for small nozzle-to-plate distance. The study claims that the RANS approach with RNG k-ε turbulence model gives better results for turbulent swirling jets in comparison to others. The results of flow with swirl were not validated against any of the experimental data in this study. Numerical studies have used different turbulence models, claiming to work better than others and being able to captured mean flow features.

This lack of consensus in the literature creates a need to further investigate into the effects of different swirl number on flow field characteristics and turbulence (mean and fluctuating velocity components) and then correlate these to heat transfer results. Flow field measurement will be done using 2D PIV, where velocity measurement at the nozzle exit will be conducted using CTA and Infrared thermography will be used to collect heat transfer data on the impingement plane. Numerical simulations will be used to provide an insight into the boundary layer interactions (at the impingement surface with the (PIV) resolved field features). In this project, the temporal evolution of surface heat transfer at various S, Re and H/D will also be examined. Temporal temperature profiles will provide insight as to how system unsteadiness can affect final temperature distribution, which is very important in terms of applications of turbulent swirling jets. This study aims to address gaps in previous studies and to answer the fundamental question of the effects of swirling jets over heat transfer.

1.3 PROJECT MOTIVATION

Impinging jets have numerous applications and have attracted investigation in regards to varying aspects for several decades [2]. Impinging jets have been studied in different operating conditions and configurations, e.g. Reynolds number, swirl intensity, impingement distance,

and multiple nozzle arrays. Despite the availability of such data on impinging jet performance, due to their complex physics, there is still a need to explore flow and heat transfer characteristics with regard to identifying the effects of:

- Upstream inflow conditions on jet development have been studied numerically [54], but its effect on impingement heat transfer for non-swirling and swirling jets has not been investigated.

- Few studies exist looking at the transient cooling effect for non-swirling impinging jets for very high-temperature surfaces. Mostly, thermocouples and Inverse Heat Conduction Problem (IHCP) methods have been utilized for temperature measurements. It can also be observed that no step-by-step guide/method is available for quantifying transient heat/mass transport phenomenon and estimation of the time to reach a steady-state. Many parameters can affect the convection properties and transient time of the process. A detailed methodology along with a method for post-processing of large experimental data has been developed for transient convective processes concerning global average and localized average quantities over the target surface.

- The temporal evolution of impingement heat transfer, in particular, due to its important role in product quality and production speed. To the best of the authors' knowledge, no study has been found that examines the effect of Reynolds number, swirl intensity, and impinging distance on transient heat transfer characteristics of impinging jets over a target surface with advance measurement techniques (e.g. Infrared thermography).

- Few studies have dealt with aerodynamically generated swirl [47,57], pressure and heat transfer characteristics as resolved at the target surface, where flow characteristics were measured using CTA at the exit of the nozzle exit and limited work has been conducted discussing the flow field of swirling (aerodynamically generated) impinging jets. The current research project also investigated the flow features of impinging jets from low to high swirl intensities for Re=11,600, 24,600, and 35,000. A non-intrusive method (Particle Image Velocimetry) is used in contrast to the intrusive method (CTA). CTA technique is also applied to measure the velocity profile at the nozzle exit, these experiments are conducted to ensure the same boundary conditions are being used for the flow field characteristics compared to previously available heat transfer data [47]. These investigations and resolutions of these flow features can be used to explain the impingement characteristics of turbulent swirling jets.

1.4 PROJECT RESEARCH QUESTIONS AND OBJECTIVES

Table 1.2 presents a summary of the methods used in association with the various research questions (RQs) in this project.

Table 1.2: Summary of research question and methodology.

	Methods		Data Needed		
	Experimental	CFD	CTA (Boundary Conditions)	Temperature (Surface Nu)	PIV(Velocity, Turbulence)
RQ 1	✔		✔	✔	
RQ 2		✔	✔		
RQ 3(a)	✔		✔		✔
RQ 3(b)	✔		✔	✔	✔

A brief description of the RQ's covered in this thesis are as follows:

RQ1: How does the temporal evolution of heat transfer compare between swirling and non-swirling impinging jets?

- **RQ1a: Develop a methodology to quantify the transient convective processes parameters using IR thermography.**

  A systematic approach is needed to quantify the transient behaviour of convective processes using IR thermography. The effect of frame rates, rate of change of Nu, image resolution, and spatial discretization is needed to study to verify their effects on time to reach steady-state, quantification of heat transfer characteristics, and extracting features of different regions of interest.

- **RQ1b: Transient heat transfer characteristics of swirling and non-swirling turbulent impinging jets.**

  The steady-state spatial distribution of heat transfer over the impingement surface, for non-swirling and swirling jets, has already been studied [47]. This current work extends this by characterizing the factors which affect the time needed to reach steady-state conditions, in both non-swirling and swirling jets.

RQ2: How do the different boundary conditions at nozzle exit affect the velocity field near the impingement surface and heat transfer characteristics?

- **RQ2a: Effect of upstream inflow conditions on the impingement heat transfer characteristics.**

Numerical studies will be conducted to understand the stagnation and wall jet region (at the impingement surface) for different upstream inflow conditions in turbulent swirling jets. CTA measurements [54] will be used to resolve boundary conditions at the nozzle exit plane (at x/D=0) for non-swirling to weakly swirling turbulent jets. Numerical modelling will use commercial code (Fluent v16.2).

- **RQ2b: Effect of geometric swirl on the impingement heat transfer characteristics.**

  Effect of high turbulent kinetic energy near the nozzle centre will be studied. This high turbulent kinetic energy at the centre is used to mimic the effect of swirl generated using a twisted tape.

RQ3: How does the time-mean flow field (velocity field) affect the heat transfer in turbulent swirling impinging jets?

Different flow field behaviours for swirling and non-swirling jets may affect impingement heat transfer characteristics. These features include vortex breakdown and time-varying instabilities, resolved in free jets [12], as well as flow separation adjacent to the surface in impinging jets [58]. Methods used in the literature to resolve these flow features include non-intrusive diagnostics such as PIV, as well as flow visualization in both (free) swirling and non-swirling jets [59,60]. In the present project, the research questions consider whether any links exist between flow field behaviours and the heat transfer characteristics of impingement. Addressing this research question can be completed in two distinct parts.

- **RQ3a: How does the transition from low swirling (S=0.30) to a high swirling (S=0.74) jet affect the flow field of impinging jets?**
  Features likely to be studied will include vortex breakdown and flow separation at the surface. Experiments will be conducted over a range of swirl numbers (S) and Reynolds numbers (Re) as well as impingement distances (H/D). The analysis will only include the effect of the above on the physical/spatial extent of the flow domain and turbulence field.

- **RQ3b: For impinging jets, what is the correlation between flow field features (resolved in RQ1a) and heat transfer at the surface?**
  Experimental heat transfer data will be characterized by its uniformity over the radial distance of r/D_{nozzle} (<2), and its intensity (peaks, distributions). This will be achieved by comparing the velocity domains resolved (in RQ1a) with already published heat

transfer data resolved using IR imaging [47]. Additional heat transfer data may also be acquired using the thin foil method as outlined by Ahmed et al., [47].

1.5 RESEARCH METHODOLOGY

Experimental and numerical studies will be conducted to answer the fundamental questions in the proposed PhD project. Experimental work will be the core of the project (RQ1 and RQ3), where computational methods will be used to better understand flow and heat transfer at the surface. Computational methods are very helpful when the physical system (experimental setup) reaches its limitations.

1.5.1 Experimental Methods
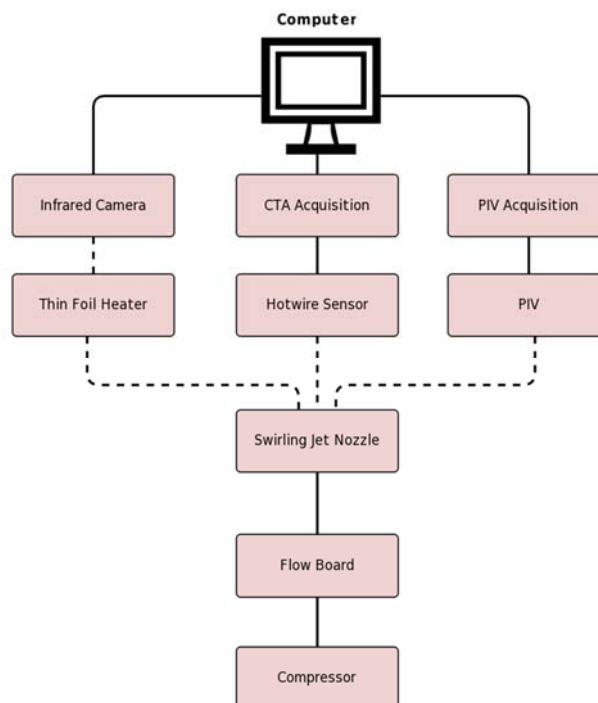
Figure 1.5: Schematic for the experimental setups (solid lines show the physical connection).

Three different types of measurements have been formed to answer the above-mentioned research questions; velocity measurements (boundary conditions), heat transfer measurements, and flow field measurements. The following equipment and methods will be used in the subsequent experimental study.

- Swirling jet nozzle
- Thin foil heater
- Infrared camera
- Constant Temperature Anemometer (CTA)

- Particle Image Velocimetry (PIV)

A specially designed nozzle will be used to supply aerodynamically generated swirling jets. Details about the above-mentioned equipment and their usage in the experimental setups will be discussed in later chapters. Chapters 2 and 3 will discuss the experimental setup, which will be used for measuring the transient heat transfer data. Chapter 5 and Chapter 6 will discuss the details flow field measurement setup.

1.5.2 Computational Methods

RANS (Reynolds-Averaged Navier Stokes) equations will be solved for momentum and energy transport quantities via ANSYS FLUENT and different turbulent models (k-ε STD, k-ω STD, k-ε RNG, k-ω RNG, and k-kl-ω) used to solve flow turbulence. Each model will first be tested against experimental data sets derived from current experiments and the literature. The numerical setup will be confirmed following a range of essential testings such as mesh sensitivity analysis (independence), numerical domain and mesh first layer heights. Initial results show that k-kl-ω performs much better compared to the other turbulence model, where further details are described in Chapter 4.

1.6 THESIS STRUCTURE
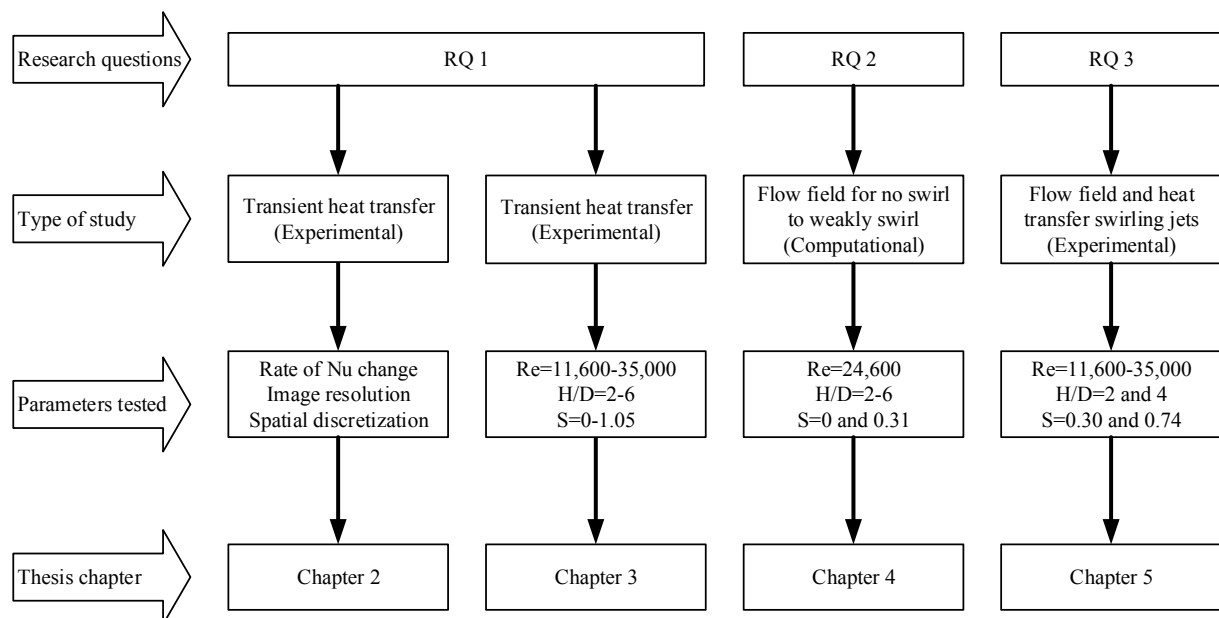
Figure 1.6: Thesis structure.

This thesis is structured in a format of "Thesis with publication[1]". Thesis chapters are organized and presented as follow:

Chapter 1 discusses the thesis topic and its practical applications. This chapter also presents a brief literature review of turbulent impinging jets and identifies the research gaps. Based on identified research gaps, project motivation and research questions are then structured. This chapter also concisely expounds the thesis structure, methodology, and data management plan.

Chapter 2 presents a methodology developed for temporal and spatially resolved transient convection using infrared thermography. This methodology discusses the selection of different parameters like IR image frame rates, image resolution, and the inverse slope of the rate of change of Nu. This chapter also explains the uncertainty in heat transfer experiments and the data processing algorithm. Further experimentation on transient heat transfer characteristics turbulent swirling impinging jet will utilize this method. The chapter is published with a title of "Methodology for spatially resolved transient convection processes using infrared thermography" in the journal Experimental Heat Transfer journal in the year 2020.

Chapter 3 discusses transient heat transfer characteristics of non-swirling and swirling turbulent impinging jets. The temporal evolution of heat transfer is studied for different Reynolds numbers, swirling intensities, and nozzle-to-plate distances. The chapter is published with a title of "Transient heat transfer characteristics of swirling and non-swirling turbulent impinging jets" in the journal Experimental Thermal and Fluid Science journal (Volume: 109, Issue: 1) in the year 2019.

Chapter 4 investigates upstream inflow conditions' effect on flow and heat transfer characteristics for non-swirling and swirling impinging jets. This chapter discusses both flow and heat transfer characteristics using a numerical method. The chapter is published with a title of "Nozzle exit conditions and the heat transfer in non-swirling and weakly swirling turbulent

---

[1] "Thesis with Publication" is an acceptable format of thesis for postgraduate research at ECU policy. The current thesis has been written based on the guideline provided at https://intranet.ecu.edu.au/__data/assets/pdf_file/0007/674035/Research-Training-Procedure-5-Requirements-of-a-Thesis-by-Publication.pdf. In this format, the submitted thesis can consist of publications that have already been published, are in the process of being published, or a combination of these.

impinging jets" in the journal Heat and Mass Transfer journal (Volume: 56, Issue: 1) in the year 2019.

Chapter 5 presents the experimental flow field data for low and high turbulent impinging jets. This chapter also discusses the effect of near-impingement velocity profiles corresponding to heat transfer results for the impingement surface.

Chapter 6 provides an overall discussion on the results which are presented in individual chapters and addresses the integration of chapters into the thesis.

Chapter 7 summarises findings from thesis chapters and outlines possible future research questions/suggestions as an extension to this project.

1.7 DATA MANAGEMENT PLAN

In this project, data types include:

(1) Experimental data;

(2) Computational data; and

(3) Supporting documentation needed to understand both (1) and (2) in the form of text (e.g., log files with operating conditions, environmental parameters, macros/code written for image processing, etc. as necessary/applicable.)

Data management will involve different formats of this data:

(a) Raw (unprocessed) data generated during the course of using various data acquisition systems, geometry/mesh and boundary conditions for CFD; and

(b) Post-processed data derived from (2) or from (1, 2) for the purpose of plotting inside thesis chapters/papers.

The relevant ECU policies (Research Data Management[2]) and guidelines will apply to 1-3 (a/b).

Table 1.3: Data management plan.

<table>
<tr><td colspan="4">Data Management Plan During the
Active Phase of the PhD Project and Upon Completion</td></tr>
<tr><td colspan="4"></td></tr>
<tr><td rowspan="3">Project Active Phase</td><td colspan="3"><u>Research Candidate (local desktop)</u>: Ongoing of most recent files (previous backup: overwrite)</td></tr>
<tr><td colspan="3"><u>Research Candidate (portable media/drive stored in ECU lab)</u>: Monthly backup of most recent files (previous backup: overwrite)</td></tr>
<tr><td colspan="3"><u>University Based Virtual Drive</u>: Quarterly (previous backup: retain)</td></tr>
<tr><td rowspan="2">Project Completion Phase</td><td><u>Data supporting results presented in each thesis chapter/paper:</u> Archive in the form of digital appendices at the end of the thesis (format b, types 1-3).</td><td><u>Data supporting results presented in each thesis chapter/paper:</u> Archive in the form of digital files (format a, types 1-3) on a (to be decided) supervisor nominated drive inside ECU (e.g., the Thermofluids Research Group webpage).</td><td><u>Data not featuring in any thesis chapter/paper:</u> Archive in the form of digital files (format a/b, types 1-3) with the research candidate.</td></tr>
<tr><td colspan="3"></td></tr>
</table>

[2] Research Data Management, http://www.ecu.edu.au/GPPS/policies_db/policies_view.php?rec_id=0000000421

1.8 CHAPTER REFERENCES

[1]   J. Ferrari, N. Lior, J. Slycke, An evaluation of gas quenching of steel rings by multiple-jet impingement, J. Mater. Process. Technol. 136 (2003) 190–201. doi:10.1016/S0924-0136(03)00158-4.

[2]   N. Zuckerman, N. Lior, I. Summary, Jet impingement heat transfer: Physics, correlations, and numerical modeling, Adv. Heat Transf. 39 (2006) 565–631. doi:10.1016/S0065-2717(06)39006-5.

[3]   M. Rantala, R. Karvinen, Heat transfer under an impinging jet at long nozzle-to-surface distances, in: 13th Int. Heat Transf. Conf., Begell House Inc., Sydney, Australia, 2006. doi:10.1615/IHTC13.p16.210.

[4]   J.-C. Han, Je-Chin, Recent Studies in Turbine Blade Cooling, Int. J. Rotating Mach. 10 (2004) 443–457. doi:10.1155/S1023621X04000442.

[5]   N. Zuckerman, N. Lior, Impingement heat transfer: correlations and numerical modeling, J. Heat Transfer. 127 (2005) 544. doi:10.1115/1.1861921.

[6]   Han, Je-Chin, Sandip Dutta, and S. Ekkad, Gas turbine heat transfer and cooling technology, CRC Press, 2012.

[7]   K.H. Lee, R. Viskanta, Quenching of flat glass by impinging air jets, Numer. Heat Transf. Part A Appl. 33 (1998) 5–22. doi:10.1080/10407789808913925.

[8]   J. Eggers, E. Villermaux, Physics of liquid jets, Rep. Prog. Phys. 71 (2008) 36601–79. doi:10.1088/0034-4885/71/3/036601.

[9]   H. Martin, Heat and Mass Transfer between Impinging Gas Jets and Solid Surfaces, Adv. Heat Transf. 13 (1977) 1–60. doi:10.1016/S0065-2717(08)70221-1.

[10]   S.B. Pope, Turbulent Flows, IOP Publishing, 2001. doi:10.1088/0957-0233/12/11/705.

[11]   A. Ianiro, G. Cardone, Heat transfer rate and uniformity in multichannel swirling impinging jets, Appl. Therm. Eng. 49 (2012) 89–98. doi:10.1016/j.applthermaleng.2011.10.018.

[12]   Y.M. Al-Abdeli, A.R. Masri, Recirculation and flowfield regimes of unconfined non-

reacting swirling flows, Exp. Therm. Fluid Sci. 27 (2003) 655–665. doi:10.1016/S0894-1777(02)00280-7.

[13] M. Stöhr, I. Boxx, C. Carter, W. Meier, Dynamics of lean blowout of a swirl-stabilized flame in a gas turbine model combustor, Proc. Combust. Inst. 33 (2011) 2953–2960. doi:10.1016/j.proci.2010.06.103.

[14] Y. Huang, V. Yang, Effect of swirl on combustion dynamics in a lean-premixed swirl-stabilized combustor, Proc. Combust. Inst. 30 (2005) 1775–1782. doi:10.1016/j.proci.2004.08.237.

[15] N. Syred, J.M.M. Beér, Combustion in swirling flows: A review, Combust. Flame. 23 (1974) 143–201. doi:10.1016/0010-2180(74)90057-1.

[16] W.L.H. Hallett, R. Günther, Flow and mixing in swirling flow in a sudden expansion, Can. J. Chem. Eng. 62 (1984) 149–155. doi:10.1002/cjce.5450620123.

[17] L.Y. Hu, L.X. Zhou, J. Zhang, M.X. Shi, Studies on strongly swirling flows in the full space of a volute cyclone separator, AIChE J. 51 (2005) 740–749. doi:10.1002/aic.10354.

[18] B. Wang, D.L. Xu, K.W. Chu, A.B. Yu, Numerical study of gas–solid flow in a cyclone separator, Appl. Math. Model. 30 (2006) 1326–1342. doi:10.1016/j.apm.2006.03.011.

[19] A. Dewan, R. Dutta, B. Srinivasan, Recent Trends in Computation of Turbulent Jet Impingement Heat Transfer, Heat Transf. Eng. 33 (2012) 447–460. doi:10.1080/01457632.2012.614154.

[20] M.P. Escudier, J. Keller, Recirculation in swirling flow - A manifestation of vortex breakdown, AIAA J. 23 (1985) 111–116. doi:10.2514/3.8878.

[21] Y.M. Al-Abdeli, A.R. Masri, Review of laboratory swirl burners and experiments for model validation, Exp. Therm. Fluid Sci. 69 (2015) 178–196. doi:10.1016/j.expthermflusci.2015.07.023.

[22] A. Nozaki, Y. Igarashi, K. Hishida, The Heat Transfer Mechanism of a Swirling Impinging Jet in the Stagnation Region., Trans. Japan Soc. Mech. Eng. Ser. B. 32 (2003) 663–673. doi:10.1299/kikaib.68.2300.

[23]   P. Meliga, F. Gallaire, J.-M. Chomaz, A weakly nonlinear mechanism for mode selection in swirling jets, J. Fluid Mech. 699 (2012) 216–262. doi:10.1017/jfm.2012.93.

[24]   A. Gorbunova, A. Klimov, N. Molevich, I. Moralev, D. Porfiriev, S. Sugak, I. Zavershinskii, Precessing vortex core in a swirling wake with heat release, Int. J. Heat Fluid Flow. 59 (2016) 100–108. doi:10.1016/j.ijheatfluidflow.2016.03.002.

[25]   Y.M. Al-Abdeli, A.R. Masri, & Assaad, R. Masri, A.R. Masri, Precession and recirculation in turbulent swirling isothermal jets, Combust. Sci. Technol. 176 (2004) 645–665. doi:10.1080/00102200490427883.

[26]   A.J. Yule, Large-scale structure in the mixing layer of a round jet, J. Fluid Mech. 89 (1978) 413–432. doi:10.1017/S0022112078002670.

[27]   J.W. Baughn, S. Shimizu, Heat transfer measurements from a surface with uniform heat flux and an impinging jet, J. Heat Transf. (Transactions ASME). 111 (1989) 1988–1990. doi:10.1115/1.3250776.

[28]   C. Kinsella, B. Donnelly, T.S. O'Donovan, D.B. Murray, Heat transfer enhancement from a horizontal surface by impinging swirl jets, in: 5th Eur. Therm. Conf. , The Netherlands, 2008.

[29]   K. Kataoka, M. Suguro, H. Degawa, K. Maruo, I. Mihata, The effect of surface renewal due to largescale eddies on jet impingement heat transfer, Int. J. Heat Mass Transf. 30 (1987) 559–567. doi:10.1016/0017-9310(87)90270-5.

[30]   R. Viskanta, Heat Transfer to Impinging Isothermal Gas and Flame Jets, Exp. Therm. Fluid Sci. 6 (1993) 111–134. doi:10.1016/0894-1777(93)90022-B.

[31]   K. Jambunathan, E. Lai, M.A.A.A. Moss, B.L.L.L. Button, A review of heat transfer data for single circular jet impingement, Int. J. Heat Fluid Flow. 13 (1992) 106–115. doi:10.1016/0142-727X(92)90017-4.

[32]   E.M. Sparrow, T.C. Wong, Impingement transfer coefficients due to initially laminar slot jets, Int. J. Heat Mass Transf. 18 (1975) 597–605. doi:10.1016/0017-9310(75)90271-9.

[33]   L.W. Florschuetz, C.R. Truman, D.E. Metzger, Streamwise flow and heat transfer

distributions for jet array impingement with crossflow, J. Heat Transfer. 103 (1981) 337–342. doi:10.1115/81-GT-77.

[34]   N.A. Chigier, A. Chervinsky, Experimental investigation of swirling vortex motion in jets, J. Appl. Mech. 34 (1967) 443. doi:10.1115/1.3607703.

[35]   R. Gardon, J.C. Akfirat, The role of turbulence in determining the heat-transfer characteristics of impinging jets, Int. J. Heat Mass Transf. 8 (1965) 1261–1272. doi:10.1016/0017-9310(65)90054-2.

[36]   J.A. Fitzgerald, S. V. Garimella, A study of the flow field of a confined and submerged impinging jet, Int. J. Heat Mass Transf. 41 (1998) 1025–1034. doi:10.1016/S0017-9310(97)00205-6.

[37]   K. Bilen, K. Bakirci, S. Yapici, T. Yavuz, Heat transfer from a plate impinging swirl jet, Int. J. Energy Res. 26 (2002) 305–320. doi:10.1002/er.785.

[38]   F.P. D'Aleo, H.-M. Prasser, Transient heat flux deduction for a slab of finite thickness using surface temperature measurements, Int. J. Heat Mass Transf. 60 (2013) 616–623. doi:10.1016/J.IJHEATMASSTRANSFER.2013.01.049.

[39]   A. Ryfa, R.A. Bialecki, Retrieving the heat transfer coefficient for jet impingement from transient temperature measurements, Int. J. Heat Fluid Flow. 32 (2011) 1024–1035. doi:10.1016/J.IJHEATFLUIDFLOW.2011.06.005.

[40]   L.-K. Liu, W.-S. Su, Y.-H. Hung, Transient convective heat transfer of air jet impinging onto a confined ceramic-based MCM disk, J. Electron. Packag. 126 (2004) 159–172. doi:10.1115/1.1649239.

[41]   H. Yazici, M. Akcay, M. Golcu, M.F. Koseoglu, Y. Sekmen, Experimental investigation of transient temperature distribution and heat transfer by jet impingement in glass tempering processing, Trans. Mech. Eng. 39 (2015) 337–349. doi:10.22099/IJSTM.2015.3244.

[42]   M.-Y. Wen, K.-J. Jang, An impingement cooling on a flat surface by using circular jet with longitudinal swirling strips, Int. J. Heat Mass Transf. 46 (2003) 4657–4667. doi:10.1016/S0017-9310(03)00302-8.

[43] H.Q. Yang, T. Kim, T.J. Lu, K. Ichimiya, Flow structure, wall pressure and heat transfer characteristics of impinging annular jet with/without steady swirling, Int. J. Heat Mass Transf. 53 (2010) 4092–4100. doi:10.1016/j.ijheatmasstransfer.2010.05.029.

[44] L. Huang, M.S.S. El-Genk, Heat transfer and flow visualization experiments of swirling, multi-channel, and conventional impinging jets, Int. J. Heat Mass Transf. 41 (1998) 583–600. doi:10.1016/S0017-9310(97)00123-3.

[45] D. Hee Lee, S. Youl Won, Y. Taek Kim, Y. Suk Chung, Turbulent heat transfer from a flat surface to a swirling round impinging jet, Int. J. Heat Mass Transf. 45 (2002) 223–227. doi:10.1016/S0017-9310(01)00135-1.

[46] J. Ward, M. Mahmood, Heat transfer from a turbulent, swirling, impinging jet, in: Proc. 7th Int. Heat Transf. Conf., Munich, West Germany, 1982: pp. 401–407.

[47] E.P. Volchkov, V. V. Lukashov, S. V. Semenov, Heat transfer in an impact swirling jet, Heat Transf. Res. 27 (1996) 14–24.

[48] K. ICHIMIYA, K. Tsukamoto, Heat Transfer from an Inflow-Type Swirling Turbulent Impinging Jet, JSME Int. J. Ser. B. 49 (2006) 995–999. doi:10.1299/jsmeb.49.995.

[49] I.K. Toh, D. Honnery, J. Soria, Axial plus tangential entry swirling jet, Exp. Fluids. 48 (2010) 309–325. doi:10.1007/s00348-009-0734-2.

[50] Z.U. Ahmed, Y.M. Al-Abdeli, F.G. Guzzomi, Heat transfer characteristics of swirling and non-swirling impinging turbulent jet, Int. J. Heat Mass Transf. 102 (2016) 991–1003. doi:10.1016/j.expthermflusci.2015.07.017.

[51] A. Ianiro, D. Violato, F. Scarano, G. Cardone, Three dimensional features in swirling impinging jets, in: 15th Int. Symp. Flow Vis., June 25-28, 2012, Minsk, Belarus, 2012.

[52] S. Eiamsa-Ard, K. Nanan, K. Wongcharee, Heat transfer visualization of co/counter-dual swirling impinging jets by thermochromic liquid crystal method, Int. J. Heat Mass Transf. 86 (2015) 600–621. doi:10.1016/j.ijheatmasstransfer.2015.03.031.

[53] Z.U. Ahmed, Y.M. Al-Abdeli, F.G. Guzzomi, Corrections of dual-wire CTA data in turbulent swirling and non-swirling jets, Exp. Therm. Fluid Sci. 70 (2016) 166–175. doi:10.1016/j.expthermflusci.2015.09.007.

[54] X. Yang, N. Gui, G. Xie, J. Yan, J. Tu, S. Jiang, Anisotropic Characteristics of Turbulence Dissipation in Swirling Flow : A Direct Numerical Simulation Study, 2015 (2015).

[55] A. Khelil, H. Naji, L. Loukarfi, M.H. Meliani, M. Braikia, Numerical simulation of the interactions among multiple turbulent swirling jets mounted in unbalanced positions, Appl. Math. Model. 40 (2016) 3749–3763. doi:10.1016/j.apm.2015.10.047.

[56] M. Wannassi, F. Monnoyer, Fluid flow and convective heat transfer of combined swirling and straight imping jet arrays, Appl. Therm. Eng. 78 (2015) 62–73. doi:10.1016/j.applthermaleng.2014.12.043.

[57] Z.U. Ahmed, Y.M. Al-Abdeli, M.T. Matthews, The effect of inflow conditions on the development of non-swirling versus swirling impinging turbulent jets, Comput. Fluids. 118 (2015) 255–273. doi:10.1016/j.compfluid.2015.06.024.

[58] M.J. Tummers, J. Jacobse, S.G.J. Voorbrood, Turbulent flow in the near field of a round impinging jet, Int. J. Heat Mass Transf. 54 (2011) 4939–4948. doi:10.1016/j.ijheatmasstransfer.2011.07.007.

[59] M. Fairweather, G. Hargrave, Experimental investigation of an axisymmetric, impinging turbulent jet. 1. Velocity field, Exp. Fluids. 33 (2002) 464–471. doi:10.1007/s00348-002-0479-7.

[60] Z.U. Ahmed, Y.M. Al-Abdeli, F.G. Guzzomi, Impingement pressure characteristics of swirling and non-swirling turbulent jets, Exp. Therm. Fluid Sci. 68 (2015) 722–732. doi:10.1016/j.expthermflusci.2015.07.017.

[61] C. Shekhar, K. Nishino, Oscillation and heat transfer in upward laminar impinging jet flows, Int. J. Heat Fluid Flow. 50 (2014) 316–329. doi:10.1016/j.ijheatfluidflow.2014.09.001.

[62] R. Santhosh, S. Basu, Acoustic response of vortex breakdown modes in a coaxial isothermal unconfined swirling jet, Phys. Fluids. 27 (2015) 0–22. doi:10.1063/1.4913703.

[63] H.D. Zhang, C. Han, T.H. Ye, J.M. Zhang, Y.L. Chen, Large eddy simulation of

unconfined turbulent swirling flow, Sci. China Technol. Sci. 58 (2015) 1731–1744. doi:10.1007/s11431-015-5912-2.

Chapter 2: Methodology for Spatially Resolved Transient Convection Using Infrared Thermography

This chapter discusses the method for the quantification of heat transfer characteristics using infrared camera. Effect of the measuring parameters (image resolution, and spatial discretization) and physical parameter (e.g. rate of change of Nusselt number) is studied on heat transfer distribution and time to reach steady-state.

2.1 INTRODUCTION

Quantification of convective heat transfer fluxes bears significance in numerous industrial applications in relation to bettering product quality and maintaining process control. Several methods have been developed over the course of time to monitor surface temperatures including RTDs (Resistance Temperature Detectors), thermocouples, pyrometers, and IR (Infrared) thermography [1,2]. The latter has an advantage over other methods in that surface temperatures can be mapped with high spatial resolution, is non-intrusive in nature, has a high sensitivity (as low as 20mK) and very low response time (down to 20 μs). Moreover, infrared thermography can be employed efficiently for both steady-state and transient convective heat transfer [3,4].

In many experiments, the heated thin foil method is used along with IR thermography for steady-state (time-averaged) heat transfer measurements. Researchers have used this approach extensively in thermo-fluid dynamics research [2,5]. Since many turbulent flows are inherently unsteady, with many being three-dimensional in nature, time-averaged (steady-state measurements) sometimes do not suffice when resolving transient heat transfer characteristics. In such cases, temporally resolved analyses are needed to explore the underlying physics. However, limited literature exists into methods used to define transient heat transfer characteristics over a surface. A seminal work from Nakamura [6] described the reason behind the limited experimental work conducted into transient heat transfer using IR thermography and attributed this to the challenges of accurately monitoring temperatures because of the fluctuations, thermal inertia of substrate, and the temperature distributions from the turbulent flow.

Hetsroni and Rozenblit [7] studied transient heat transfer in a flume, specifically focusing on thermal interactions in particle-laden turbulent flows over a heated plate. They observed that the addition of particles increases the temperature fluctuations. Sanimuel Vila et al. [8] studied

transient convection in water over a horizontal plane and identified three subsequent phases for the onset of horizontal convection. These three different phases are pure conduction across the fluid layer, the transition phase (Rayleigh-Benard Convection), and longitudinal rolls which evolved over time. Nakamura and Yamada [9] made time-resolved unsteady flow measurements in the turbulent boundary layer over a flat plate for a backward-facing step in what can be considered amongst the few successful experiments using optical thermography in contrast to the current experiments which are conducting transient effect of convection when system exposed to the flow to system reach to steady-state. Greco et al. [10] and Raiola et al. [4] performed experiments for transient heat transfer in a periodic flow, i.e. synthetic jet [11–15] (impingement). They described Proper Orthogonal Decomposition (POD) and a polynomial filter for the reduction of random noise in temperature measurements. However, in almost all these works there is a little exploration of the intricacies for these methods which limits their application. Hence, there exists a need to develop and present detailed methodologies for capturing transient heat transfer characteristics and identify factors affecting these techniques. To bridge this gap, this paper presents a detailed methodology for the characterization of both spatially and temporally resolved convective transient heat transfer when swirling and non-swirling turbulent jets impinge onto a thin foil heater [16].

It is worth noting that whilst many researchers have studied transient heat transfer in impinging jets [17–20], most have used thermocouples or RTDs because of their high sampling rate, which comes at the cost of coarse spatial resolution. In this regard, Mitsutake and Monde [21] studied transient heat transfer for an impinging liquid jet, with the impingement surface kept at very high temperatures (initially at 250 °C). Heat transfer was measured using (low spatial resolution, intrusive) thermocouples, whereby wetting and non-wetting regions were observed using high-speed imaging (at 2000 fps). Liu et al. [22] investigated the heat transfer from a Multi-Chip-Module (MCM) using thermocouples with impinging jets and developed correlations for predicting steady-state heat transfer at different ranges of Grashof number $(2.753 \times 10^5 - 1.368 \times 10^6)$, Reynolds number (867-14470), and nozzle-to-plate spacing (H/D=1-12). Yazici et al. [17] investigated transient temperature distribution for a glass plate at 700 °C over three different points (r/D=0, 1, and 2) using thermocouples too. They observed that the system needed a longer time to reach steady-state for the lowest Reynolds number tested (Re=20,000), but exhibited the shortest time (34.5sec) needed for nozzle-to-plate spacing H/D=6. Dou et al. [19] used the ICHP (Inverse Heat Conduction Problem) method to evaluate temperatures on the front surface for a thick metallic impinging plate. The temperatures were

measured at the back of the plate using thermocouples, but this method introduced extra uncertainty in the experimental results compared to the IR thermography method. Thick metallic plates cannot be utilized for their high thermal capacity, excessive thermal inertia, and lateral conduction. **Table 2.1** summarizes some of the transient heat transfer studies conducted and shows that methods used with the vast majority of high Reynolds number flows have unfortunately been based largely on a thick substrate and (spatially intrusive) thermocouples. As such, there is an opportunity to develop and disseminate the details of more accurate transient methodologies (image processing methods), compatible with non-intrusive techniques (e.g. IR) and featuring low thermal capacity heated surfaces (e.g. heated foils).

Table 2.1: Summary of experimental research into convective transient heat transfer characteristics.

Authors	Temperature Measurement	Set-up	Jet Fluid	Re	Heater Type
Guo et al. [38]	T	IJ	G	14,000-53,000	TM
Yazici et al. [17]	T	IJ	G	20,000-40,000	TM
Dou et al. [19]	T	IJ	G	22,000-31,000	TM
Mitsutake and Monde [21]	T	IJ	L	10,000-30,000	TM
Hetsronu and Rozenblit [7]	IRT	FPBL	L	5,100-15,400	TF
Liu et al. [22]	IRT	IJ	G	800-15,000	TM
Raiola et al. [4]	IRT	SJ	G	5,100	TF
Greco et al. [10]	IRT	SJ	G	5,100	TF
Yi et al. [39]	TLC	IJ	G	3500	TM
Nakamura and Yamda [9]	IRT	BFS	G	280-925	TF
Sanimuel Vile et al. [8]	IRT	FPBL	L	NA	TF
Nakamura [6]	IRT	FPBL	G	NA	TF

T: Thermocouple, IRT: Infrared Thermography, TLC: Thermo-Chromic Liquid Crystal
IJ: Impinging Jet, FPBL: Flat Plate Boundary Layer, BFS: Backward Facing Step, SJ: Synthetic Jet
Jet Fluid- L: Liquid, G: Gaseous
TM: Thick Metallic, TF: Thin Foil

Infrared thermography has probably not been explored much for transient heat transfer because of the thermal conductivity and inertia of a target surface, subjected to turbulent flow, experience high rates of temperature fluctuations which then requires image processing to resolve the quickly changing (dynamic) field of view [6]. And so, the availability of affordable IR cameras with high sensitivity and low response time provides an opportunity to explore different filtration techniques (reduction of random noise) and the application of proper orthogonal decomposition and polynomial filtration [4,10]. To date, it is believed that no study has presented a methodical approach for obtaining transient heat transfer for thin foil heater in processes using IR thermography whilst also discussing the systematic procedures for

acquiring and quantitatively post-processing the imaged (infrared) data. Few studies mentioned in the Table 2.1, which used the IR thermography for impinging jet used thick metallic plates and obtained conjugate heat transfer data. Since the thick metallic plates have high thermal inertia which is why it does not allow to isolate the convective effect from the conjugate heat transfer phenomena. After outlining the parameters governing the main flow dynamics of the turbulent jets which form the basis of the heat transfer processes studied in this paper, the time-resolved indicators of heat transfer are detailed. These are then used as the basis for the ensuing sensitivity analysis, which also presents the effects of data processing rate of image acquisition (frame) rate and data filtration techniques have on defining the extent of the start-up period over which the jets transition to steady-state. The paper concludes with several cases used to test the methods presented using the MATLAB image processing code developed (see Chapter Appendices).

2.2 EXPERIMENTAL SETUP

Figure 2.1 shows the schematic diagram of the experimental setup utilized which consists of a nozzle supplying a steady axisymmetric jet, a PC based data acquisition system, an infrared camera, and a (heated) impingement plate. The infrared camera (make: FLIR, model: A325) which operates between the spectral range of 7.5-13μm is used to map the temperature distribution. This infrared camera has 76,800 (320 x 240) micro-bolometer detectors having a pixel-to-pixel pitch of 25μm, low response time (7ms), and ±2% accuracy. Swirl numbers for the turbulent jets are selected to avoid any periodicity generated by a precessing vortex core. The $<u>$ and $<w>$ are measured using CTA at the centre of the nozzle exit, where $<u>$ and $<w>$ are the local axial and tangential velocities are the nozzle exit. The transient time calculated in the results are therefore not due to any fluidic time periodicity, but rather transient heat transfer characteristics. Although the methods described in this paper are applied to resolving the transient heat transfer during the initial stabilization of a steady impinging jet [16], they can be transferred with phase-locked imaging to a periodic/oscillating (synthetic jet) flow [4]. They are also applicable to steady or time-varying behaviours associated with boundary layer heat transfer problems [8], or other flow dynamics such as a backward-facing step [23]. The nozzle, in which swirl is aerodynamically generated using three tangential ports and two axial ports [24], allows a range of Reynolds numbers and swirl intensities to be established, independent of each other in contrast to swirling flows that utilize geometrical inserts/vanes. The nozzle exit diameter (D) is 40mm with a sharp (knife) edge (0.2mm) at the jet exit plane which reduces flow separation [25].

Convective heat transfer measurements are made using infrared thermography along with the thin foil constant heat flux technique. Flow from the nozzle impinges vertically upward over an uncooled target surface placed at a distance (H), whereas only the backside of the impingement plate is painted matt black (make: VHT, model: flameproof) with an emissivity of 0.97, estimated from another experiment [26,27]. The (other, opposite) unpainted face of the heated foil faces the flow and constitutes the impingement plane. The infrared camera resolves the temperature distribution over the painted side. A high current DC power supply (make: Powertech, Model: MP3094) is used to heat up the 25μm thick stainless steel foil (AISI316) having dimensions of 320 x 200 mm. The foil is energized using the Joule effect by applying 120watts (40A, 3V). The heat flux variation is evaluated as ±2% [27], hence it is considered constant for the whole heater surface.
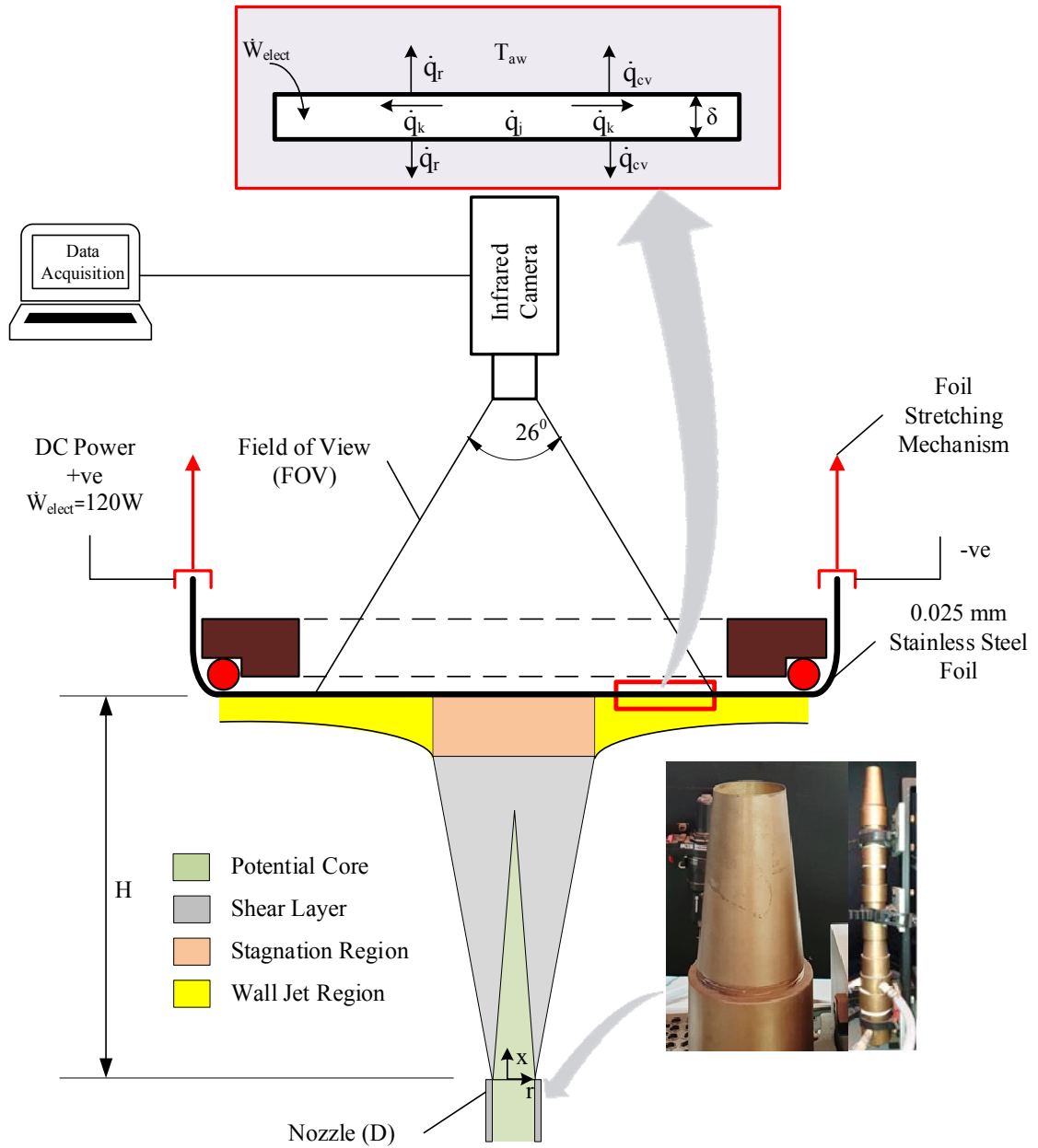
Figure 2.1: Experimental setup and the characteristic regions of an unconfined axisymmetric (cool) jet impinging onto a heated surface (also shows a schematic diagram of the experimental setup). The inset shows the energy balance across a heated thin foil (top) as well as an image of the nozzle and it's head (bottom).

Global properties for the jets studied herein are described by the Reynolds and swirl number, as defined by Equations (2-1) and (2-2), respectively. Where Q is the combined flow rate from the tangential and axial ports on the nozzle.

$$Re = \frac{\rho U_b D}{\mu} = \frac{4Q}{\pi D \nu} \tag{2-1}$$

$$S = \frac{W_b}{U_b} \qquad (2\text{-}2)$$

In the presented results, the Reynolds number (Re) is kept constant at 35,000 (with 4% experimental uncertainty [27]) whilst the swirl number (S) is varied from 0 (non-swirling) to 1.05 (highly swirling) for three nozzle-to-plate spacing (H/D=2-6). The bulk axial (U_b) and tangential (W_b) velocities are estimated using the velocity profiles measured 1 mm above at the nozzle exit plane using Constant Temperature Anemometry (CTA, make: Dantec, model: 90N10 (Streamware processor)) [16,28]. The bulk velocities are computed using Equations (2-3) and (2-4).

$$U_b = \frac{2}{R^2} \int_0^R r \langle u \rangle dr \qquad (2\text{-}3)$$

$$W_b = \frac{2}{R^2} \int_0^R r \langle w \rangle dr \qquad (2\text{-}4)$$

The energy balance for a thin foil (Figure 2.1) is expressed by Equation (2-5), where c, ρ, k_{foil}, and δ denote the specific heat coefficient, density, thermal conductivity, and thickness of the foil heater respectively. The applied heat flux (joule effect) is q̇ and can be estimated as q̇=EI, whereas q̇$_k$, q̇$_r$, and q̇$_{cv}$ represent the heat flux through conduction (lateral), radiation, and convection, respectively. The wall temperature (T_w) is considered constant along with the foil thickness and heat transfer through the side (q̇$_k$), which is not subjected to the turbulent flow, is insignificant and can be neglected [27]. This assumption can be justified since the Biot number (Bi=hδ/k$_{foil}$) is significantly lesser than unity in contrast to the Fourier number F$_o$=kfoil/(ρcπfδ2), which is significantly greater than one.

$$\underbrace{\dot{q}}_{\substack{Input \\ Heat\ Flux}} = \underbrace{c\rho\delta\frac{dT_w}{dt}}_{\substack{Thermal \\ Capacitance}} + \underbrace{k_{foil}\delta\nabla^2 T_w}_{\substack{Condutive \\ Flux}} - \underbrace{h(T_w - T_{aw})}_{\substack{Convective \\ Flux}} - e.\underbrace{\beta\left(T_w{}^4 - T_{amb}{}^4\right)}_{\substack{Radiative \\ Flux}} \qquad (2\text{-}5)$$

Each term in Equation (2-5) presents the heat flux which adds up to the total heat flux supplied to the thin foil heater. In relation to the radiation term (e: emissivity, β: Stefan Boltzmann constant), the operating temperatures (at constant heat flux) are less than 100 °C, and hence

radiative heat transfer is insignificant and neglected (this should be quantified for higher temperatures using the Stefan Boltzmann law). Additionally, the metallic foil heater's very small thickness in the lateral direction (25μm) means temperatures (in that direction) are relatively constant in each 33ms time interval, unlike much of the other research conducted with thicker substrates having thicknesses of 1 to 10mm [17–19,29,30]. With infrared images acquired at a 30Hz frame rate, but impinging jet thermal processes requiring at least 10sec to stabilize [16], each computational time step is only 0.33% of the entire transient process which justifies cancelling the time dependence nature of the conductive term in every time step (i.e., assumed steady over any 33ms). The thermal storage term in Equation (2-5) for the 25μm metallic foil due to its low thermal mass, compared to the (turbulent) convective fluxes over its 300mm x 200mm area. Hence, they are also neglected unless infrared imaging is done at microsecond level [9], something that is not necessary for the current experiments where thermal stability occurs after ~10sec [16] (see also Figure 2-A1 in the Chapter Appendices). By applying all the assumptions, Equation (2-5) reduces to a time-resolved definition of heat transfer coefficient as described by Equation (2-6) [31], where the pixel location is denoted by j and k, and t is the time stamp for each quantity, which can be estimated from the time series of IR. The adiabatic wall temperature (Tref) is measured while the jet was running without power to the heater (i.e. ambient temperature).

$$h(j,k,t) = \frac{q - q_l(j,k,t)}{T_w(j,k,t) - T_{aw}(j,k,t)} \tag{2-6}$$

Pixel-to-pixel (local) heat transfer (spatially resolved) can be estimated using Equation (2-7), whilst the average Nusselt number ($\overline{Nu}$) over the imaged area (A) can be calculated by Equation (2-8).

$$Nu(x,y,t) = \frac{h(x,y,t)D}{\lambda} \tag{2-7}$$

$$\overline{Nu}(r) = \frac{1}{A}\int_A Nu(r)dA \tag{2-8}$$

It is worth noting here that in Equation 8 the area (A) over which $\overline{Nu}(r)$ is calculated can be spatially selected, as will appear later with several regions of interest discretized (A1-A5,

Aavg). The conversion from pixel to Cartesian coordinates is achieved by imaging an object of known dimension and also verified3. In summary, through Equations (2-7) and (2-8), the heat transfer characteristics (represented by the Nusselt number) are both temporally (Equation (2-7)) and spatially resolved (Equation (2-8)).

2.3 IMAGE PROCESSING METHODOLOGY

2.3.1 Frame Rates

The infrared thermography sample/frame rate is crucial in transient heat transfer analyses. Unnecessary high sampling rates can lead to larger than needed data, which later might be computationally expensive to process whilst adding little substance to the outcomes. A lower than necessary sampling rate can, however, bias the outcomes by failing to capture transients. For periodic flows, phase-locking can also yield highly resolved heat transfer characteristics over each cycle if the camera does not permit very high frame rates [4].
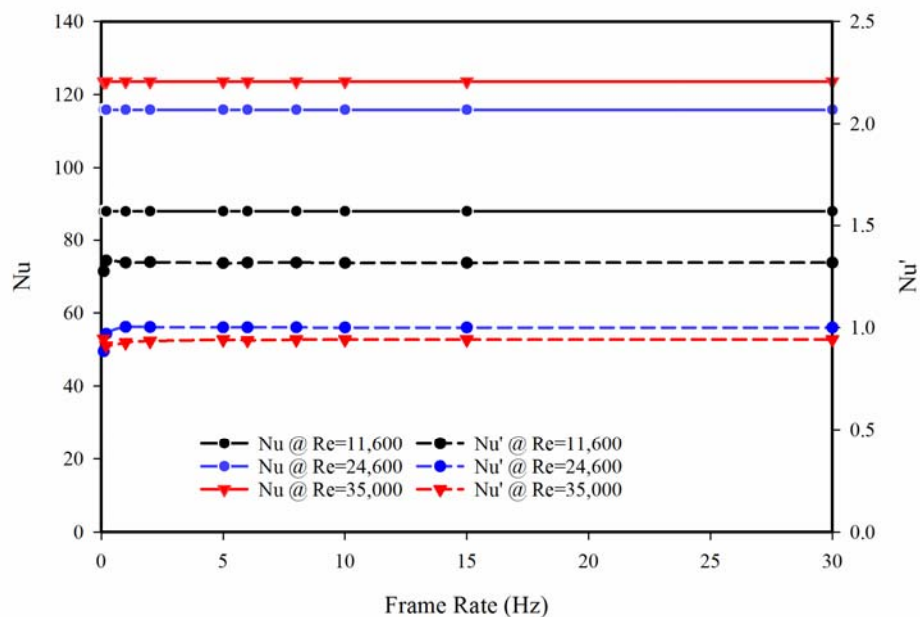
Figure 2.2: Selection of suitable frame rate for the current transient heat transfer characteristics based on $\overline{Nu}_{st-st}$ **(H/D = 2, S = 0).**

Figure 2.2 analyses effects of frame rate and their impact on the post-processed Nusslet number and its fluctuation $\overline{Nu}_{st-st}$ and Nu'_{st-st} when calculated using Equation (2-9) and (2-10). To

---

[3] http://flir.custhelp.com/app/utils/fl_fovCalc/pn/48001-1001/ret_url/%252Fapp%252Ffl_download_datasheets%252Fid%252F8

35

achieve this, imaged data acquired at 30 Hz in non-swirling jets (S=0) over a range of Reynolds numbers (Re=11,600, 24,600, and 35,000) is filtered to effectively yield different frame acquisition rates (e.g. when every other image is considered, an effective rate of 15Hz is simulated). Figure 2.2 confirms that an image acquisition frequency of 30Hz does not bias the $\overline{Nu}_{st-st}$ and Nu'_{st-st} calculated by applying Equation 9 and 10. It is observed that $\overline{Nu}_{st-st}$ and Nu'_{st-st} are largely independent of frame rate beyond 2 Hz. As such, the 30Hz image acquisition rate used throughout this study is deemed adequate.

$$\overline{Nu}_{st-st} = \frac{\sum_{i=1}^{M} Nu_i}{M} \tag{2-9}$$

$$Nu'_{st-st} = \sqrt{\frac{\sum_{i=1}^{M} (Nu_i - Nu_{avg})^2}{M-1}} \tag{2-10}$$

2.3.2 Data Filtration

There is a need to reduce noise in captured IR data. The polynomial filter, Proper Orthogonal Decomposition (POD), and hybrid filter (polynomial + POD) method have been widely used in turbulent flows and their transient heat transfer characteristics. In this context, Raiola et al. [4] discussed the implementation of proper orthogonal decomposition filtration for periodic flows and also explored polynomial filters along with POD for the heat transfer characteristics (transient/periodic) of synthetic jet actuators. Narayanan and Patil [32] implemented the POD filter for slot jet impingement over a thin foil heater [24,33]. The POD filter is highly recommended [34] for periodic flow and heat transfer measurements as is claimed to increase the dynamic range of measurements and improves the data spectra with high frequency. The Savitzky-Golay filter also known as a polynomial (i.e. first-order moving average in the current paper) is used in digital signal processing, which is recommended by some researchers for smoothing time series temperature data [35].

A 1-D moving average filter is good enough to damp out the unwanted fluctuations from captured data and help resolve the initial transient stage. This is the most commonly used digital signal processing technique for time-domain data [19]. Equations (2-11) to (2-14) are used for the implementation of data filtration. This is also known as the data convolution method [35].

$$B'(i) = \frac{B\left(i - \frac{n-1}{2}\right) + \cdots + B\left(i + \frac{n-1}{2}\right)}{n} \tag{2-11}$$

$$E(i) = B(i) - B'(i) \tag{2-12}$$

$$E'(i) = \frac{E\left(i - \frac{n-1}{2}\right) + \cdots + E\left(i + \frac{n-1}{2}\right)}{n} \tag{2-13}$$

$$F(i) = B'(i) - E'(i) \tag{2-14}$$

In this regard, B(i) is the spatially averaged Nu over the imaged area (region of interest) based on (unfiltered) data while B′(i) is its moving average over n (number of) values. E(i) and E'(i) are the absolute error and its moving average, respectively, which are used to calculate F(i). In the applied 1-D median filter for smoothing data, n=10 as recommended [19,35]. The effect of this filtering is shown in Figure 2.3 where it can be seen that fluctuations are damped and the resulting (smoothed) F(i) data helps better define the onset of the steady-state period compared to the raw data B(i). The time needed to achieve the steady-state condition for Nu is then estimated by analyzing the slope of the F(i) time series (detailed in section 3.3). Data smoothing avoids noise perturbations (fluctuation) that might affect the accuracy of establishing the time needed to reach steady-state [19].
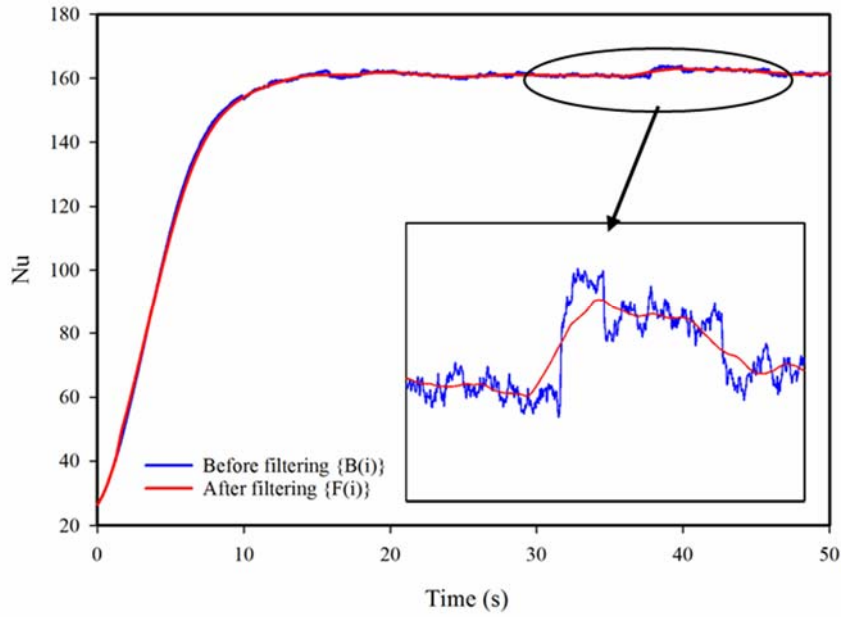
Figure 2.3: 1-D moving average filter applied to time series of $\overline{Nu}$ (30Hz; frame rate) for the region of interest (Aavg). Jet conditions: S=0, Re=35,000, and H/D=6.

2.3.3 Defining the Transient Period

The heat transfer (Nusselt number) characteristics typically vary as time progresses during transient (start-up) periods and become constant when the steady-state condition is achieved. For many industrial applications, this transient time affects drying, cooling or heating processes, which is why estimating the time to reach steady-state (t_{steady}) is crucial for many industrial processes. Because non-uniformity of heat transfer over an impingement surface, in some cases t_{steady} is not constant for all portions of a target surface. For this purpose, different Regions Of Interest (ROIs) are used in the present study to also test the methods described in their ability to spatially resolve transient heat transfer periods for different parts of the impingement plate (r/D=0 to 2). To achieve this, the impingement plate is divided into five equally sized concentric areas labelled as A_1-A_5 and their sum (which forms a sixth ROI) is denoted as A_{avg}. The six spatially resolved Nusselt number values are evaluated over each time step (t=1/30) to represent that based on A_1 (r/D=0-0.89), A_2 (r/D=0.89-0.1.27), A_3 (r/D=1.27-1.55), A_4 (r/D=1.55-1.79), A_5 (r/D=1.79-2.00), and A_{avg} (r/D=0-2.00). The graphical representation of these ROIs are shown in Figure 2.4, which also visualizes the time at which F(i) reaches steady-state in each ROI. The slope (rate of change) of time series representing the average Nusselt number (Nu´´) for each ROI is also shown in Figure 2.4 (jet cooling at S=0,

38

Re=35,000, and H/D=6). It is also worth noting here that although data filtering has been applied (Equations (2-11) to (2-14)), filtration cannot damp large fluctuations. If further smoothing is required, then other filtration techniques (POD or Hybrid) can be employed. Theoretically, when the change in the F(i) slope of d(Nu) reaches zero, that point is considered the end of the transient stage (start of steady-state). This is achieved through the image processing code (see Chapter Appendices).
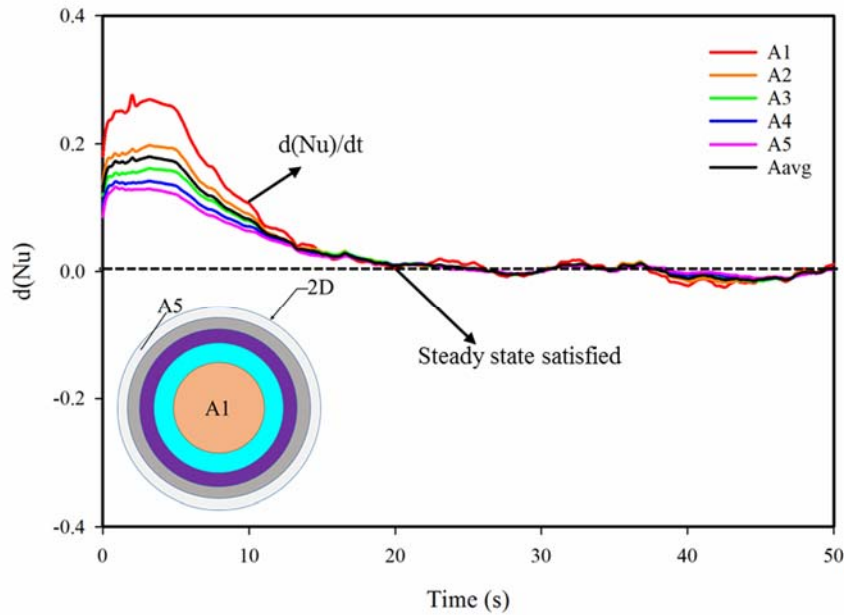
Figure 2.4: Data reduction and steady-state calculation over the six regions of interest at the impingement plate. The dashed line shows the chosen slope of d(Nu). Jet conditions: S=0, Re=35,000, and H/D=6.

Post-processing of the IR data occurs in two stages as shown in Figure 2.5. Firstly, the spatially resolved adiabatic surface temperature [27] is derived, which is achieved by measuring surface temperatures with the jet impinging, but without power supply to the heater (i.e., heat flux is zero). This value only needs to be established once for each jet condition and is described using sub-process 1, 2b, and 3 in the code (see Chapter Appendices). Following this, the spatially resolved transient heat transfer characteristics are computed using sub-process 1, 2a, and 3 as the jets transition from start-up to steady-state over a period t_{steady}. In sub-process 1, the centre of the imaged area (x=0, y=0) is defined as well as the spatial resolution (1.01mm/pixel when the distance between camera and target surface is 750mm). Each region of interest (A_1 to A_5) is also mapped against pixels in the imaged field. Region A_{avg} is also obtained by summing up A_1 to A_5. Sub-process 2a is used to evaluate the time-resolved temperatures of the impingement

39

plate, which is later used to calculate the temperature difference (using data from sub-process 2b) and time-varying Nusselt number in sub-process 3 (Equation (2-6) and (2-7)). Following this in sub-process 3, data filtration (Equation (2-11) to (2-14)) is employed.
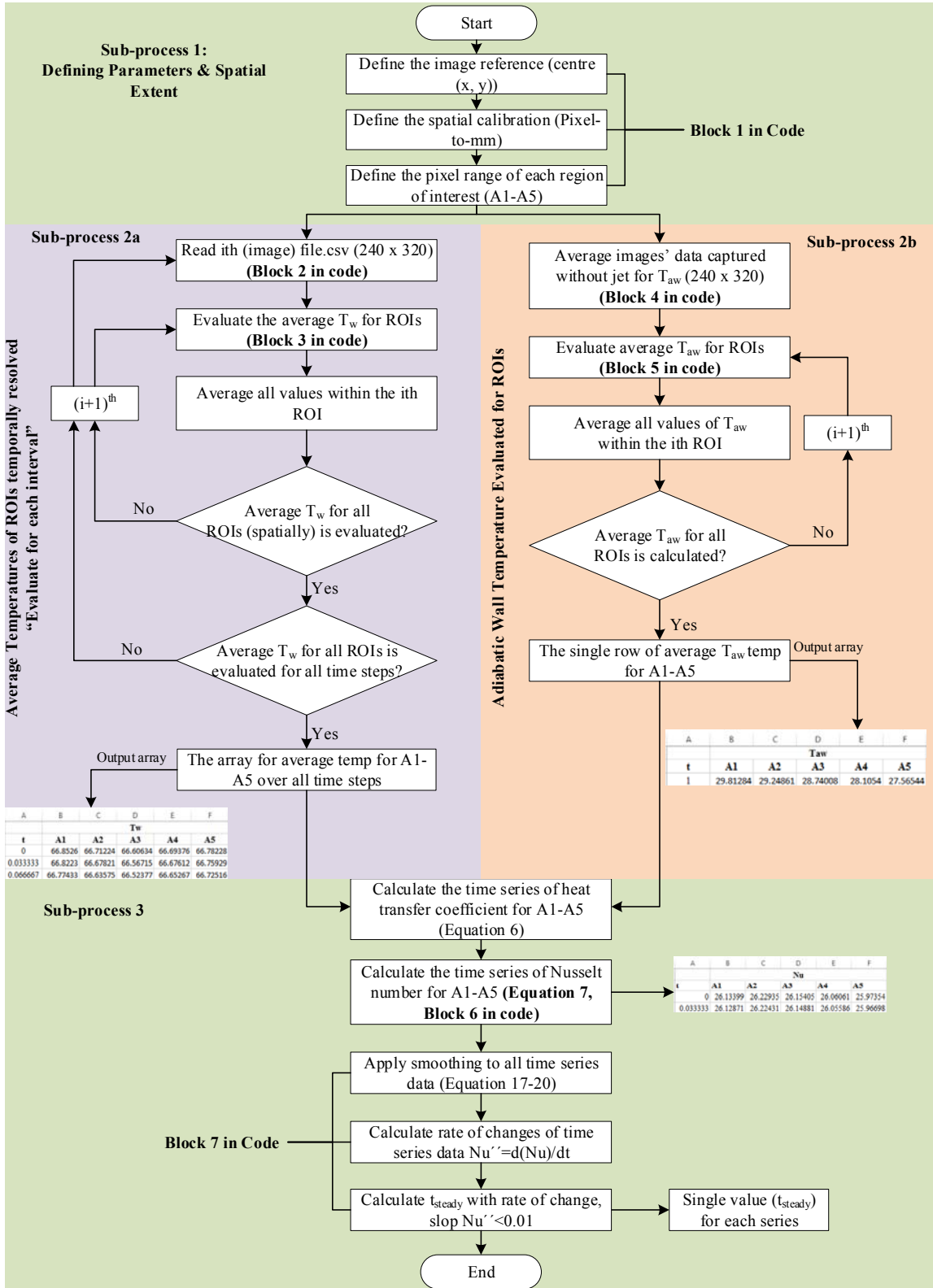
Figure 2.5: Method for evaluating transient heat transfer characteristics (Sub-process 1, 2a, and 3 are used to evaluate adiabatic surface temperatures whereas 1, 2b, and 3 are for heat transfer). Code shown is for an image size of 240 x 320 pixels.

2.3.4 Uncertainty Analysis

Heat transfer data (like many others) is subject to uncertainty which should be quantified [36]. Techniques such as Constant Temperature Anemometry, Micromanometers, and infrared imaging are quite robust but not error-free. This section will describe the uncertainties associated with the experiments.

The error associated with any measurement expressed by Equation (2-15) is the combination of systematic error ε_s and random error ε_r [26,37].

$$\varepsilon = \pm\sqrt{\varepsilon_s^2 + \varepsilon_r^2} \qquad (2\text{-}15)$$

Systematic/fixed errors do not change but remain constant. This kind of error is typically related to the tolerance and accuracy of the equipment, and include the measurement limits of equipment, calibration errors, as well as data collection and reduction operations. These errors continue and pass unaltered from one test to another. The resultant (limit) systematic error can be calculated using the root-sum-square technique for all the components and is expressed by Equation (2-16), where n is the number of sources for the error.

$$\varepsilon_s = \sqrt{\sum_{i=1}^{n} \varepsilon_{s,i}^2} \qquad (2\text{-}16)$$

In contrast to random errors associated with each measurement, and which can be estimated through the repetition of experiments, the resultant random error from different sources can be estimated (like the systematic error) in Equation (2-17).

$$\varepsilon_r = \sqrt{\sum_{i=1}^{n} \varepsilon_{r,i}^2} \qquad (2\text{-}17)$$

Statistical methods (e.g. standard deviation, σ_s) can evaluate the random error for a measurement/system as expressed in Equation (2-18) to (2-20), where N is the number of samples, Φ_i is the measured value of the variable, and $\bar{\Phi}$ is the mean quantity.

$$\varepsilon_r = \sqrt{\frac{\sum_{i=1}^{N}(\Phi_i - \bar{\Phi})^2}{N(N-1)}} = \frac{\sigma_s}{\sqrt{N}} \qquad (2\text{-}18)$$

$$\% \, Error = \frac{\varepsilon_{r,i}}{\bar{\Phi}} * 100 \qquad (2\text{-}19)$$

$$\bar{\Phi} = \frac{1}{N}\sum_{i=1}^{N} \Phi_i \qquad (2\text{-}20)$$

The systematic error in the heat transfer measurements is attributed to the accuracy limit of the thermal imaging camera, which further propagates with the mathematical operations performed on the (raw) temperature data during post-processing. The systematic error in the IR measurements is ±2% [26]. The random error is calculated by repeating each experiment three times (denoted Exp1, Exp2, and Exp3) for jets at Re=11,600-35,000 and H/D=2-6. It is observed that the maximum random error for Nu is around 4.6%, with this considered as the uncertainty in the measurement. The overall Nu error in measurements is considered around 5% as shown in Table 2.2. The confidence level is 95% which is equivalent to 2-sigma, since some of the experimental data (used to estimate the uncertainty) does not lie with 1-sigma of the mean value.

Table 2.2: Uncertainty in Nu calculation.

H/D	Re	$\overline{Nu}$			Nu_{avg}	Std Dev	% Error
		Exp1	Exp2	Exp3			
	11,600	78.67	86.04	89.43	84.71	5.20	3.74
2	24,600	103.43	113.87	117.09	111.46	7.374	3.69
	35,000	120.95	140.07	124.15	128.39	13.51	4.60
	11,600	88.73	90.38	89.55	89.55	0.825	0.53
4	24,600	120.29	107.32	113.80	113.80	6.48	3.29
	35,000	144.94	127.56	136.25	136.25	8.69	3.68
	11,600	87.41	83.35	85.38	85.38	2.87	1.37
6	24,600	115.51	124.30	116.56	118.79	6.21	2.33
	35,000	138.32	138.83	127.25	134.80	6.54	3.77

2.4 RESULTS AND DISCUSSION

The role of three different parameters (rate of Nu change, image resolution, and spatial discretization) as they each influence the resolved t_{steady} is now explored. Experiments are carried out for non-swirling (S=0) and swirling (S=0.27-1.05) turbulent impinging jets (H/D=2-6) at Re=35,000.

2.4.1 Rate of Nu Change

Figure 2.6 shows the effect of changing 1/Slope (Nu´´). As the steady-state period is approached (steady), the rate of change in Nu (designated Nu´´) varies. In the image processing applied, a threshold value (for the rate of change in Nu) needs to be selected. The inverse of the rate of change of Nu with respect to the time is on the horizontal axis while the vertical axis denotes time. The 1/slope of Nu´´ is plotted for better data visualization compared to (merely)

43

the slope Nu´´ as the latter attains very small numbers once steady-state is approached which makes it difficult to visualize.
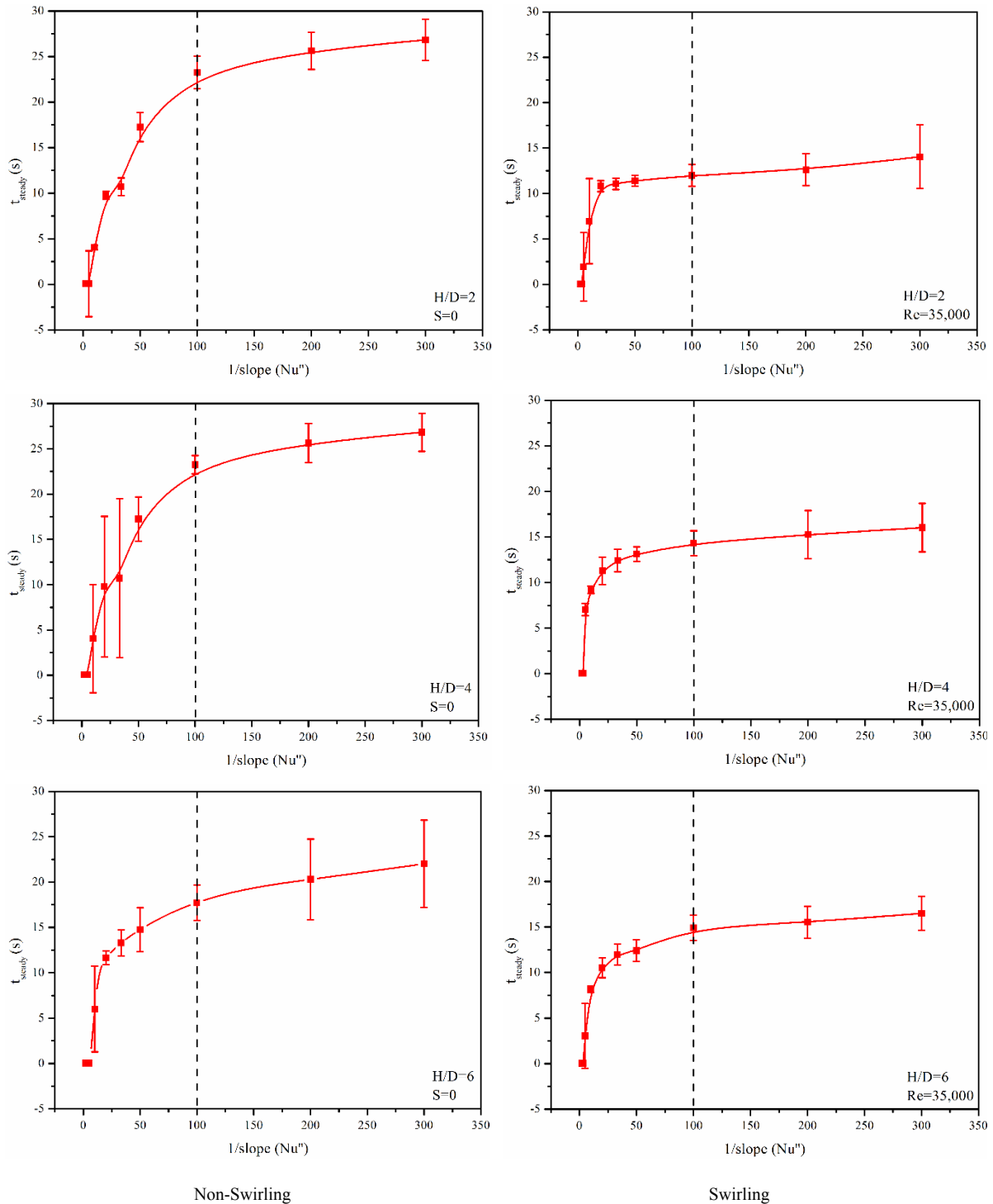
Figure 2.6: Delta slope selection for t_{steady} calculation for time series data of $\overline{Nu}$ evaluated at Aavg. The dashed line shows the chosen value for 1/slope (Nu´´). Left: non-swirling jet, Right: swirling jet

The error bars for the non-swirling cases show the range for values obtained for different Reynolds numbers (Re=11,600, 24,600, and 35,000). In contrast. the error bars in the swirling

44

case show the range of values obtained for different Swirl numbers (S=0.27, 0.45, 0.77, and 1.05). These results show that smaller values of slope (which correspond to higher 1/slope (Nu´´)) yield longer time intervals to reach t_{steady}. It is also observed that the majority of trend lines are stabilized when 1/slope (Nu´´) reaches 100 (dashed line). This value is subjected to change and can be chosen differently for different experimental setups. In the current tests, this threshold value is also used in subsequent image processing. With this in mind, t_{steady} can be estimated by finding the corresponding value of time where the rate of change of Nusselt number is negligible or zero (Nu´´), which can be decided using the method described above.

2.4.2 Image Resolution

Figure 2.7 and Figure 2.8 look at the effect of different IR image resolution on time to reach steady-state. Figure 2.7 shows the effect of 1/slope (Nu´´) for non-swirling (S=0) and swirling (S=1.05) impinging jets. To help visualize the effect of the resolution, Figure 2.8 presents the Nusselt number distribution over the impingement surface at various time steps for images of 240 x 320 (higher resolution) to 30 x 40 (lower resolution). The resolution of the thermal image is lowered by binning the pixel in the IR image. The pixel binning is carried out by averaging the neighboring pixels. For the range explored, it is evident that image resolution does not appear to significantly affect the time reach to steady-state for three values of 1/slope (Nu´´). Additionally, reduced image resolution limits the amount of data need for processing, which means less computational power and time compared to full-sized images. For example, the computational time needed for images with 240 x 320 is 16 times longer than with the images at 30 x 40. Image resolution also appears not to affect the time needed to attain steady-state even when the threshold value selected for the rate of Nu changes (1/slope (Nu´´)).
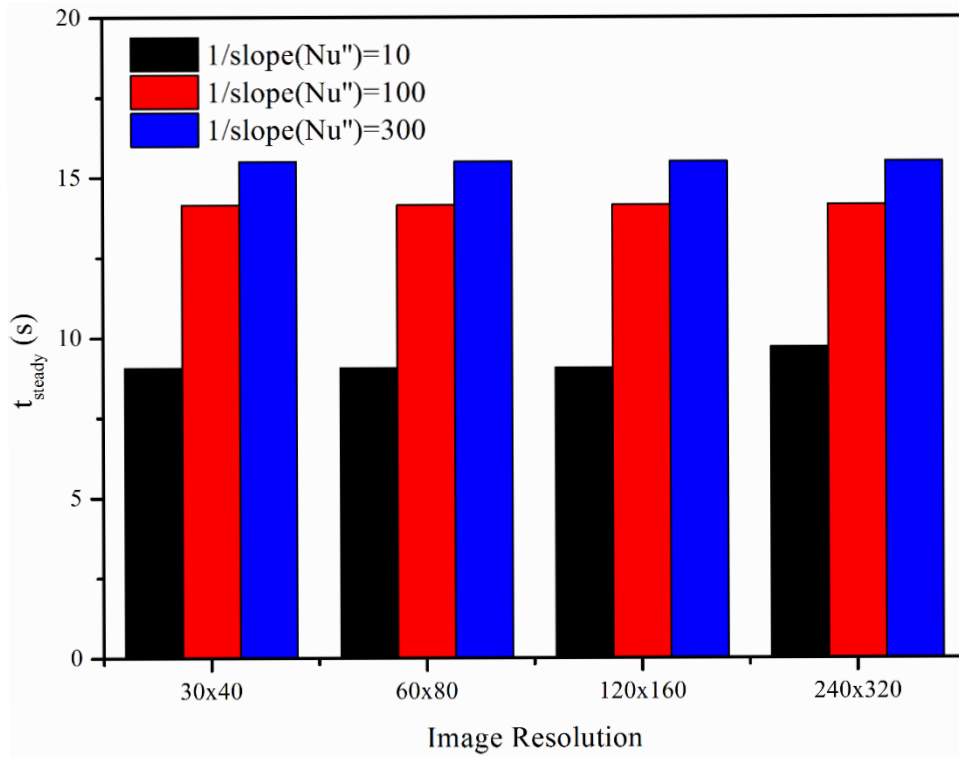
(a)
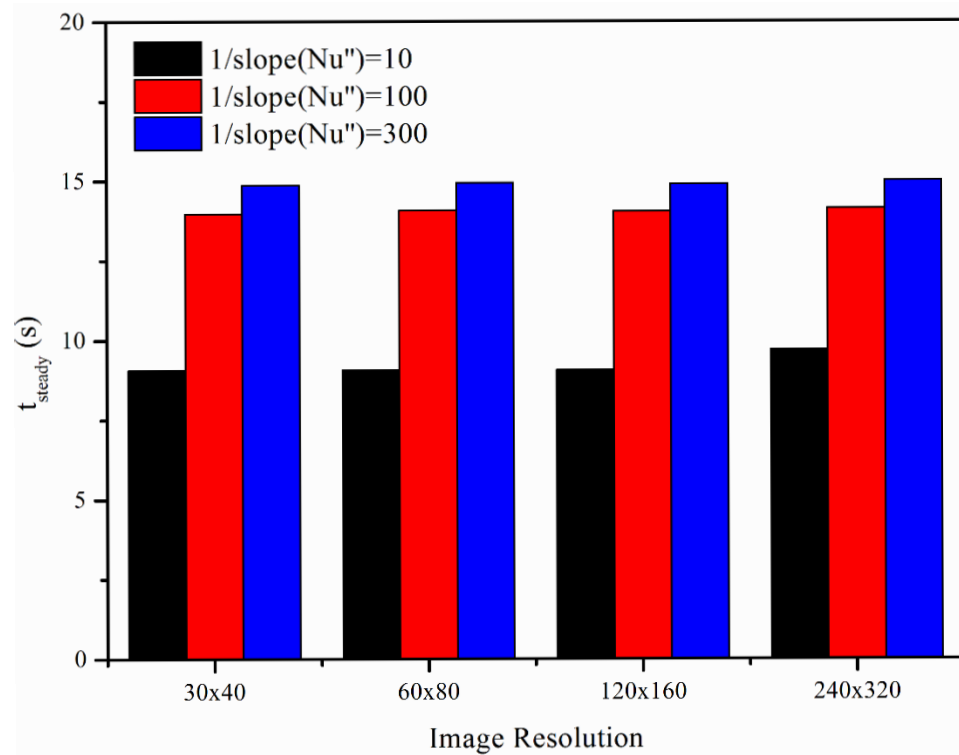
(b)

Figure 2.7: Effect of pixel binning on time to reach steady state for Aavg at H/D=2 with respect to various 1/slope(Nu´´) values (a) S=0 and (b) S=1.05.
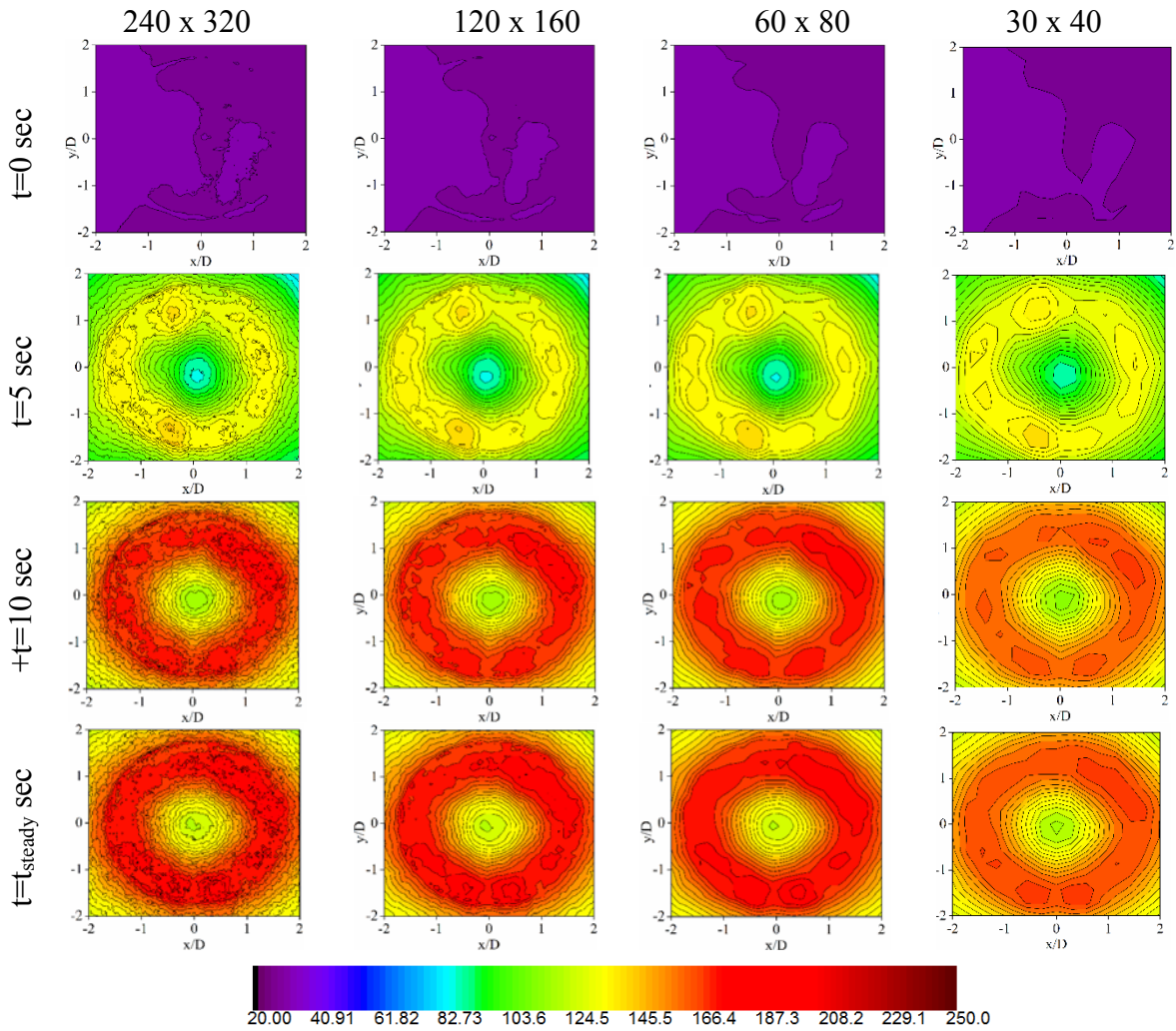
Figure 2.8: Nusselt number contour plot for swirling impinging jet (S=1.05, Re=35,000, and H/D=2) at 30 Hz frame rate for various image resolution.

2.4.3 Spatial Discretization

Figure 2.9 shows the transient heat transfer characteristics of the average Nusselt number and temperatures over five discretized regions of interest (A1-A5) and (Aavg). Nusselt number for the stagnation zone at t_{steady} (which corresponds to A_1 and A_2) is the highest compared to the other regions of interest (A_3 to A_5). It is also evident from these results that spatial discretization using the methods described shows different behaviour in the far wall jet region (A_5), where data for all conditions over S=0 to S=1.05 collapse onto a single t_{steady}, in contrast to the stagnation zone (A_1 to A_2) where t_{steady} varies between swirl numbers. The methods used are also sensitive enough to capture differences between the spatial areas A_1 and A_5 during the acute rates of change over the first few seconds. Heat transfer characteristics are therefore not only affected by the swirl number but also the spatial extent. The data also shows that the rate

47

of change for Nusselt number in the wall jet region (A₄ and A₅) is generally the lowest compared to the other regions of interests.
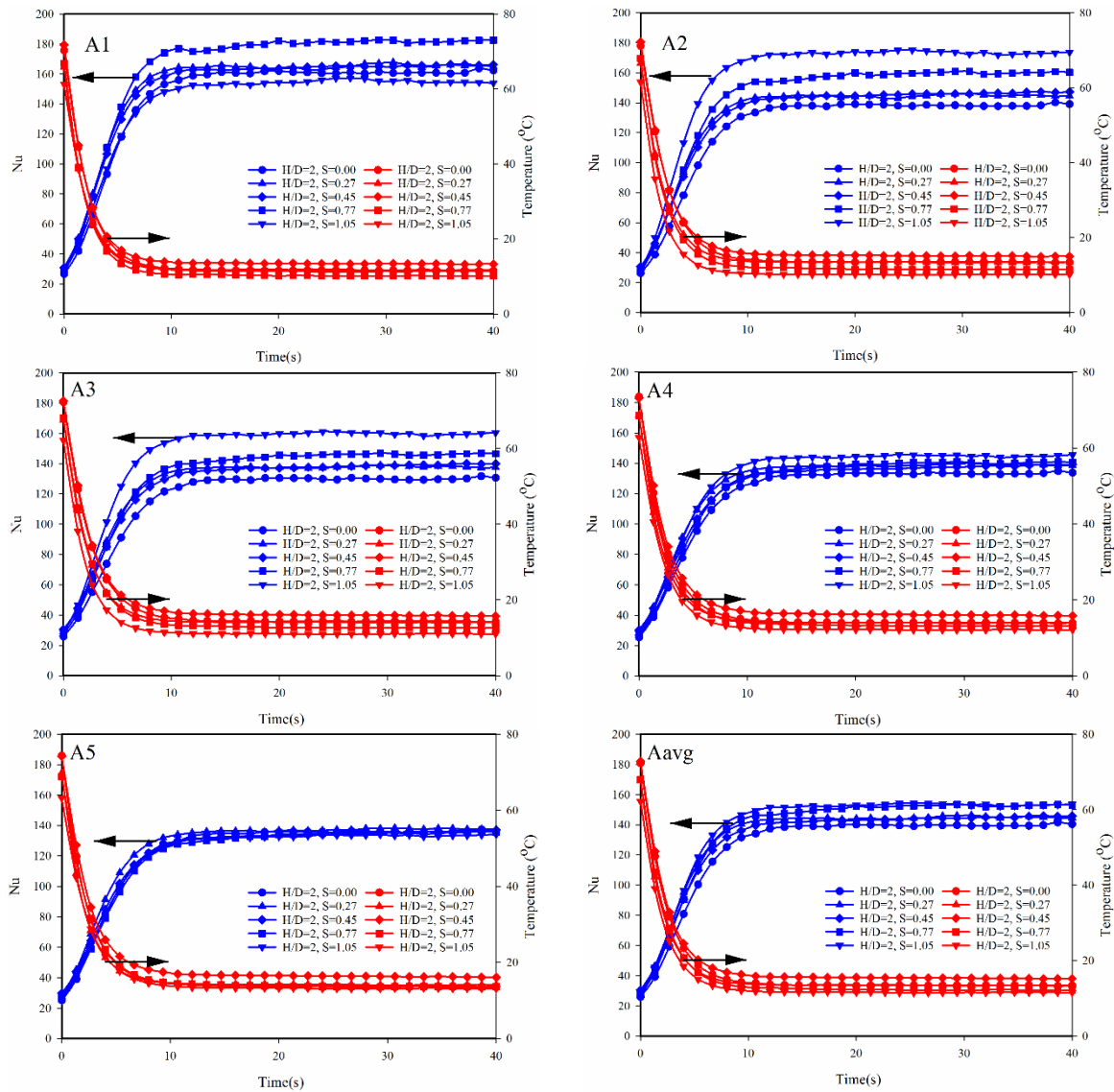
Figure 2.9: Temporal evolution of spatially discretized Nusselt number and temperature over different areas on the heated impingement plate for swirling and non-swirling impinging jets at Re=35,000, H/D=2.

Figure 2.10 summarizes the time to steady-state (t_{steady}) for non-swirling and swirling impinging jets with respect to specified regions of interest. It can be seen that for the swirling cases the system reaches steady-state quicker than the non-swirling impinging jet. The necessity of using spatial discretization when analyzing the time over which different jet conditions reach steady-state also becomes apparent in Figure 2.11, which shows the profile of jet impingement for S=0 and 1.05 at steady-state and demonstrates the need to spatially resolve the heat transfer when non-uniformity is present. For non-swirling impinging jets at H/D=2, the Nusselt number peaks are closer to the centerline at $0.3 < r/D < 0.7$. For high swirl (S=1.05)

a trough-shaped profile is evident with a peak shifted into the radial direction and located at $0.5 < r/D < 1.0$.
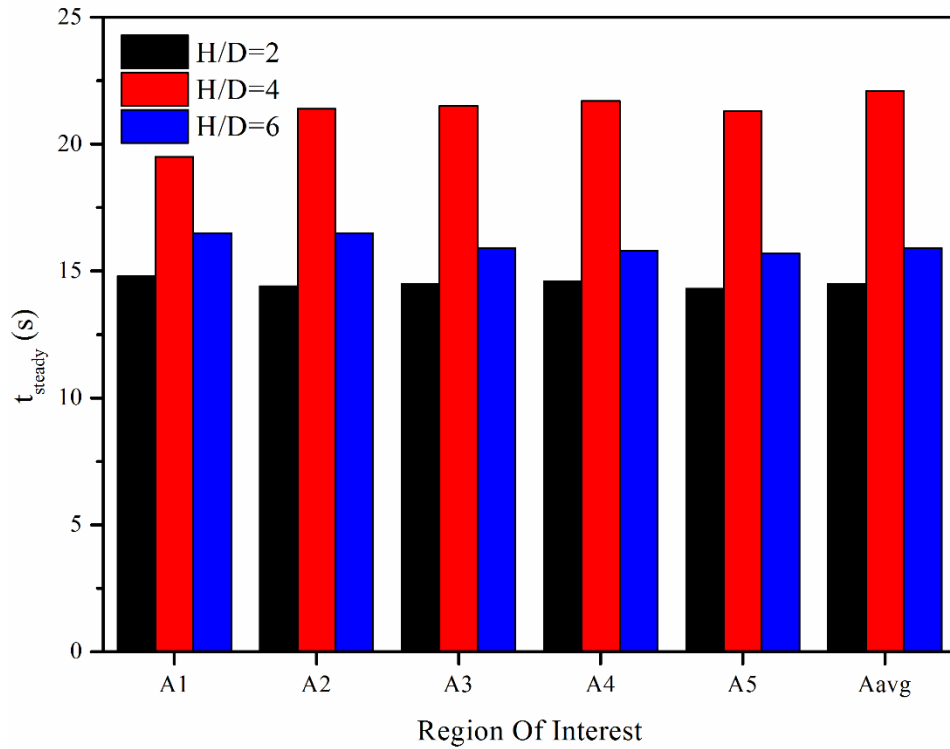
(a)
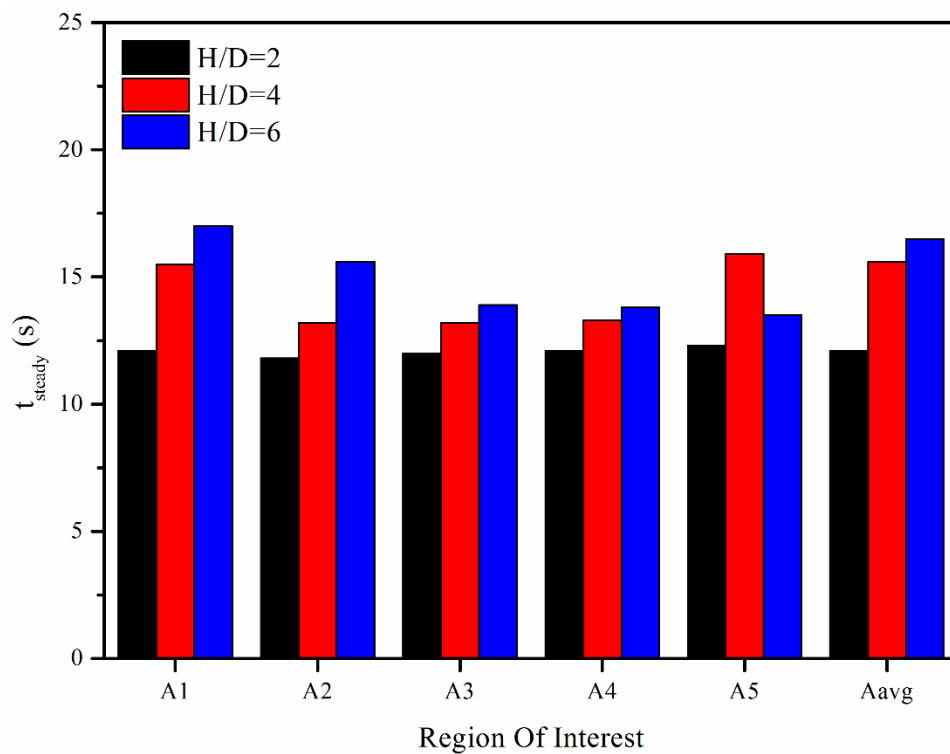
(b)

Figure 2.10: Time (seconds) to reach steady-state for (a) non-swirling (S=0) and (b) swirling (S=1.05) impinging jets at slope d(Nu)/dt=0.01
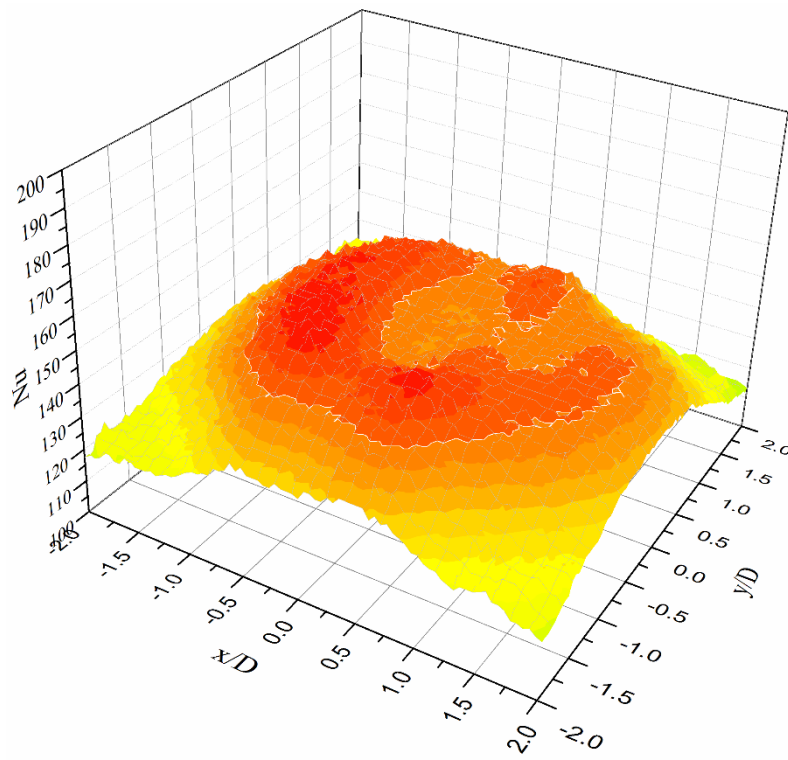
(a)
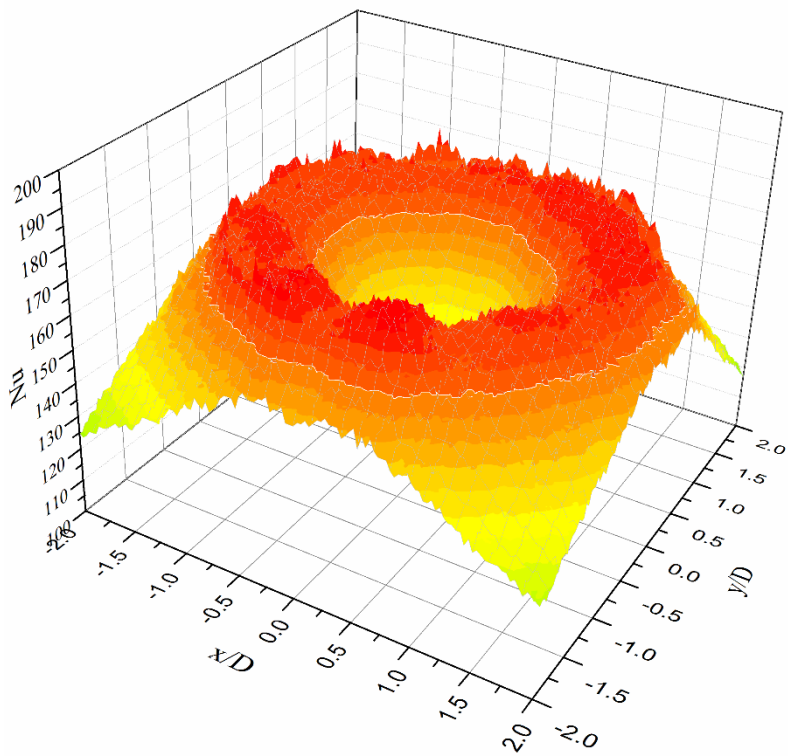
(b)

Figure 2.11: Surface contour of Nu at H/D=2 (a) S=0 and (b) S=1.05.

2.5 CONCLUSIONS

A method for the characterization of transient convection processes using infrared thermography is discussed. Turbulent non-swirling and swirling impinging jets along with the thin foil heater technique have been used to test and develop the image processing methodology used to accurately estimate the time needed to reach steady-state. The role of three process parameters on affecting t_{steady} has been investigated, namely the threshold values of time-dependent Nusselt number, image resolution, and the spatial discretization. Whilst the rate of Nu change appears as an influencing parameter, the spatial resolution does not appear to influence the outcomes. The techniques have demonstrated that variations in jet behaviour do not only manifest themselves in the overall time to reach steady-state, but that differences become apparent even in the first few seconds despite the complex thermal footprint involved.

2.6 CHAPTER REFERENCES

[1]   Deng H, Wang J, Bai L, Zhu J. Heat transfer characteristics in a rotating wedge-shaped ribbed trailing edge with impingement jet. Exp Heat Transf 2020:1–18. doi:10.1080/08916152.2020.1713256.

[2]   Carlomagno GM, Cardone G. Infrared thermography for convective heat transfer measurements. Exp Fluids 2010;49:1187–218. doi:10.1007/s00348-010-0912-2.

[3]   Zhao X, Yin Z, Zhang B. Experimental study on transient heat transfer characteristics of intermittent spray cooling. Exp Heat Transf 2019:1–20. doi:10.1080/08916152.2019.1707909.

[4]   Raiola M, Greco CS, Contino M, Discetti S, Ianiro A. Towards enabling time-resolved measurements of turbulent convective heat transfer maps with IR thermography and a heated thin foil. Int J Heat Mass Transf 2017;108:199–209. doi:10.1016/j.ijheatmasstransfer.2016.12.002.

[5]   Carlomagno GM, Ianiro A. Thermo-fluid-dynamics of submerged jets impinging at short nozzle-to-plate distance: A review. Exp Therm Fluid Sci 2014;58:15–35. doi:10.1016/j.expthermflusci.2014.06.010.

[6]   Nakamura H. Frequency response and spatial resolution of a thin foil for heat transfer measurements using infrared thermography. Int J Heat Mass Transf 2009;52:5040–5. doi:10.1016/J.IJHEATMASSTRANSFER.2009.04.019.

[7]   Hetsroni G, Rozenblit R. Heat transfer to a liquid—solid mixture in a flume. Int J Multiph Flow 1994;20:671–89. doi:10.1016/0301-9322(94)90038-8.

[8]   Sanmiguel Vila C, Discetti S, Carlomagno GM, Astarita T, Ianiro A. On the onset of horizontal convection. Int J Therm Sci 2016;110:96–108. doi:10.1016/J.IJTHERMALSCI.2016.06.019.

[9]   Nakamura H, Yamada S. Quantitative evaluation of spatio-temporal heat transfer to a turbulent air flow using a heated thin-foil. Int J Heat Mass Transf 2013;64:892–902. doi:10.1016/j.ijheatmasstransfer.2013.05.006.

[10]   Greco CS, Ianiro A, Cardone G. Time and phase average heat transfer in single and twin circular synthetic impinging air jets. Int J Heat Mass Transf 2014;73:776–88. doi:10.1016/J.IJHEATMASSTRANSFER.2014.02.030.

[11] Ikhlaq M, Ghaffari O, Arik M. Effect of actuator deflection on heat transfer for low and high frequency synthetic jets. Thermomechanical Phenom. Electron. Syst. -Proceedings Intersoc. Conf., Institute of Electrical and Electronics Engineers Inc.; 2014, p. 882–8. doi:10.1109/ITHERM.2014.6892374.

[12] Ghaffari O, Ikhlaq M, Arik M. An Experimental Study of Impinging Synthetic Jets for Heat Transfer Augmentation. Int J Air-Conditioning Refrig 2015;23:1550024. doi:10.1142/S2010132515500248.

[13] Ikhlaq M, Dogruoz B, Ghaffari O, Arik M. A computational study on the momentum and heat transfer distribution of a low frequency round impinging synthetic jet. InterPACK2015 July 6-9, 2015, San Fr. California, USA, vol. 3, ASME; 2015, p. V003T10A016. doi:10.1115/IPACK2015-48094.

[14] Ghaffari O, Solovitz SA, Ikhlaq M, Arik M. An investigation into flow and heat transfer of an ultrasonic micro-blower device for electronics cooling applications. Appl Therm Eng 2016;106:881–9. doi:10.1016/j.applthermaleng.2016.06.094.

[15] Ikhlaq M, Ghaffari O, Arik M. Predicting Heat Transfer for Low- and High-Frequency Central-Orifice Synthetic Jets. IEEE Trans Components, Packag Manuf Technol 2016;6:586–95. doi:10.1109/TCPMT.2016.2523809.

[16] Ikhlaq M, Al-Abdeli YM, Khiadani M. Transient heat transfer characteristics of swirling and non-swirling turbulent impinging jets. Exp Therm Fluid Sci 2019;109:109917. doi:10.1016/j.expthermflusci.2019.109917.

[17] Yazici H, Akcay M, Golcu M, Koseoglu MF, Sekmen Y. Experimental investigation of transient temperature distribution and heat transfer by jet impingement in glass tempering processing. Trans Mech Eng 2015;39:337–49. doi:10.22099/IJSTM.2015.3244.

[18] Kadam AR, Hindasageri V, Kumar GN. Transient heat transfer characterization of impinging hot/cold jets by analytical IHCP. IOP Conf. Ser. Mater. Sci. Eng., vol. 376, IOP Publishing; 2018, p. 12027. doi:10.1088/1757-899X/376/1/012027.

[19] Dou R, Wen Z, Zhou G. 2D axisymmetric transient inverse heat conduction analysis of air jet impinging on stainless steel plate with finite thickness. Appl Therm Eng 2016;93:468–75. doi:10.1016/j.applthermaleng.2015.10.021.

[20] Jambunathan K, Lai E, Moss MAA, Button BLL. A review of heat transfer data for single circular jet impingement. Int J Heat Fluid Flow 1992;13:106–15. doi:10.1016/0142-727X(92)90017-4.

[21] Mitsutake Y, Monde M. Heat transfer during transient cooling of high temperature surface with an impinging jet. Heat Mass Transf 2001;37:321–8. doi:10.1007/s002310000141.

[22] Liu L-K, Su W-S, Hung Y-H. Transient convective heat transfer of air jet impinging onto a confined ceramic-based MCM disk. J Electron Packag 2004;126:159–72. doi:10.1115/1.1649239.

[23] Yamada S, Nakamura H. Construction of 2D-3C PIV and high-speed infrared thermography combined system for simultaneous measurement of flow and thermal fluctuations over a backward facing step. Int J Heat Fluid Flow 2016;61:174–82. doi:10.1016/J.IJHEATFLUIDFLOW.2016.04.010.

[24] Al-Abdeli YM. Experiments in turbulent swirling non-premixed flames and isothermal flows. 2004.

[25] Thomas BK, Ahmed ZU, Al-Abdeli YM, Matthews MT. The optimisation of a turbulent swirl nozzle using CFD. Aust. Combust. Symp. Perth, Aust., 2013, p. 271–4.

[26] Ahmed ZU. An experimental and numerical study of surface interactions in turbulent swirling jets. Edith Cowan University, 2016.

[27] Ahmed ZU, Al-Abdeli YM, Guzzomi FG. Heat transfer characteristics of swirling and non-swirling impinging turbulent jet. Int J Heat Mass Transf 2016;102:991–1003. doi:10.1016/j.expthermflusci.2015.07.017.

[28] Ahmed ZU, Al-Abdeli YM, Guzzomi FG. Corrections of dual-wire CTA data in turbulent swirling and non-swirling jets. Exp Therm Fluid Sci 2016;70:166–75. doi:10.1016/j.expthermflusci.2015.09.007.

[29] Yu P, Zhu K, Shi Q, Yuan N, Ding J. Transient heat transfer characteristics of small jet impingement on high-temperature flat plate. Int J Heat Mass Transf 2017;114:981–91. doi:10.1016/j.ijheatmasstransfer.2017.06.112.

[30] Zhu K, Yu P, Yuan N, Ding J. Transient heat transfer characteristics of array-jet impingement on high-temperature flat plate at low jet-to-plate distances. Int J Heat Mass

Transf 2018;127:413–25. doi:10.1016/J.IJHEATMASSTRANSFER.2018.07.099.

[31] Liu QS, Shibahara M, Fukuda K. Transient Heat Transfer for Forced Convection Flow of Helium Gas Over a Horizontal Plate. Exp Heat Transf 2008;21:206–19. doi:10.1080/08916150802072859.

[32] Narayanan V, Patil VA. Oscillatory thermal structures induced by unconfined slot jet impingement. Exp Therm Fluid Sci 2007;32:682–95. doi:10.1016/J.EXPTHERMFLUSCI.2007.09.002.

[33] Al-Abdeli YM, Masri AR, Assaad &, Masri R, Masri AR. Precession and recirculation in turbulent swirling isothermal jets. Combust Sci Technol 2004;176:645–65. doi:10.1080/00102200490427883.

[34] Raiola M, Discetti S, Ianiro A. On PIV random error minimization with optimal POD-based low-order reconstruction. Exp Fluids 2015;56. doi:10.1007/s00348-015-1940-8.

[35] Hauksson ÁT. Experimental study of boiling heat transfer during water jet impingement on a hot steel plate. University of British Columbia, 2001.

[36] Moffat RJ. Describing the uncertainties in experimental results. Exp Therm Fluid Sci 1988;1:3–17. doi:10.1016/0894-1777(88)90043-X.

[37] Montgomery DC, Runger GC. Applied statistics and probability for engineers. John Wiley & Sons; 2010.

[38] Guo Q, Wen Z, Dou R. Experimental and numerical study on the transient heat-transfer characteristics of circular air-jet impingement on a flat plate. Int J Heat Mass Transf 2017;104:1177–88. doi:10.1016/J.IJHEATMASSTRANSFER.2016.09.048.

[39] Yi SJ, Kim M, Kim D, Kim HD, Kim KC. Transient temperature field and heat transfer measurement of oblique jet impingement by thermographic phosphor. Int J Heat Mass Transf 2016;102:691–702. doi:10.1016/J.IJHEATMASSTRANSFER.2016.06.062.

2.7 CHAPTER APPENDICES

Image Processing Code

```
1. clear all
2. clc
3. %%Sub-process 1%%
4. %%Block 1%%
5. %% Defining Parameters & Spatial Extent%%
6. %%Initialization & Basic Parameter Definition%%
7. Lambda=0.0264  %%Air conductivity%%
8. Frame_rate=30; %%Defining camera frame rate%%
9. t=[0:1/frame_rate:100]';
10.   D=0.04            %%Nozzle diameter%%
11.   E=3               %%Applied voltage%%
12.   I=40        %%Applied current%%
13.   A=0.2*0.3   %%Heater area%%
14.   Q=E*I/A     %%Applied heat flux%%
15.
16.   %%Define the image reference (centre (x, y))%%
17.   centre=[118,169];
18.
19.   %%Define the pixel range of each region of interest (A1-A5)%%
20.   R = [35.6,50.8,62,71.6,80]; %%[A1, A2, A3, A4, A5]
21.
22.   %%Define the spatial calibration (Pixel-to-mm)%%
23.   for i=1:length(R)
      23.1.1.     R_pixel(i) = ceil(1.01*R(i));
24.   end
25.   %% Average Temperatures of ROIs temporally resolved "Evaluate for
  each interval"%%
26.   %%Sub-process 2i%%
27.   %%Block 2%%
28.   %%Read ith (image) file.csv (240 x 320)%%
29.   index=1;
30.   srcFolder_Tw = 'IR Captured image data files location'; %% the folder
  in which images exists%%
31.   srcFiles_Tw = dir( strcat(srcFolder_Tw,'\*.csv'));      %% Reading
  all CSVs%%
32.   %%%%%%%%% ADDED BELOW %%%%%%%%%%%%
33.   %%%%%%%%%%%%%% we sort in numerical%%%%%
34.   %%%% order by natsortfiles function available at mathworks website by
  some good uploader ;)
35.   baseFileNames = natsortfiles({srcFiles_Tw.name});
36.   %%%%%%%%%%%%%%%%%%%%%%%%%%%%%%%%%%%%%%%%%%%%%%%%%%%%%%%%%%%%%%%
37.
38.   for k = 1:(length(srcFiles_Tw))    %%Iterate through all files%%
39.   filename = strcat(srcFolder_Tw,baseFileNames{k}); %% Path to the IR
  images%%
40.   fprintf(1, 'Now reading %s\n', filename);
41.   temp_file=load(filename);
42.     sum=0;
43.     count=0;
44.   %%Block 3%%
```

```matlab
45.    for r_i =1:length(R_pixel)      %%Iterate through all ROIs%%
46.    for h = 1: 240                   %%Iterate through all rows%%
47.    for w =1: 320        %%Iterate through all columns%%
48.    if(sqrt((centre(1)- h)^2 +(centre(2)- w)^2)<R_pixel(r_i) && r_i==1)%%
    If circles%%
49.    sum = sum + eval(sprintf('temp_file(h,w)')); %% Sum of temperatures
    for inner circle%%
50.    count = count+1;
51.
52.    elseif (sqrt((centre(1)- h)^2 +(centre(2)- w)^2)<R_pixel(r_i) &&
    sqrt((centre(1)- h)^2 +(centre(2)- w)^2)>R_pixel(r_i-1) ) %%If rings%%
53.    sum = sum + eval(sprintf('temp_file(h,w)')); %% Sum of temperatures
    for all rings except inner circle%%
54.    count = count+1;
55.
56.
57.            end
58.        end
59.    end
60.    %%Average temperatures of all ROIs per time step%%
61.    avg = sum/count;
62.    averages_Tw(index,r_i) = avg;
63.    sum=0;
64.    count=0;
65.    end
66.    %%Reading next time step data%%
67.    clear temp_file
68.    index=index+1;
69.    end
70.    %%Sub-process 2ii%%
71.    %%Block 4%%
72.    %%Average images' data captured without jet for Taw (240 x 320)%%
73.    %%Evaluate average Taw for ROIs%%
74.    index=1;
75.    srcFolder_Taw = 'IR Captured image data files location';%% the folder
    in which images exists%%
76.    srcFiles_Taw = dir( strcat(srcFolder_Taw,'\*.csv'));  %% Reading all
    CSVs%%
77.    filename = strcat(srcFolder_Taw,fileList.name);
78.    fprintf(1, 'Now reading %s\n', filename);
79.    load(filename);
80.
81.    for k1 = 1:(length(srcFiles_Taw))   %%Iterate through all files%%
82.    sum1=0;
83.    count1=0;
84.    %% Adiabatic Wall Temperature Evaluated for ROIs%%
85.    %%Block 5%%
86.    for r_i1 =1:length(R_pixel)%%Iterate through all ROIs%%
87.    for h1 = 1: 240              %%Iterate through all rows%%
88.    for w1 =1: 320        %%Iterate through all columns%%
89.    if(sqrt((centre(1)- h1)^2 +(centre(2)- w1)^2)<R_pixel(r_i1) &&
    r_i1==1)%% If circles%%
90.    sum1 = sum1 + eval(sprintf('AWT_%d(h1,w1)',(k1-1))); %% Sum of
    temperatures for inner circle%%
```

```matlab
91.   count1 = count1+1;
92.   elseif (sqrt((centre(1)- h1)^2 +(centre(2)- w1)^2)<R_pixel(r_i1) &&
      sqrt((centre(1)- h1)^2 +(centre(2)- w1)^2)>R_pixel(r_i1-1) ) %%If
      rings%%
93.   sum1 = sum1 + eval(sprintf('AWT_%d(h1,w1)',(k1-1))); %% Sum of
      temperatures for all rings except inner circle%%
94.   count1 = count1+1;
95.           end
96.         end
97.   end
98.   avg1 = sum1/count1;
99.   averages_Taw(index1,r_i1) = avg1; %%The single row of average Taw
      temp for A1-A5%%
100.  sum1=0;
101.  count1=0;
102.  end
103.  index1=index1+1;
104.  end
105.  %%Sub-process 3%%
106.  %%Block 6%%
107.  %% Equation 7%%
108.  Delta_T = bsxfun(@minus,averages_Tw,averages_Taw); %% Calcualted
      temperature difference (Tw-Taw) %%
109.  Nu=(Q*D/Lambda)./Delta_T     %%Nusslet number%%
110.
111.  %%Block 7%%
112.  %%Apply smoothing to all time series data and t_steady calculation%%
113.  %%Equation 17-20%%
114.  n=10;
115.  mask=ones(1, n)/n;
116.  Nu_Smooth=conv(Nu, mask, 'same');
117.  Nu_Diff=diff(Nu_Smooth);
118.  tmp_setTime=find(Nu_Smooth<0.01)+1;
119.  t_steady=t(tmp_setTime(1));
```
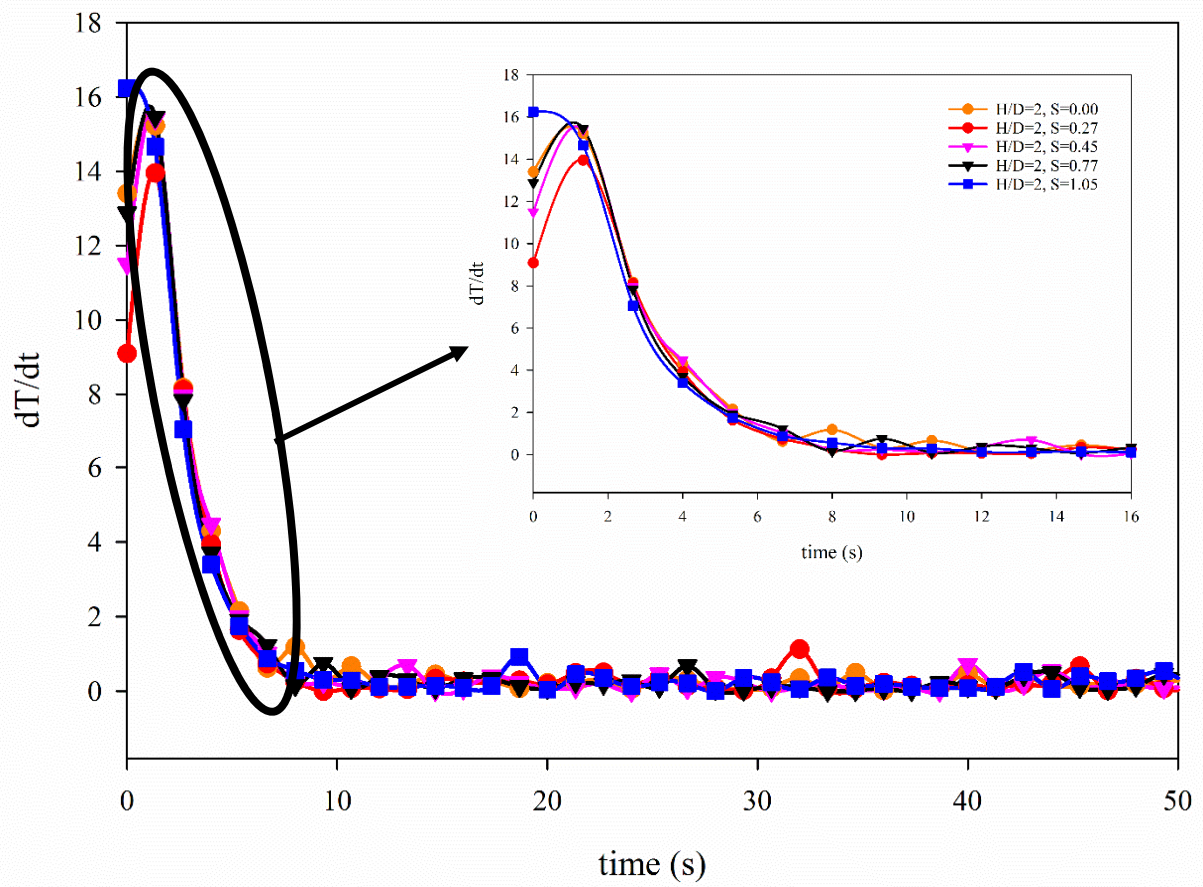
Figure 2-A1: Rate of temperature variation over the region of interest A2 for swirling and non-swirling impinging jets at Re=35,000, H/D=2.

Chapter 3: Transient Heat Transfer Characteristics of Swirling and Non-Swirling Turbulent Impinging Jets

The chapter addresses the gap discussed in RQ2 by using highly resolved (time series) imaged (infrared) data in conditions spanning Re=11,600, 24,600, and 35,000. The experiments are based on an electrically heated foil (0.025 mm) with jets over S=0–1.05 and nozzle-to-plate-distances, H/D=2, 4, and 6.

3.1 INTRODUCTION

Impinging jets have been studied because of their industrial applications such as turbine blade cooling [1], cooling of electronic devices [2], glass tempering [3], and paper drying [4]. The flow field between the jet nozzle and impingement surface can be categorized into three regions: free jet region, stagnation zone, and the wall jet region as shown in Figure 3.1. These regions are distinct in terms of their heat transfer and flow characteristics [1]. Most studies investigating gaseous impinging jets have only been conducted under steady-state conditions whilst considering the effects of Reynolds number (Re), nozzle-to-plate distance (H/D), and swirl intensity (S). The studied effects have been the uniformity and magnitude of heat transfer [5–7]. In such studies, a foil type metallic target is heated by passing high current through it so that it forms the impingement surface [8,9]. Since many practical applications utilize impinging jets for cooling or heating within a short period [10], it is therefore also necessary to understand the transient characteristics of impinging jets as the heat transfer field approaches steady-state. This requires that the role of various process parameters, in both non-swirling and swirling conditions, be investigated which forms the focus of the present paper.

Of the few studies that have dealt with the transient characteristics of turbulent impinging jets, Table 3.1 shows that none has considered the effects of swirl on transient heat transfer. Additionally, almost all transient experimental studies have utilized thick metallic plates (with high surface temperatures) whereby temperatures are measured at the back of the plate through the Inverse Heat Conduction Problem (IHCP) approach to evaluate heat removal from the front surface. Such techniques carry a number of drawbacks. Firstly, IHCP introduces an extra ambiguity/uncertainty to the results because non-homogeneity and defects (in the plate material) cannot be taken into account for analytical calculations. Moreover, a thicker heated plate having a bigger thermal capacity will be relatively insensitive to short time-frame

transient (surface) temperature changes from gaseous jets. In this regard, a constant heat flux (uniform property, heated) thin foil has advantages over thicker metallic plates.
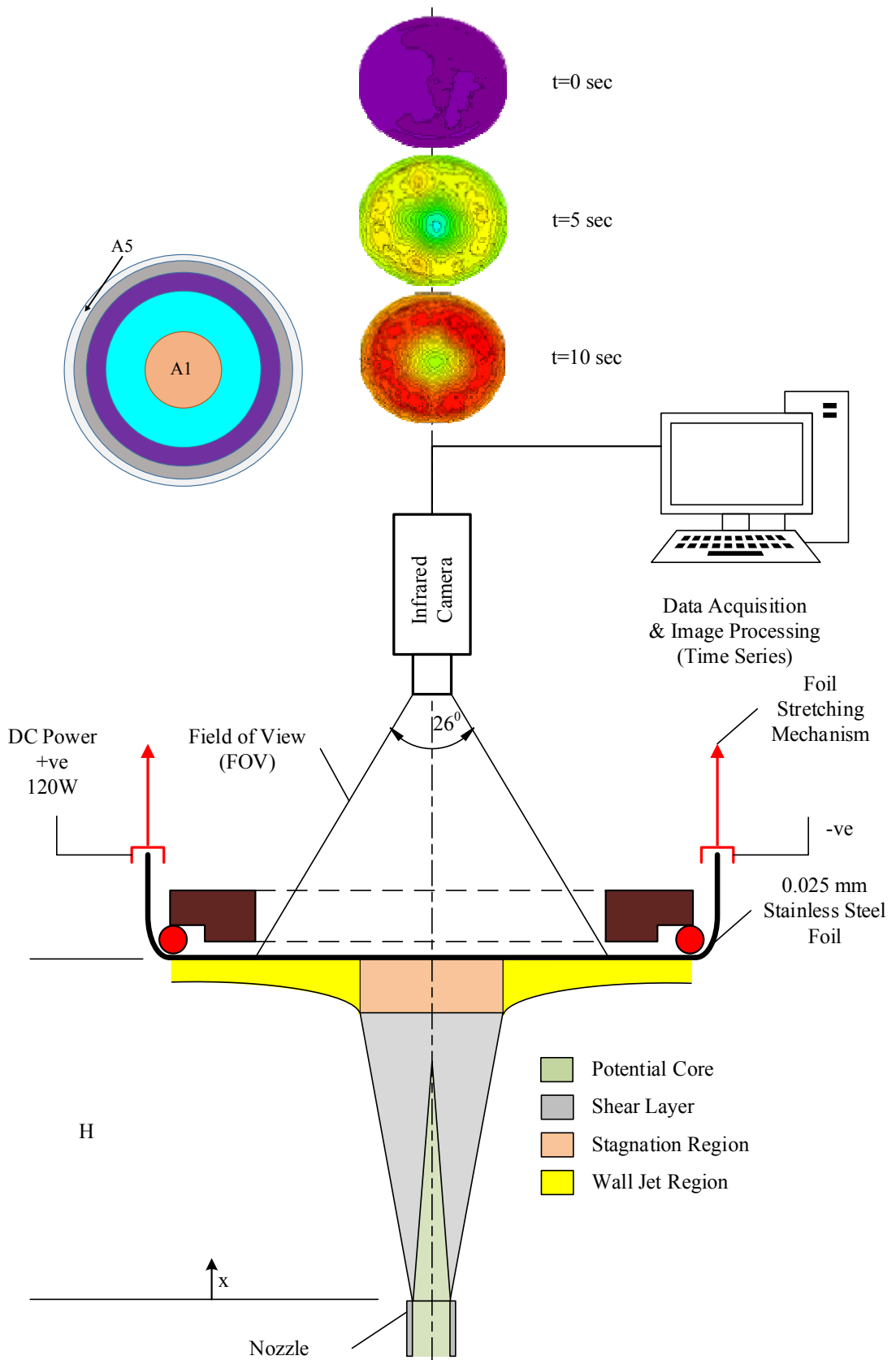
Figure 3.1: Experimental setup and the characteristic regions of an unconfined axisymmetric (cool) jet impinging onto a heated surface.

In relation to non-swirling liquid jet impingement, Fujimoto et al. [11] investigated the transient cooling between a hot solid block and a free circular jet. It was noted that at H/D=1 the stagnation zone heat transfer rates were very high but this decreased as cooling advanced in time and steady-state conditions prevailed. Mitsutake and Monde [12] also studied transient cooling of a high-temperature surface with a liquid impinging jet and found that peak heat transfer occurs around nucleate boiling. The position of the wetting region studied, with respect to the wetting front where nucleate boiling starts, has also been measured and correlated with a power function of time ($r_{wet}=a.t^n$), where a and n are experimentally determined constants and r_{wet} is the radius of the wetting front). Rahman and Lallave [13] numerically investigated liquid jets impinged onto a rotating disk and found that the time to reach steady-state heat transfer reduces for higher Reynolds numbers and greater thermal diffusivity of the rotating disk material.

Table 3.1: Summary of experimental and numerical transient heat transfer studies of non-swirling gaseous impinging jets.

Authors	Methodology	Nozzle Diameter (mm)	Re	Plate Thickness (mm)	H/D
Liu et al., [14]	E	6.4	800-15,000	---	1-10
Yang and Tsai [15]	N	---	16,100-29,600	---	4-10
Amici et al., [16]	E	8.0	20,000-40,000	4	1-10
Yi et al., [17]	E	2.0	3,500	---	4-8
Dou et al., [18]	E	6.0	22,000-31,000	10	4
Yu et al., [39]	N	5.0	20,000-60,000	2	0.2-2
Madam et al., [19]	N	---	1,333-34,000	1	4
Guo et al., [40]	E & N	6.0	14,000-53,000	---	4-8
Zhu et al., [41]	N	5.0	7,000-30,000	2	0.2-1
Methodology- N: numerical, E: experimental					

As for gaseous non-swirling impinging jets, Liu et al. [14] studied transient heat transfer from a horizontal ceramic-based MCM (Multi-Chip-Module) disk having a similarly sized confinement orifice around the jet in the upstream, thereby using conditions promoting both forced and buoyancy-driven convection. The temperatures were measured using thermocouples. The effects of Grashof number, Reynolds number, and nozzle-to-plate spacing were reported as well as a proposed prediction of the time needed for steady-state. Yang and Tsai [15] conducted a numerical study which focused on conjugate heat transfer for a flat circular plate at 373 K and observed that the time needed for a circular plate to attain its steady-state condition decreased as the Reynolds number increased. Yazici et al. [16] researched the transient temperature distribution during the tempering of the 4mm thick glass plate (up to 700

°C) using air jets (H/D=1-10). Three-point measurements were made over the heated glass surface. The highest Nu and shortest time to steady-state was achieved at the highest Reynolds numbers, but this was realized at an intermediate impingement distance (H/D=6) in the range tested. Yi et al. [17] also investigated the transient heat transfer and temperature distributions in an oblique impinging jet onto a thermographic phosphor-coated plate. The initial temperature was set as 360 °C for jets operated at Re=3,500 over H/D=4-8. Results showed that Nusselt numbers vary over time and that they were highest at the stagnation point earlier in the experiments but these declined as the steady-state time period was approached. Dou et al. [18] and Kadam et al. [19] utilized the Inverse Heat Conduction Problem (IHCP) method to calculate the temperature and heat transfer distribution at the impingement surface by using temperatures at the back of a thick impingement plate. The Nu_{equ} was calculated using the IHCP method, but some uncertainty arises in the results due to the indirect measurement of temperatures over the impingement surface. Duo et al. [18] observed that the stagnation region heat transfer needed 20 sec to reach steady-state. The above studies, therefore, emphasize the dependency of impingement heat transfer on operating conditions and that both its uniformity and magnitude both vary over time as steady-state is approached.

In comparison to non-swirling jets, induced swirl into the jet can drastically alter the steady-state flow field of a jet, introduce time-varying flow instabilities [20], and affect impingement pressure/heat transfer distributions [21,22]. Huang and El Genk [6] studied the flow field and heat transfer of a swirling impinging jet using a smoke generator. They showed that a spiral-based motion, caused by a tangential velocity component for the impinging jet, widened the impingement and wall jet area, which caused improvement in the average/local (near the stagnation region) Nusselt number at intermediate jet spacing when compared to non-swirling impinging jets. However, for the large nozzle-to-jet spacing the non-swirling impinging jets have higher Nusselt number values in the vicinity of stagnation region. Furthermore, they observed that swirl also affects both the radial distribution and uniformity of steady-state heat transfer. However, Ward and Mahmood [5] when studying the heat and mass transfer for swirling impinging jets showed that significantly lower steady-state heat transfer rates are achieved in swirling, compared to non-swirling, impinging jets. Lee et al. [7] conducted a study for swirling impinging jets using nozzle inserts and found strong heat transfer dependency on swirl intensity. They showed that for H/D<2, a swirling jet provides high heat transfer rates with good radial uniformity but for larger H/D (near H/D equal 10) the heat transfer enhancement of swirl vanishes. Wen and Jang [23] compared heat transfer data in jets with

crossed-swirling-strip inserts and longitudinal swirling-strip inserts and found that the former showed 4-5% better performance. Yuan et al. [24] also observed that stagnation point heat transfer drops to some degree with swirl, but climbs in the wall jet region. They also inferred that the radial uniformity of heat transfer can be improved with the addition of swirl. However, none of these studies have analyzed transient heat transfer in swirling impinging jets nor compared it to the non-swirling jets.

With the above in mind, it appears that little (or no) work has been done to deal with the transient heat transfer characteristics comparison between non-swirling and swirling jets, particularly using highly sensitive methods employing non-intrusive infrared imaging combined with the thin foil technique. This study utilizes highly resolved spatial and temporal methods to resolve the impingement plates ($0 \leq r/D \leq 2$) transient heat transfer characteristic in both swirling and non-swirling turbulent impinging jets (S=0-1.05) over Re=11,600-35,000 (H/D=2-6). A thin foil metallic (constant flux) heater is utilized in order to avoid the ambiguity with other methods (IHCP) as has occurred in earlier works [8,9]. The time to reach steady-state for the different operating parameters is studied using (time series based) infrared thermography and image processing.

3.2 METHODOLOGY

The experiments to resolve the transient characteristics are conducted using the same nozzle deployed earlier for studies into (only) the steady-state heat transfer of both swirling and non-swirling impinging jets [21,25–27]. Jets (unconfined) are operated with compressed (room temperature) air supplied from a flow board comprising various flow meters (variable area type) supplied by a screw compressor having an integrated dryer and filter (make: Atlas Copco, model: GA15-10). A schematic diagram of the test rig (swirl nozzle, heater plate, and thermal camera) is shown in Figure 3.1.

3.2.1 Swirl Nozzle

Turbulent swirling and non-swirling gaseous (air) jets are generated using the multi-port nozzle shown in Figure 3.2. The nozzle is optimized for the angle of tangential ports, total length, and the ratio of axial-to-tangential inflow [28]. The 743mm long nozzle comprises seven (modules) sections that are assembled together. The inner diameter of the bottom two sections is 50mm, while the top four sections have an inner diameter of 40mm. The nozzle is supplied through five inlet ports, two of which are radially opposite and provide axial air (56mm from the bottom) with another three ports for tangential air (170mm from the bottom). The tangential

ports are situated at 120° over the periphery of the nozzle and at 20° with the horizontal plane. An aluminum honeycomb structure and mesh screen are used for flow conditioning after the axial ports. The third section from the bottom has an area contraction ratio of 1.56, thereby reducing the inner cavity diameter from 50mm down to 40mm. This assists with coalescing the individual inflows into a single stream. The inner contour of this section is CFD optimized using a cubic polynomial in order to minimize boundary layer separation [28]. The third, fourth, and fifth nozzle sections are identical and all developing the flow as well as further enhancing its uniformity. The nozzle final (seventh) section's diameter is 40mm with sharp edges ~ 0.2mm in order to minimize/avoid vortex shedding from the thin edge at the exit plane. This geometry also allows for the incremental (aerodynamic) transition between non-swirling to swirling jets without the central blockages, which is associated with helical inserts or radial vanes. In this manner, the swirl and Reynolds numbers can be independently changed by varying the ratio of axial to tangential streams.
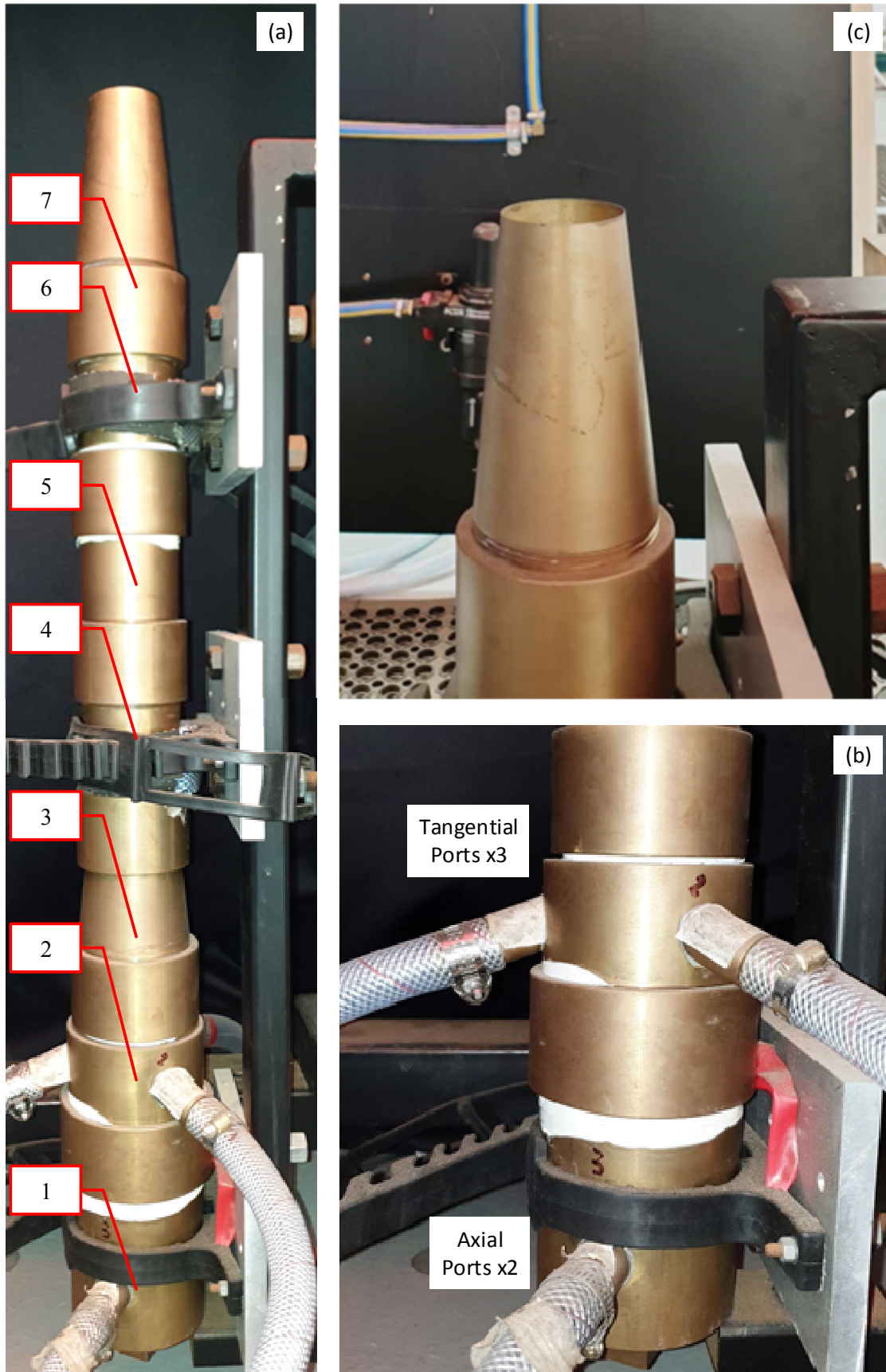
Figure 3.2: (a) Jet nozzle showing different sections (overlay on white background); (b) lower end of the nozzle with two axial and three tangential ports; and (c) nozzle top section showing "knife" edge.

The global Reynolds and the swirl numbers can be defined as follows:

$$Re = \frac{\rho U_b D}{\mu} = \frac{4Q}{\pi D \nu} \tag{3-1}$$

$$S = \frac{W_b}{U_b} \tag{3-2}$$

where Q is the total volume flow rate through the axial and tangential ports. The bulk axial velocity (U_b) and the bulk tangential velocity (W_b) are expressed at the exit plane and measured using Constant Temperature (hotwire) Anemometry (CTA):

$$U_b = \frac{2}{R^2} \int_0^R r \langle u \rangle dr \approx \frac{2}{R^2} \sum_{r=0}^{r=R} r \langle u \rangle dr \tag{3-3}$$

$$W_b = \frac{2}{R^2} \int_0^R r \langle w \rangle dr \approx \frac{2}{R^2} \sum_{r=0}^{r=R} r \langle w \rangle dr \tag{3-4}$$

3.2.2 Constant Temperature Anemometry

CTA is used to measure boundary conditions at the nozzle exit using a system consisting of a temperature module (make: Dantec Dynamics, model: 90C20), three CTA channels (model: 90C10), and a streamline mainframe (model: 90N10). An automatic gaseous calibrator (model: 90H10) along with an air filter (model: 90H04) is used to pre-filter air supplied to the calibrator and correlate measured voltage from each CTA channel with respect to velocities from the nozzle on the calibrator. Temperature variations are compensated by utilizing data from a temperature probe [29]. The axial <u> and azimuthal <w> velocity components are determined by a miniature x-wire (dual sensor) probe (model: 55P61). The repeatability of CTA measurements in swirling jets was quantified previously as 4% [27,30].
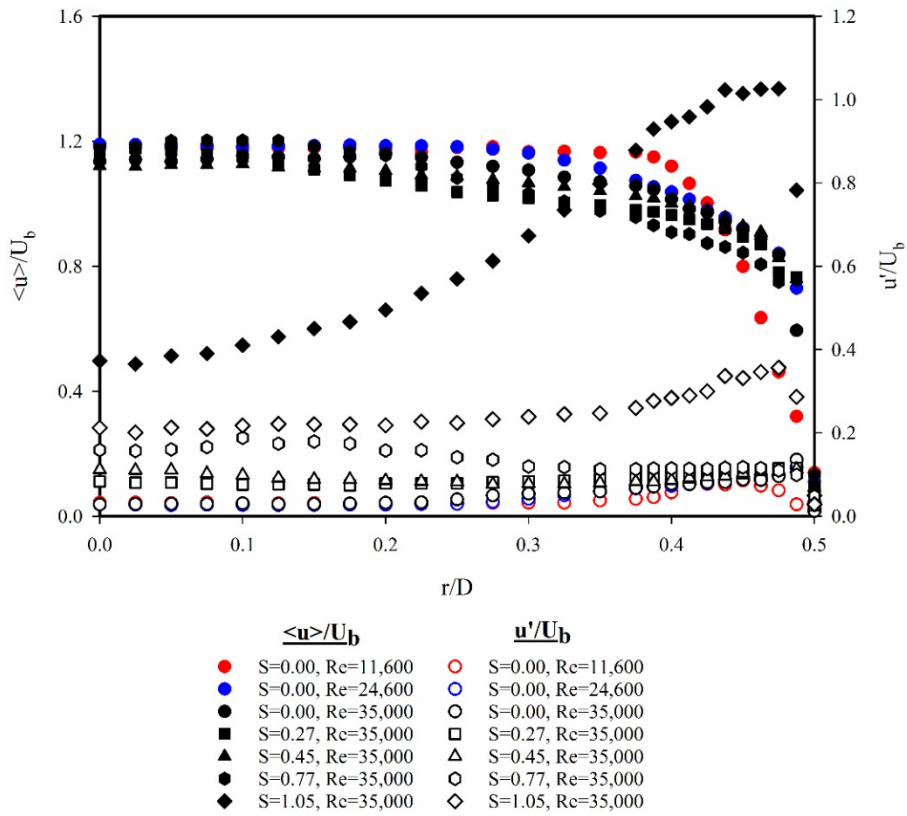
(a)
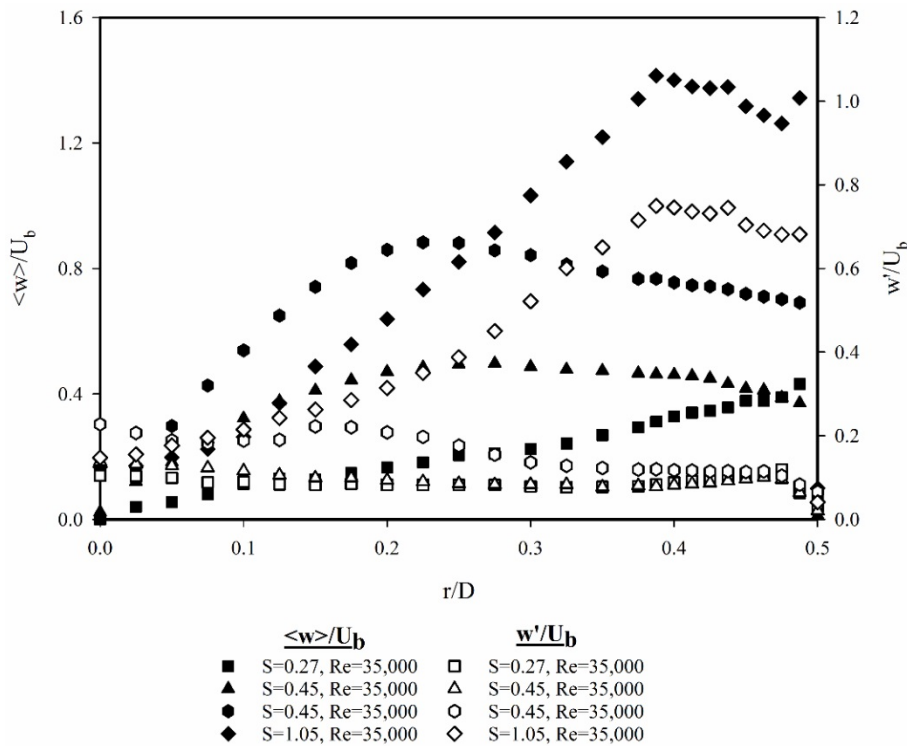
(b)

Figure 3.3: Normalised (a) axial (<u>/Ub) and (b) tangential (<w>/Ub) mean velocity and their respective fluctuations for non-swirling and swirling test cases. Measurements are taken at 1mm above the exit plane (x/D=0.025).
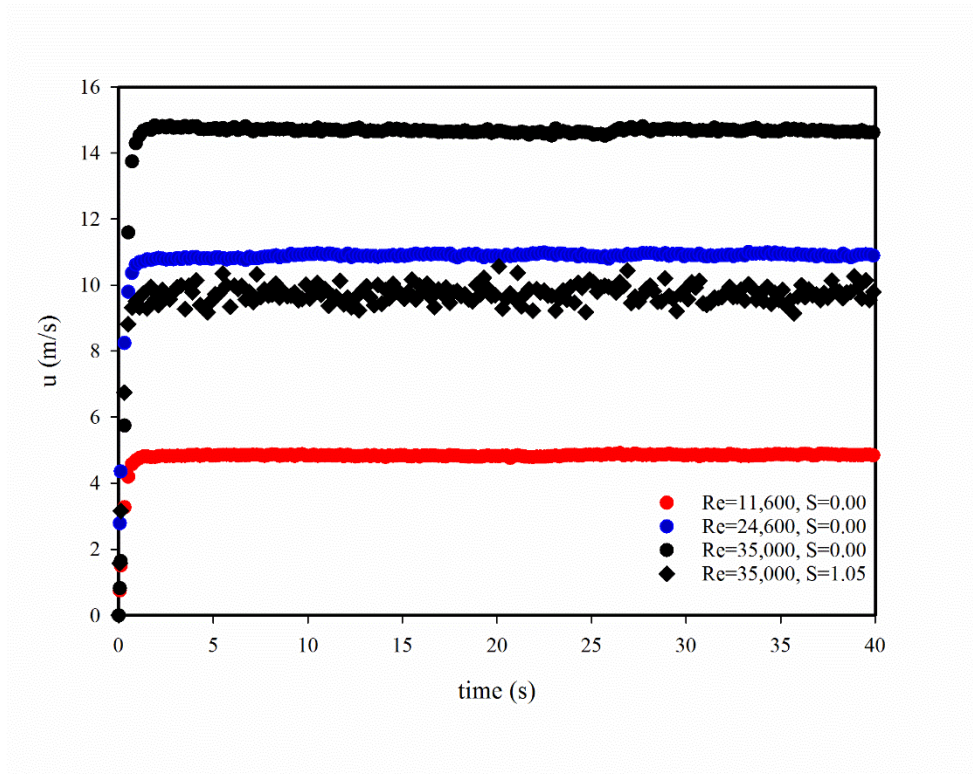
(a)
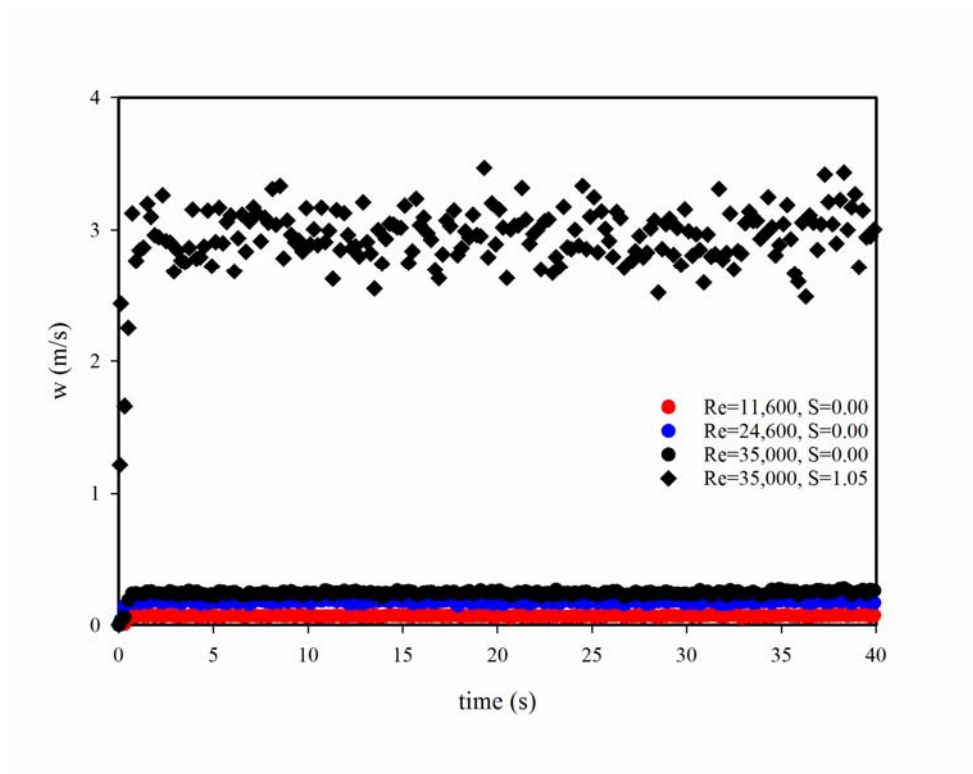
(b)

Figure 3.4: Effect of shut-off valve opening on (a) axial <u> and (b) azimuthal <w> velocity component with respect to time.

Figure 3.3(a) and (b) show the upstream normalized mean axial and tangential (azimuthal) velocity components with their fluctuations respectively, measured 1mm above the nozzle exit plane. The velocity components are normalized using the bulk axial velocity. The tangential velocity component for non-swirling jets is zero. The axial velocity distribution for all the cases is similar except for the highest swirl case at S=1.05 and Re=35,000. Results show that the tangential velocity profile continuously changes as the swirl intensity increases from weakly to high swirl.

In acquiring data for the transient heat transfer characteristics, the procedure used first involved setting up the flow meters supplying the axial and tangential ports to the nozzle. Once readied, a shut-off valve was then applied (i.e., no flow from the nozzle). Secondly, the heated impingement plate was then operated until its steady-state condition with no jets impinging (additional details in the next section). Once readied, stabilized and after commencing the acquisition of data, the 'shut-off valve is then opened' with this instant designated t=0 sec in the ensuing results. To identify the time period needed for the jet to fully develop (from t=0 sec), Figure 3.4 presents CTA measured <u> and <w> data at the centre of the nozzle exit plane when this process is repeated on a free jet. It is evident that the three non-swirling jets (Re=11,600, 24,600, and 35,000; S=0) and (highest) swirling case (Re=35,000; S=1.05) stabilize within 1-2 sec of the shut-off valve being opened. As such, this initial short period for the jets to flow dynamically stabilize is around ~10% relative to the period needed for heat transfer to reach steady-state as will later be presented (Figure 3.8 and Figure 3.11).

3.2.3 Heated Impingement Plate

A custom-designed and assembled constant flux (electric) heated impingement surface is used to quantify the heat transfer characteristics of the non-swirling and swirling turbulent impinging jets. The heated surface is achieved with a 0.025mm thick foil (316 stainless steel) stretched using foil tensioning clamp, sized 320 x 200 x 0.025mm. This is coated on its back with a thin layer of VHT flameproof paint (to withstand 1093°C) which is matt black having an emissivity of 0.97 (measured). The use of a single type of heated impingement plate throughout ensures the trends presented are largely jet (and not thermal mass) dependent. The thin foil technique [9,31,32] is applied in order to avoid lateral conduction heat loss. A high current (~40amp) DC power source (make: Micron, model: Q0966) is used to apply 120Watt power over the impingement plate, the spatial variation in heat flux distribution over the surface is ± 2% [30]. Stainless steels offer a relatively low change in their resistivity (77.7x10-8-

82.5x10-8, Ω.m, i.e., ~6%) [33] over temperatures typical of those observed with convective cooling from jets in the current experiments (45-100°C). This supports the assumption that the applied heat flux is reasonably constant for the impingement conditions tested and explains why no appreciable power fluctuations were observed to the power supply current during operation. Heated surfaces reach a maximum of 95-100°C with no jet impingement. Experiments were conducted to measure the emissivity of both the painted (back) and unpainted (impingement front) surfaces. Further details can be found in an earlier study [30]. The paint layer is relatively uniform, as evident from the ensuing results (t=0, Figure 3.1, Figure 3.6, and Figure 3.7).
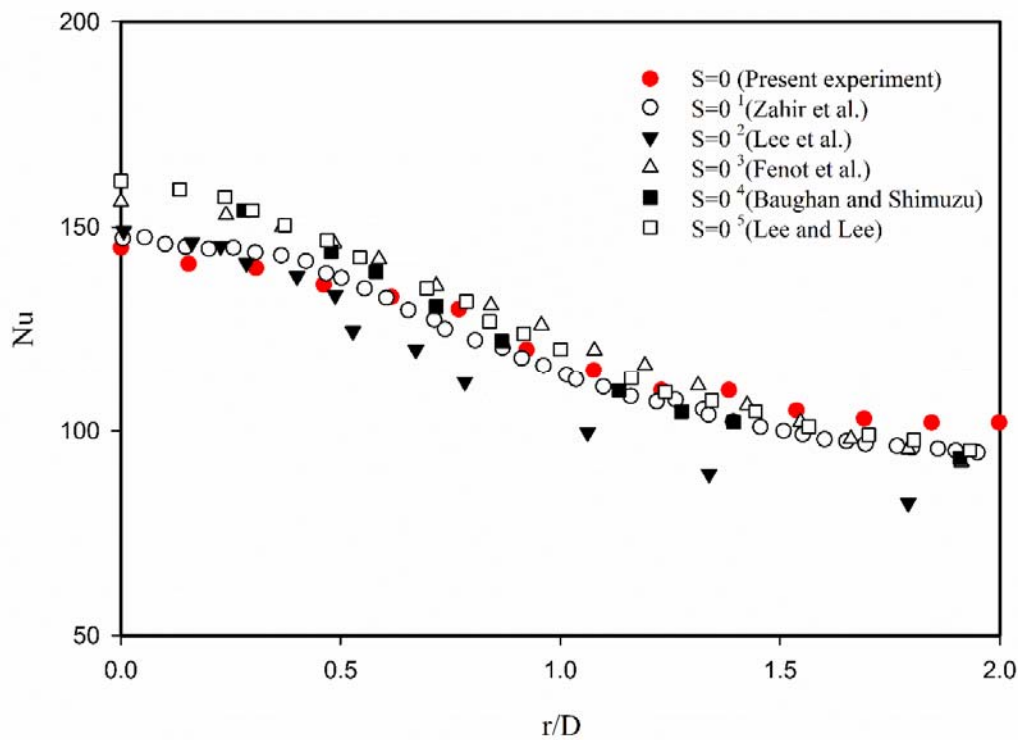
Figure 3.5: Nusselt number comparison for Re~24,000, H/D=6 ([1]Zahir et al. [21], [2]Lee et al. [42], [3]Fenot et al. [43], [4]Baughan and Shimizu [44], and [5]Lee and Lee [45].

Before any transient jet impingement data is acquired, steady-state conditions are first achieved by heating the plate without jet (flow). The heated impingement plate then takes a further 60-90 minutes to reach a steady-state condition which obviously takes into view both any (minimal) thermal storage associated with the extremely thin foil, any connecting fixations as well as buoyancy-driven losses from its surfaces (fluctuations stabilize at ± 2°C). Figure 3.5

shows the relevancy of steady-state heat transfer (Nusselt number) for non-swirling jets in the current setup compared to other studies at Re=23,000-25,000 and H/D=6.

3.2.4 Infrared Imaging

Thermal imaging is utilized to measure spatially resolved temperatures over the heated impingement plate. An infrared camera (make: FLIR, model: A325) which operates between the spectral range of 7.5-13μm is used to map the temperature distribution. This infrared camera has 76,800 (320 x 240) micro-bolometer detectors having a pixel-to-pixel pitch of 25μm, low response time (7ms), and ±2% accuracy. By mapping the distribution of surface temperatures over time, the convective heat transfer is quantified through post-processing. The IR images captured using a thermal camera then post-processed using the image processing toolbox in MATLAB (version 2015b). The spatially resolved local heat transfer coefficient (h) is calculated using an energy balance method for each imaged pixel using Equation (3-5).

$$h(j,k,t) = \frac{q - q_l(j,k,t)}{T_w(j,k,t) - T_{ref}(j,k,t)}$$
(3-5)

In this context, j and k are the pixel location, T_{ref} is the adiabatic wall temperature for an incompressible impinging jet [34], and q is the heat flux applied to the heater using the DC power supply (~1875W/m^2). Preliminary testing with jets impinging resolve T_{ref} [9]. The heat flux q is defined as the product of applied voltage (V) and current (I) divided by the area of the impingement surface, q=VI/A. In Equation (3-5), q_l is the summation of total heat loss by radiation and lateral conduction from the thin foil and ascertained by imaging the temperature distribution on the rear surface. As such, it includes both forced convective heat transfer from the front face as well as any natural convection from the rear face that was subject to throughout the experiments to a quiescent atmosphere. Since the thickness of the thin foil is very small and the heater operating temperatures are typically < 100°C, q_l is found to be less than 5% of the applied heat flux [21]. Wall temperatures (T_w) can be taken as uniform along with the foil thickness since the Biot number (Bi=hδ/k_{foil}) is significantly lesser than unity for this set-up (0.1 [30]) in contrast to the Fourier number F_o=k_{foil}/(ρcδ^2), which is significantly greater than one. Additionally, heat transfer through the exposed sides (ends) of the heated plate (not subjected to jet flow), is insignificant and can be considered negligible [21]. Equation (3-6) is used to measure local (spatially resolved) convective heat transfer (Nusselt number) in Cartesian coordinates over the impingement surface, whereas Equation (3-7) is used to obtain

surface averaged $\overline{Nu}$. By imaging an object of known physical size, the conversion of the Field of View (FOV) from pixels to cartesian coordinates was achieved[4].

$$Nu(x, y, t) = \frac{h(x, y, t)D}{\lambda} \tag{3-6}$$

$$\overline{Nu}(r) = \frac{1}{A} \int_A Nu(r) dA \tag{3-7}$$

where λ and D are the thermal conductivity of air and nozzle diameter respectively. The ensuing results for the transient heat transfer characteristics will consider the spatially averaged Nusselt numbers over both the entire target surface, as well as its value over five equally sized areas (segments) [21]. The aim here is to further analyze the uniformity of Nu. To achieve this, the impingement surface is divided into five equally sized areas as shown at the upper left corner of Figure 3.1. As such, the average Nusselt number is calculated for r/D=0-0.89 (A1), 0.89-1.27 (A2), 1.27-1.55 (A3), 1.55-1.79 (A4), 1.79-2.00 (A5), and 0.00-2.00 (Aavg) using Equation (3-7). This will identify if different portions of the target surface together reach the steady-state condition or not and the effects of Re, S, and H/D on this transient period.

The 1-D median filter method is utilized for smoothing the data derived from Equation (3-7) for each of the spatially resolved areas (A1-A5 and Aavg), as recommended by [35]. Subsequently, the derivative (rate of change) of Nu versus time is calculated. The transitional stage (time to reach steady-state) is evaluated by analyzing the slope of the derivative of Nu reached.

3.2.5 Uncertainty Analysis

An uncertainty analysis was also carried as a function of systematic (ε_s) and random (ε_r) errors in relation to the specified Reynolds and Nusselt numbers using the method proposed by Moffat [36]. Systematic errors are evaluated based on the accuracy (specified by the manufacturer) of the equipment (IR camera, CTA, and Flowmeters) and found to be ~±2%. The overall uncertainty ($\varepsilon_s+\varepsilon_r$) in the Reynolds number comes from the flow meter readings and is estimated as ± 4%. The uncertainty in Nusselt number is found to be ~ ± 5%. Further, details

---

[4] http://flir.custhelp.com/app/utils/fl_fovCalc/pn/48001-1001/ret_url/%252Fapp%252Ffl_download_datasheets%252Fid%252F8

can also be found in the earlier study [21]. All results presented for the transient heat transfer characteristics are based on two repetitions of the same test condition.

3.3 RESULTS AND DISCUSSION
3.3.1 Non-Swirling Impinging Jets

Three different Reynolds numbers (11,600, 24,600, and 35,000) and nozzle-to-plate distances (H/D=2, 4, and 6) have been investigated in this study. The transient heat transfer characteristics for non-swirling impinging jets are presented first (Figure 3.6, Figure 3.7, and Figure 3.8) followed by swirling jets (Figure 3.10, and Figure 3.11). In this context, the time to reach steady-state spans the interval needed for the hydrodynamic equilibrium of jet, development of the thermal boundary layer, and any effects from the (small) thermal inertia of the (thin) impingement plate, all of which are interlinked and reflected in the summary data presented.

Figure 3.6 shows the time evolution of spatially resolved Nusselt number for different Reynolds numbers (H/D=2), with Table 3.2 identifying the time needed to reach to steady-state (t_{steady}) in each non-swirling jet. It can be seen that for each time step within Figure 3.6, the first peak of the Nusselt number appears over a ring-shaped area at r/D~0.7 and continues to intensify with time. Also noticeable is that the Nusselt number of the (inner) stagnation zone and (peripheral) wall jet region continue to develop with time until steady-state. These experimental results also show that peak Nusselt numbers in higher Reynolds number jets are consistently greater, at any time interval, over the transient period in comparison to lower Reynolds number jets. Similar to every forced convective process, transient heat transfer (Nusselt number) of swirling and non-swirling impinging jets also starts from the value of natural convection and reaches to maximum (steady-state) value corresponds to the each jet operating condition.
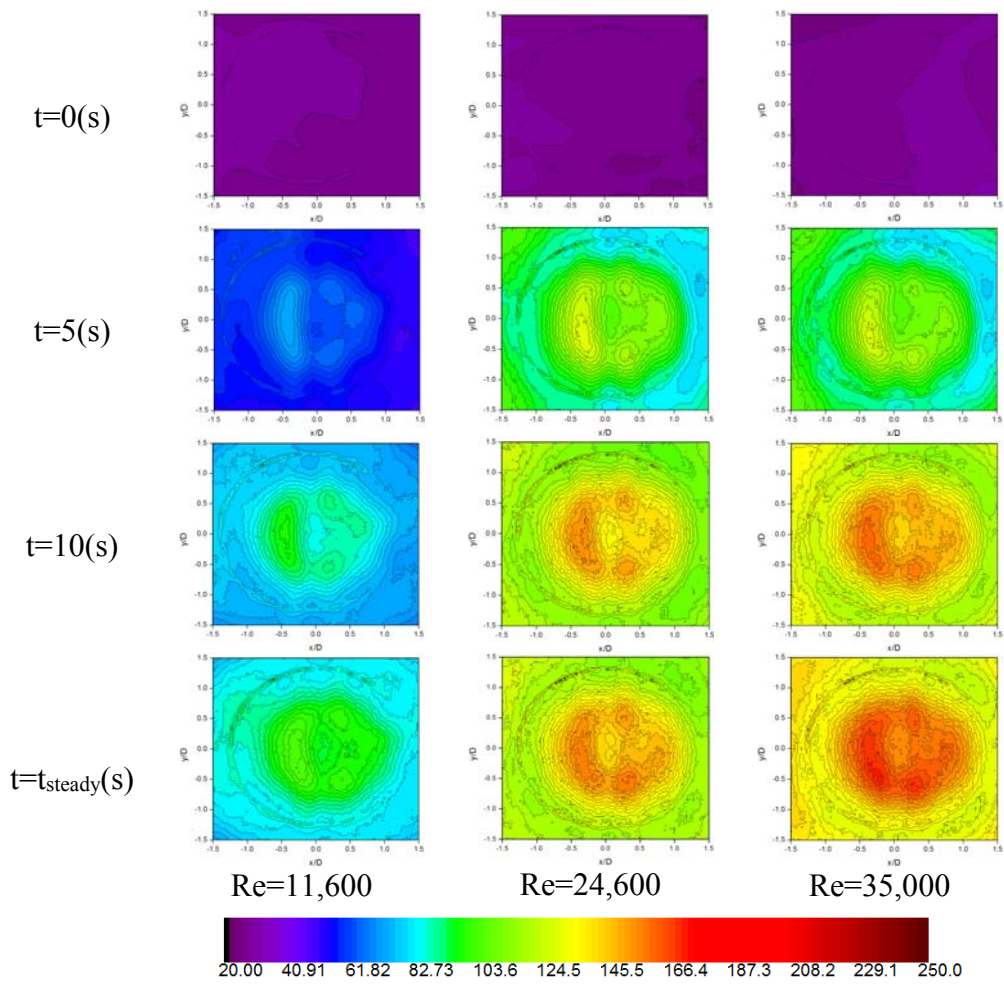
Figure 3.6: Nusselt number contour plot at H/D=2 for different Reynolds numbers for non-swirling impinging jets.
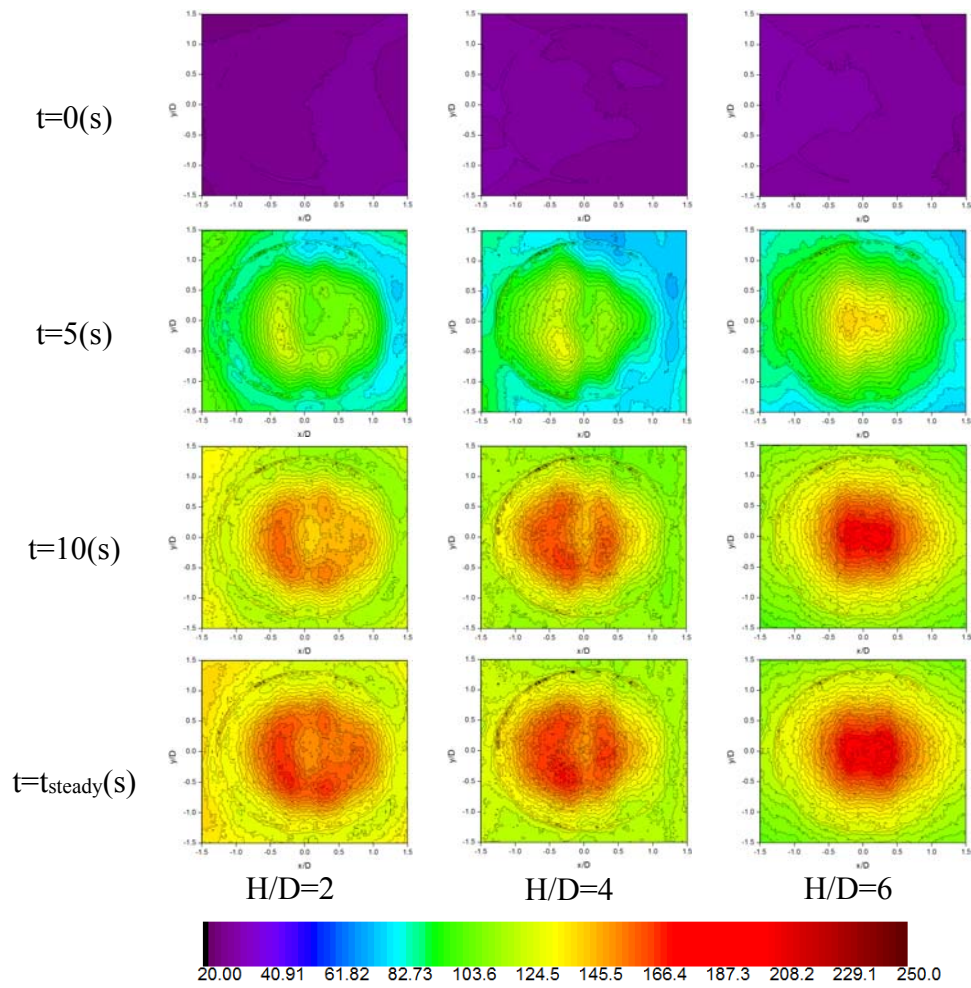
Figure 3.7: Nusselt number contour plot for different impingement distances at Re=35,000 for non-swirling impinging jets.
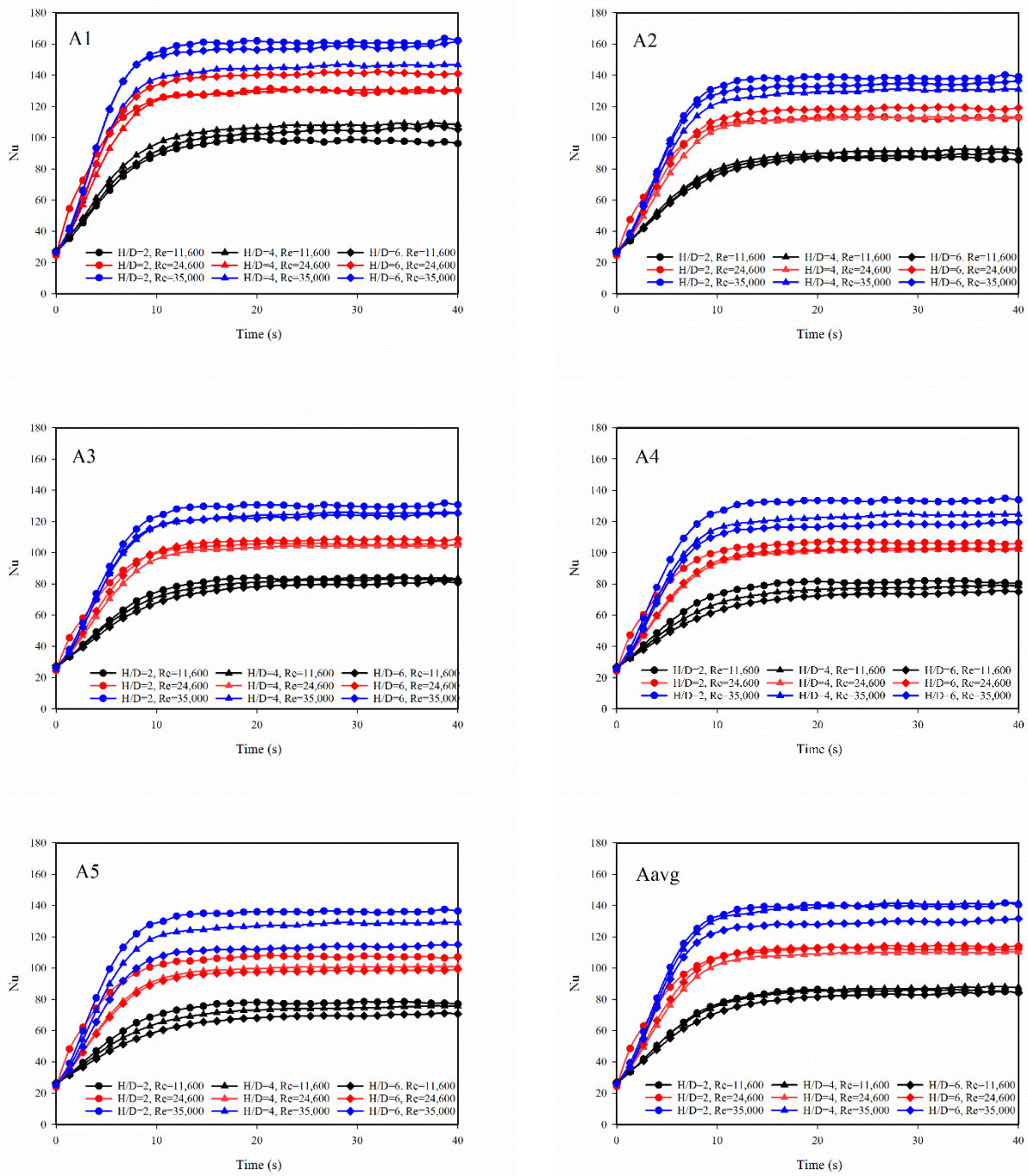
Figure 3.8: Temporal evolution of Nusselt number averaged over different areas on the heated impingement plate for non-swirling impinging jets. Each colour corresponds to a specific Reynolds number.

Figure 3.7 depicts experimental data for the effect of impingement distance (H/D=2, 4, and 6) on heat transfer in non-swirling jets at Re=35,000. From these it is evident that both the (transient) stagnation zone and wall jet region's Nusselt numbers are affected by H/D but with peak Nusselt number occurring at the stagnation zone for H/D=6 instead of the ring link formation visible at H/D=2. As such, the results show that the transient behaviour (uniformity) of heat transfer in these jets also changes over time and that such variations are not confined to steady-state differences. For t=5 sec the central peak at H/D=6 is larger compared to H/D=2 but with the passage of time, the peak occupies the entire stagnation zone.

Figure 3.8 presents summary data for the temporal evolution of average Nusselt number over five equally sized areas starting from the stagnation zone (A1, A2, A3, A4, and A5). The overall surface average (Aavg) bound by r/D=2 is also given. This data resolves that the rate of change in heat transfer not only varies between jets but that both the transient and steady-state Nusselt numbers (Nu_{st-st}) increase with Re. The time (t_{steady}) to reach to Nu_{st-st} decreases with Reynolds number as evidenced by the steeper rates of change in Nu with time. As such, whilst the initial rate of increase in Nu with time is mostly linear over a t=0-10 sec, jets with a higher Re induce a more acute rate of cooling at the start.

Table 3.2: Time (s) to reach steady-state for non-swirling impinging jets.

		H/D=2	H/D=4	H/D=6
Re=11,600 U_b=4.39(m/s) S=0	A1	18.2	23.9	19.4
	A2	18.1	24.4	19.8
	A3	18.1	24.5	22.3
	A4	18.2	24	22.5
	A5	18.1	22.9	22.5
	Aavg	18.1	24.1	19.8
Re=24,600 U_b=9.32(m/s) S=0	A1	15.4	21.7	17.8
	A2	15.5	23.6	17.4
	A3	16.4	23.5	17.5
	A4	16.5	23.5	17.5
	A5	16.7	23.6	17.4
	Aavg	17	23.6	17.5
Re=35,000 U_b=13.23(m/s) S=0	A1	14.8	19.5	16.5
	A2	14.4	21.4	16.5
	A3	14.5	21.5	15.9
	A4	14.6	21.7	15.8
	A5	14.3	21.3	15.7
	Aavg	14.5	22.1	15.9

These data also show that with the exception of locations akin to the wall jet region (A4, A5), there appear to be insignificant effects of H/D on the spatially resolved rate of change value of Nu at each Reynolds number. The entire spatial distribution of Nu incrementally and uniformly develops with time. Additionally, regions A4 and A5 which are more representative of the wall jet region can exhibit (at H/D=6) a slower rate of increase in Nu with time compared to H/D=2. In contrast to these results, Yazici et al., [16] reported that for non-swirling gaseous jet the shortest time for (a much thicker 4 mm) target surface to reach steady-state is at the highest Re and H/D=6. Table 3.2 also shows that the time to steady-state (at Re=11,600) is similar between H/D=2 (t=18.1 sec) and H/D=6 (t=19.8 sec) compared to interim distance H/D=4 (t=24.1 sec). This similarity between the time to steady-state at H/D=2 and H/D=6 also repeats itself in Table 3.2 for Re=24,000 and 35,000. As such, the time evolution of heat transfer at the intermediate nozzle-to-plate distance (H/D=4) appears distinct in these results from that with near-field (H/D=2) or far-field (H/D=6) impingement. Whilst this behaviour (in transient heat transfer) appears consistent with Yazici et al. [16] who found the (steady-state) heat transfer at an interim H/D=6 to be distinct from others over the range H/D=1-10, further research is warranted into the flow field at this intermediate H/D=4.

3.3.2 Swirling Impinging Jets

The effect of low-to-high swirl numbers (S=0.27, 0.45, 0.77, and 1.05) on the transient Nu distribution are studied with respect to three different nozzle-to-plate spacing (H/D= 2, 4, and 6) for Re=35,000.

Figure 3.9 illustrates the colour contour map for turbulent swirling impinging jets at H/D=2. At low-to-intermediate swirl (S=0.27, 0.45), the peak Nusselt number surrounds the central stagnation zone for all time steps. At t=5 sec, the maximum Nusselt number manifests itself in the shape of a lobe, but beyond t=10 sec, a well-developed (solid) circular region of high Nu is instead situated at the central stagnation zone at low and intermediate swirl (S=0.27, 0.45, and 0.77) but not high (S=1.05). However, the slight asymmetries observed at the early stages in some of the jets (**Figure 3.6: Nusselt number contour plot at H/D=2 for different Reynolds numbers for non-swirling impinging jets.**Figure 3.6 and Figure 3.7) do not manifest themselves at later time intervals, and so are unlikely to affect the total time to reach steady state. This result also shows that the distribution of Nu can significantly change with time within very short intervals. Whether these Nu troughs and peaks are likewise associated with the development of small pockets of recirculating gases, which have been predicted numerically with the steady-state Nu

distributions for such flows [37], requires further investigation. For moderate-to-high swirl (S=0.77, 1.05) the Nusselt number peak deviates from the centre of the plate and forms a hollow (peripheral) shape with peaks at the wall jet region. For moderate swirl, the peak is located at $0.3 < r/D < 0.8$ and for higher swirl its lies between $0.5 < r/D < 1.0$.
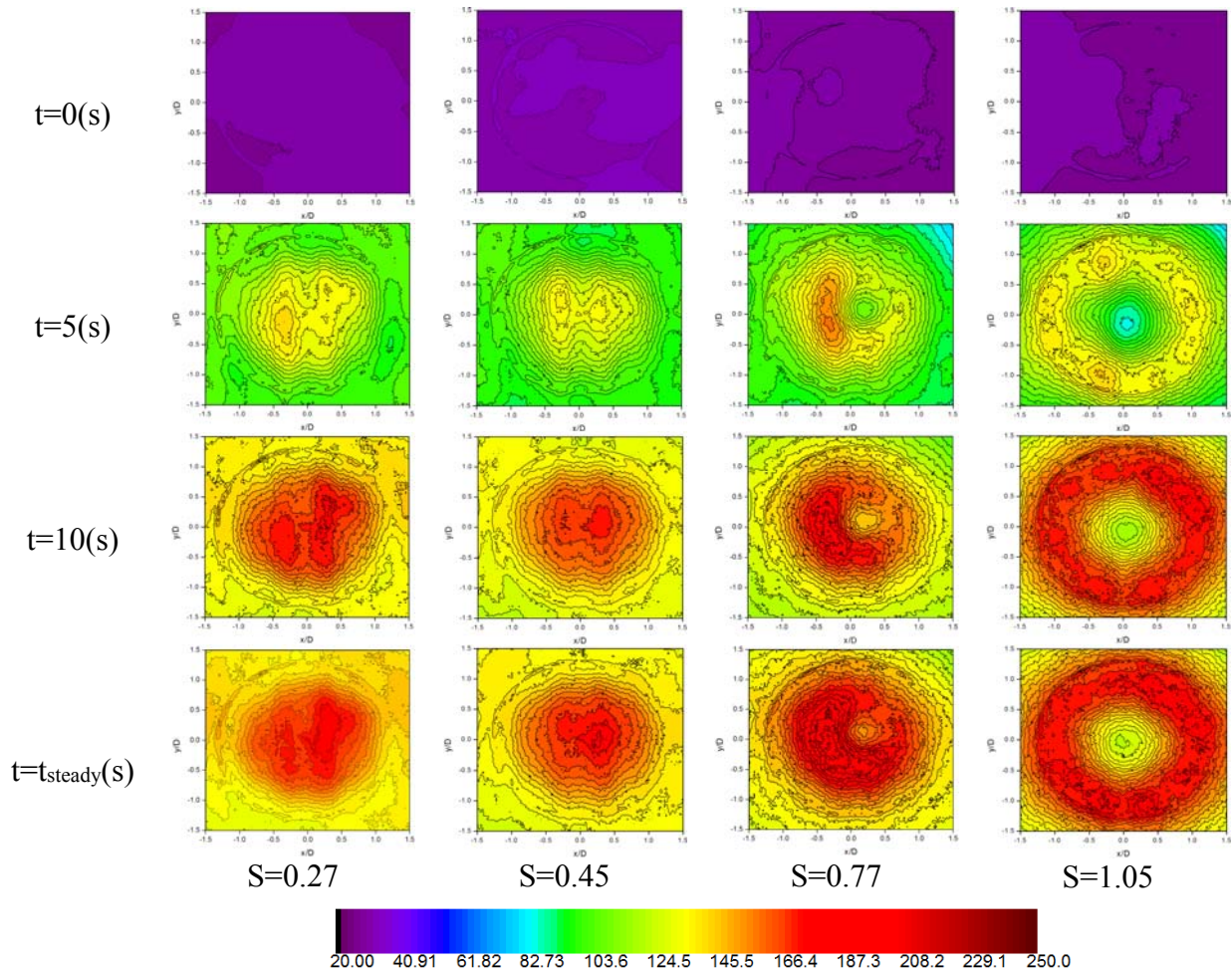
Figure 3.9: Nusselt number contour plot for different swirl numbers at Re=35,000 for swirling impinging jets at H/D=2.

Figure 3.10 highlights data for the effect of different nozzle-to-plate spacing on highly swirling jets (S=1.05) at Re=35,000. It can be seen that as the impingement distance increases, the distinct ring-shaped heat transfer area observed at H/D=2 fades and a more uniform heat transfer distribution develops over the impingement plate. In contrast to H/D=2, for H/D=4 and 6 (at t=5 sec), no distinct heat transfer feature is noticeable, but as time passes low Nusselt number values continue to be observed. This is likely due to the high momentum transfer and jet spread associated with a stronger swirl. At high impingement distances for this high swirling jet at S=1.05, the jet momentum quickly dissipates resulting in a wider jet spread compared to

its non-swirling jet counterpart. This can be seen by evaluating the heat transfer coefficient distribution of these two jets (Figure 3.7 and Figure 3.10).

Table 3.3: Time (s) to reach steady-state for swirling impinging jets.

		H/D=2	H/D=4	H/D=6
Re=35,000 U_b**=13.14(m/s)** **S=0.27**	A1	11.3	12.6	11.1
	A2	11.5	12.8	11.4
	A3	12.7	13.3	14.4
	A4	12.8	13.4	14.4
	A5	13	13.4	14.5
	Aavg	11.8	13.0	14.6
Re=35,000 U_b**=13.74(m/s)** **S=0.45**	A1	11.6	14.2	15.0
	A2	13.2	14.3	14.2
	A3	14.0	14.6	14.3
	A4	14.1	14.7	14.8
	A5	14.3	14.8	16.1
	Aavg	13.3	14.6	14.9
Re=35,000 U_b**=13.71(m/s)** **S=0.77**	A1	10.8	11.3	11.7
	A2	10.6	12.3	13.7
	A3	11.3	12.7	13.9
	A4	13.8	14.2	14.0
	A5	13.8	16.5	14.1
	Aavg	10.8	14.1	13.7
Re=35,000 U_b**=17.57(m/s)** **S=1.05**	A1	12.1	15.5	17.0
	A2	11.8	13.2	15.6
	A3	12	13.2	13.9
	A4	12.1	13.3	13.8
	A5	12.3	15.9	13.5
	Aavg	12.1	15.6	16.5
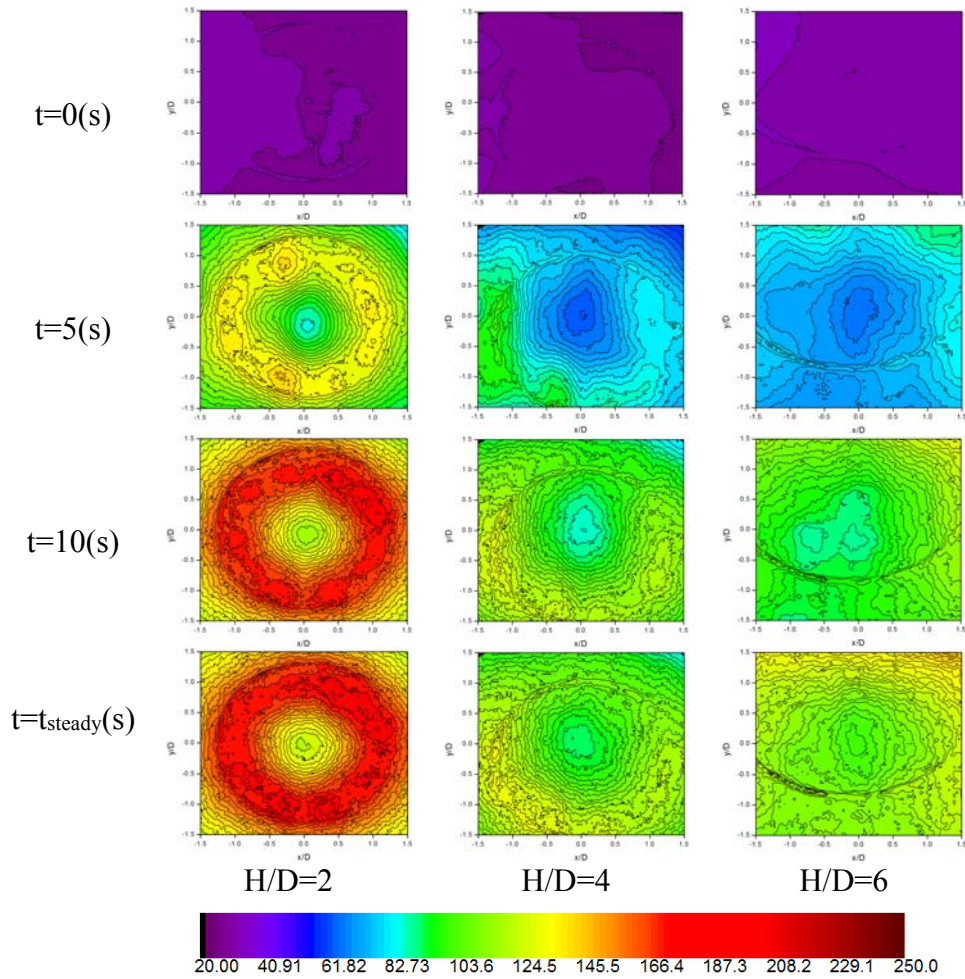
Figure 3.10: Nusselt number contour plot for different impingement distances at Re=35,000 and S=1.05 for swirling impinging jets.

Figure 3.11 summarizes the temporal development of the average Nusselt number for different areas (A1-A5, and Aavg) at the impingement plate. For near-field impingement (H/D=2), stagnation zone steady-state Nusselt number is the lowest for S=1.05 in contrast to low and moderate swirl (S=0.27-0.77). In the intermediate region between the stagnation and wall jet region (A3) the greater swirl has higher Nu_{st-st} because of the shift in peak heat transfer radially outwards from the stagnation zone. For H/D=4 and 6 at the stagnation, lower the swirl, higher the Nu_{st-st} for all swirl cases. For the regions, A2-A5 Nu_{st-st} decreases with the increase of swirl excluding for S=1.05, which showed Nu_{st-st} magnitudes more than at S=0.77. For H/D=6 at A4 and A5 (wall jet region), jets with lower swirl number (S=0.27) have the slowest induced rate of increase in Nu. This increase appears to become more acute with the increase of swirl (from 0.45 to 0.77 and then 1.05). However, at H/D=2, this difference in the rate of increase diminishes. Table 3.3 illustrates t_{steady} for swirling jets over different areas of the impingement plate. At each swirl number, all areas reach steady-state almost at the same time in contrast to the variations exhibited in non-swirling jets (Table 3.2). For the low swirling cases (S=0.27

and 0.45), the wall jet region (A4, A5) takes slightly more time than the stagnation zone (A1), while for the high swirling case (S=1.05) the variations between the time to steady-state diminish across all regions at H/D=2, but can still occur for H/D=4 and 6.
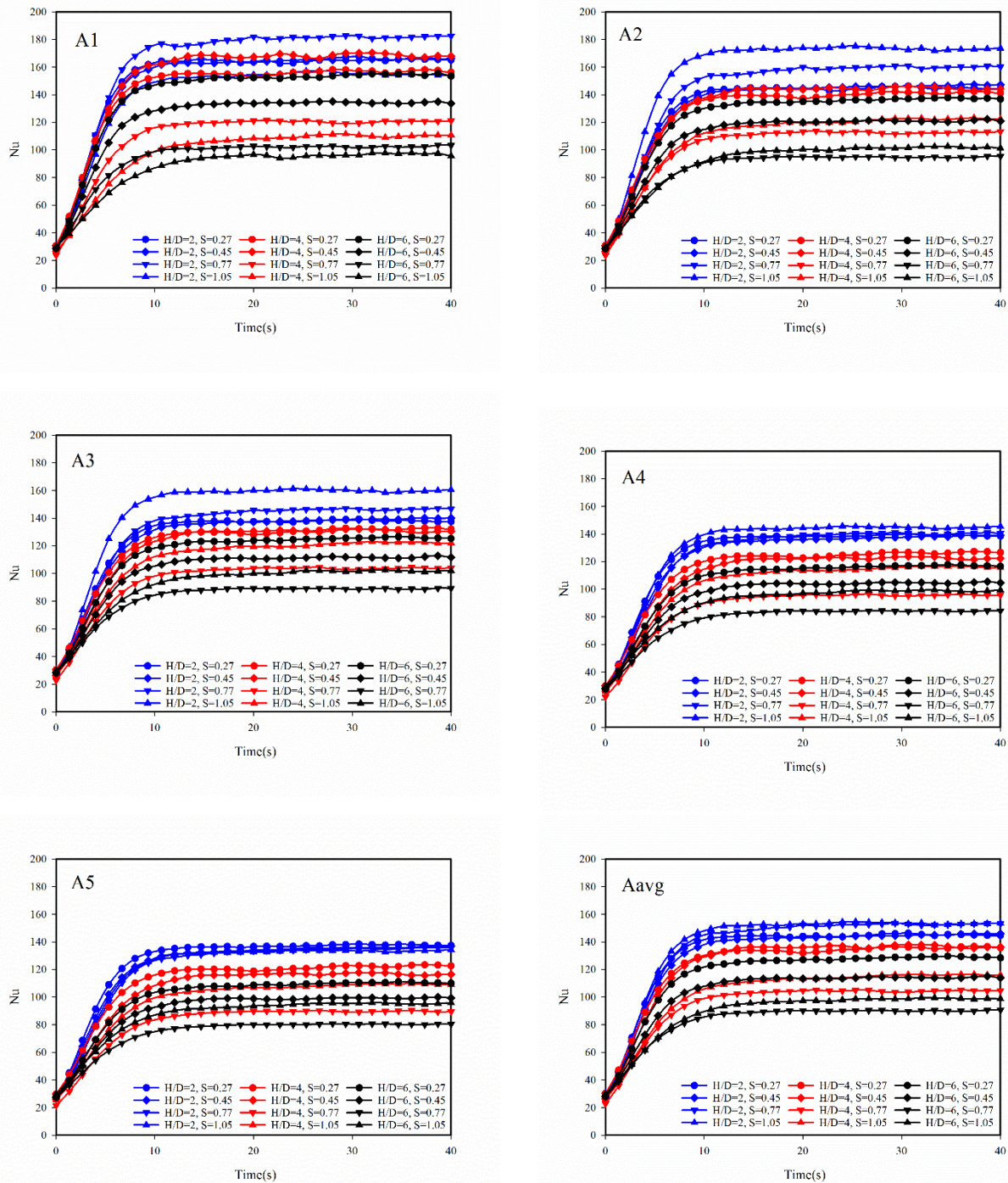
Figure 3.11: Temporal evolution of Nusselt number averaged over different areas on the heated impingement plate for swirling impinging jet at Re=35,000. Each color corresponds to a specific nozzle-to-plate distance.

The time constant for the thin foil can be calculated using Equation (3-8) by assuming a fixed temperature in the thickness direction and that both conductive and radiative heat fluxes are sufficiently small. The time constant is used to normalize the t_{steady} of Nu for A_{avg}, results are shown in Figure 3.12 [38].

$$\tau = \frac{c\rho\delta}{h} \tag{3-8}$$

Figure 3.12 shows the average steady-state Nusselt number and normalized time to reach steady-state with respect to Reynolds number (a) and swirl number (b). Results show that for the non-swirling impinging jets, Reynolds number has a direct dependency with heat transfer for all impingement distances H/D=2, 4, and 6. Nozzle-to-plate spacing does not show a significant effect on the average Nusselt number. It is also observed that if the effect of impingement plate material and thickness has added to the steady-state time the behaviour may be changed. The normalized time to steady-state is directly proportional to the Reynolds number. For actual time to steady-state (Table 3.3) shows inverse relation, Re=11,600 take a larger time to reach steady-state compared to Re=24,600 and 35,000. The time required to reach steady-state for H/D=4 is considerably more than H/D=2 and 6 for all Reynolds numbers. The results of H/D=4 indicate some change in the flow behaviour of the jet may be the cause of this variation in contrast with H/D=2 and 6. Additional experimental and computational results can provide more insight into helping explain this behaviour in the heat transfer. Figure 3.12(b), the effect of swirl on reducing the time to reach the steady-state is marginal, irrespective of the swirl intensity variation between low (S=0.27) and high (S=1.05) does not affect the time to stabilize significantly. Nu_{st-st} generally decreases as H/D increases to 2, 4, and 6. The normalized time to steady-state, t_{steady}, for H/D=2 and 4 (at high swirl) is less than t_{steady} for S=0 (non-swirling), but as H/D increases not much difference is found.

$$\frac{q_j}{q_{st-st}} = 1 - e^{(-1.3t)} \tag{3-9}$$

$$\frac{Nu_A}{Nu_{A_{st-st}}} = 1 - e^{(-0.25t)} \tag{3-10}$$

$$\frac{Nu_A}{Nu_{A_{st-st}}} = 1 - e^{(-0.35t)} \tag{3-11}$$
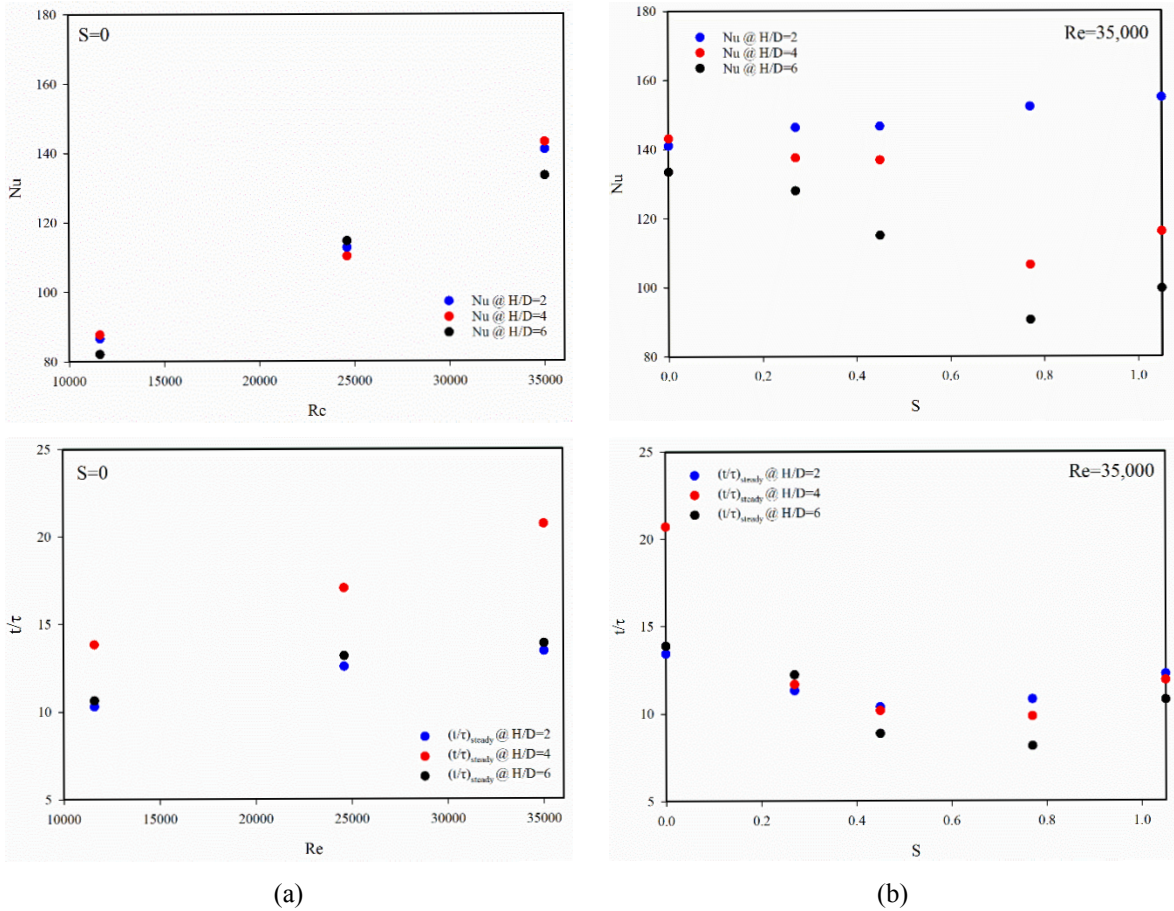
Figure 3.12: Steady-state average Nusselt number and time to reach steady-state: (a) for non-swirling impinging jets, (b) swirling impinging jet.
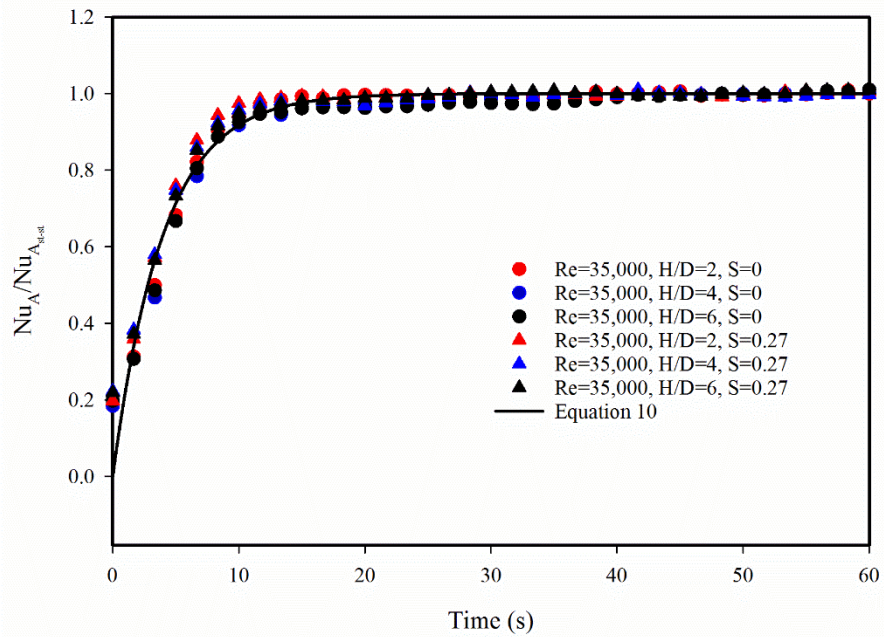
(a)
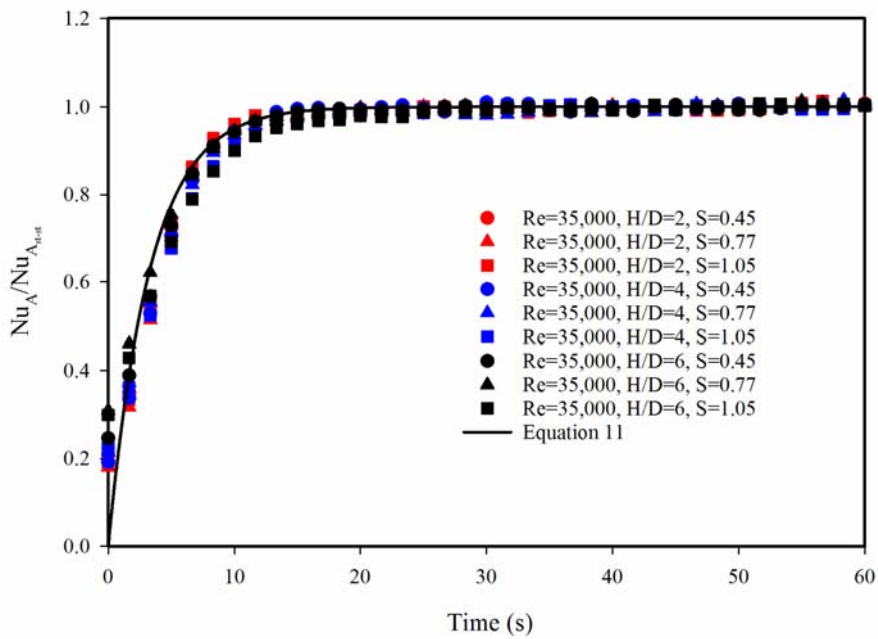
(b)

Figure 3.13: (a) Effect of H/D on transient Nu for non-swirling (S=0) and low swirl (S=0.27), (b) Effect of H/D on transient Nu for moderate swirl to high swirl (S=0.45, 0.77, and 1.05)

Equation (3-9) gives the transient heat loss prediction for non-swirling impinging jet for Re< 15,000 proposed by Liu et al. [14] for confined MCM disk. Although, t in there study is in minutes, but similar data fitting can be utilized to evaluate the constant but considering t in seconds. The application of this fit to the data in the present study is given in Figure 3.13. The negative constant of the exponential is calculated using the curve fitting method on transient average Nusselt number of the impingement plate. With this in mind, two different correlations (first for no or low swirl and second for S=0.45-1.05) are now proposed for the calculation of transient Nusselt number at Re=35,000. Figure 3.13(a) and Figure 3.13(b) show the fitting of Equation (3-10) and Equation (3-11) with the normalized experimental Nusselt number values.

3.4 CONCLUSIONS

Transient heat transfer characteristics have been investigated experimentally in both turbulent non-swirling and swirling impinging jets. A constant flux thin-foil heater is utilized along with an infrared camera in order to quantify the heat removal from the impingement surface. Two correlations have also been developed for the prediction of time to reach steady-state based Re=35,000. It is observed that for non-swirling and low-swirling impinging jets, similar transient behaviour (t_{steady}) can be calculated using Equation (3-10), but for intermediate and higher swirl cases Equation (3-10) does not satisfy the experimental data that is why another constant for negative exponential is calculated as shown in Equation (3-11).

In non-swirling impinging jets:

- For each time step, the location of the peak Nusselt number remains fixed for higher Reynolds numbers, in contrast to lower Reynolds number jets.
- The t_{steady} at H/D=4 is higher compared to that at H/D=2 and 6. In contrast, the average Nu_{st-st} is directly proportional to the Reynolds number. The nozzle-to-plate distance does not have a significant effect on Nu_{st-st}.
- Since the time reach to steady-state is in the magnitude of tens of sec, a small interval of time can significantly influence the impingement heat transfer. The transient effect does not only affect the magnitude of heat transfer (Nusselt number) but also changes the heat transfer distribution (uniformity).

In swirling impinging jets:

- Both the (inner) stagnation zone and (outer) peripheral wall jet regions appear to incrementally develop throughout the period leading to steady-state.

- For H/D=2, the highest Nusselt number lies at the stagnation zone for low-to-moderate (S=0.27 and 0.45) swirl. The peak Nusselt number for S=0.77 and S=1.05 lies at 0.3 < r/D < 0.8 and 0.5 < r/D < 1.0 respectively.

- The circular ring of high heat transfer observed at H/D=2 for S=1.05 and Re=35,000 for all time steps fades as the impingement distance increases, leading to a comparatively uniform heat transfer distribution developing over time.

- A slower rate of change of Nu for low swirl and large impingement distance is observed compared to the moderate and higher swirl. This effect vanishes for small nozzle-to-plate distances.

Whilst the results presented have given for the first time a valuable insight into the transitional heat transfer characteristics of both swirling and non-swirling impinging jets, more research is warranted to identify the exact interplay between flow dynamics and the impingement surface, and how this influences the observed development of Nusselt number. Research into this area is already underway [37].

3.5 CHAPTER REFERENCES

[1]   Zuckerman N, Lior N. Jet impingement heat transfer: Physics, correlations, and numerical modeling. Adv Heat Transf 2006;39:565–631. doi:10.1016/S0065-2717(06)39006-5.

[2]   Ikhlaq M, Ghaffari O, Arik M. Predicting Heat Transfer for Low- and High-Frequency Central-Orifice Synthetic Jets. IEEE Trans Components, Packag Manuf Technol 2016;6:586–95. doi:10.1109/TCPMT.2016.2523809.

[3]   Fairweather M, Hargrave GK. Experimental investigation of an axisymmetric, impinging turbulent jet. 2. Scalar field. Exp Fluids 2002;33:539–44. doi:10.1007/s00348-002-0480-1.

[4]   Kurnia JC, Sasmito AP, Tong W, Mujumdar AS. Energy-efficient thermal drying using impinging-jets with time-varying heat input – A computational study. J Food Eng 2013;114:269–77. doi:10.1016/j.jfoodeng.2012.08.029.

[5]   Ward J, Mahmood M. Heat transfer from a turbulent, swirling, impinging jet. Proc. 7th Int. Heat Transf. Conf., vol. 3, Munich, West Germany: 1982, p. 401–7.

[6]   Huang L, El-Genk MS. Heat transfer and flow visualization experiments of swirling, multi-channel, and conventional impinging jets. Int J Heat Mass Transf 1998;41:583–600. doi:10.1016/S0017-9310(97)00123-3.

[7]   Hee LD, Youl WS, Taek KY, Suk CY, Hee Lee D, Youl Won S, et al. Turbulent heat transfer from a flat surface to a swirling round impinging jet. Int J Heat Mass Transf 2002;45:223–7. doi:10.1016/S0017-9310(01)00135-1.

[8]   Puzu N, Prasertsan S, Nuntadusit C. Heat transfer enhancement and flow characteristics of vortex generating jet on flat plate with turbulent boundary layer. Appl Therm Eng 2019;148:196–207. doi:10.1016/J.APPLTHERMALENG.2018.11.035.

[9]   Ianiro A, Cardone G. Heat transfer rate and uniformity in multichannel swirling impinging jets. Appl Therm Eng 2012;49:89–98. doi:10.1016/j.applthermaleng.2011.10.018.

[10]   Yazici H. Determination of optimum cooling unit configuration in automobile glass

tempering process by different Reynolds numbers. Karabuk Univ Inst Sci Technol Karabuk 2013.

[11]   Fujimoto H, Takuda H, Hatta N, Viskanta R. Numerical simulation of transient cooling of a hot solid by an impinging free surface jet. Numer Heat Transf Part A Appl 1999;36:767–80. doi:10.1080/104077899274444.

[12]   Mitsutake Y, Monde M. Heat transfer during transient cooling of high temperature surface with an impinging jet. Heat Mass Transf 2001;37:321–8. doi:10.1007/s002310000141.

[13]   Rahman MM, Lallave JC. Transient Conjugate Heat Transfer During Free Liquid Jet Impingement on a Rotating Solid Disk. Numer Heat Transf Part A Appl 2009;55:229–51. doi:10.1080/10407780802628987.

[14]   Liu L-K, Su W-S, Hung Y-H. Transient convective heat transfer of air jet impinging onto a confined ceramic-based MCM disk. J Electron Packag 2004;126:159–72. doi:10.1115/1.1649239.

[15]   Yang Y-T, Tsai S-Y. Numerical study of transient conjugate heat transfer of a turbulent impinging jet. Int J Heat Mass Transf 2007;50:799–807. doi:10.1016/j.ijheatmasstransfer.2006.08.022.

[16]   Yazici H, Akcay M, Golcu M, Koseoglu MF, Sekmen Y. Experimental investigation of transient temperature distribution and heat transfer by jet impingement in glass tempering processing. Trans Mech Eng 2015;39:337–49. doi:10.22099/IJSTM.2015.3244.

[17]   Yi SJ, Kim M, Kim D, Kim HD, Kim KC. Transient temperature field and heat transfer measurement of oblique jet impingement by thermographic phosphor. Int J Heat Mass Transf 2016;102:691–702. doi:10.1016/J.IJHEATMASSTRANSFER.2016.06.062.

[18]   Dou R, Wen Z, Zhou G. 2D axisymmetric transient inverse heat conduction analysis of air jet impinging on stainless steel plate with finite thickness. Appl Therm Eng 2016;93:468–75. doi:10.1016/j.applthermaleng.2015.10.021.

[19]   Kadam AR, Hindasageri V, Kumar GN. Transient heat transfer characterization of

impinging hot / cold jets by analytical IHCP. IOP Conf Ser Mater Sci Eng 2018;376:012027. doi:10.1088/1757-899X/376/1/012027.

[20] Al-Abdeli YM, Masri AR. Review of laboratory swirl burners and experiments for model validation. Exp Therm Fluid Sci 2015;69:178–96. doi:10.1016/j.expthermflusci.2015.07.023.

[21] Ahmed ZU, Al-Abdeli YM, Guzzomi FG. Heat transfer characteristics of swirling and non-swirling impinging turbulent jet. Int J Heat Mass Transf 2016;102:991–1003. doi:10.1016/j.expthermflusci.2015.07.017.

[22] Al-Abdeli YM. Experiments in turbulent swirling non-premixed flames and isothermal flows. 2004.

[23] Wen M-Y, Jang K-J. An impingement cooling on a flat surface by using circular jet with longitudinal swirling strips. Int J Heat Mass Transf 2003;46:4657–67. doi:10.1016/S0017-9310(03)00302-8.

[24] Yuan ZX, Chen YY, Jiang JG, Ma CF. Swirling effect of jet impingement on heat transfer from a flat surface to CO2 stream. Exp Therm Fluid Sci 2006;31:55–60. doi:10.1016/j.expthermflusci.2005.12.007.

[25] Ahmed ZU, Al-Abdeli YM, Guzzomi FG. Flow field and thermal behaviour in swirling and non-swirling turbulent impinging jets. Int J Therm Sci 2017;114:241–56. doi:10.1016/j.ijthermalsci.2016.12.013.

[26] Ahmed ZU, Al-Abdeli YM, Guzzomi FG. Impingement pressure characteristics of swirling and non-swirling turbulent jets. Exp Therm Fluid Sci 2015;68:722–32. doi:10.1016/j.expthermflusci.2015.07.017.

[27] Ahmed ZU, Al-Abdeli YM, Guzzomi FG. Corrections of dual-wire CTA data in turbulent swirling and non-swirling jets. Exp Therm Fluid Sci 2016;70:166–75. doi:10.1016/j.expthermflusci.2015.09.007.

[28] Thomas BK, Ahmed ZU, Al-Abdeli YM, Matthews MT. The optimisation of a turbulent swirl nozzle using CFD. Aust. Combust. Symp. Perth, Aust., 2013, p. 271–4.

[29] Jorgensen FE. How to measure turbulence with hot-wire anemometers-A practical

guide. Dantec Dyn Skovlunde, Denmark 2005.

[30]   Ahmed ZU. An experimental and numerical study of surface interactions in turbulent swirling jets. PhD Dissertation, Edith Cowan University, 2016.

[31]   Buchlin JM. Convective heat rransfer in impinging- gas-jet arrangements. J Appl Fluid Mech 2011;4:137–49.

[32]   Zuckerman N, Lior N. Impingement heat transfer: correlations and numerical modeling. J Heat Transfer 2005;127:544. doi:10.1115/1.1861921.

[33]   Chu TK, Ho CY. Thermal Conductivity and Electrical Resistivity of Eight Selected AISI Stainless Steels. Therm. Conduct. 15, Springer US; 1978, p. 79–104. doi:10.1007/978-1-4615-9083-5_12.

[34]   Astarita T, Carlomagno GM. Infrared thermography for thermo-fluid-dynamics. Springer Science & Business Media; 2012.

[35]   Hauksson ÁT. Experimental study of boiling heat transfer during water jet impingement on a hot steel plate. University of British Columbia, 2001.

[36]   Moffat RJ. Describing the uncertainties in experimental results. Exp Therm Fluid Sci 1988;1:3–17. doi:10.1016/0894-1777(88)90043-X.

[37]   Ikhlaq M, Al-Abdeli YM, Khiadani M. Nozzle exit conditions and the heat transfer in non-swirling and weakly swirling turbulent impinging jets. Heat Mass Transf 2019. doi:10.1007/s00231-019-02710-1.

[38]   Nakamura H. Frequency response and spatial resolution of a thin foil for heat transfer measurements using infrared thermography. Int J Heat Mass Transf 2009;52:5040–5. doi:10.1016/J.IJHEATMASSTRANSFER.2009.04.019.

[39]   Yu P, Zhu K, Shi Q, Yuan N, Ding J. Transient heat transfer characteristics of small jet impingement on high-temperature flat plate. Int J Heat Mass Transf 2017;114:981–91. doi:10.1016/j.ijheatmasstransfer.2017.06.112.

[40]   Guo Q, Wen Z, Dou R. Experimental and numerical study on the transient heat-transfer characteristics of circular air-jet impingement on a flat plate. Int J Heat Mass Transf

2017;104:1177–88. doi:10.1016/J.IJHEATMASSTRANSFER.2016.09.048.

[41]   Zhu K, Yu P, Yuan N, Ding J. Transient heat transfer characteristics of array-jet impingement on high-temperature flat plate at low jet-to-plate distances. Int J Heat Mass Transf 2018;127:413–25. doi:10.1016/J.IJHEATMASSTRANSFER.2018.07.099.

[42]   Lee DH, Song J, Jo MC. The effects of nozzle diameter on impinging jet heat transfer and fluid flow. J Heat Transfer 2004;126:554. doi:10.1115/1.1777583.

[43]   Fenot M, Dorignac E, Lalizel G. Heat transfer and flow structure of a multichannel impinging jet. Int J Therm Sci 2015;90:323–38. doi:10.1016/j.ijthermalsci.2014.12.006.

[44]   Baughn J, Shimizu S. Heat transfer measurements from a surface with uniform heat flux and an impinging jet. J Heat Transf (Transactions ASME) 1989;111:1988–90. doi:10.1115/1.3250776.

[45]   Lee Sang-Joon JL. Stagnation region heat transfer of a turbulent axisymmetric jet impingement. Exp Heat Transf 1999;12:137–56. doi:10.1080/089161599269753.

Chapter 4: Nozzle Exit Conditions and the Heat Transfer in Non-Swirling and Weakly Swirling Turbulent Impinging Jets

The chapter presents the study of axisymmetric turbulent weakly swirling (S = 0.31) jets (D = 40 mm) impinging onto a heated plate. Parameters varied include inflow conditions and the effects of impingement distance (H/D = 2, 4, and 6). The Reynolds Averaged Navier Stokes (RANS) equations are used to model the jets using the k-kl-ω turbulence model, which is benchmarked against other models. Three azimuthal (<w>) velocity profiles at a Reynolds (Re) number of 24,600 are used at the nozzle exit plane: Uniform (UP), Solid Body Rotation (SBR), and Parabolic Profiles (PP).

4.1 INTRODUCTION

In industrial applications, it is often critical to achieve specific surface temperatures. This affects the rates of heat and mass transfer, and through it, product quality and performance. The cooling of stock material in metal forming, the thermal management of electronic devices, heat removal in nuclear reactors, drying, and chemical vapour deposition are typical heat and mass transfer applications of impinging jets [1–4]. When the jet impingement is used to enhance heat transfer over a target surface, both the magnitude and the uniformity (distribution) of the heat transfer coefficient are important considerations. For example, in the cooling of electronic devices, high heat transfer rates are required [5] while in glass manufacture both uniformity and high heat transfer rates are sought to minimize surface defects [6]. It is for this significance that the present research examines whether the introduction of even low values of swirl into an axisymmetric jet improves the magnitude and uniformity of heat transfer at the impingement surface. The imposition of low swirl has the merit of avoiding many of the flow perturbations that accompany high swirl number jets as will be described later. Additionally, whilst it is known that Reynolds number affects both the flow field and observed heat transfer distributions [7, 8], the results derived from low Reynolds number studies are likely not immediately transferrable to impinging jets at much higher Reynolds numbers (as occurs in the present study).

Figure 4.1 shows that the flow field of an unconfined (non-swirling) impinging jet can be divided into three distinct regions: free jet, stagnation, and wall jet. The free jet region is comprised of the potential core and shear layer, whilst the stagnation zone is located around the spot geometrically centred below the impinging jet. When the flow deflects and moves radially outwards in the direction of the surface, it forms the wall jet region. The characteristics

of the free jet, the impingement zone, and the wall jet region are discussed in detail by Zuckerman and Lior [9] as well as others [6, 10, 11]. In such cases, the flow field is largely defined by the Reynolds number (Re), nozzle size (D), and shape as well as the impingement distance (H). One way to study the impinging jet heat transfer problem is by using a non-heated jet that impinges orthogonally over a flat heated surface. This method has been utilized by different researchers [6, 12, 13] to investigate both the flow field and heat transfer characteristics. However, whilst most research in this area has sought to characterise the heat transfer at the impingement surface, very few studies have attempted to correlate this to the (upstream) inflow conditions at the jet nozzle exit plane. These types of analyses are significant because of the diversity of results to date related to heat transfer at the surface. Moreover, most swirling impinging jets are ejected from nozzles featuring either geometric inserts or tangential ports (aerodynamic swirl) which affects the boundary conditions at the nozzle exit plane. To bridge the gap of uncertainty on the factors influencing impingement heat transfer, this study focuses on resolving the effects of nozzle exit (boundary) conditions for weakly swirling turbulent jets. The weakly swirling flow does not experience flow reversals from vortex breakdown which might occur in high swirl cases.
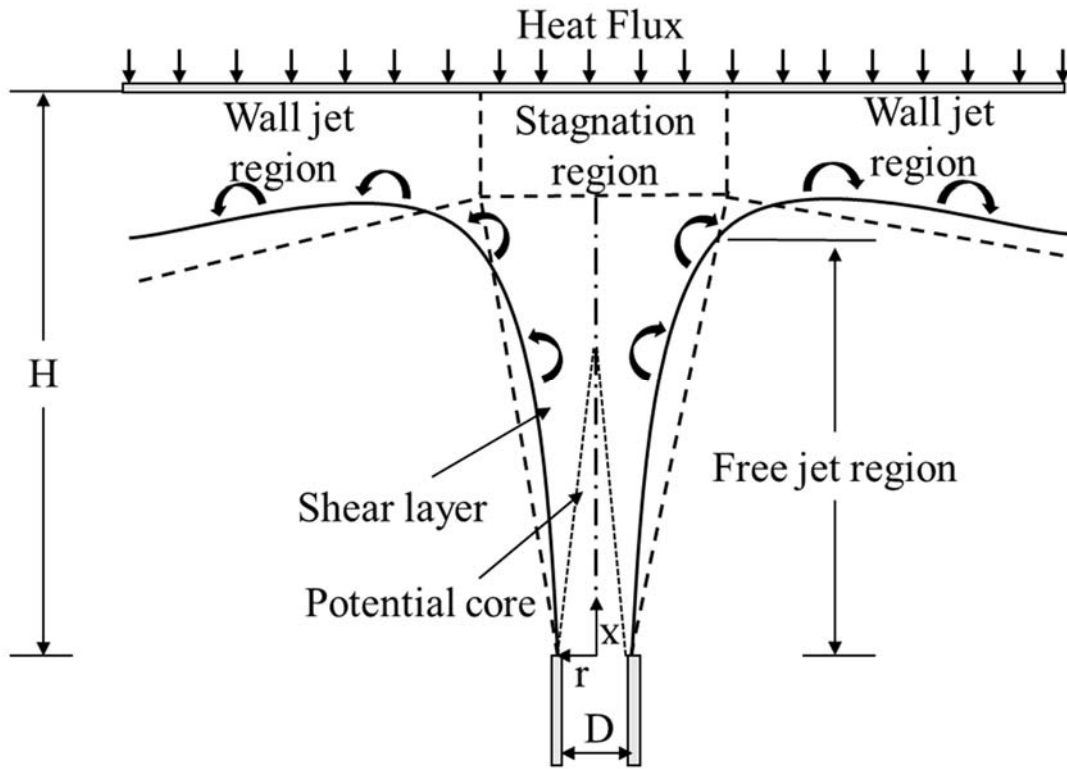
(a)
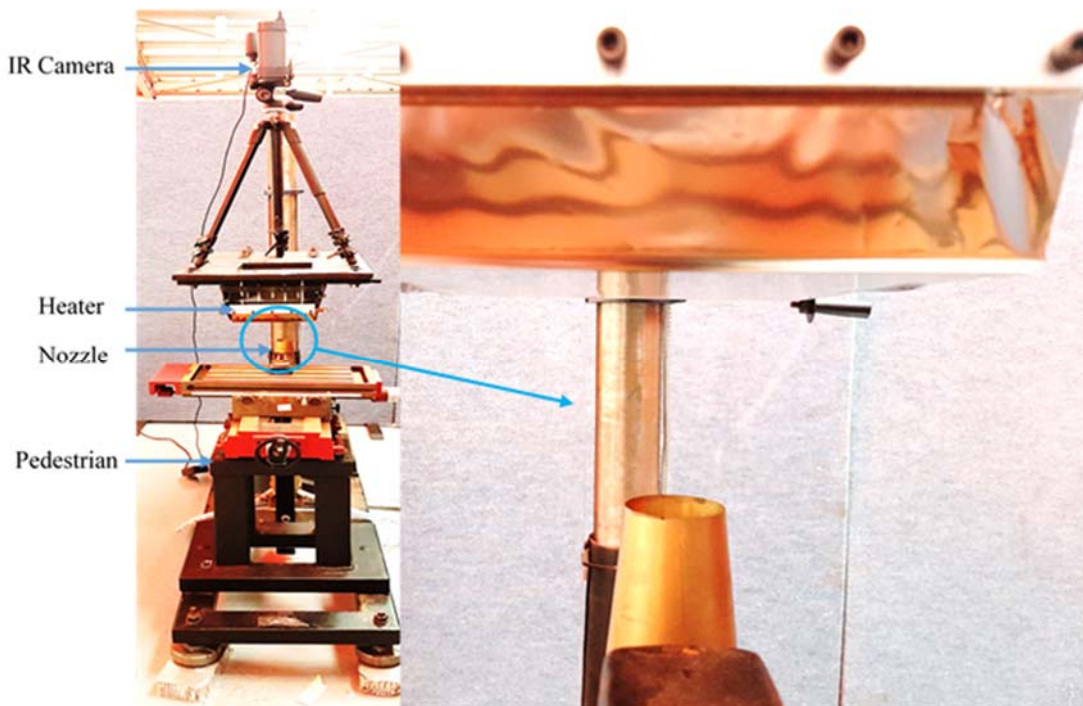
(b)

Figure 4.1: (a) The characteristic regions of an unconfined axisymmetric (cool) jet impinging onto the heated surface (b) The experimental setup which forms the basis of the flow domain and imposed boundary condition in this computational study.

The uniformity of heat transfer across an impingement surface has received much attention with one or two (Nusselt number) peaks being observed over the radial direction on the surface. In relation to non-swirling impinging jets, one of the earliest heat transfer studies conducted by Baughn and Shimizu [14] utilized a single circular (ambient temperature) turbulent jet. The Nusselt number distribution at H/D=2 was found to exhibit a minima when the heat impingement surface was at r/D=1.3 and a maxima further out (radially) at r/D=1.8. These results and others have largely supported the fact that heat transfer characteristics are non-uniform. Lytle and Webb [15] and Behnia et al. [16] reported that the maximum Nusselt number occurs radially away from the impingement point for an H/D<0.5, but that a secondary peak is also observed when impingement distance increases to H/D<6. However, the existence or location of the secondary Nu peak depends on Re and H/D, and heat transfer continuously decays in the wall jet region beyond it. Additionally, Cooper et al. [17] looked at the effect of nozzle-to-plate distance (H/D) on heat transfer and reported H/D=4 as the optimal impingement distance for high heat transfer rates at Re=23,000. Lee and Lee [18] studied the effect of different nozzle shapes and found a 15% heat transfer enhancement for an elliptical nozzle compared to a circular nozzle. To summarise, Figure 4.2(a) shows the normalised Nusselt numbers in several studies covering similar conditions (Re=23,000-25,000, H/D=2-6) [12, 14, 19–21]. It is observed that for non-swirling impinging jets, the maximum heat transfer can occur at, or near, the stagnation point but that the presence of a secondary peak is not always observed. At H/D ≤ 2, studies [12] have reported that the first Nusselt number peak can be displaced radially away from the stagnation point (0.5<r/D<0.7) whilst the second peak is observed further outwards r/D=2.4 (Re=24,000) [22]. O'Donovan et al. [11] noted that the secondary peak could be due to the transition of the wall jet boundary layer to a fully turbulent flow. Whilst the occurrence of a secondary peak has been observed in some non-swirling impinging jets, this only occurs at small impingement distances and relatively high Reynolds number. However, the effects of nozzle exit conditions on the Nu distribution have not been investigated to date, even though exit conditions affect both jet development [10] and the surface pressure distribution [23]. With this in mind, the reason for the occurrence of the secondary Nu peak also remains vaguely understood and its correlation to nozzle exit conditions forms part of the objectives from this study.
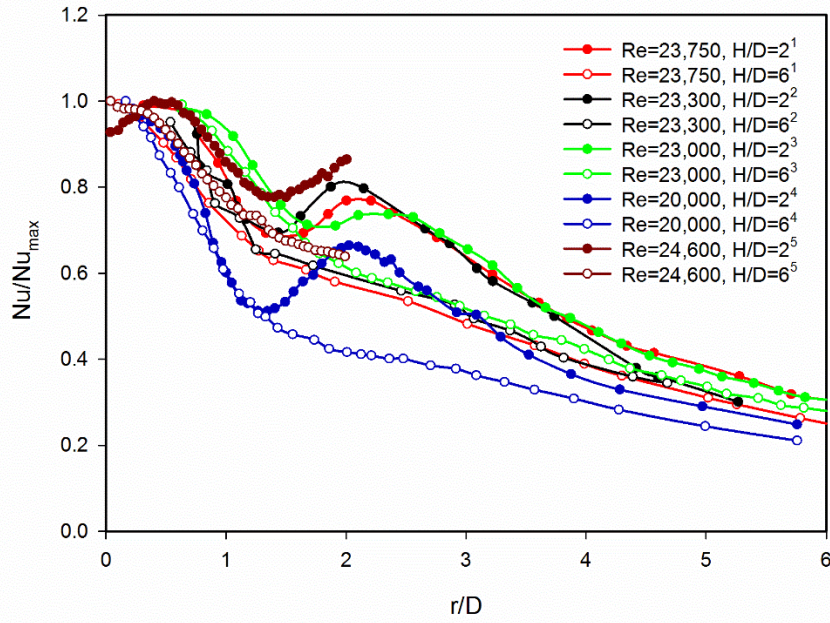
(a)
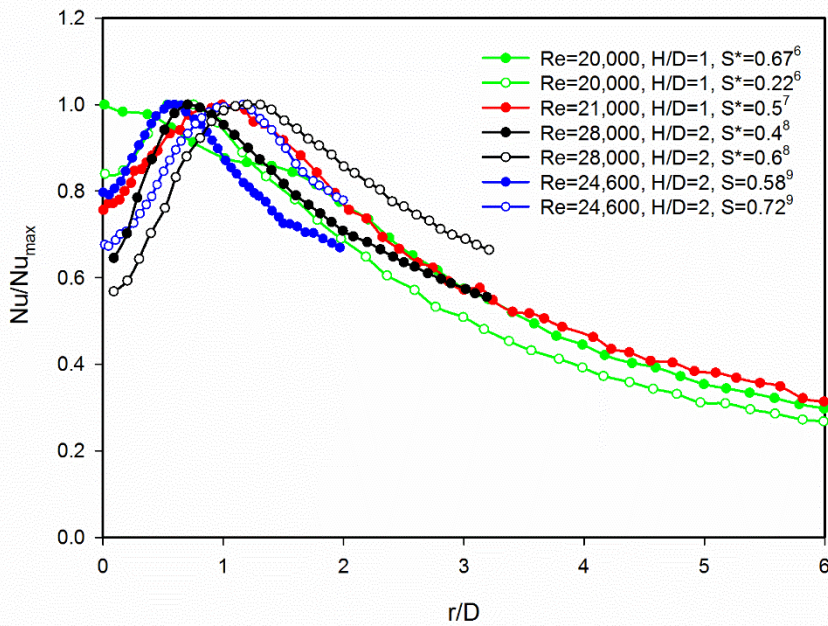
(b)

Figure 4.2: (a) Distribution of normalized Nusselt number for non-swirling impinging jets (Re=23,000-25,000 and H/D=2, 6): [1]**Baughn and Shimizu [14],** [2]**Baughn et al. [19],** [3]**Katti et al. [20],** [4]**Brown et al. [21],** [5]**Ahmed et al. [12] (b) Distribution of normalized Nusselt number for swirling impinging jets (Re=20,000-25,000, H/D=1, 2, and S=0.2-0.72):** [6]**Brown et al. [21],** [7]**Abrantes et al. [43],** [8]**Inairo and Cardone [6],** [9]**Ahmed et al. [12]. Swirl numbers designated by S* are derived from various studies and may be defined differently.**

Swirl has been imparted into free (unconfined) jet flows so as to affect mixing [24] and earlier studies have concluded that swirl jet turbulence may be a strong factor influencing heat transfer with impingement [12]. Swirl can be introduced into the flow using two different methods. Geometrically, it can be induced by inserting oriented blades [25, 26], helical inserts [27–29], and twisted strips [30, 31] so as to impart a rotary motion into an axisymmetric jet emitted from a nozzle. Aerodynamically, swirl can also be induced by using tangential ports into the main (axial) flow in a jet nozzle [12, 23, 32]. This method has the advantage of being able to modify the swirl number (S) independent of Reynolds number. It also avoids the perturbations (artificially) imposed onto the heat transfer from dead zones formed near the central blockages in the geometrically formed swirl and their subsequent effect on heat transfer. In jet studies, swirl intensity or swirl number (S) can be defined by the ratio of bulk tangential velocity (W_b) relative to bulk axial velocity (U_b) [24], but also in several other ways [33].

The tendency of a swirling (free) turbulent jet to undergo vortex breakdown [34, 35] and time-periodic behaviour [36–38] have received much attention, but even so very few studies have dealt with vortex breakdown in impinging jets. Vortex breakdown affects the heat transfer over a flat plate [39, 40] and is known to cause non-uniformities in the heat transfer distribution [6]. In impinging jet research, studies have also considered the effects of swirl on the Nusselt number and the uniformity of heat transfer [41, 42]. Bakirci and Bilen [28] studied the effect of swirl motion on the stagnation region and the average Nusselt number over a target surface for $12 \leq H/D \leq 28$ and $10,000 \leq Re \leq 30,000$. They observed that both the Nusselt number at the stagnation zone and the average Nusselt number over the impinging plate decreased as the swirl number increased. Yuan et al. [31] studied the effect of the Reynolds number (Re=7,500-28,300) at H/D=6 and reported a decrease in the Nusselt number at the stagnation point, but compared to non-swirling jets (at the same Re) the average Nusselt number was more uniform and greater. Numerical simulations by Amini et al. [29] ($4 \leq H/D \leq 16$, $4,000 \leq Re \leq 16,000$) have found the optimal operating conditions for heat transfer to occur are at H/D=12 and 16 with the maximum Nusselt number positioned at the stagnation point, but moving radially outwards as impingement distance decreased (H/D=4 and 8).

As such, in addition to the ambiguity which exists as the effects of nozzle exit conditions on impingement heat transfer, there has been an interest in seeing how the introduction of swirl also affects impingement heat transfer. In this context, Figure 4.2(b) summarises the typical heat transfer distribution for turbulent swirling impinging jets over different swirl intensities at H/D=1-2 [6, 12, 21, 43]. The data shown which covers Reynolds numbers similar to those for

non-swirling jets (Figure 4.2(a)) indicates that only one Nu peak (i.e., no secondary peak) is present and this appears somewhat radially displaced from the stagnation region. The location of the peak Nu depends on parameters such as Re and H/D but also likely affected by the way swirl is induced into the flow and hence the jet development [10]. Lee et al. [27] observed a 35% enhancement in performance when the impinging jet was swirling and operated at H/D=4 (Re=20,000). Wen and Jang [30] conducted a study with a wide range of operating parameters (3 ≤ H/D ≤ 16 and 500 ≤ Re ≤ 27,000). Longitudinal swirling strips introduced swirl into the flow and the authors observed a 5% heat transfer enhancement at the stagnation point. The highest Nusselt number was observed at H/D=6 for Re=27,000. Ianiro et al. [6] reported that the global heat transfer increased for some swirl intensities, but decreased at other swirl intensities. The authors also commented that the nozzle exit area is also changed because of the (geometric) insert into the nozzle compared to a circular impinging jet. The study conducted by Brown et al. [21] showed at low swirl number (calculated based on insert geometry), the Nu peak was displaced from the stagnation point, while for high swirl Nu peak is at the stagnation point. These results are somewhat contrary to others. In summary, for impinging jet (near field) 0<H/D<4, the introduction of swirl increases the overall heat transfer at the impingement. At H/D=4, the average Nu for low to medium swirl numbers is higher than the average Nu in the case of non-swirling impinging jets. For the high swirl, the opposite trend is observed [12, 21]. In far-field impingement at H/D>4 overall heat transfer decreases and drastic reduction is observed at high swirl intensities. As such, it would appear that impingement heat transfer is improved up to some critical value of swirl number, but that further increases in swirl can deteriorate heat transfer at the target surface [12]. This also gives significance for studies into jet impingement at low swirl. Due to the multitude of definitions of swirl number, this critical value cannot be generalised. It is also dependent on how the swirl intensity is characterised.

Despite the fact that DNS and LES are considered more reliable computational methods compared to linear eddy viscosity closure methods, both techniques are highly sensitive to the quality of grid and availability of boundary conditions. Additionally, since both DNS and LES are more expensive computationally, RANS is still being utilized for many practical applications. Table 4.1 summarizes the numerical studies related to impinging jets including swirling and non-swirling impinging jets. Various turbulence models were utilized by different researchers, who studied different aspects of impinging jets. Recent studies [44–46] reported that RNG k-ε and SST k-ω turbulence models showed good agreement with experimental data.

Ahmed et al. [10] and Sunden and Larocque [39] utilized different turbulence models of swirl motion and to study their effects on jet development.

Table 4.1: Numerical studies for non-swirling and swirling (single) impinging jets.

	STUDY	REYNOLDS NUMBER (Re)	A/G	TURBULENCE MODELS	PARAMETERS INVESTIGATED
Non-Swirling	Angioletti et al. [55]	1,000-4,000	---	RNG k–ε, SST k–ω, RSM	$|V|$, Nu, H/D = 4.5
	Isman et al. [56]	4,000-12,000	---	STD k–ε, RNG k–ε, two other nonlinear models	$|V|$, Nu, H/D = 4–10
	Pulat et al. [57]	4,000-12,000	---	Different k–ε and k–ω models	Nu, H/D=6
	Ramezanpour et al. [58]	4,000-16,000	---	RNG k–ε, RSM	Streamlines, Nu, H/D = 4–10
	Dianat et al. [59]	23,000	---	STD k–ε, RSM	$|V|$, u_i', $\overline{u_i'u_j'}$, H/D = 2, 8, 12
	Merci and Dick [60]	23,000	---	Low-Re k–ε, Low-Re nonlinear k–ε	$|V|$, $\overline{u_i'u_j'}$, H/D = 2, 6
	Sagot et al. [61]	23,000	---	Realizable k–ε, RNG k–ε, STD k–ω, SST k–ω	Nu, H/D = 6
	Craft et al. [62]	23,000 and 70,000	---	Low-Re k–ε, RSM, and two SMC models	$|V|$, u_i', $\overline{u_i'u_j'}$, k
	Behnia et al. [60]	23,000-70,000	---	STD k–ε, $v2$–f	$|V|$, Nu, k, H/D = 2 & 6
	Jaramillo et al. [63]	23,000 and 70,000	---	Different k–ε, k–ω models	$|V|$, Nu, H/D = 2, 6
Swirling	Oguic et al. [64]	5,300	A	DNS	$\overline{u_r}, \overline{u_i}, \overline{u_\theta}$, Nu_R, Nu_AVG
	Hu et al. [44]	4,000-12,000	G	RNG k–ε	Nu, Nu_AVG, H/D=1-8, k
	Amini et al. [29]	7,000-16,000	G	RNG k–ε	Nu, H/D=2-8
	Ortega-Casanova and Granados-Ortiz [65]	7,000-19,000	G	SST k–ω, Standard k–ε, Enhanced k–ε	Nu, H/D=5,10,30
	Ortega-Casanova [25]	7,000-20,000	G	SST k–ω	Nu, H/D=5,10,30
	Zahir et al. [10]	23,000	A	RNG k–ε	$\overline{u_i'}, \overline{u_i'u_j'}$, τ_ω, k
	Ortega-Casanova and Molina-Gonzalez [66]	23,000	A	SST k–ω	Nu, Nu_AVG, k, Π(PUMPING POWER)
	Ortega-Casanova and Castillo-Sanchez [46]	23,000	A	SST k–ω	Nu, Nu_AVG, Σ
	Zahir et al. [45]	35,000	A	SST k–ω	$\overline{u_i'}, \overline{u_i'u_j'}$, Nu, Nu_AVG, τ_ω, k, H/D=1,6

NOTE:
A: Studies involving swirl generated via aerodynamic means (azimuthal velocity component is introduced, rotating disk)
G: Studies involving swirl generated via geometric means (insert, vanes, blades)

With the above in mind, there is a need to further research the effects of inflow conditions on impingement heat transfer. The present study looks into the fundamental mechanisms by which changes to the exit conditions at different H/D, affect the magnitude and uniformity of Nu in weakly swirling turbulent jets in comparison to (benchmark) non-swirling cases. The range of Reynolds numbers selected are similar to other studies (Re=23,000 [47] and 24,600) [12] in which the role of exit conditions was not tested. In this paper, three different azimuthal inlet profiles, namely uniform profile (UP), solid body rotation (SB), and parabolic profile (PP) are used with weakly swirling jets. The later part of the paper also looks at the effect of the central blockages; typical in the case of geometric swirl, which influences the impingement heat transfer when it affects nozzle exit condition. This effect of central blockage mimics the effect of the insert or vane which can also be used for the producing the swirling flows. The results are derived using numerical modelling of the velocity field over the flow domain (H=2-6) and heat transfer at the impingement surface. This research also uses published experimental data for establishing nozzle boundary conditions [12].

4.2 METHODOLOGY
4.2.1 Numerical approach

Figure 4.3 shows the 2D computational domain and the boundary conditions which are used as part of the simulation in this study. The domain is considered to be 10D wide so as to capture all impinging regions and this approach is adopted by other researchers as well [10, 46]. Atmospheric pressure is applied to the pressure outlet boundaries and the jet centreline is considered as the axis of symmetry.
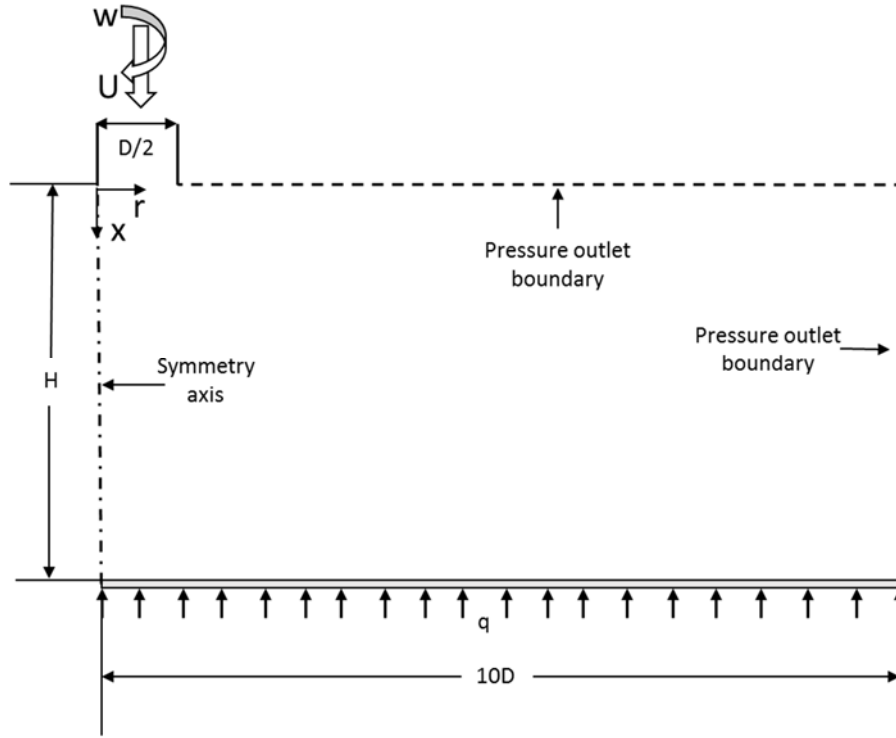
Figure 4.3: Computational domain

Steady-state, incompressible, axisymmetric, and turbulent flow are the basic assumptions made throughout this paper. The velocity magnitude used in the numerical study are well below the 0.3 Mach number which is why in this stud the flow is considered incompressible. ANSYS Fluent© 16.2 is utilized to simulate both swirl and non-swirl flow conditions. The pressure-based formulation with the COUPLED scheme for pressure-velocity coupling and the second-order upwind method are employed for the spatial discretization of convective terms in the governing equations. The PRESTO method is utilized for a pressure interpolation scheme which is recommended for high-speed rotating and swirling flows [48]. Fluent uses a turbulence length scale based on mixing length which is considered as 7% of hydraulic diameter [48]. The governing equations (two-dimensional) of continuity, momentum, and energy in tensor notation are given in Equations (4-1) to (4-3), respectively. Figure 4-A1 of the chapter appendices also shows the logic flow used to derive the (spatially resolved, two-dimensional) heat transfer and velocity field at the impingement plate.

$$\frac{\partial u_j}{\partial x_j} = 0 \tag{4-1}$$

$$\frac{\partial (u_i u_j)}{\partial x_j} = -\frac{1}{\rho}\frac{\partial P}{\partial x_i} + \nu \frac{\partial}{\partial x_j}\left[\frac{\partial u_i}{\partial x_j} + \frac{\partial u_j}{\partial x_i} - \frac{2}{3}\delta_{ij}\frac{\partial u_i}{\partial x_i}\right] + \frac{\partial}{\partial x_j}\left[-\rho\overline{u_i' u_j'}\right] \tag{4-2}$$

$$\frac{\partial}{\partial x_i}[u_i(\rho e + P)] = \frac{\partial}{\partial x_j}\left[K_{eff}\frac{\partial T}{\partial x_j}\right] \qquad (4\text{-}3)$$

Whereby, u_j represents the axial, radial, and azimuthal velocity components, while P, T, and e are pressure, temperature, and enthalpy respectively. Furthermore, Dirac's delta is denoted by δ_{ij}, K_{eff} is the sum of thermal conductivity and turbulent thermal conductivity, and turbulent thermal conductivity is defined as $k_t = c_p\mu_t/Pr_t$; where c_p denotes the fluid heat capacity, μ_t is the turbulent dynamic viscosity, and Pr_t is the turbulent Prandtl number which in ANSYS-Fluent© represents the wall Prandtl number. Due to the closure problem of RANS equations, the fluctuating components of the velocities need to be estimated from turbulence models. Ahmed et al. [10] reported the RNG k-ε with enhanced wall treatment gave good agreement while Ortega-Casanova and Castillo-Sanchez [46] showed that the SST k-ω turbulence model accurately predicted the flow field. Preliminary checks tested the use of different turbulence models including k-kl-ω, RNG k-ε, and SST k-ω, and showed better results with the former (k-kl-ω). The k-kl-ω turbulence model was initially proposed by Walters and Leylek [49]. With this in mind, the laminar kinetic energy (kl, streamwise flucatuations within the transitional boundary layer described as Laminar Kinetic Energy), turbulent kinetic energy (k), and turbulent dissipation rate (ω) within the k-kl-ω model can be resolved using Equation (4-4), (4-5), and (4-6) respectively:

$$P_{k_T} + R_{BP} + R_{NAT} - \omega k_T - D_T + \frac{\partial}{\partial x_j}\left[\left(\nu + \frac{\alpha_T}{\sigma_k}\right)\frac{\partial k_T}{\partial x_j}\right] = 0 \qquad (4\text{-}4)$$

$$P_{k_L} - R_{BP} - R_{NAT} - D_L + \frac{\partial}{\partial x_j}\left[\nu\frac{\partial k_t}{\partial x_j}\right] = 0 \;\; (5) \qquad (4\text{-}5)$$

$$C_{\omega 1}\frac{\omega}{k_T}P_{k_T} + \left(\frac{C_{\omega R}}{fw} - 1\right)\frac{\omega}{k_T}(R_{BP} + R_{NAT}) - C_{\omega 2}\omega^2 + C_{\omega 3}f_\omega\alpha_T f_W^2\frac{\sqrt{k_T}}{d^3}$$
$$+ \frac{\partial}{\partial x_j}\left[\left(\nu + \frac{\alpha_T}{\sigma_\omega}\right)\frac{\partial \omega}{\partial x_j}\right] = 0 \qquad (4\text{-}6)$$

Where D_L and D_K are the anisotropic dissipation. P_{KL} and P_{KT} are the production of laminar and kinetic energy terms by mean strain rate respectively. R_{BP} and R_{NAT} are the bypass tranisition production and natual transition production terms respectively. The different terms in Equation (4-4), (4-5), and (4-6) represent the production, destruction, and transport

mechanisms. Each term in Equation (4-4) to (4-6), along with all the constants, are discussed in detail by Furst et al. [49] as well as by Walters and Cokljat [50].

Before the models were applied, a mesh sensitivity or grid convergence study is conducted and uncertainty due to discretization is calculated using the method described by Celik et al. [51]. At least one mesh node is needed within the viscous sub-layer according to the law of the wall in order to evaluate quantities such as wall shear stress, pressure, and heat transfer to/from the surface of the impinging plate. It is necessary to resolve the boundary layer correctly and for this, it is recommended that $y^+ \approx 1$ at the wall region [52]. Three different jet impingement distances H/D=2, H/D=4, and H/D=6 are used in this study and grid independence is conducted for each configuration by keeping $y^+ \approx 1$ near the wall which helped to evaluate the change in magnitude with the change of a number of cells.

Table 4.2: Grid convergence study results (S=0, Re=24,600).

GRID	N_i	R_I	WALL SHEAR (PA)	$GCI_{I+1,I}$
H/D=2				
Fine (N1)	309,600	2	0.11685	0.21%
Medium (N2)	77,400	2	0.11705	1.04%
Coarse (N3)	19,350	1*	0.118025	-
H/D=4				
Fine (N1)	516,000	2	0.11100	0.26%
Medium (N2)	129,000	2	0.11121	0.94%
Coarse (N3)	32,250	1*	0.11205	-
H/D=6				
Fine (N1)	722,400	2	0.10788	0.91%
Medium (N2)	180,600	2	0.10710	3.85%
Coarse (N3)	45,150	1*	0.10380	-

NOTE:
1*: Base size or initial size of the grid.

The Grid Convergence Index (GCI) method is used to quantify the error associated with each mesh. Ideally, GCI indicates the amount by which the magnitude of the corresponding variable will change with further refinement of the grid size by exploiting Richardson's extrapolation method [51]. Theoretically, Richardson's extrapolation gives the value of the particular variable (shear stress, pressure) with infinite grid cells, further increases to the mesh density show insignificant impact, the grid convergence is achieved. In this study, the cell size associated with the grid is calculated as $h_i = \sqrt{A_j/N_i}$ [51], where N_i is the number of cells in ith mesh and A_j is the domain area (j is 1, 2, and 3 for H/D=2, H/D=4, and H/D=6 respectively). The refinement ratio is defined as $r_i=h_{i+1}/h_i$ and it is used to calculate the GCI. The area-weighted average wall shear was selected as a representative magnitude to calculate GCI, the refinement ratio was set at 2 as recommended by Celik et al. [51] (r_i should be larger than 1.3). Any wall quantity (wall shear, Nusselt number, etc.) can be chosen to conduct the grid convergence study and wall shear is chosen randomly in this study. The selection of the quantity will not affect the final result since Nusselt number is later validated against the experimental results. Table 4.2 presents the corresponding results associated with each grid size, where $GCI_{i+1,i}$ gives the discretization error associated with each refinement calculated along with Richardson's extrapolation. $GCI_{I+1, I}$ is the error bar in Figure 4.4. These results are also presented graphically in Figure 4.4. The fine mesh (N1) is associated with the smallest uncertainty calculated using GCI and can be considered as the optimal mesh size for calculation purposes. The simulations are carried for H/D=2, 4, and 6 at 309k, 516k, and 722k cells, respectively.
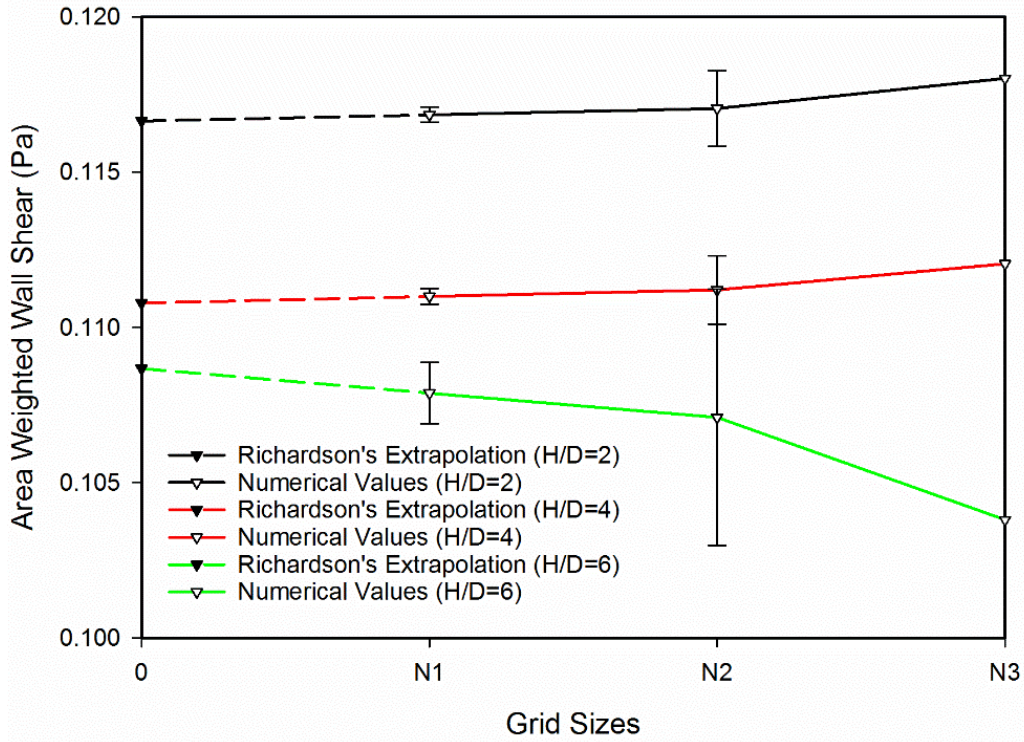
Figure 4.4: Grid convergence study used to determine the optimal mesh size (Re=24,600, S=0).

4.2.2 Non-dimensional parameters

Reynolds (Re), Swirl (S), heat transfer coefficient (h), and Nusselt (Nu) numbers, as well as the Coefficient of Pressure (C_p), defined through Equations (4-7)-(4-11) respectively, are the basic parameters used to characterise turbulent swirling jets.

$$Re = \frac{\rho U_b D}{\mu} \tag{4-7}$$

$$S = \frac{W_b}{U_b} \tag{4-8}$$

$$h = \frac{q - q_l}{T_w - T_{ref}} \tag{4-9}$$

$$Nu = \frac{hD}{\lambda} \tag{4-10}$$

$$C_p = \frac{P - P_\infty}{\frac{1}{2}\rho U_\infty^2} \tag{4-11}$$

Where P_∞ and U_∞ are the ambient pressure and velocity obtained from the total volume flow rate respectively. The average Nusselt number (Nu_A) over the impingement surface (r/D= 0 to

108

2) is estimated from Equation (4-12). Heat transfer uniformity is another important measure for the performance of impinging jets which can be calculated from Equation (4-13) using standard deviation (σ) of Nusselt numbers on the impinging plate [6].

$$Nu_A = \frac{1}{A_p} \int_{A_p} Nu(r)\, dA_p \qquad (4\text{-}12)$$

$$\sigma = \frac{\sqrt{\frac{1}{A_p}\left(\int_{A_p}(Nu(r) - Nu_A)^2\, dA_r\right)}}{Nu_A} * 100 \qquad (4\text{-}13)$$

Turbulent kinetic energy (k) is based on Equation (4-14) [48], whereas the energy dissipation rate (ε) or specific energy dissipation rate (ω) are calculated from Equations (4-15) and (4-16) [45]. The turbulence length scale is equal to 0.07D (in fully developed pipe flow turbulence length scale can be approximated as 3.8% of hydraulic diameter). In the jets simulated at Re=24,600, the turbulence intensity at the exit plane is derived from Equation (4-17) [48] and estimated around 5%.

$$k = \frac{1}{2}\left(\overline{(u')^2} + \overline{(v')^2} + \overline{(w')^2}\right) \qquad (4\text{-}14)$$

$$\varepsilon = \frac{C_\mu^{3/4} k^{3/2}}{l} \qquad (4\text{-}15)$$

$$\omega = \frac{k^{1/2}}{C_\mu^{1/4} l} \qquad (4\text{-}16)$$

$$I = \frac{u'}{U_{avg}} = 0.16(Re_{D_H})^{-\frac{1}{8}} \qquad (4\text{-}17)$$

4.2.3 Validation

Published velocity boundary conditions measured at the nozzle exit plane [12] are used as inlet conditions in this study to initially test the validity of the modelling approach used. In this context, the ability of these models to accurately predict (published) radial distributions of impingement plane pressure and Nusselt number [10] are first undertaken. For these validations, a constant heat flux boundary condition is applied at the impingement surface [12]. Experimentally, this is achieved by running the heater plate at 40 amp and 3 volts over an effective surface area of 0.06 m².
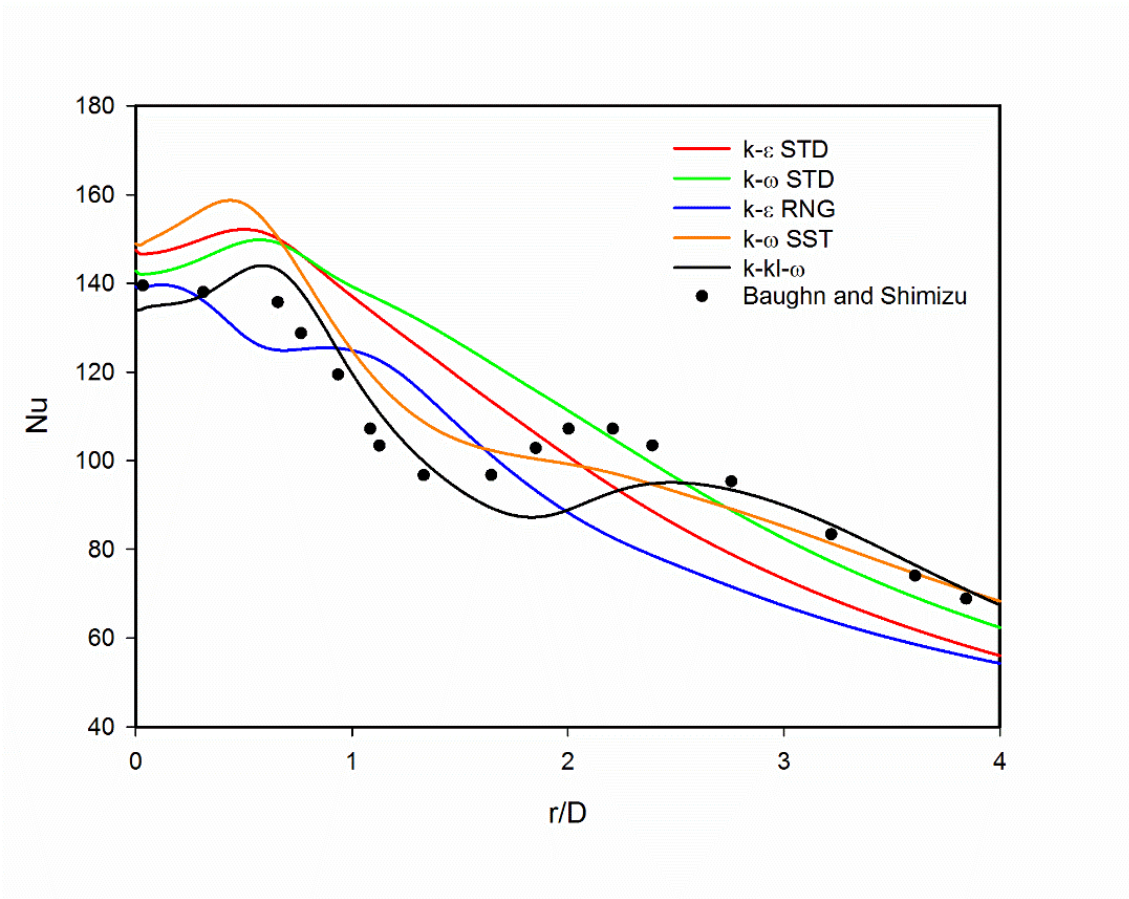
Figure 4.5: Estimation of Nu using different turbulence models and comparison with experimental data (Baughn and Shimizu [14]) at H/D=2, Re=24,600 and S=0.

Figure 4.5 shows the validation of computational results for a non-swirling impinging jet at the impinging surface using different turbulence models against experimental data. It is seen that the k-ε RNG and k-ω SST are able to predict Nu close to the experimental values but they do not give the secondary peak in Nu distribution. However, the k-kl-ω turbulence model is able to better predict the Nusselt number qualitatively and quantitatively compared to the other turbulence models. Additionally, k-kl-ω also captured the secondary peak in the wall jet region whereby this difference compared with other turbulence models may be due to the fact that k-kl-ω takes into account a transitional regime in the wall jet region [50]. As such, the remaining results presented in this paper are based on k-kl-ω model.
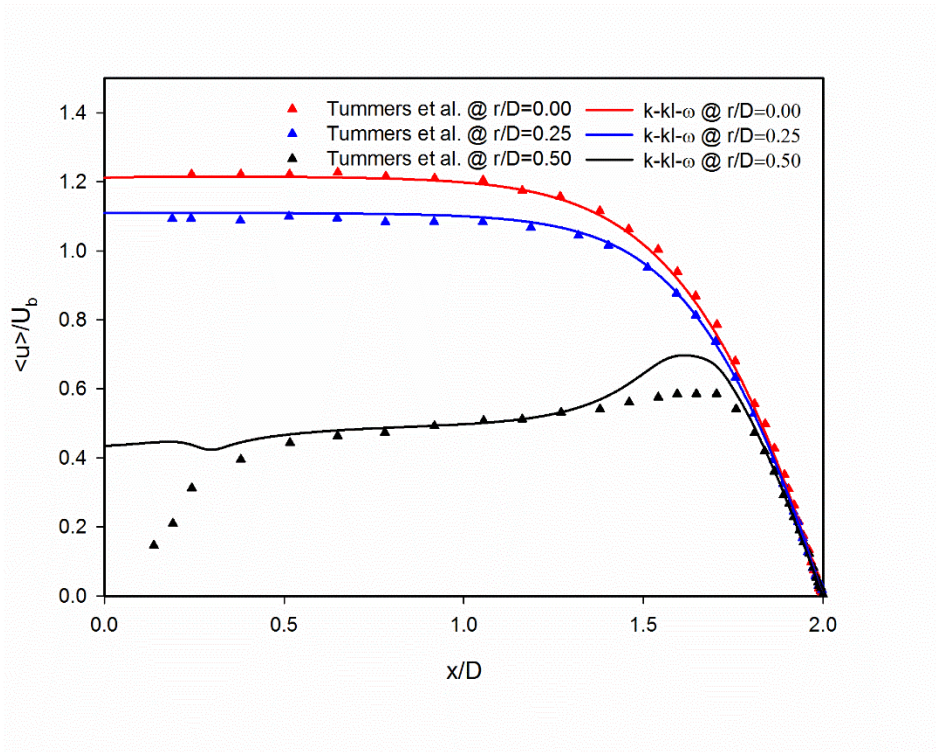
(a)
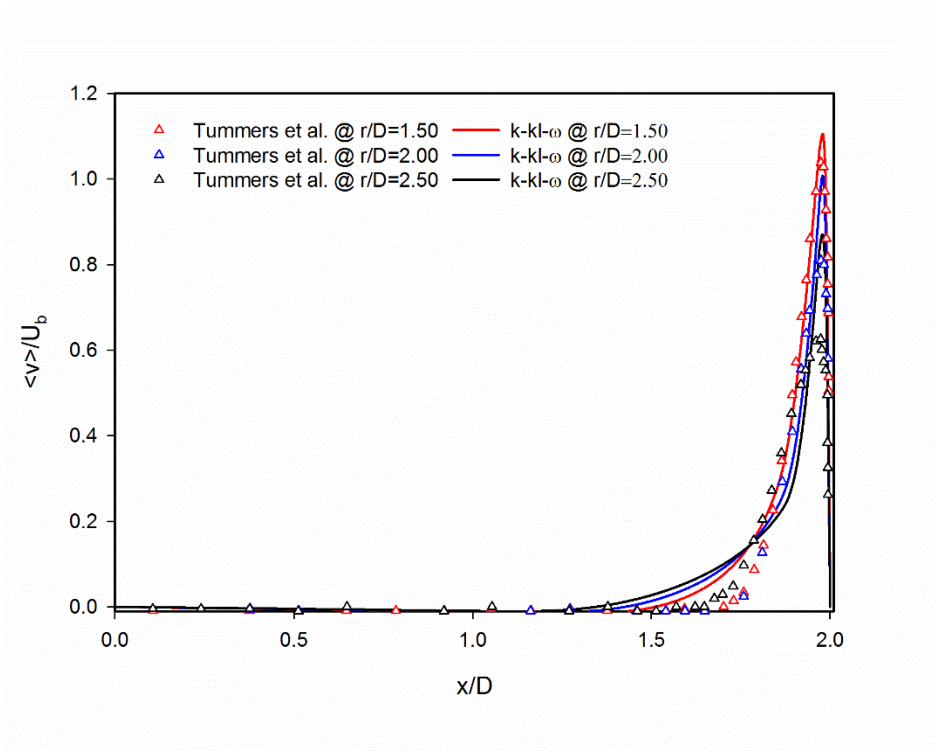
(b)

Figure 4.6: Comparison of normalised axial <u> (a) and radial <v> (b) velocities between computed and measured data (U$_b$=9.32 m/s) [47].

Figure 4.6 and Figure 4.7 show the validation of computational results with experimental data from the literature. Figure 4.6 confirms that the k-kl-ω model is able to accurately predict the

flow features, particularly near the impingement plane (x/D=2) with experimental data from Tummers et al. [47]. For easier readability, only three axial and radial velocity profiles from Tummers et al. [47] are presented in Figure 4.6. The maximum axial velocity occurs at the centreline of the jet and the numerical results of the axial velocity component show good agreement with the experimental data as seen in Figure 4.6(a). The radial velocity component starts increasing from zero at the jet centreline after it impinges and reaches its maximum value and starts to decline as it moves further into the wall jet region. The radial velocity component at r/D=1.50, 2.0, and 2.50 are shown in Figure 4.6(b), the model is able to predict radial velocity profiles correctly (qualitatively) against experimental data quite accurately, some discrepancies occur which can be reduced by increasing the number of mesh elements near the wall. The numerical results over predicted velocity and this over prediction increases as the radial distance increases. Figure 4.7 shows the validation graphs for the Nusselt number and coefficient of pressure with experimental data for Re=24,600 and S=0.31 [12, 53]. Pressure characteristics are in good agreement with experiments and the Nusselt number profile is also predicted qualitatively and quantitatively with a minor deviation in the stagnation point Nu and the location of the peak Nu.
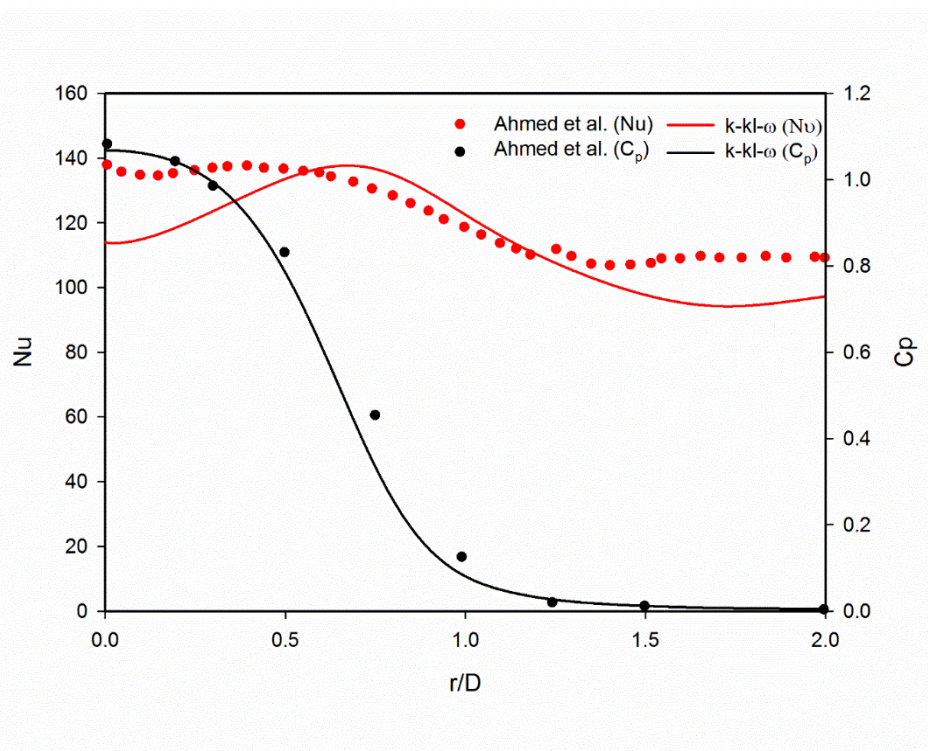
Figure 4.7: Validation for Nusselt number and coefficient of pressure at Re=24,600, H/D=2, and S=0.31 with experimental data [54].

112

4.3 RESULTS AND DISCUSSION

Following the mesh sensitivity analysis and the validation for the k-kl-ω numerical model, a number of numerical simulations were performed to assess the effects of impingement distance and weak swirl (S=0.31) for varied nozzle exit conditions, on the localised Nusselt number, Nusselt number uniformity, and flow features very near to the impingement surface. Exit conditions (for the same swirl number) were varied by using three different tangential velocity profiles for the same axial velocity. These conditions mimicked aerodynamically induced swirl. The role of elevated levels of turbulence near the centreline of inserts used for geometrically induced swirl was also tested by imposing an (artificial) elevated turbulent kinetic energy at the exit plane that modified the exit conditions. Since the steady-state analysis has conducted the turbulent length scales cannot be estimated due to the RANS modelling. Vorticity production through vanes is the similar problem as vortex shedding which is also a time and frequency dependent phenomenon.

Whilst the analyses were done at different impingement distances they only extend to relatively low swirl numbers because earlier studies have shown these to have similar distributions of radial pressure at the impingement surface [53] in both non-swirling and weakly swirling jets. Moreover, the imposition of higher swirl number brings about more fundamental changes to the flow domain of non-reacting (air) jets which take the form of vortex breakdown and flow-induced recirculation, either at or near the nozzle exit plane [32, 35]. Whilst Reynolds numbers from 1,000 to 70,000 spanning the laminar-to-turbulent jet regimes have already been studied in the literature, the present research is focussed at the intermediate range Re=24,600. In doing so, the results are not only relevant to the turbulent regime, but also maintain a comparative benchmark to other studies summarised in Figure 4.2. The ultimate aim of these analyses is to shed light on the effects of even moderate variation to the upstream velocity or turbulence profiles (in both aerodynamically and geometrically induced swirl) on the Nusselt number distribution and whether any flow features (near the impingement surface) correlate to the observed peaks in the Nu (Figure 4.2).

In order to facilitate comparisons with experimental data, radial distributions of heat transfer on the impingement plate from r/D=0 to 10 (Figure 4.3) are considered so as to adequately capture the transitional zones between the stagnation and wall jet regions (Figure 4.1). The numerical solutions are obtained for non-swirling and weakly swirling jets with different types of nozzle (inflow) conditions for impingement distances spanning H/D=2, 4, and 6. A total of four impinging jets representing aerodynamically generated swirl at Re=24,600 (U_b=9.32 m/s)

are modelled, with the first of these based on an (earlier) experimentally measured velocity profile at the nozzle exit (boundary conditions) [34]. The three swirl conditions utilize a single (assumed) axial velocity profile as the nozzle inflow condition, but three different tangential velocity distributions. In this manner cases S031-UP, S031-SBR, and S031-PP also resolve the effects of varied exit profiles, but at the same swirl number (S=0.31). The inflow conditions for these computed impinging jets are shown in Figure 4.8. They utilise a single axial velocity <u> approximated using fifth-order power law [10]. The straight horizontal (black) line represents the uniform profile of azimuthal velocity (S031-UP), the green line which is linearly increasing in radial direction shows the azimuthal velocity profile for the case of solid body rotation (S031-SBR), and the curved (blue) line represents the parabolic azimuthal velocity profile (S031-PP).
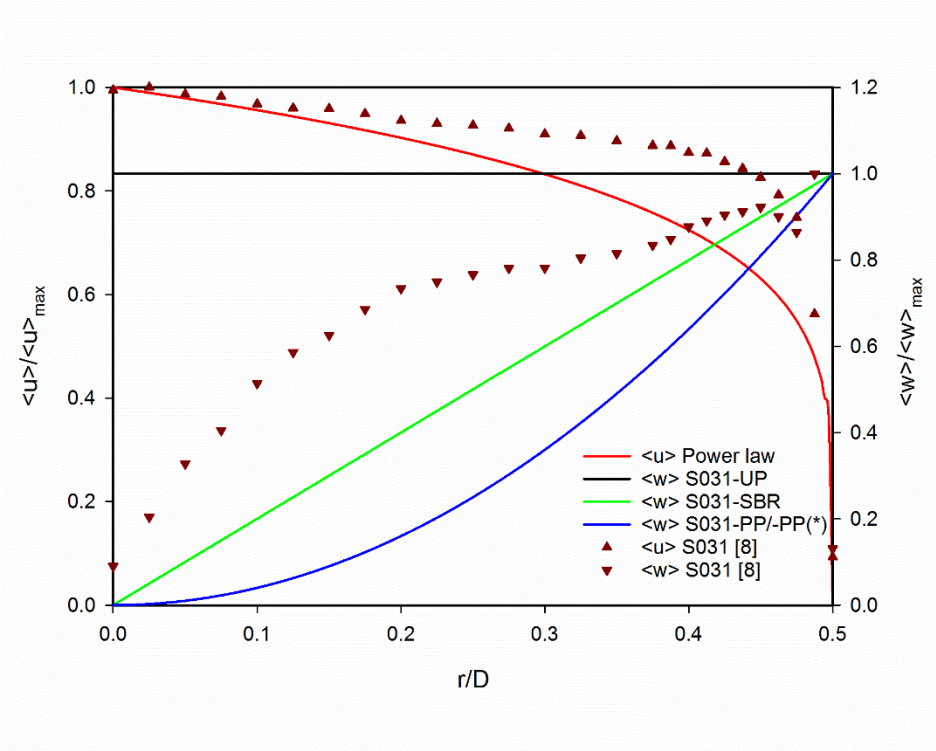
(a)
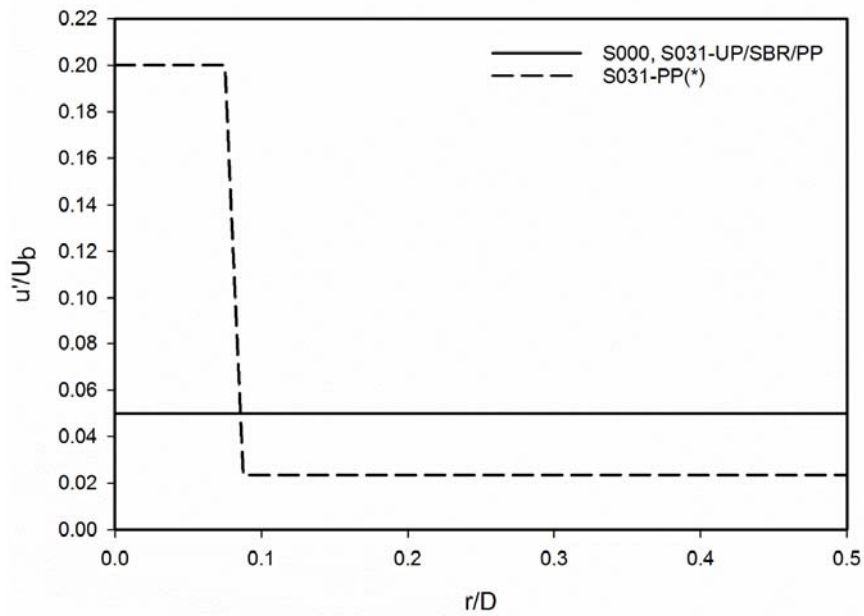
(b)

Figure 4.8: (a) Computed (S031-UP, S031-SBR, S031-PP) and measured (S031 [10]) conditions used in the computation of weakly swirling jets at Re=24,600. (b) Turbulence intensity inflow conditions at x/D=0 in the five jet investigated.

115

Additionally, another (fifth) swirl case named S031-PP(*) with elevated turbulence levels near the centreline is also modelled. Whilst this uses the same velocity profiles of <u> and <w> for S031-PP, its turbulence inflow condition is modified near the centreline (0<r/D<0.075). The effects of modified inflow (turbulence) condition, for the same swirl number is tested using case S031-PP(*) to resemble the use of geometric swirl inserts (at the centreline).

4.3.1 Swirling Impinging Jets

Computations of the velocity field and heat transfer characteristics in a benchmark (non-swirling) impinging jet are included in the chapter appendices which accompany this paper. Summary observations derived in non-swirling impinging jets point to the link between the start of the wall jet region and elevated turbulence levels. The computations indicate a relationship between the spatial locations whereby a jet transcends the stagnation to the wall jet region, with the locations of Nu peaks. These regions of elevated k appear at H/D=6 to penetrate closer to the impingement plane and also spread radially inwards towards r/D=0, compared to near-field impinging jets at H/D=2. Figure 4-A2 and Figure 4-A3 of the chapter appendices present this data. The upstream similarity between non-swirling and weakly swirling jets at x/D=1.25 and 1.75 is evident by the data in Figure 4-A4 (chapter appendices) which shows radial profiles of jet width.

With the flow and heat transfer characteristics of the baseline (S=0) cases resolved, the results for weakly swirling (turbulent) impinging jet with varied inflow conditions mimicking aerodynamically induced swirl. Figure 4.9 shows the effect of three azimuthal velocity profiles on the distribution of the Nusselt number over the impingement surface. For each condition, the corresponding turbulent kinetic energy at x/D=0.25 away from the impingement plate is also depleted. Figure 4.9(a) S031-UP shows at H/D=2 a sharp dip in Nu at the stagnation point and then Nu rises to ~160. The sharp dip in Nu creates a hot spot at the stagnation point but this effect fades as H/D increases. The difference between Nu at the stagnation point and the peak value (at ~r/D=0.9) falls. Similar to the earlier observation in non-swirling jet S000, as the impingement distance grows the peak Nu moves closer towards the stagnation point. Also noticeable is that whilst the heat transfer (Nu) remains very low near the stagnation point (at H/D=2), there is an apparent recovery in the level of turbulence (k) between r/D=0 and ~0.3. The reason for this will become apparent from the later flow field results (to be presented). Figure 4.9(b) and Figure 4.9(c) also show the Nu and k distributions for S031-SBR which uses

a $<w>$ profile akin to solid-body rotation and S031-PP which has a parabolic profile (PP), respectively (Figure 4.8(a)).
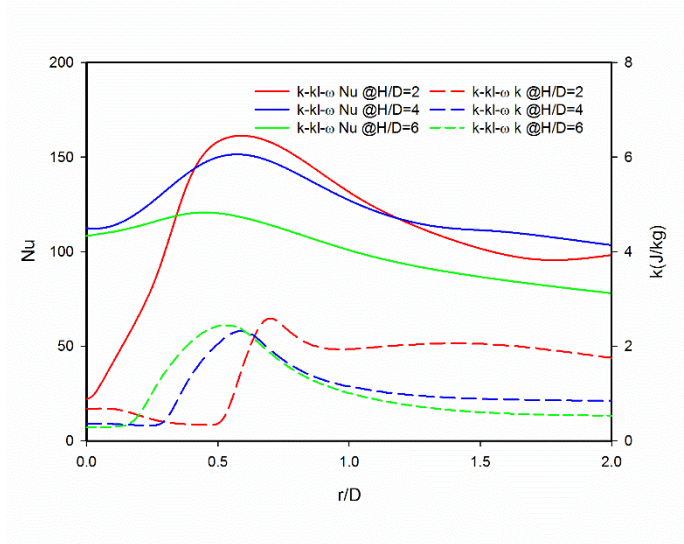
(a)
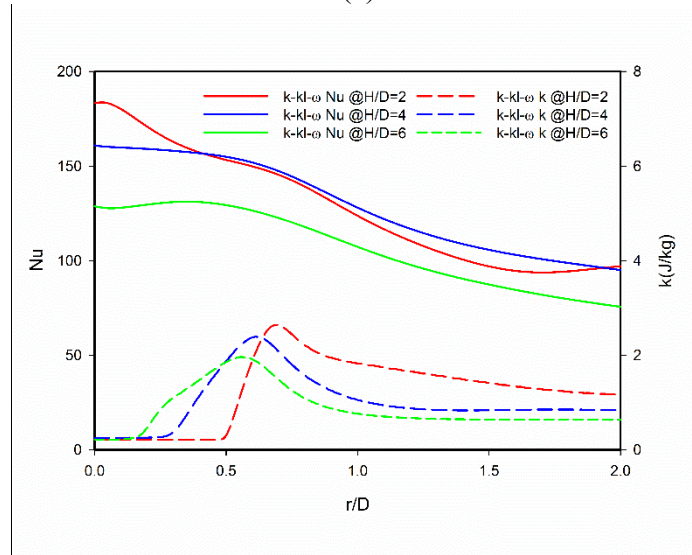
(b)
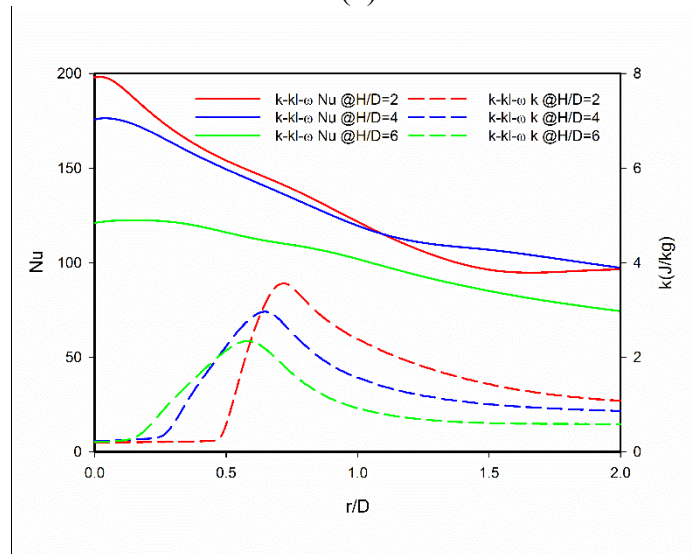
(c)

Figure 4.9: Computed Nusselt number (Nu) and turbulent kinetic energy (k), (a) S031-UP (b) S031-SBR (c) S031-PP.

At all values of H/D the peak Nu occurs at the stagnation point except in the case of SBR at H/D=6. A significant increase is observed in peak Nu at the stagnation point Nusselt number for H/D=2; however, a small change is observed for H/D=4 and reduced for H/D=6. For azimuthal velocity in the case of SBR and PP, a large velocity gradient occurs near the nozzle boundary, while in the case of UP velocity gradients are equally distributed in the radial direction. The peak turbulent kinetic energy is decreased with impingement distance for SBR and PP velocity profiles.

Figure 4.10 presents the velocity field for all three inflow conditions (UP, SBR, and PP) at S=0.31 and H/D=2. Jets S031-SBR and S031-PP appear to relatively flat <u> velocity profiles all the way to impingement plane. In contrast, condition S031-UP has a small pocket of low velocity (stagnant) fluid at the impingement plane over r/D=0 to ~0.3. Also worth noting that the start of the stagnation zone (as denoted by elevated <v> velocities) appears displaced from the stagnation point and only commences at r/D~0.3. In S031-SBR and S031-PP, the <v> velocities pick up closer to the centreline. This reflects the occurrence of a radially displaced Nu peak in the data for S031-UP, but peaks at the centreline in S031-SBR and S031-PP (Figure 4.9).
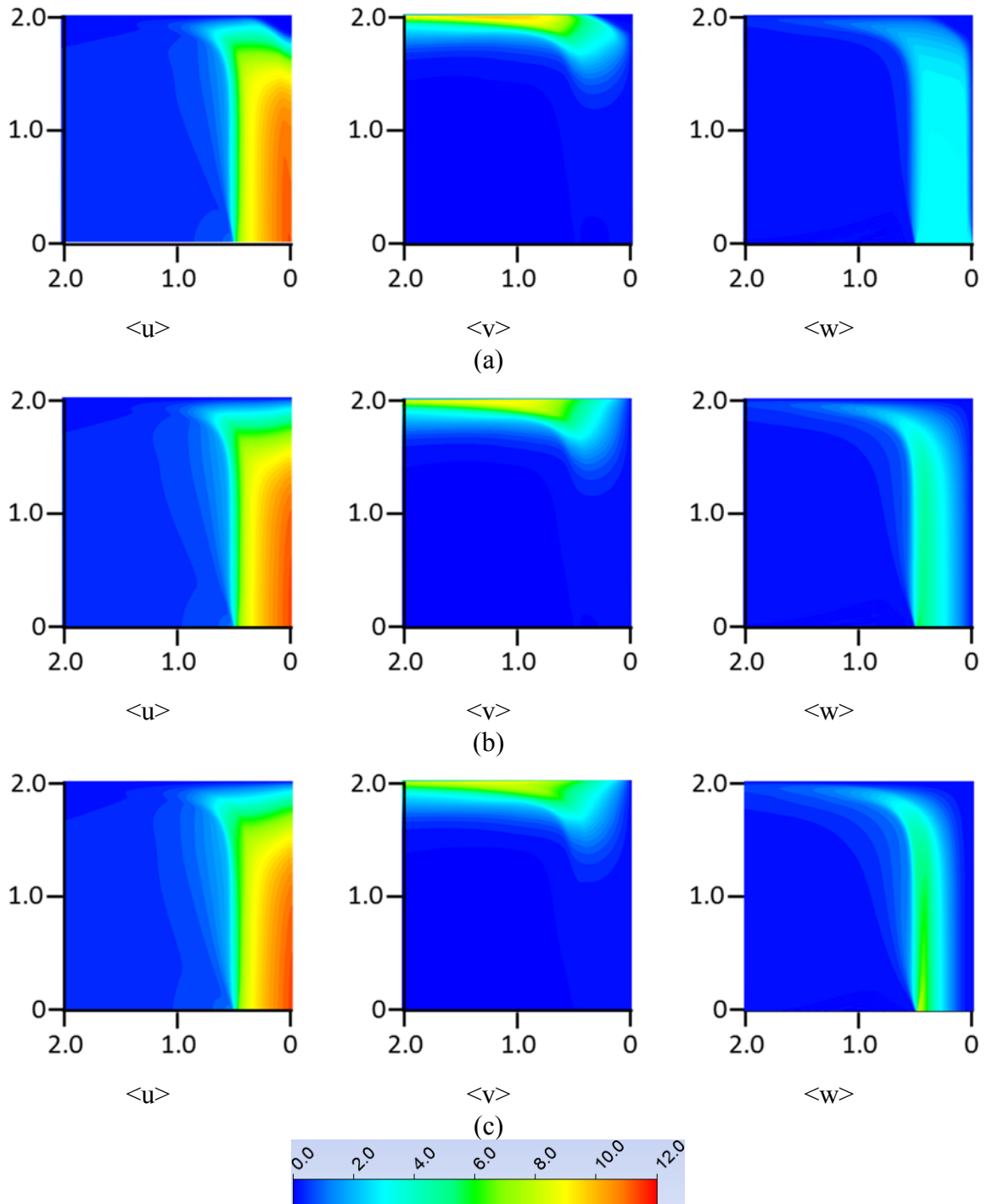
Figure 4.10: **<u>, <v>, and <w> velocity fields (a) S031-UP, (b) S031-SBR, and (c) S031-PP at H/D=2. The velocity magnitudes are given in m/s, the horizontal axis is r/D while vertical axis is x/D.**

Figure 4.11 shows the near field velocity vectors at the stagnation zone between $0 \leq r/D \leq 0.5$ in near-field impingement (H/D=2) for jets S031-UP, S031-SBR, and S031-PP. Only the domain close to the plane at $1.50 \leq x/D \leq 2.00$ is shown. Figure 4.11(a) shows that (on top) for S031-UP recirculation zone is formed on the impingement plane over r/D=0 to ~0.3 and this appears to overlap with the observed dips in Nu with S031-UP (Figure 4.9(a)).
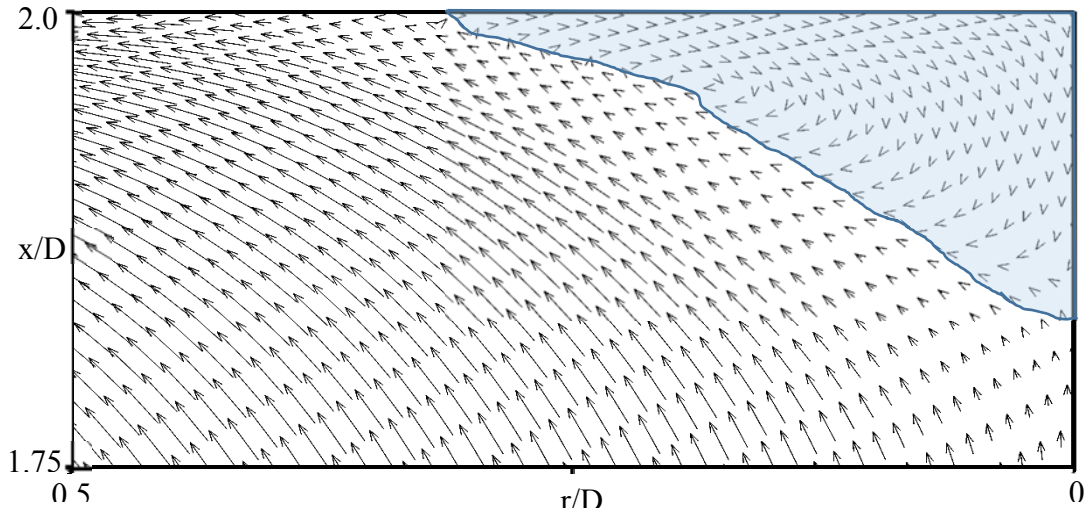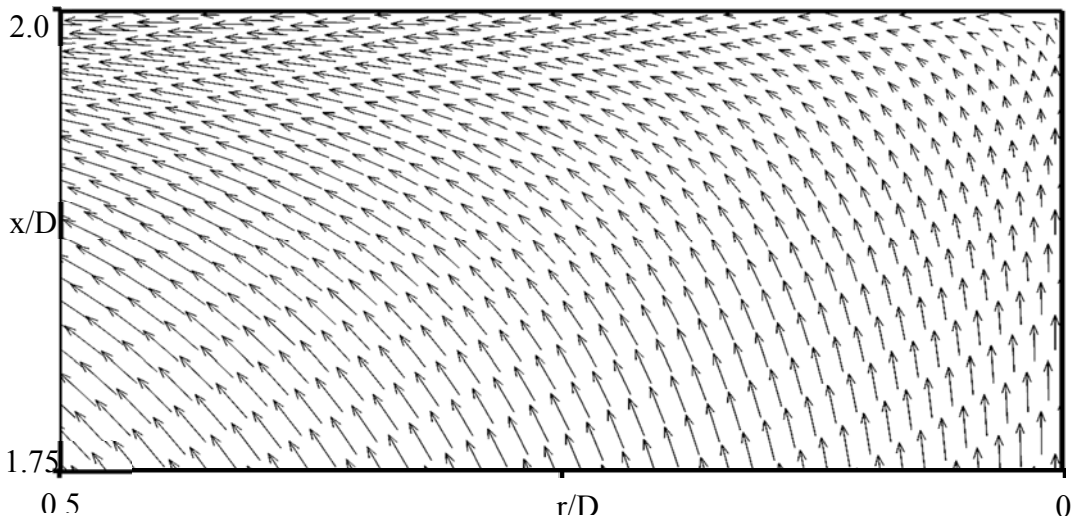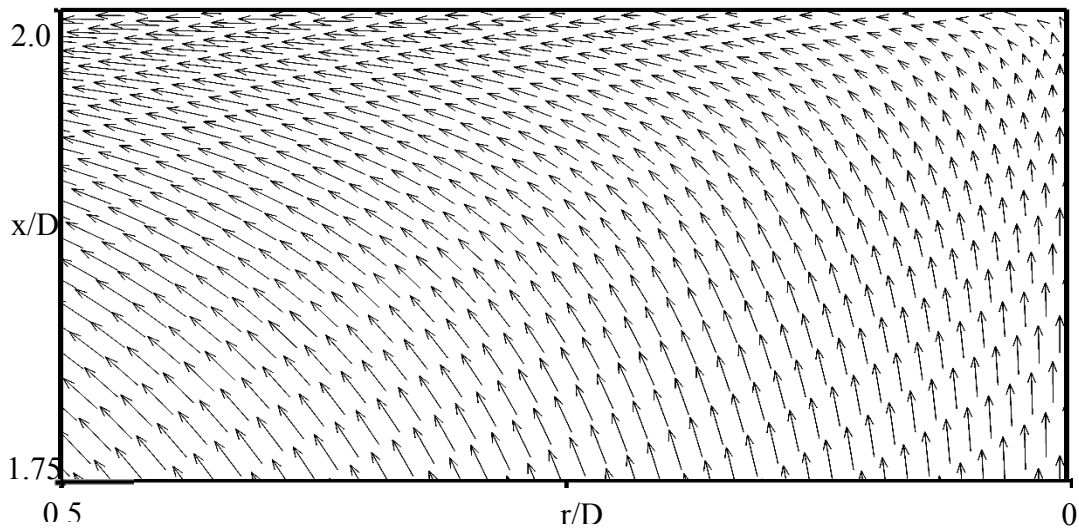
Figure 4.11: Vector field plots for impingement at H/D=2 in weakly swirling jets (a) S031-UP (shaded area denotes recirculation zone), (b) S031-SBR, and (c) S031-PP. Only the last x/D=0.25 of the flow field is shown.

121

Table 4.3 presents the stagnation point Nusselt number (Nu_0), the average Nusselt number (Nu_A) over for $r/D \leq 2$, and the measure of uniformity (σ) for the experimental data of Ahmed et al. [12] at S=0. Equations (4-12) and (4-13) are used to calculate the Nusselt numbers and standard deviation in non-swirling and weakly swirling impinging jets.

Table 4.3: Nu_0, Nu_A, and σ calculated from experimental data at Re=24,600 [12].

H/D	NON-SWIRLING (S=0)			WEAKLY SWIRLING (S=0.31)		
	Nu_0	Nu_A	σ	Nu_0	Nu_A	σ
2	115.3	109.8	8.9	137.8	121.9	9.9
4	124.1	113.0	11.7	157.2	127.5	15.6
6	147.4	117.6	16.1	123.0	103.2	13.4

For comparison, Table 4.4 shows Nu_0, Nu_A, and σ for the computational results and indicates that the inflow conditions for weakly swirling jets have a significant effect on the uniformity for H/D=2. Stagnation point Nusselt number (Nu_0) S031-UP is much smaller than S031-SBR and S031-PP for all impingement distances, whilst they are comparable with each other. For all inflow conditions, σ falls with an increase of H/D except in the case of the uniform profile. Computed results show a decrease in the average Nusselt number for all inflow conditions except the UP case, which showed inclining and declining trend as the impinging distance is increasing. The stagnation point Nusselt number in case of the UP boundary condition shows a close to average Nusselt number over the impinging surface. At H/D=2 a very low Nusselt number is also observed at the stagnation point. S031-SBR and S021-PP average Nusselt number are similar and greater than S031-UP. The average Nusselt number of non-swirling jet is more than S031-UP but less than the S031-SBR and S031-PP.

Table 4.4: Nu_0 (stagnation point), Nu_A (average over r/D=0 to 2), and σ calculated from Computational data at Re=24,600.

H/D	S000			S031-UP			S031-SBR			S031-PP		
	Nu_0	Nu_A	σ_A	Nu_0	Nu_A	σ_A	Nu_0	Nu_A	σ_A	Nu_0	Nu_A	σ_A
2	120	104	11.1	22	112	30.6	183	128	23.2	198	129	25.6
4	127	111	18.0	112	124	12.4	161	129	18.3	176	128	19.9
6	137	115	19.1	108	100	14.3	129	106	18.5	121	100	16.2

Figure 4.12(a) demonstrates the dimensionless wall shear stress and turbulent kinetic energy at x/D=0.25 away from a target surface ($0 \leq r/D \leq 2$) for non-swirling and swirling jets. These trends show that jet S031-UP which exhibits a recirculation zone on the stagnation plane (over r/D=0 to 0.3) also has distinct wall shear stress distribution with suppressed τ_w in the stagnation zone. This occurs even though the imposition of swirl does not affect the upstream jet width as

shown in Figure 4-A4 of the chapter appendices. Figure 4.12(b) presents the temperature distribution very near the impingement wall for $0 \leq r/D \leq 0.5$. The results in this figure confirm that fluid temperatures increase as the surface is approached and that this effect covers r/D=0 to 0.3. In summary, these observations indicated that with S031-UP the stable recirculation zone suppressed Nu and τ_w which leads to a higher temperature in the stagnation zone.
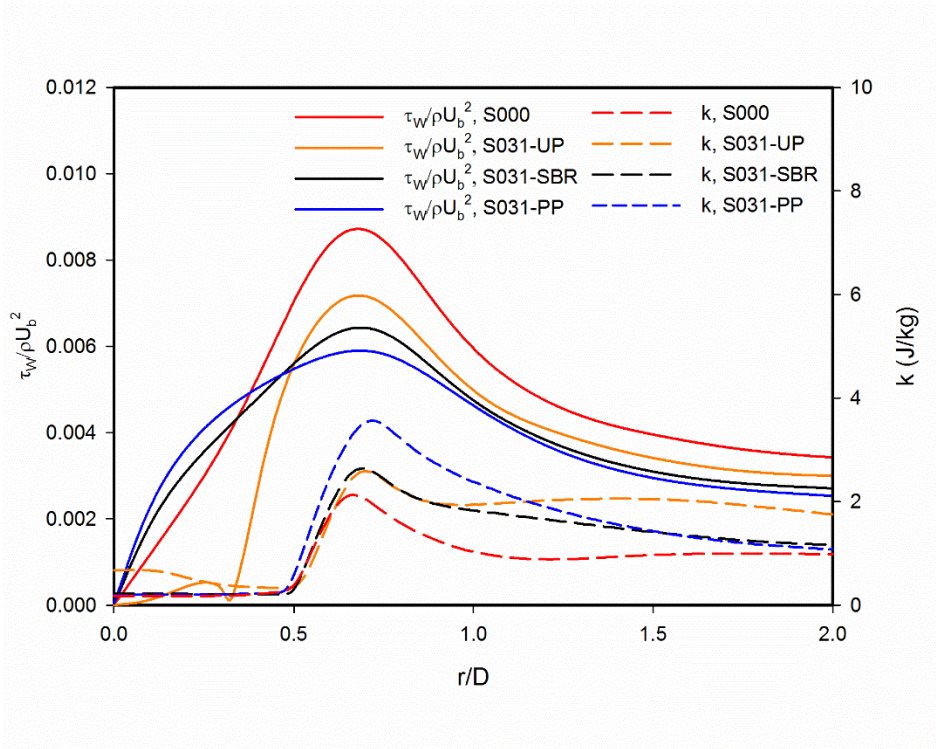
(a)
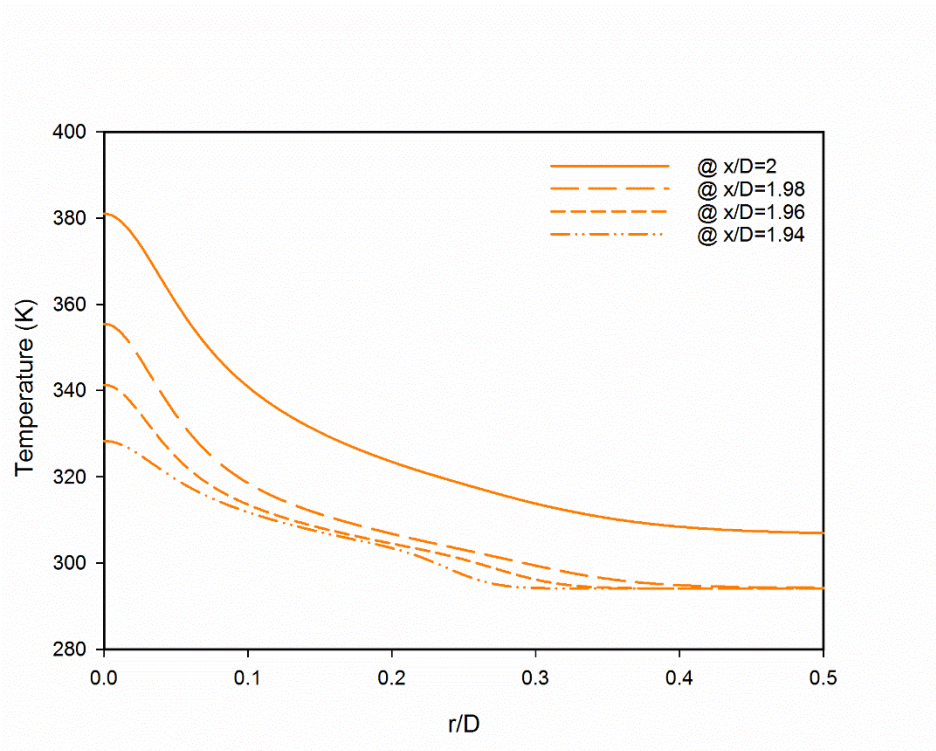
(b)

Figure 4.12: (a) Non-dimensionalised wall shear stress and turbulent kinetic energy at H/D=2 (b) Near-wall temperature of the stagnation zone for S031-UP.

124

4.3.2 Geometric Swirl Modelling

Inlet
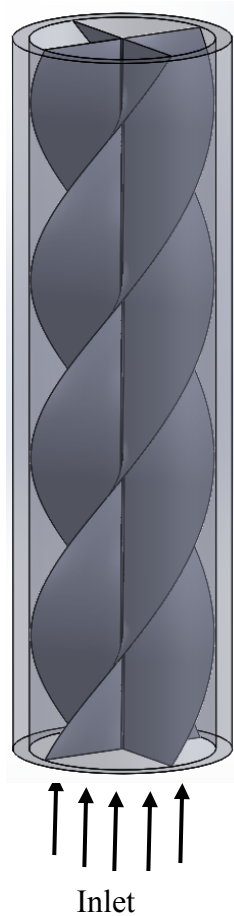
Figure 4.13: A typical configuration (concept drawing only) to visualise the likely reasons for elevated turbulence near the centreline when geometric swirl inserts are used.

Swirl can be generated either (geometrically) using vanes/inserts or aerodynamically by the induction of tangential flow components into a streamwise (axial) jet. Figure 4.13 shows the configuration of a typical swirling nozzle with twisted tape, where the flow enters axially into the nozzle and swirl motion is added into the flow. It is reasonable to assume that in such cases there is a zone at the centre of the nozzle where shear stresses are relatively high. In this context, the azimuthal velocity closely resembles a parabolic profile with high turbulence intensity at the centre. Flow from the nozzle with inserts cannot be modelled with an axisymmetric assumption because the flow is not symmetric in nature as the jet can bifurcate into multiple streams [6]. It is thus worth looking at the explicit effects of turbulence intensity at the nozzle inflow plane (x/D=0) and to see how it can affect impingement heat transfer at (H/D=2, 4, and 6). In order to understand the effects of high turbulence intensity near the centre simulations were conducted for an S031-PP(*) with a turbulence intensity which is 4 times greater than another swirling jet (S031-PP) as shown in Figure 4.8(b). However, the total turbulence

intensity was kept constant by adjusting its value for other radial positions at the inlet. The comparison between S031-PP (Figure 4.9 (c)) and S031-PP(*), therefore, shows the effect of (only) higher turbulence at the inflow with all other features kept the same.
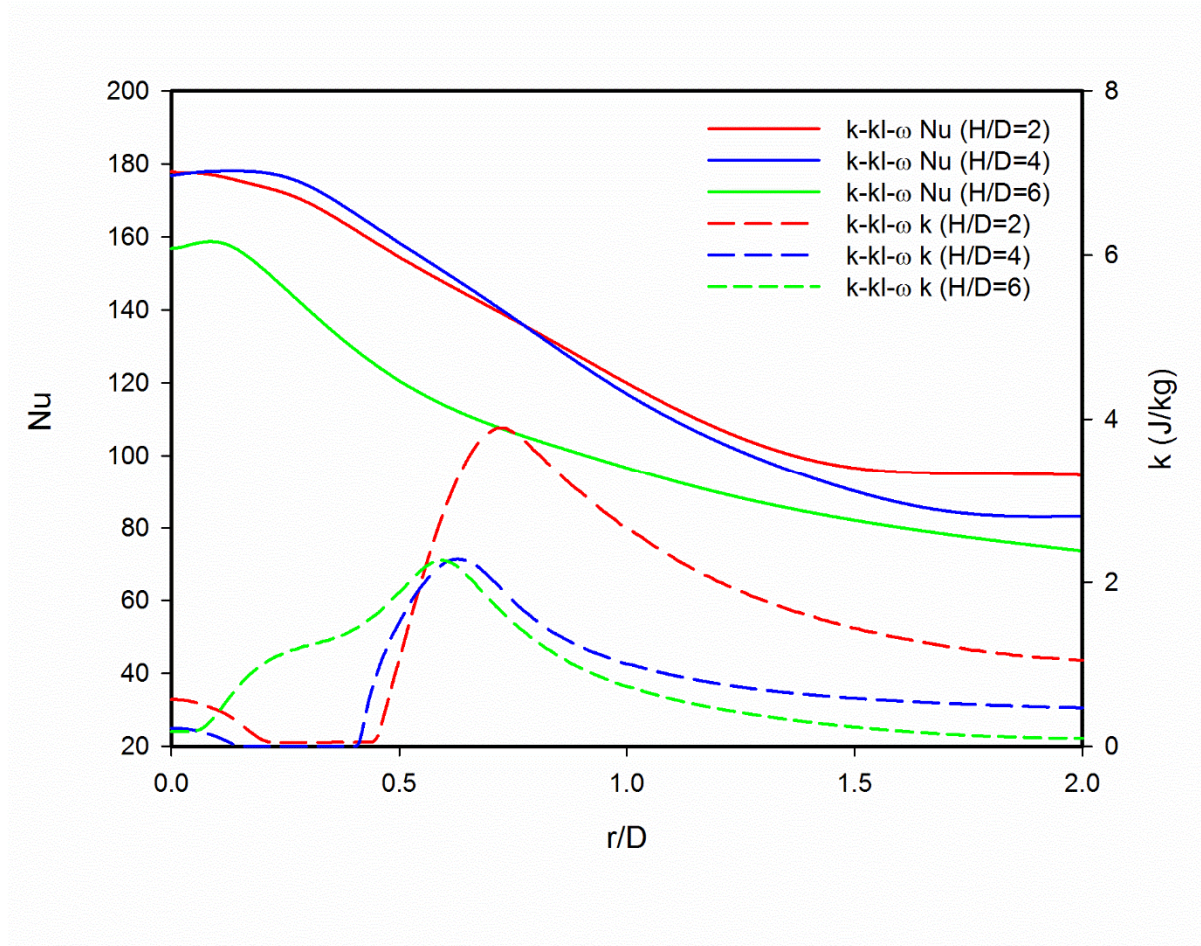
Figure 4.14: Nu distribution for swirling jet S031-PP(*) (Re=24,600, H/D=2, 4, and 6).

Figure 4.14 presents the results of Nusselt number distribution for S031-PP(*) near the centre of the nozzle at H/D=2, 4, and 6. It is clear that both the impingement surface heat transfer (Nu) and turbulence close to the impingement plane (k) are affected. Figure 4.15 which presents the velocity and turbulence field also shows that apparent recovery in Nu at H/D=6 at the stagnation zone (Figure 4.14) is not attributed to a recirculation zone as occurred with S031-SBR at H/D=2 (Figure 4.9 (a)). In order to enhance further understanding of this situation, a 3D transient simulation is required.
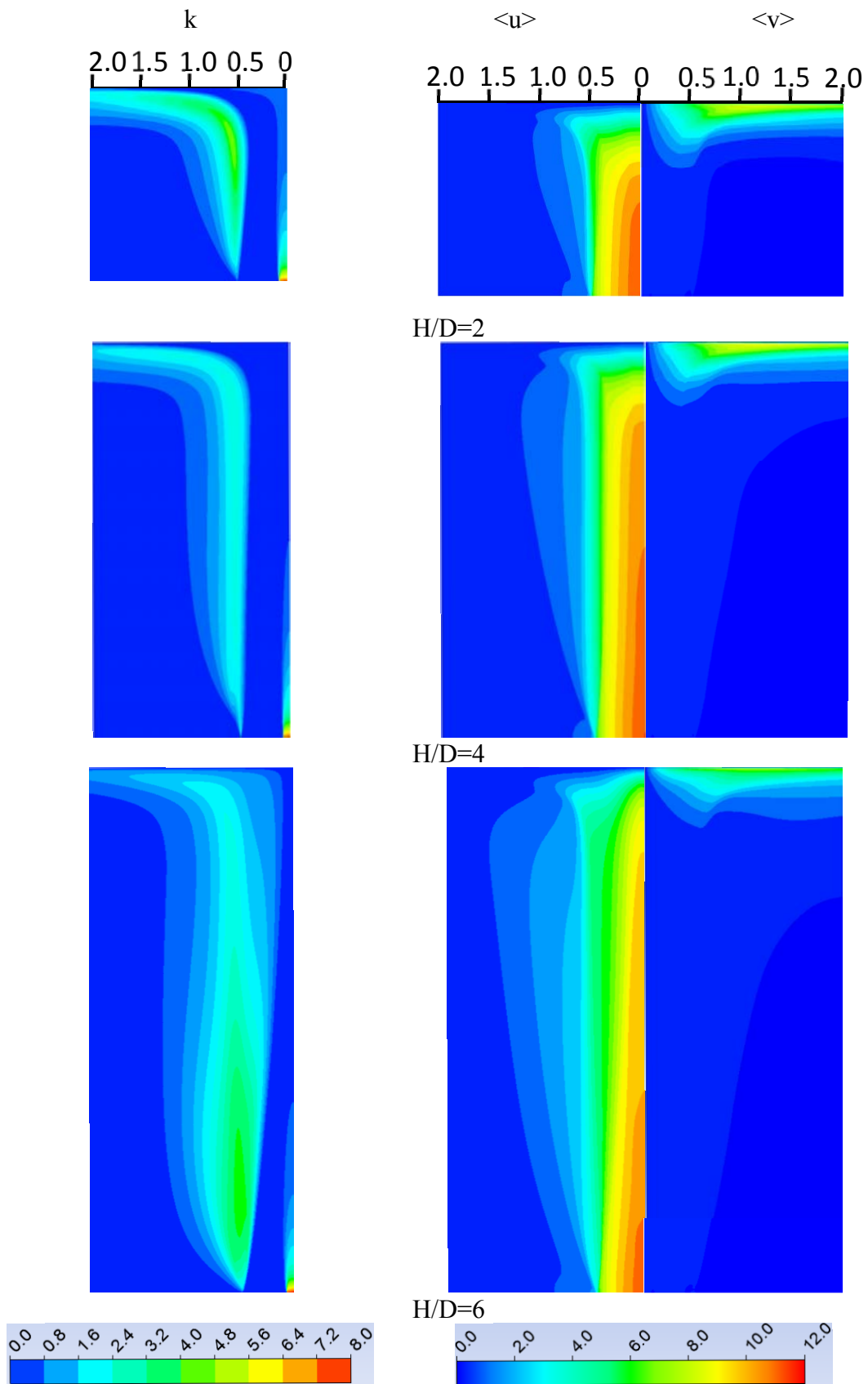
Figure 4.15: Computed turbulent kinetic energy (k) and velocity component (<u>, <v>) for S031-PP(*) at H/D=2, 4, and 6. The velocity magnitudes are given in m/s, the horizontal axis is r/D while vertical axis is x/D.

4.4 CONCLUSIONS

ANSYS Fluent (v 16.2) has been used (H/D=2, 4, and 6) to examine impingement heat transfer in weakly swirling (S=0.31) turbulent jets having three inflow conditions when compared to non-swirling jets. The effects of geometric swirl inserts have also been studied. Flow field and heat transfer predictions are validated against the experimental data [12, 47]. The results can be summarized as follows:

- **Turbulence models:** For the conditions tested, the k-kl-ω model more accurately predicts impingement heat transfer compared to other models. Results are validated for both non-swirling (S=0, Figure 4-A2) and weakly swirling jets (S=0.31, Figure 4.7).

- **Weakly swirling jets (S=0.31):** In non-swirling jets, upstream turbulence strongly affects the distribution (uniformity) of impingement heat transfer with flow regions experiencing high Turbulent Kinetic Energy (k) also exhibiting peaks in Nusselt number (Figure 4-A2). Additionally, for non-swirling jets, the start of the wall jet region (signified by the relatively high radial velocities) appears to overlap with (the first) Nu and k peaks (Figure 4-A2 and Figure 4-A3). These peaks (and the approximate starting location for the wall jet region) appear to shift closer to the stagnation point (r/D=0) as impingement distance (H/D) increases (Figure 4-A3). Similar observations are noted in weakly swirling jets, with peaks radially displaced from the centreline in S031-UP but at the stagnation zone with S031-SBR and S031-PP (Figure 4.9 and Figure 4.10). At S=0.31, nozzle inflow conditions significantly affect the Nu distribution at the impingement plane (over H/D=2 to 6), with some weakly swirling inflow conditions (S031-UP) likely to suppress heat transfer in near-field impingement (H/D=2). This is caused by the presence of a recirculation zone which stabilizes on the impingement plane (Figure 4.10 and Figure 4.11). The same behaviour is not observed in non-swirling jets (S000) or other weakly jets at the same swirl number (S031-SBR and S031-PP, Figure 4.11). Wall shear stresses are negligible at the recirculation region. For H/D=4 and 6 the difference between the stagnation point Nusselt number and the peak Nusselt number reduces.

- **High turbulence intensity inflows (geometric swirl):** Increased turbulence intensity as would probably occur with geometric swirl inserts affects both the heat transfer (Nu) and turbulence (k) near the impingement plane. For the jets with far-

field impingement (H/D=6), a Nu peak can occur in the stagnation zone with jets exhibiting higher inflow turbulence S031-PP(*) compared to others S031-PP

4.5 CHAPTER REFERENCES

[1]   M. Fairweather and G. Hargrave, "Experimental investigation of an axisymmetric, impinging turbulent jet. 1. Velocity field," *Exp. Fluids*, vol. 33, no. 3, pp. 464–471, Sep. 2002.

[2]   N. Zuckerman and N. Lior, "Impingement heat transfer: correlations and numerical modeling," *J. Heat Transfer*, vol. 127, no. 5, p. 544, 2005.

[3]   O. Ghaffari, S. A. Solovitz, M. Ikhlaq, and M. Arik, "An investigation into flow and heat transfer of an ultrasonic micro-blower device for electronics cooling applications," *Appl. Therm. Eng.*, vol. 106, pp. 881–889, 2016.

[4]   J. C. Kurnia, A. P. Sasmito, W. Tong, and A. S. Mujumdar, "Energy-efficient thermal drying using impinging-jets with time-varying heat input − A computational study," *J. Food Eng.*, vol. 114, pp. 269–277, Jan. 2013.

[5]   M. Ikhlaq, O. Ghaffari, and M. Arik, "Predicting Heat Transfer for Low- and High-Frequency Central-Orifice Synthetic Jets," *IEEE Trans. Components, Packag. Manuf. Technol.*, vol. 6, no. 4, pp. 586–595, Apr. 2016.

[6]   A. Ianiro and G. Cardone, "Heat transfer rate and uniformity in multichannel swirling impinging jets," *Appl. Therm. Eng.*, vol. 49, pp. 89–98, 2012.

[7]   N. Uddin, S. O. Neumann, and B. Weigand, "LES simulations of an impinging jet: On the origin of the second peak in the Nusselt number distribution," *Int. J. Heat Mass Transf.*, vol. 57, pp. 356–368, Jan. 2013.

[8]   T. Dairay, V. Fortuné, E. Lamballais, and L.-E. Brizzi, "Direct numerical simulation of a turbulent jet impinging on a heated wall," *J. Fluid Mech.*, vol. 764, pp. 362–394, Feb. 2015.

[9]   N. Zuckerman and N. Lior, "Jet impingement heat transfer: Physics, correlations, and numerical modeling," *Adv. Heat Transf.*, vol. 39, pp. 565–631, 2006.

[10]   Z. U. Ahmed, Y. M. Al-Abdeli, and M. T. Matthews, "The effect of inflow conditions on the development of non-swirling versus swirling impinging turbulent jets," *Comput. Fluids*, vol. 118, pp. 255–273, 2015.

[11]   T. S. O'Donovan and D. B. Murray, "Jet impingement heat transfer - Part I: Mean and root-mean-square heat transfer and velocity distributions," *Int. J. Heat Mass Transf.*,

vol. 50, pp. 3291–3301, 2007.

[12] Z. U. Ahmed, Y. M. Al-Abdeli, and F. G. Guzzomi, "Heat transfer characteristics of swirling and non-swirling impinging turbulent jet," *Int. J. Heat Mass Transf.*, vol. 102, pp. 991–1003, 2016.

[13] M. Fairweather and G. K. Hargrave, "Experimental investigation of an axisymmetric, impinging turbulent jet. 2. Scalar field," *Exp. Fluids*, vol. 33, no. 4, pp. 539–544, Oct. 2002.

[14] J. Baughn and S. Shimizu, "Heat transfer measurements from a surface with uniform heat flux and an impinging jet," *J. Heat Transf. (Transactions ASME)*, vol. 111, pp. 1988–1990, 1989.

[15] D. Lytle and B. W. Webb, "Air jet impingement heat transfer at low nozzle - plate spacings," *Inl . J . Heal Mass Transf.*, vol. 31, pp. 1687–1697, 1994.

[16] M. Behnia, S. Parneix, Y. Shabany, and P. a. Durbin, "Numerical study of turbulent heat transfer in confined and unconfined impinging jets," *Int. J. Heat Fluid Flow*, vol. 20, pp. 1–9, 1999.

[17] D. Cooper, D. C. Jackson, B. E. Launder, and G. X. Liao, "Impinging jet studies for turbulence model assessment-l. Flow-field experiments," *Int. J. Heat Mass Transf.*, vol. 36, pp. 2675–2684, 1993.

[18] J. Lee and S.-J. Lee, "The effect of nozzle aspect ratio on stagnation region heat transfer characteristics of elliptic impinging jet," *Int. J. Heat Mass Transf.*, vol. 43, pp. 555–575, Feb. 2000.

[19] J. W. Baughn, A. E. Hechanova, and X. Yan, "An experimental study of entrainment effects on the heat transfer from a flat surface to a heated circular impinging jet," *J. Heat Transfer*, vol. 113, pp. 1023–1025, Nov. 1991.

[20] V. Katti and S. V Prabhu, "Experimental study and theoretical analysis of local heat transfer distribution between smooth flat surface and impinging air jet from a circular straight pipe nozzle," *Int. J. Heat Mass Transf.*, vol. 51, pp. 4480–4495, 2008.

[21] K. J. Brown, T. Persoons, and D. B. Murray, "Heat transfer characteristics of swirling impinging jets," in *14th International Heat Transfer Conference, Volume 5*, 2010, pp. 657–665.

[22] J. M. Buchlin, "Convective heat rransfer in impinging- gas-jet arrangements," *J. Appl. Fluid Mech.*, vol. 4, pp. 137–149, 2011.

[23] Z. U. Ahmed, Y. M. Al-Abdeli, and F. G. Guzzomi, "Corrections of dual-wire CTA data in turbulent swirling and non-swirling jets," *Exp. Therm. Fluid Sci.*, vol. 70, pp. 166–175, 2016.

[24] Y. M. Al-Abdeli and A. R. Masri, "Review of laboratory swirl burners and experiments for model validation," *Exp. Therm. Fluid Sci.*, vol. 69, pp. 178–196, 2015.

[25] J. Ortega-Casanova, "CFD and correlations of the heat transfer from a wall at constant temperature to an impinging swirling jet," *Int. J. Heat Mass Transf.*, vol. 55, pp. 5836–5845, 2012.

[26] H. Q. Yang, T. Kim, T. J. Lu, and K. Ichimiya, "Flow structure, wall pressure and heat transfer characteristics of impinging annular jet with/without steady swirling," *Int. J. Heat Mass Transf.*, vol. 53, no. 19–20, pp. 4092–4100, Sep. 2010.

[27] D. Hee Lee, S. Youl Won, Y. Taek Kim, and Y. Suk Chung, "Turbulent heat transfer from a flat surface to a swirling round impinging jet," *Int. J. Heat Mass Transf.*, vol. 45, pp. 223–227, Jan. 2002.

[28] K. Bakirci and K. Bilen, "Visualization of heat transfer for impinging swirl flow," *Exp. Therm. Fluid Sci.*, vol. 32, pp. 182–191, 2007.

[29] Y. Amini, M. Mokhtari, M. Haghshenasfard, and M. Barzegar Gerdroodbary, "Heat transfer of swirling impinging jets ejected from Nozzles with twisted tapes utilizing CFD technique," *Case Stud. Therm. Eng.*, vol. 6, pp. 104–115, 2015.

[30] M.-Y. Wen and K.-J. Jang, "An impingement cooling on a flat surface by using circular jet with longitudinal swirling strips," *Int. J. Heat Mass Transf.*, vol. 46, no. 24, pp. 4657–4667, Nov. 2003.

[31] Z. X. Yuan, Y. Y. Chen, J. G. Jiang, and C. F. Ma, "Swirling effect of jet impingement on heat transfer from a flat surface to CO_2 stream," *Exp. Therm. Fluid Sci.*, vol. 31, pp. 55–60, 2006.

[32] Y. M. Al-Abdeli, "Experiments in turbulent swirling non-premixed flames and isothermal flows," 2004.

[33] I. K. Toh, D. Honnery, and J. Soria, "Axial plus tangential entry swirling jet," *Exp.*

Fluids, vol. 48, no. 2, pp. 309–325, Feb. 2010.

[34] Y. M. Al-Abdeli and A. R. Masri, "Recirculation and flowfield regimes of unconfined non-reacting swirling flows," *Exp. Therm. Fluid Sci.*, vol. 27, pp. 655–665, May 2003.

[35] Y. M. Al-Abdeli and A. R. Masri, "Precession and recirculation in turbulent swirling isothermal jets," *Combust. Sci. Technol.*, vol. 176, pp. 645–665, May 2004.

[36] A. Guo, B., Fletcher, D., Rojas Marquez, G., Al-Abdeli, Y., Starner, S., Masri, "Rans calculations and measurements of instabilities in swirl-stabilised jets and flames.," in *Australian Symposium on Combustion & the 8th Australian Flame Days*, 2003.

[37] Y. M. Al-Abdeli, A. R. Masri, G. R. Marquez, and S. H. Starner, "Time-varying behaviour of turbulent swirling nonpremixed flames," *Combust. Flame*, vol. 146, no. 1–2, pp. 200–214, 2006.

[38] Y. M. Al-Abdeli and A. R. Masri, "Turbulent swirling natural gas flames : stability characteristics, unsteady behavior and vortex breakdown," *Combust. Sci. Technol.*, vol. 179, no. 1–2, pp. 207–225, Jan. 2007.

[39] B. Sunden and J. Larocque, "Simulation of heat transfer from swirling impinging jets," in *Volume 3: Turbo Expo 2005, Parts A and B*, 2005, pp. 765–772.

[40] S. Z. Shuja, B. S. Yilbas, and M. Rashid, "Confined swirling jet impingement onto an adiabatic wall," *Int. J. Heat Mass Transf.*, vol. 46, pp. 2947–2955, 2003.

[41] A. Ianiro, D. Violato, F. Scarano, and G. Cardone, "Three dimensional features in swirling impinging jets," in *15th International Symposium on Flow Visualization*, 2012.

[42] L. Huang and M. S. El-Genk, "Heat transfer and flow visualization experiments of swirling, multi-channel, and conventional impinging jets," *Int. J. Heat Mass Transf.*, vol. 41, no. 3, pp. 583–600, Feb. 1998.

[43] J. K. J. Abrantes, L. Azevedo, L. Fernando, and A. Azevedo, "Fluid flow characteristics of a swirl jet impinging on a flat plate," in *13th Internationaal Symposium on Application of Laser Techniques to Fluid Mechanics*, 2006, pp. 26–29.

[44] L. Xu, J. Lan, Y. Ma, J. Gao, and Y. Li, "Numerical study on heat transfer by swirling impinging jets issuing from a screw-thread nozzle," *Int. J. Heat Mass Transf.*, vol. 115, pp. 232–237, 2017.

[45] Z. U. Ahmed, Y. M. Al-Abdeli, and F. G. Guzzomi, "Flow field and thermal behaviour in swirling and non-swirling turbulent impinging jets," *Int. J. Therm. Sci.*, vol. 114, pp. 241–256, 2017.

[46] J. Ortega-Casanova and S. I. Castillo-Sanchez, "On using axisymmetric turbulent impinging jets swirling as Burger's vortex for heat transfer applications. Single and multi-objective vortex parameters optimization," *Appl. Therm. Eng.*, vol. 121, pp. 103–114, 2017.

[47] M. J. Tummers, J. Jacobse, and S. G. J. Voorbrood, "Turbulent flow in the near field of a round impinging jet," *Int. J. Heat Mass Transf.*, vol. 54, pp. 4939–4948, 2011.

[48] "ANSYS Inc. (2015). ANSYS Fluent 16.2: User's Guide." .

[49] J. Fürst, J. Příhoda, and P. Straka, "Numerical simulation of transitional flows," *Computing*, vol. 95, pp. 163–182, 2013.

[50] D. K. Walters and D. Cokljat, "A three-equation eddy-viscosity model for Reynolds-Averaged Navier–Stokes simulations of transitional flow," *J. Fluids Eng.*, vol. 130, p. 121401, Dec. 2008.

[51] I. B. Celik, U. Ghia, and P. J. Roache, "Procedure for estimation and reporting of uncertainty due to discretization in CFD applications," *J. Fluids Eng.*, vol. 130, p. 078001, Jul. 2008.

[52] T. Wang and T. S. Dhanasekaran, "Calibration of CFD model for mist/steam impinging jets cooling," in *Volume 4: Heat Transfer, Parts A and B*, 2008, pp. 703–716.

[53] Z. U. Ahmed, Y. M. Al-Abdeli, and F. G. Guzzomi, "Impingement pressure characteristics of swirling and non-swirling turbulent jets," *Exp. Therm. Fluid Sci.*, vol. 68, pp. 722–732, 2015.

[54] M. Angioletti, E. Nino, and G. Ruocco, "CFD turbulent modelling of jet impingement and its validation by particle image velocimetry and mass transfer measurements," *Int. J. Therm. Sci.*, vol. 44, pp. 349–356, Apr. 2005.

[55] M. K. Isman, E. Pulat, A. B. Etemoglu, and M. Can, "Numerical investigation of turbulent impinging jet cooling of a constant heat flux surface," *Numer. Heat Transf. Part A Appl.*, vol. 53, pp. 1109–1132, 2008.

[56] E. Pulat, M. Kemal Isman, A. Burak Etemoglu, and M. Can, "Effect of turbulence

models and near-wall modeling approaches on numerical results in impingement heat transfer," *Numer. Heat Transf. Part B Fundam.*, vol. 606, pp. 486–519, 2011.

[57]   A. Ramezanpour, I. Mirzaee, D. Firth, and H. Shirvani, "A numerical heat transfer study of slot jet impinging on an inclined plate," *Int. J. Numer. Methods Heat Fluid Flow*, vol. 17, pp. 661–676, 2007.

[58]   M. Dianat, M. Fairweather, and W. P. Jones, "Predictions of axisymmetric and two-dimensional impinging turbulent jets," *Int. J. Heat Fluid Flow*, vol. 17, pp. 530–538, Dec. 1996.

[59]   M. Behnia, S. Parneix, and P. A. Durbin, "Prediction of heat transfer in an axisymmetric turbulent jet impinging on a flat plate," *Int. J. Heat Mass Transf.*, vol. 41, pp. 1845–1855, Jun. 1998.

[60]   B. Sagot, G. Antonini, A. Christgen, and F. Buron, "Jet impingement heat transfer on a flat plate at a constant wall temperature," *Int. J. Therm. Sci.*, vol. 47, pp. 1610–1619, Dec. 2008.

[61]   T. J. Craft, L. J. W. Graham, and B. E. Launder, "Impinging jet studies for turbulence model assessment-II. An examination of the performance of four turbulence models," *Int. J. Heat Mass Transf.*, vol. 36, pp. 2685–2697, 1993.

[62]   J. E. Jaramillo, C. D. Pérez-Segarra, I. Rodriguez, and A. Oliva, "Numerical study of plane and round impinging jets using RANS models," *Numer. Heat Transf. Part B Fundam.*, vol. 543, pp. 213–237, 2008.

[63]   R. Oguic, S. Poncet, and S. Viazzo, "High-order direct numerical simulations of a turbulent round impinging jet onto a rotating heated disk in a highly confined cavity," *Int. J. Heat Fluid Flow*, vol. 61, no. October, pp. 366–378, 2016.

[64]   J. Ortega-Casanova and F. J. Granados-Ortiz, "Numerical simulation of the heat transfer from a heated plate with surface variations to an impinging jet," *Int. J. Heat Mass Transf.*, vol. 76, pp. 128–143, 2014.

[65]   J. Ortega-Casanova and F. Molina-Gonzalez, "Axisymmetric numerical investigation of the heat transfer enhancement from a heated plate to an impinging turbulent axial jet via small vortex generators," *Int. J. Heat Mass Transf.*, vol. 106, pp. 183–194, 2017.

4.6 CHAPTER APPENDICES
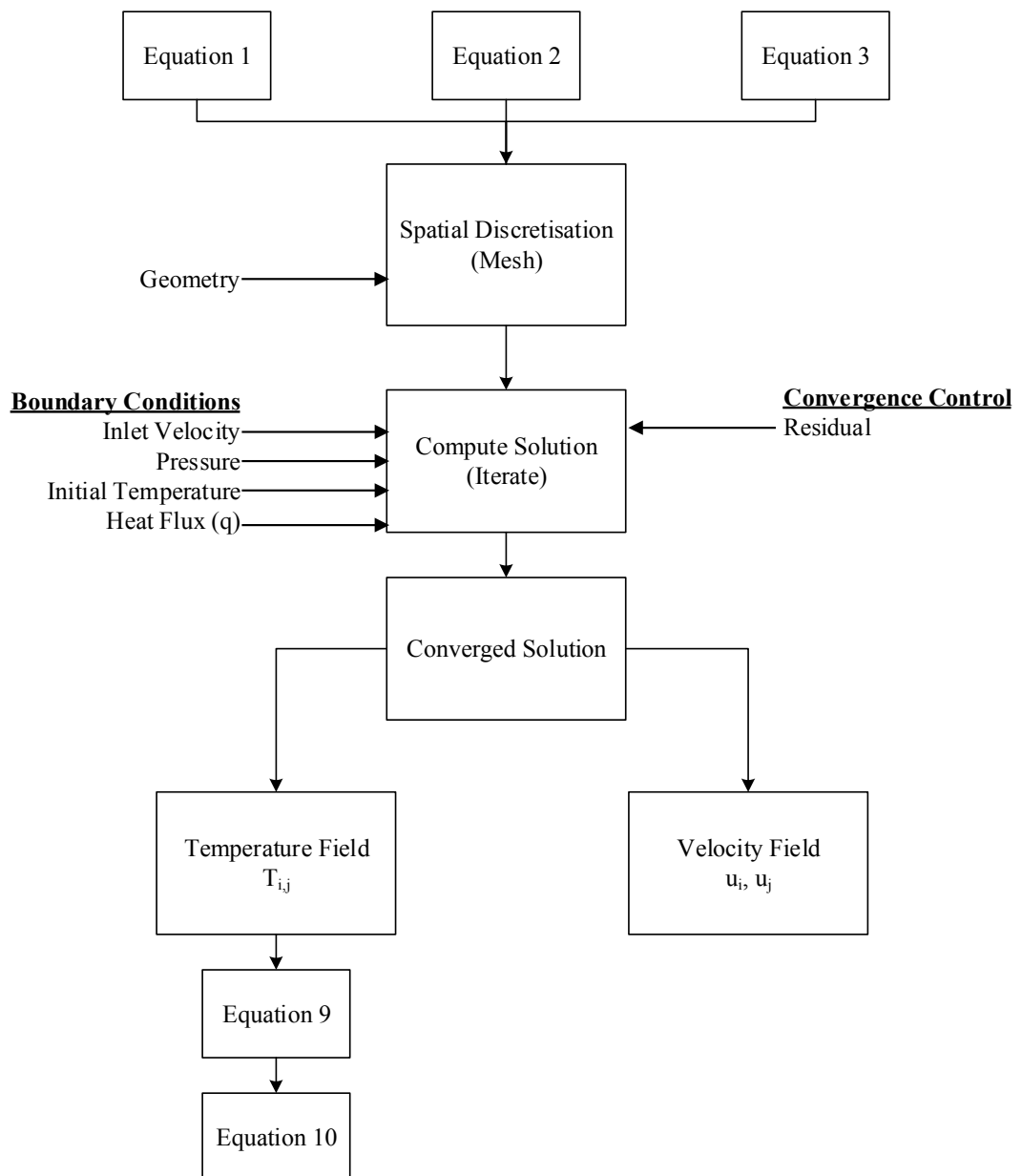
Figure 4-A1: Logic flow for the computation of the heat transfer and velocity field.

Benchmark Non-swirling Impinging Jets

Figure 4-A2 shows the computed Nusselt number distribution against measurements [12] for a non-swirling impinging jet at H/D=2, 4, and 6. At H/D=2 and 4, both experimental and numerical results demonstrate very good qualitative and quantitative agreement but the computations somewhat under-predict Nu in the wall jet region at r/D>1.5. At H/D=2 and 4, the experimental data from Ahmed et al. [12] as well as the computations show a (first) Nu peak at r/D=0.5-0.7 which is also noted by Buchlin [22]. At H/D=6 experiments show that the maximum Nusselt number occurs at the stagnation point while the numerical results obtained

using the k-kl-ω model show that the peak occurs radially away at r/D~0.2 from the stagnation point. However, these computations using the k-kl-ω model predict much better (at H/D=6) compared to the SST k-ω [45] which had significantly over predicted heat transfer (h) in the stagnation zone for non-swirling jets. Another observation which can be made from the present k-kl-ω computations is that the first Nusselt number peak appears to move closer to the stagnation point with an increase in the impingement distance. The experiments also showed that with further increases in H/D, the Nu peak approaches the stagnation point. In both the CFD and experiments Nu again increases from r/D>1.5 which reflects the transition to a secondary Nu peak as observed in the literature (Figure 2(a)). Both experimental and computational results show a plateauing in Nu at r/D>1.5, but with the transition to a secondary Nu peak for near field impingement (H/D=2). The secondary peak has been attributed to a transition in the flow from laminar to turbulent [9, 11], but there is a need for further modelling with LES/DNS to resolve the wall-flow features. Figure 4-A2 also shows that the Turbulent Kinetic Energy (k), just before the impingement plane (x/D=0.25), also experiences peaks at locations similar to those for Nu. These observations indicate that upstream turbulence influences the uniformity of impingement heat transfer (Nu peaks).

To add further clarity on the flow conditions upstream of the impingement plane which leads to the exhibited Nu distributions, Figure 4-A3 shows the computed velocity (<u>, <v>) and Turbulence Kinetic Energy (k) fields in the non-swirling jet (S=0). These results indicate that jet divergence near the impingement plane appears to start near r/D=0.5. In this context the stagnation zone where the jet has <u> and <v> ~0 spans r/D=0 to 0.5. As the jet then spreads radially outward this is followed by the wall jet region where <v> picks up in the vicinity r/D=0.5 to 1.0. This appears to signify that the start of the wall jet region overlaps with the first observed peaks in Nu (Figure 4-A2). Also of interest is the observation that for H/D=6 the regions of high turbulent kinetic energy spread much closer to the stagnation point (at the impingement plane) compared to H/D=4 and H/D=2. This closer proximity of (higher) k to the stagnation point is reflected in Nu peaks (Figure 4-A2) which also move closer to the stagnation zone.
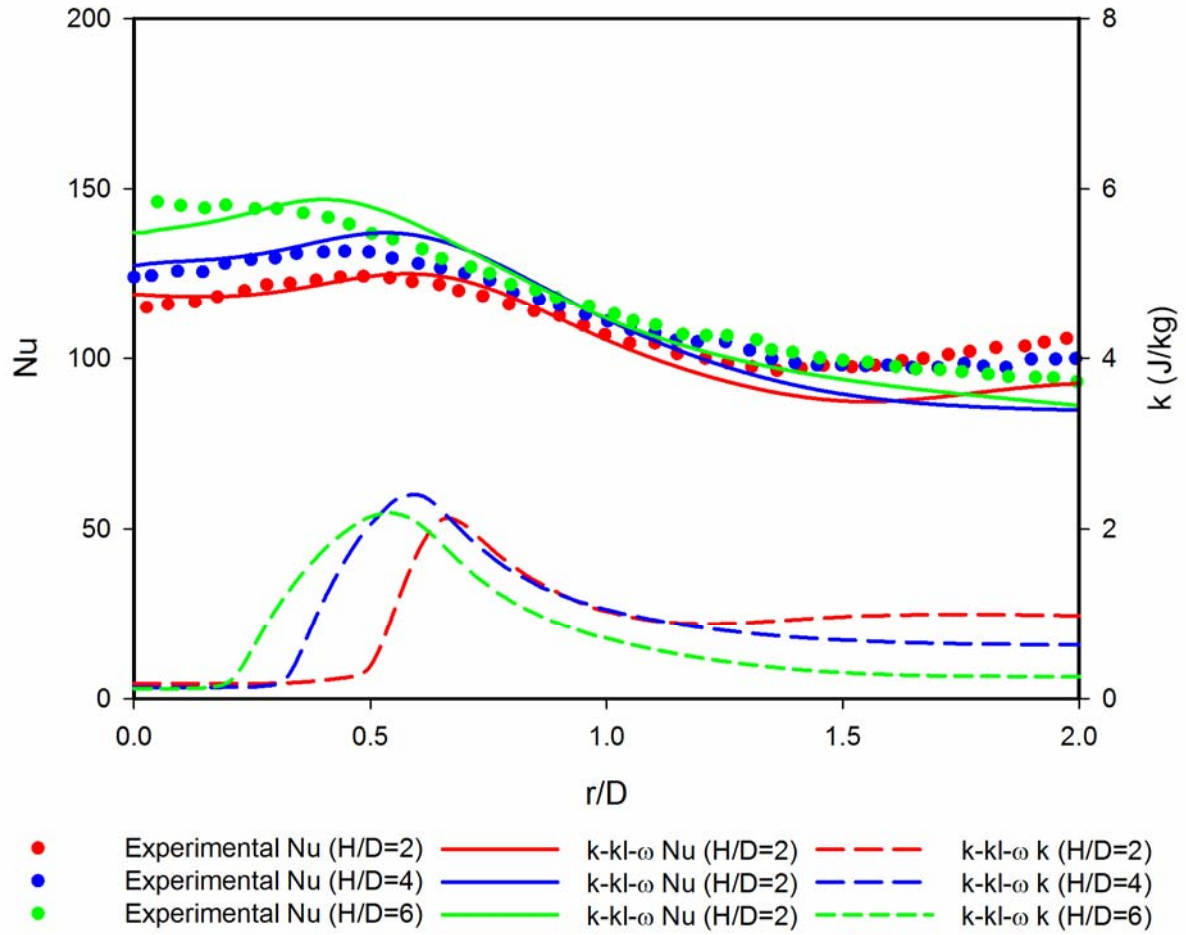
Figure 4-A2: Computed Nusselt number (at the impingement plane) and turbulent kinetic energy (at x/D=0.25 from the target surface) in non-swirling jets (S=0). Experimental data [54] is also shown for validation.
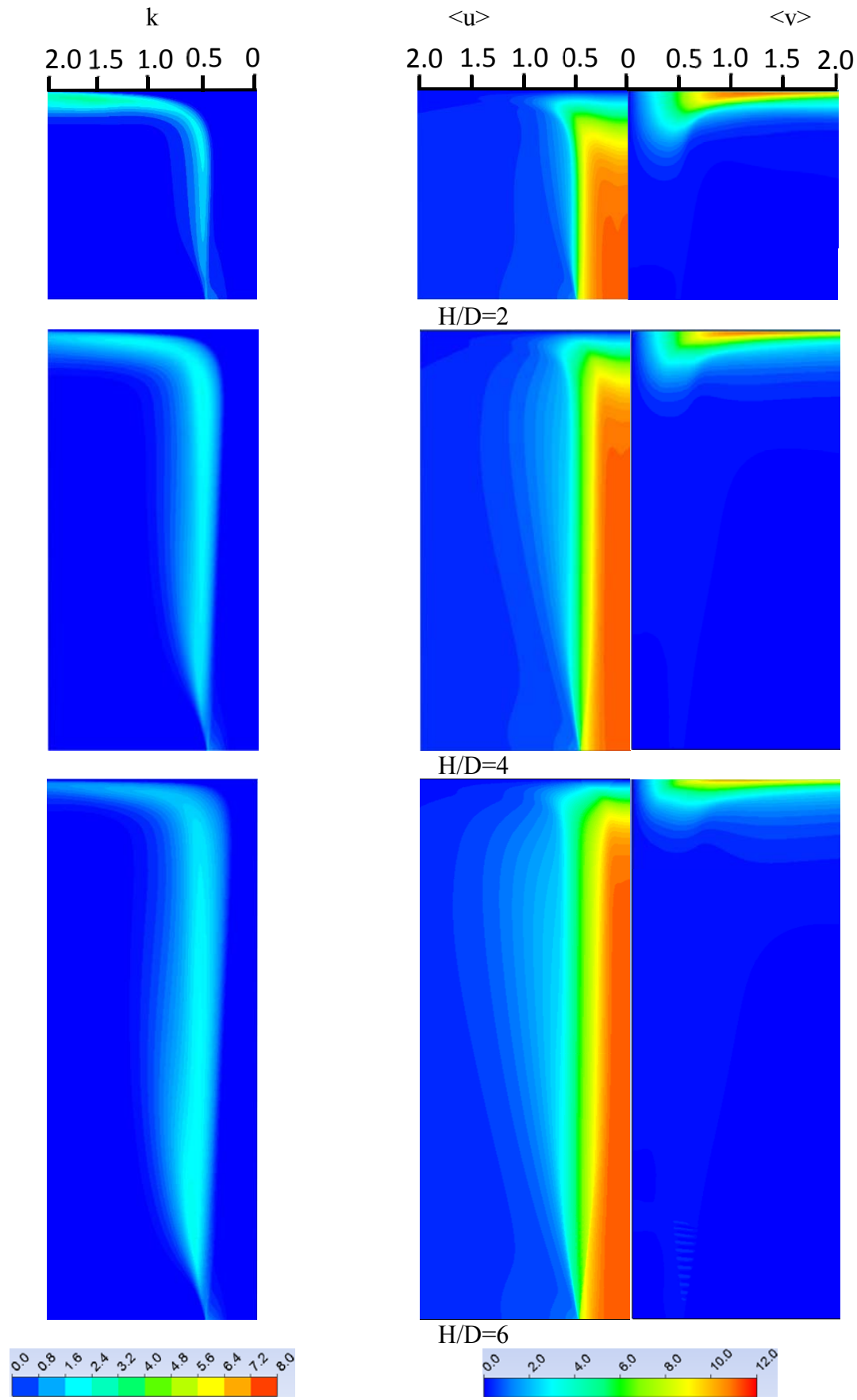
Figure 4-A3: Computed turbulent kinetic energy (k) and velocity component (<u>, <v>) for non-swirling jets (S=0) at H/D=2, 4, and 6.
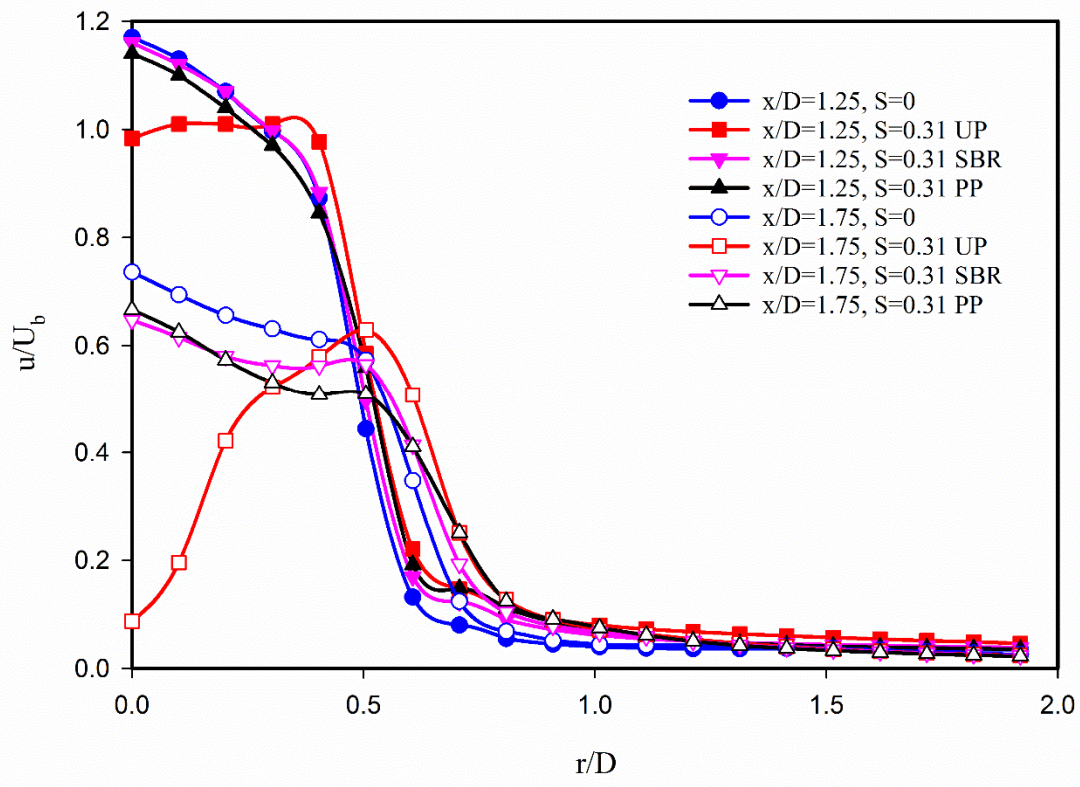
Figure 4-A4: Radial profiles for the jet width for swirling and non-swirling jets.

Chapter 5: Flow and Heat Transfer Characteristics of Turbulent Swirling Impinging Jets

The chapter addresses the gap discussed in RQ3, time-resolved Particle Image Velocimetry data is utilised to explore the flow features of turbulent swirling impinging jets. Three Reynolds numbers (Re=11,600, 24,600, and 35,000) and two swirl numbers (S=0.30 and 0.74) are tested against two impingement distances (H/D=2 and 4).

5.1 INTRODUCTION

Impinging jets, well known for their high heat/mass transfer rates in many practical applications, have been extensively studied in the literature for more than two decades [1–3]. Despite their numerous industrial uses such as in the cooling of turbine blades [4], paper drying [5], food processing [5], and glass tempering [2], the exact mechanisms by which swirl affects impingement heat transfer remain vague. Although correlations have been proposed to predict the rate and uniformity of impingement heat transfer, in both single and multiple imping jets [6], the way in which the complex fluid-heat transfer interaction is affected under swirl requires further insight. This may help explain the conflicting statements on whether swirl improves [5,7–9] or deteriorates heat transfer [10,11]. Central to this is to also understand the way in which the velocity field is affected (by impingement) and how it then influences the near impingement surface region when turbulent jets transition from non-swirling to swirling. Velocity field data derived from non-intrusive Particle Image Velocimetry PIV, when coupled with infrared imaging of the impingement surface, allow for such advances in our understanding of impingement heat transfer and is the focus of this paper. Figure 5.1 depicts a swirling impinging jet undergoing swirl induced vortex breakdown along with representative temperature and Nusselt (Nu) number distributions. When the axial velocity is superimposed with the rotational motion and the ratio of the azimuthal momentum to the axial momentum exceeds the certain level, vortex breakdown (recirculation zone or flow reversal) takes place [1,3].
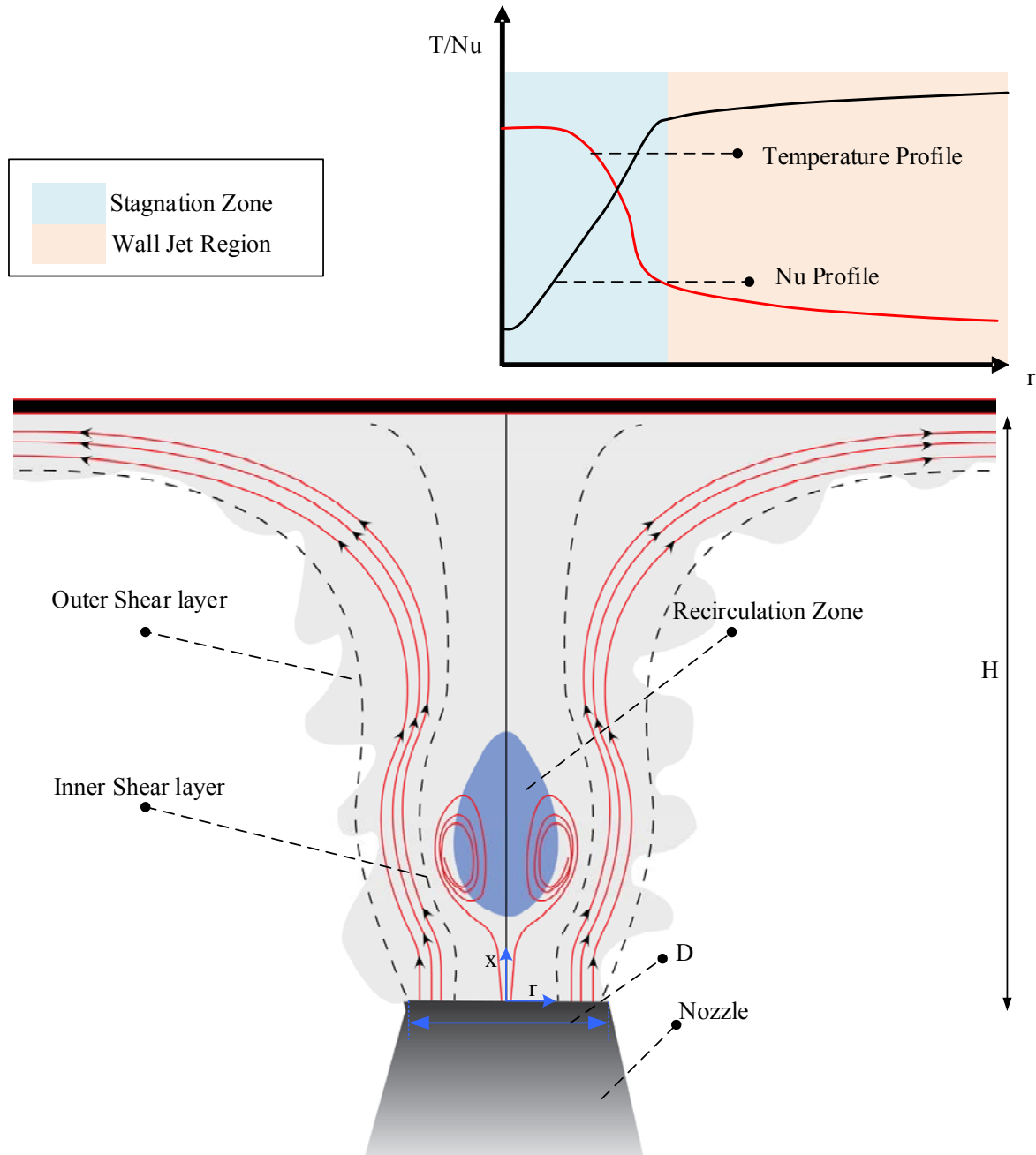
Figure 5.1: Sketch of a swirling impinging jet undergoing vortex breakdown with superimposed Nu and temperature profile.

The flow characteristics of a single circular impinging jet are well understood [12–14] and divided into three distinct zones: the free jet zone, the impingement or the stagnation zone, and the wall jet region. The attributes of each region depend on the operating conditions of the jet (Reynolds and swirl numbers), the nozzle diameter, and the impingement distance [10]. The impingement and the wall jet regions are generally taken as being (distinct) in terms of their shear stress and heat transfer characteristics [15,16]. The way in which these characteristics

vary (increase, decrease) however varies. These differences in behaviour lead to non-uniformity in the resulting heat transfer which is sometimes undesirable in some applications. For example, chemical vapour deposition requires uniform mass transfer over a surface just as electronics cooling requires relatively uniform surface heat transfer [17]. Most impinging jet research to date has addressed non-swirling turbulent jets, which are far less complex than swirling jets. In this context, flow behaviour at the free jet region [18], impingement zone [19], and wall jet region [20] has shown that the wall jet region consists of laminar, transitional, and turbulent regime [21]. Whilst swirl alters the impingement characteristics, most heat transfer characteristics [22–24] have not been coupled to flow features at the impingement plane, with the exception of some CFD predictions which have not been validated against velocity field measurements [25–27]. As such, the intricacies of the flow domain need to be investigated hand-in-hand with the resulting heat transfer. In this regard, swirl can be obtained using two different methods, i.e. geometrically and aerodynamically. Geometrical swirl can be created using helical inserts [7,19,28], twisted strips [8,29], or orientated blades [30,31]. Aerodynamic swirl is induced into an axial flow through adding tangential ports/nozzles. The advantage of aerodynamic swirl over geometric swirl is that swirl intensities that rely on the ratios of tangential to axial velocity at the exit plan can be changed independent of Reynolds number (Re). Additionally, the emerging swirling jets do not bifurcate creating a multi-zoned heat transfer behaviour [10]. The latter behaviour further complicates any interpretation of the interaction between the velocity field and heat transfer process. The present study uses aerodynamic swirl.

With the above in mind, Huang and El Genk [32] studied the flow field and arising impingement heat transfer patterns in swirling jets (geometric swirl) using flow visualisations (smoke). They noted that the spiral motion widened the impingement and wall jet areas. Nozaki et al., [33] used PIV and LIF in low Reynolds number turbulent jets (Re=4,000) at low-to-medium swirl (S=0.3 and 0.43). They reported that with the increase in swirl, the radial width of jets stretches and contributes to the heat transfer coefficient over a stretched impingement region. By utilising PIV and LDV, Abrantes et al., [34] also studied the flow field and heat transfer characteristics of swirling impinging jets in the near field at H/D=2 (Re=21,000, S=0.5). They observed the recirculation zone at the stagnation region was radially displaced. They also measured and correlated, turbulent quantities with the heat transfer data to link the radial peaks in the Nusselt number distribution with the measured peaks of turbulent velocity and its fluctuations. They measured time-averaged flow features and did not discuss

143

the time and length scale of fluctuations. Ianiro and Cardone [35] partially explained the reasons for the high heat transfer rate at the impingement plate from the literature by looking at the flow features for water jet using tomographic PIV, but their swirl was generated by inserts which introduced the more complexities into the flow. The swirl generator divided the flow into four discrete flow streams due to the central blockage. They observed that with the increase of swirl the arrival velocities at the impingement decreases and the jet width increases. They detected small turbulent structures in the outer shear layer and in the inner reversal zone for swirling jets when compared to non-swirling jets. It is also inferred that those small structures allow the turbulence penetration into the turbulent boundary layer development starting from the jet impingement region. To the author's knowledge, no study investigated the flow features of aerodynamically generated swirling impinging jets along with flow reversal (vortex breakdown). Few studies [36,37] explored the flow characteristics of aerodynamically generated swirling jets by utilising four tangential ports instead of three. They have investigated time periodicity (precessing core vortex) and vortex breakdown, whilst in this study time-averaged flow field is analysed with the vortex breakdown. Initially, Fast Fourier Transformation (FFT) check was employed to the hotwire anemometry data and no frequencies offshoots were detected.

Part of the challenge of investigating the interplay between the velocity field and heat transfer distribution in turbulent jet impingement stems from the complex flow fields involved. Swirling free jets typically undergo flow transitions including Vortex Breakdown (VB) and Precessing Vortex Cores (PVC, [38–40]). In the former, a sudden change of the flow domain leads to the formation of a stagnation zone or a region of reverse flow on the centreline [41]. Different shapes of vortex breakdown have been proposed and their likely mechanisms defined[42]. Vortex breakdown and its structure have also been addressed by numerous theoretical and numerical studies[43–46], whilst also acknowledging Benjanim's theory [47] which suggests that vortex breakdown is not a result of any flow instability, but instead a shift from one dynamically conjugate state to another. It has been shown that swirl intensity is not the only influential parameter [38–40,48,49].

The aim of the present paper is to identify how impingement affects the behaviour of swirling jets, with particular focus on the flow domain and resulting heat transfer. It uses PIV to resolve a range of turbulent swirling jets at three Reynolds numbers (Re=11,600, 24,600, and 35,000), over both low swirl (S=0.3±0.03) and high swirl (S=0.74±0.03). The distinction between "low"

144

and "high" here is not based on the (abstract) value if S, but rather on earlier observed heat transfer characteristics that show distinct behaviours between these two conditions, in both steady state [23,24] and transient impingement behaviour [50,51]. The extensive data set used in the present work (supported with Supplementary Materials) allows the construction of a much clearer understanding for the role of impingement. The velocity field data which is used as a basis for the analyses covers two impingement distances, spanning the near- and mid-field (H/D= 2 and 4) and is correlated to (spatially) resolved heat transfer characteristics originally acquired using Infra-red imaging (thin foil film technique).

5.2 METHODOLOGY

Figure 5.2(a) shows the assembled PIV system whilst Figure 5.2(b) shows a close-up view on the jet nozzle and its multiple entry ports. The swirl nozzle, CTA system, and infrared imaging methods used have been well detailed elsewhere [23,24,50,51] and will only be briefly noted here. The PIV system, the image processing methodology used, as well as the various parameters investigated will be given in more detail. Earlier experiments on this nozzle have already resolved the transient and steady-state heat transfer behaviour from turbulent swirling impinging jets[23,48,51], but without any velocity field data.

5.2.1 Swirl Nozzle

Turbulent jets are produced by feeding compressed air (room temperature) to the nozzle through a series of flow meters designed to independently control the axial and tangential streams. In this way, the flow meters allow various Reynolds and Swirl numbers to be attained (independent of each other) at the nozzle exit plane. At that location (x=0mm), the 40mm (D) nozzle has a sharp (~0.2mm) peripheral edge designed to minimize vortex shedding from this small margin at the exit plane. In the results, the impingement plane is positioned at two different locations which are reported in terms of H/D, where H is in the streamwise direction.

In the PIV experiments, part of air stream to each (of the three) tangential port is routed to multi-chambered cyclonic (particle) seeder (Figure 5.2(a)). No seeding was applied to each (of the two) axial ports as these were positioned further towards the lower end of the nozzle and below four honeycomb and wire mesh screens used for flow conditioning. Seeding the three tangential ports helps mix the emerging jet with illuminating PIV particles (de-agglomerated Al_2O_3, 0.3μm, make: Allied High Tech). As such, whilst PIV in the present set-up could only be conducted in low swirling and high swirling jets that rely on the use of the tangential (and axial) entry ports. Earlier results had shown the strong similitude between non-swirling (S=0)

145

and low swirling jets (S=0.34) for this nozzle [22,23], both in terms of impingement plane pressure and surface heat transfer. Results acquired with S=0.3 are therefore expected to be representative of non-swirling jets. Compressed air is supplied by a screw compressor (make: Atlas Copco, model: GA15-10) having a built-in dryer and filter.
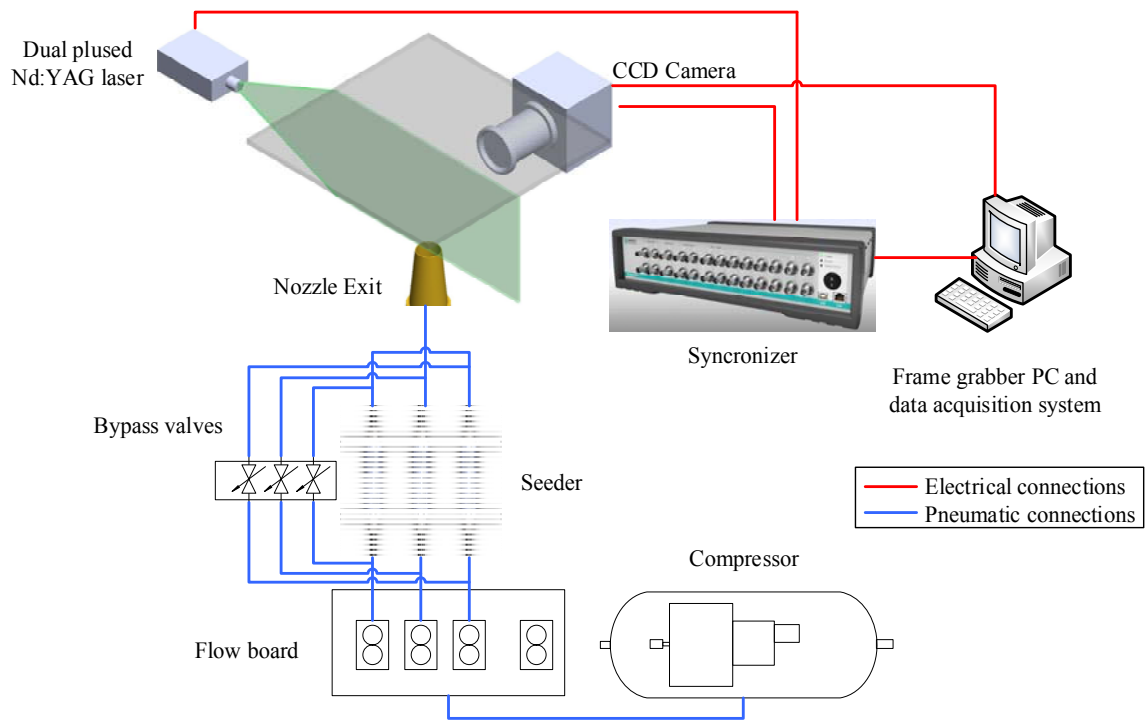
(a)
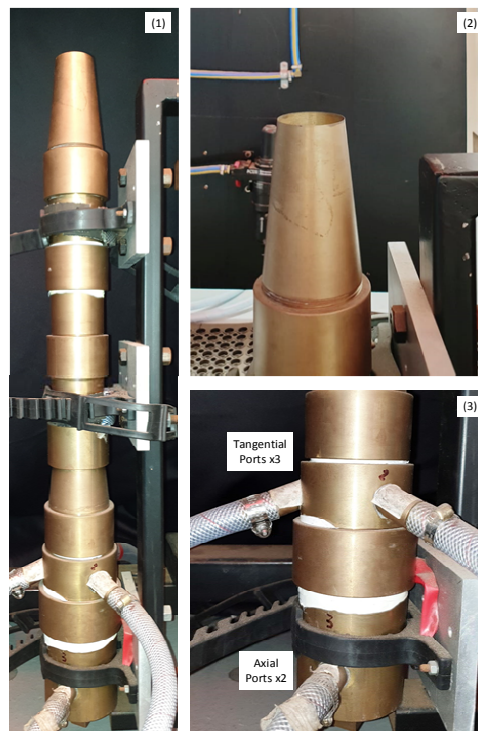
(b)

Figure 5.2: (a) Schematic diagram of the experimental setup; (b) 1-Jet nozzle, 2-axial and tangential inlet ports, and 3-knife-edge nozzle exit.

5.2.2 Constant Temperature Anemometry

Constant Temperature Anemometry (CTA) is used to measure axial (u) and tangential (w) velocity components at the nozzle exit plane (x=1mm). The system consists of three CTA channels (model: 90C10) and a temperature module (make: Dantec Dynamics, model: 90C20), all assembled into the Streamline mainframe (make: Dantec Dynamics model: 90N10). Hotwire probes are calibrated before measurements using an automated calibrator (model: 90H10) supplied with an air filter (model: 90H04). The effect of temperature variations during testing were also corrected from a system temperature probe [52].

An x-wire probe (miniaturized dual sensor, model: 55P61) was used to establish the boundary conditions. The experimental uncertainty of the hotwire measurements for swirling jets has already been estimated as 4% [53]. Figure 5.3(a) and (b) present the radial distribution of axial and azimuthal (tangential) velocity components, whilst Figure 5.3(c) gives the turbulent kinetic energy at the nozzle exit measured from fluctuations of axial and azimuthal velocity components using Equation (10). Notably, whilst the swirl number is defined based on the ratio of (bulk) tangential to axial velocities at the exit plane, the radial distributions of (u) and (w) at x/D=0.012 also show the spatially resolved S (localised swirl intensity at the nozzle exit) is also fairly uniform across r/D. Table 5.1 presents the experimental conditions along with the average values of axial velocity, tangential velocity, and normalized turbulent kinetic energy.

Table 5.1: Experimental conditions (S, Re).

Re	S	U_b (m/s)	W_b (m/s)	$\overline{k}/U_b$ (m/s)	VB
11,600	0.30	5.03	1.63	0.057	No
	0.74	5.08	3.75	0.239	Yes
24,600	0.30	9.10	2.81	0.141	No
	0.74	11.55	8.36	0.776	Yes
35,000	0.30	13.14	3.5	0.154	No
	0.74	13.71	10.51	0.451	No
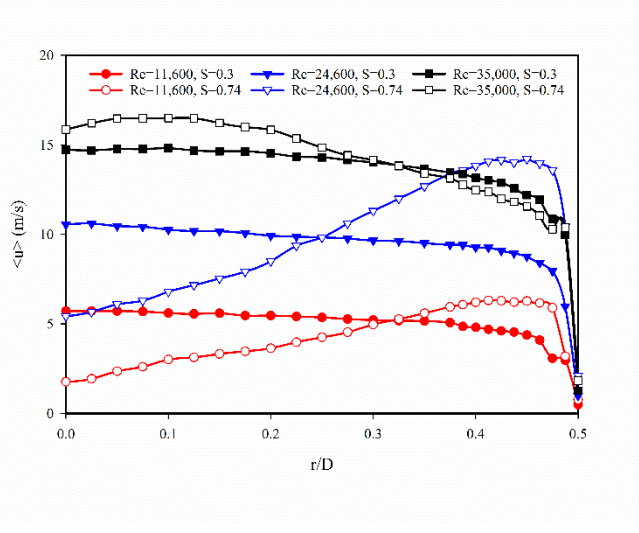
(a)
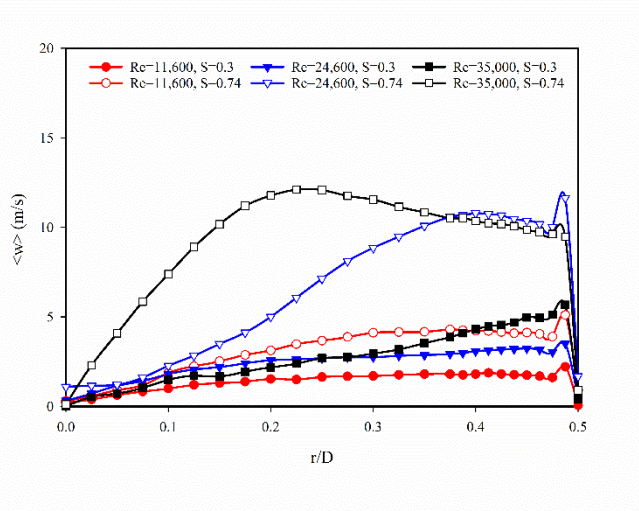
(b)
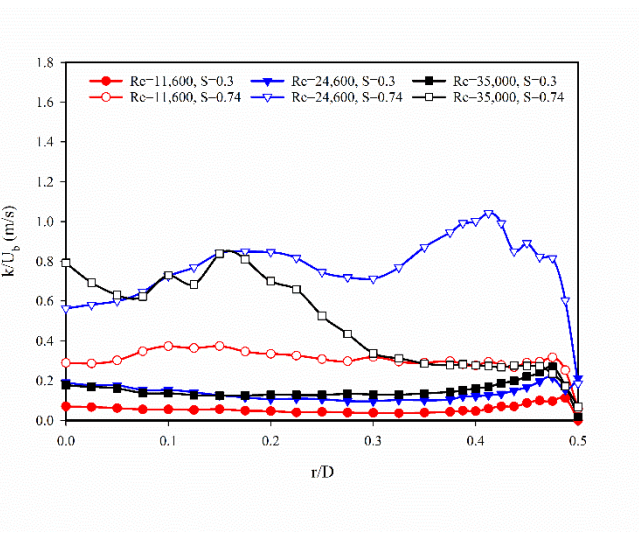
(c)

Figure 5.3: Normalised (a) mean axial velocity, (b) Mean tangential velocity, and (c) Turbulent kinetic energy at x/D=0.012.

5.2.3 Particle Image Velocimetry

The laser source was an in-line dual-pulsed Nd:YAG laser (make: Dantec Dynamics, model: Dual Power 200-15) having 200mJ/pulse at λ=532nm. Image acquisition was accomplished with a monochromatic CCD camera (make: Dantec Dynamics, model: Flow Sense EO 16M-9) having a resolution of 4920 x 3280 pixels and coupled with a Carl Zeiss (T*1.4/50) lens having a 50mm focal length. The laser and camera were positioned orthogonal to each other with their line of sight passing through the nozzle axis. For each experiment, a calibration image was acquired in order to convert pixel sizes into the physical distance (0.04mm/pixel). All raw PIV images were acquired and post processed using Dantec Dynamics's (OEM suite) DynamicStudio 5.1. Table 5.2 summarises the parameters for the PIV camera and laser. For the PIV testing, the thin metallic stainless steel foil (used in the thin foil technique for heat transfer data) was replaced with a 10mm Perspex impingement plate. This surface was coated matt black paint to minimize laser reflections during the PIV tests. Whilst this successfully minimised surface reflections, some reflections were still observed from the vicinity of the impingement surface if PIV illuminating particles were on the surface. PIV image data acquired near the exit plane of the nozzle exit lane (for x<3mm, x/D<0.08) as well as near the impingement plate were thus rejected due to excessive (direct, indirect) laser reflections. Shot-to-shot laser pulse timing was optimized (by validating PIV measurements with CTA data). Values used were 10μs for both Re=11,600 and 24,600, as well as 5μs for Re=35,000.

Table 5.2: PIV camera and laser settings

Camera resolution	4920 x 3280
Image area	210mm x 141mm
Region of interest	160mm x 120mm
Interrogation area	Min: 16 x 16 Max: 64 x 64
Interrogation overlap (horizontal and vertical)	25%
Time between laser pulses	5-10μs
Laser sheet thickness	< 2mm

5.2.4 PIV Data Processing

Image backgrounds were first removed before applying the adaptive cross-correlation algorithm. The three passes adaptive PIV algorithm (64 x 64, 32 x 32, and 16 x 16) along with peak validation and 25% overlap area were used to calculate the instantaneous velocity field for an image pair. Fixed errors associated with the PIV system, and which contribute to the relative uncertainty in the velocity magnitudes, were estimated at around 2% [54]. Time

intervals between (two) successive camera frames and laser pulses was calculated in such a way that all seeding particles did not leave the interrogation window (Table 2) during this period. Numerous steps and filters are applied to acquire a time-averaged flow field with details provided in the Supplementary Material (Figure 5-A1). In acquiring the PIV image data, results are presented over two nozzle diameters (x/D=2) in free jets as well as those impinging over H/D=2 and 4. Keeping the image (laser sheet) height constant allows for the laser sheet intensity (for the same camera pixel pitch) to also remain unchanged throughout the experiments.

Prior to reporting any results, checks were applied to determine the number of images needed to accurately predict the time-averaged flow field. The method proposed by Stafford et al. [54] was used to calculate the residuals of mean-averaged quantities using:

$$Residuals\ (\%) = 100\left(\frac{\overline{X}_{N,max} - \overline{X}_N}{X_{ref}}\right)$$
(5-1)

where $\overline{X}_{N,max}$ is the any parameter calculated from the maximum captured raw images data and $\overline{X}_N$ is the corresponding calculated parameter form considered raw images data (in this case $\overline{X}_{N,max}$ is considered to be equal to X_{ref}). At the highest Reynolds number (35,000) chosen, residuals were monitored in the potential core (r/D=0, x/D=0.15) and the stagnation region (r/D=0, x/D=1.85). In these analyses, the highest Reynolds number (Re=35,000) jets were selected as they the slowest convergence rate compared to lower Reynolds numbers (Re=11,600 and 24,600). The convergence of residuals is shown in Figure 5.4(a) and reveals that around 600 image pairs provided acceptable time-averaged flow field data for all the tested cases. Whilst the literature published on swirl jet impingement has not indicated their time-dependant behaviour, preliminary checks were also done in the present study to identify whether any time periodicity existed to the extent that they would affect the steady-state flow field data reported. Figure 5.4(b) gives data from one condition (x/D=1.00, Re=11,600, S=0.74, impinging) and shows that varying the laser and camera acquisition frequencies in these non-phase locked experiments does not lead to any changes in mean velocity. Figure 5.4(b) also infers that the use of differing frequencies does not lead to appreciably different time-averaged velocities. This is likely to indicate the absence of any appreciable time periodicity affecting the time-averaged PIV results presented. This however requires further investigation. Similar findings were also observed at other conditions. As such, in each test, and for approximately

10min, 640 images pairs were acquired at 1Hz in order to produce uncorrelated statistically independent vector (u and v) maps. An assumption of random sampling is valid since sampling time is much larger than the integral time scales of swirling jet estimated by the convective time scale [55]. The systematic/bias error in PIV can be caused by numerous factors; laser sheet thickness, camera setup, calibration setup, etc. and evaluation methods as well. The random error or experimental repeatability for the time-averaged flow field is quantified for the current experimental setup around 5% including the propagating error. For this quantification, the adaptive method is described in Particle Image Velocimetry: A Practical Guide [56]. As it is a common understanding that the measurement can have low random errors (precise) but large bias errors (inaccurate). The velocity magnitudes from the PIV measurements were verified against the CTA data.
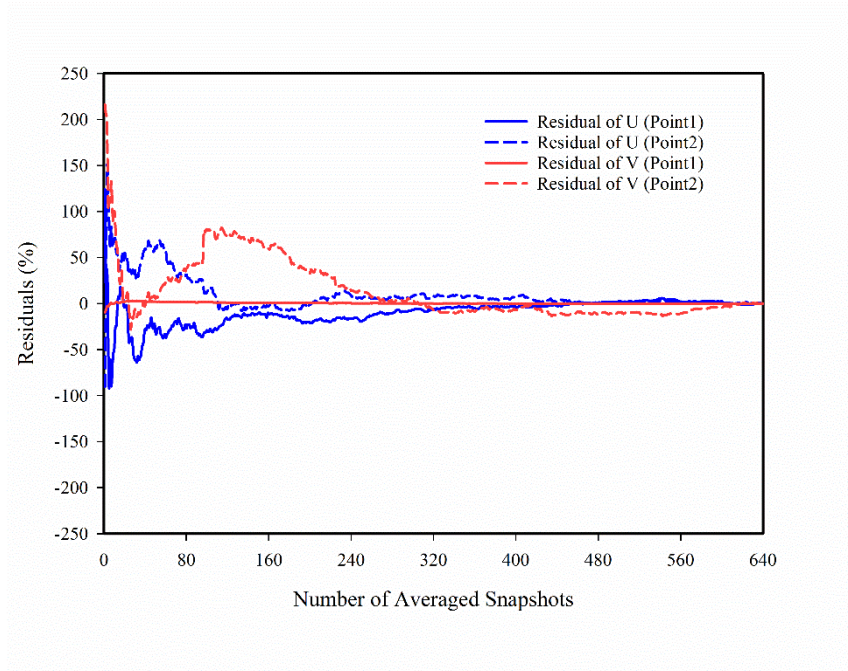
(a)
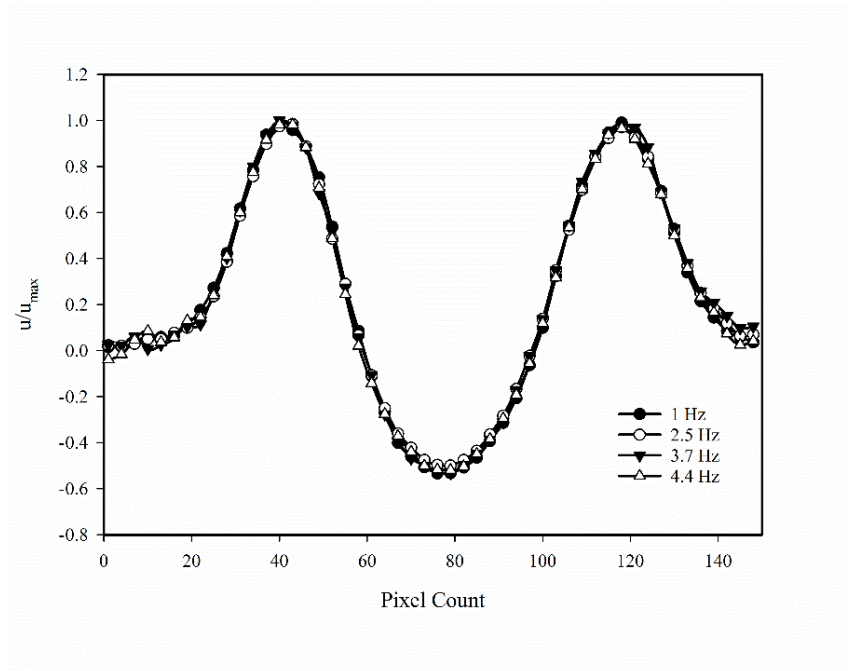
(b)

Figure 5.4: (a) Effect of number of PIV image pairs on the mean axial and radial velocities at r/D=0 and x/D=0.15 and 1.85. (b) Effect of image acquisition frequency on the steady-state flow field data (x/D=1.00, Re=11,600, S=0.74, impinging jet).

Figure 5.5 presents the PIV raw image data along with the image processing steps applied for a single pair of images. The velocity magnitudes which were calculated using the adaptive PIV algorithm are shown in the colour contour and vector maps. The left side images represent the measurement for low swirl (S=0.30) and the right-side images depict higher swirl (S=0.74), both at Re=11,600. Whilst the role of swirl on the flow field will be discussed later, this data shows that acquired images contain sufficient particle density needed for PIV cross-correlation. In the instantaneous velocity contour, the jet shear layer can be seen with eddies formed by the surrounding air entrainment.
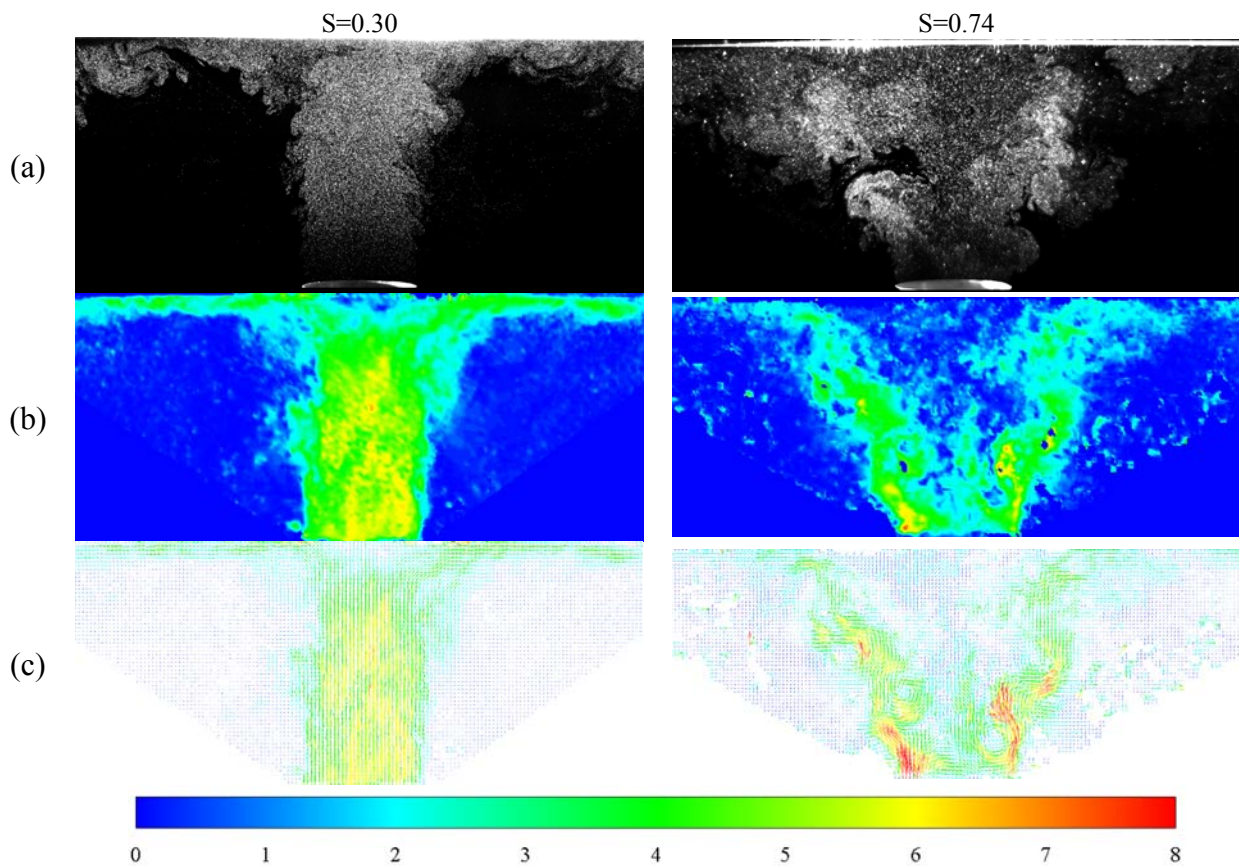
Figure 5.5: PIV image data (S=0.3, S=0.74) for H/D=2 (Re=11,600): (a) Single (instantaneous) raw image, (b) Post-processed contour map from adaptive-correlation (single image pair), and (c) Vector map from adaptive-correlation (single image pair).

5.2.5 Turbulent Jet Parameters

The following definitions of Reynolds and Swirl numbers are used in the current study, where U, D, μ, Q, and ν are the bulk normal velocity, nozzle exit diameter, dynamics viscosity, total volume flow rate (axial plus tangential), and kinematic viscosity respectively.

$$Re = \frac{\rho U_b D}{\mu} = \frac{4Q}{\pi D \nu} \tag{5-2}$$

$$S = \frac{W_b}{U_b} \tag{5-3}$$

Numerous definitions of Swirl number have been used in the literature [57]. This study considers it as the ratio of bulk tangential velocity (W_b) to bulk axial velocity (U_b). The U_b and W_b are estimated using Equation (5-4) and (5-5) from the CTA measurements at the nozzle exit [50,51].

$$U_b = \frac{2}{R^2} \int_0^R r\langle u \rangle dr \approx \frac{2}{R^2} \sum_{r=0}^{r=R} r\langle u \rangle dr \tag{5-4}$$

$$W_b = \frac{2}{R^2} \int_0^R r\langle w \rangle dr \approx \frac{2}{R^2} \sum_{r=0}^{r=R} r\langle w \rangle dr \tag{5-5}$$

The heat transfer coefficient (h) and Nusselt numbers (Nu) are defined through Equations (5-6) and (5-7) respectively. In this context, impingement plane heat transfer distributions with this nozzle acquired using infrared imaging and the thin foil constant flux heater method were used [23].

$$h = \frac{q - q_l}{T_w - T_{ref}} \tag{5-6}$$

$$Nu = \frac{hD}{\lambda} \tag{5-7}$$

The instantaneous local velocity components (u, v) for each images pair are calculated using the adaptive PIV method [56]. The time-averaged velocity magnitudes from instantaneous values were calculated using Equation (5-8).

$$\overline{U} = \frac{1}{N} \sum u_n , \overline{V} = \frac{1}{N} \sum v_n \tag{5-8}$$

Time-averaged velocity fluctuations (r.m.s) are estimated by exploiting Equation (5-9) over the N=640 captured pair of images.

$$\overline{u'^2} = \frac{1}{N-1}\sum \left(u_n - \overline{U}\right)^2 , \overline{v'^2} = \frac{1}{N-1}\sum \left(v_n - \overline{V}\right)^2 \tag{5-9}$$

The turbulence intensity in the axial (I_x) and radial (I_y) directions were evaluated from the fluctuations of axial (u`) and radial velocity components (v`) as expressed in Equation (5-10) and (5-11). The turbulence intensities (I_x and I_y) in the x and y directions are comparable, hence the assumption of isentropic flow can be made.

$$I_x = \frac{\sqrt{\frac{1}{N-1}\Sigma(u_n - \overline{U})^2}}{U_b} = \frac{\sqrt{\overline{u'^2}}}{U_b} \tag{5-10}$$

$$I_y = \frac{\sqrt{\frac{1}{N-1}\Sigma(v_n - \overline{V})^2}}{U_b} = \frac{\sqrt{\overline{v'^2}}}{U_b} \tag{5-11}$$

$$k = \frac{1}{2}[(\overline{u'})^2 + (\overline{v'})^2 + (\overline{w'})^2] \approx \frac{3}{4}[(\overline{u'})^2 + (\overline{v'})^2] \tag{5-12}$$

$$\omega_z = \frac{\partial V}{\partial x} - \frac{\partial U}{\partial r} \tag{5-13}$$

By assuming isotropic turbulence into the flow, the turbulent kinetic energy and the vorticity around the z-axis can be estimated using Equation (5-12)and (5-13) respectively.

5.3 RESULTS AND DISCUSSION

The role of impingement on the flow field, in both the upstream (near nozzle) and downstream (near impingement plate) areas, is analysed for turbulent swirling jets. The downstream velocity flow field is also correlated with emergent heat transfer characteristics.

5.3.1 Upstream Flow Field

Figure 5.6 and Figure 5.7 presents the centreline axial (u) and radial (v) velocities of six turbulent jets (Re=11,400, 24,000, and 35,000) covering two swirl numbers (S=0.3 and 0.74), in both free (Figure 5.6(a)) and impinging jets covering H/D=2 (Figure 5.6(b)) and H/D=4 (Figure 5.6(c)). This data provides insights into the role of geometrical parameters (H/D) as well as operating conditions (Re and S) on swirl induced vortex breakdown.

Whilst at low swirl (S=0.30) no negative centreline velocities are apparent, this indicating the lack of vortex break down for all H/D, Re, and S, the results do show that the length of potential core in the jet is longest in free jets where virtually no deceleration is observed. Interestingly, the strongest deceleration in impinging jets does not occur at H/D=2, where in fact the potential core only starts to deaccelerate from x/D≈1.00 since the lowest magnitude still in the 95% of nozzle exit velocity [6,59], but occurs at H/D=4 where the potential core is lost immediately after the exit plane. At this extended impingement distance, jets at the two lower Reynolds numbers investigated (Re=11,600 and Re=24,600) also show stronger deceleration compared to low swirl jets at the higher Re=35,000. Increasing the swirl number to S=0.7 causes more adverse changes to the centreline axial velocity where it becomes apparent that the for the lower Re=11,600, the strength of vortex breakdown increases as jets change from free, to impinging jets at H/D=2, and then reach H/D=4. In this regard, a stronger vortex breakdown is delineated by either more negative (u) or a wider range axial distance (x/D) over which (u) is negative [40]. Whilst the slightly greater Re=24,600 also leads to vortex breakdown in only some of the conditions observed in free jets (x/D>1), the strength of this is lower compared to Re=11,600 even at the extended impingent distance of H/D=4.

The centreline axial velocity component for low swirl are small, many studies have shown they are almost zero for the centreline velocity component. Here, the small induced swirl affect the radial component and increase the jet spread compare to the non-swirling case. This jet spread affects the low and moderate Reynolds number (Re=11,600 and 24,600) jet more when compared to Re=35,000. For the impinging jet, the jet spread for the moderate and high Reynolds number is more than the lower one, the downstream impingement affects the upstream values and increases the jet spread compared to the free jet.
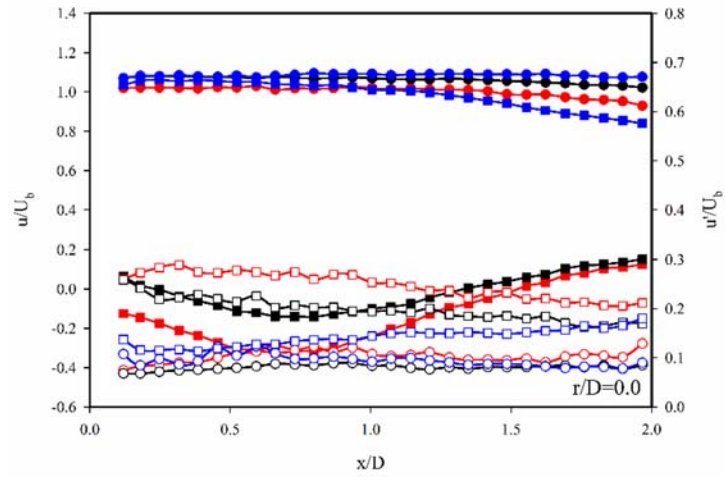
(a)
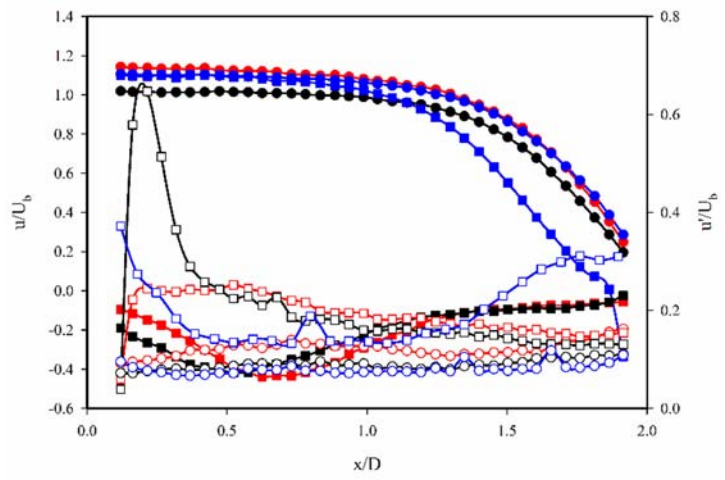
(b)
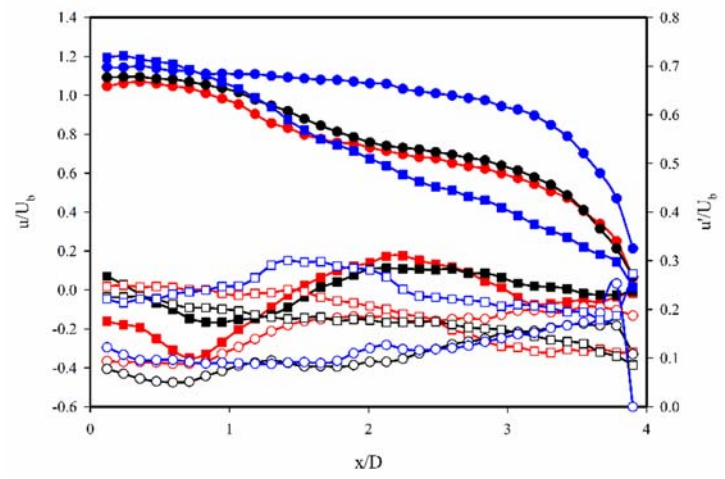
(c)
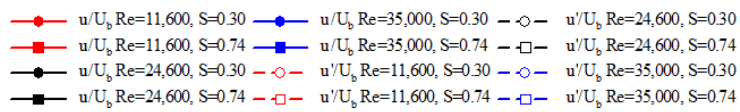
Figure 5.6: Centreline (r/D=0) axial velocity (u) profiles: (a) Free jet, (b) impinging jet at H/D=2, and (c) impinging jet at H/D=4.

158

(a)

(b)

(c)

v/U_b Re=11,600, S=0.30	v/U_b Re=35,000, S=0.30	v'/U_b Re=24,600, S=0.30
v/U_b Re=11,600, S=0.74	v/U_b Re=35,000, S=0.74	v'/U_b Re=24,600, S=0.74
v/U_b Re=24,600, S=0.30	v'/U_b Re=11,600, S=0.30	v'/U_b Re=35,000, S=0.30
v/U_b Re=24,600, S=0.74	v'/U_b Re=11,600, S=0.74	v'/U_b Re=35,000, S=0.74

Figure 5.7: Centreline (r/D=0) radial velocity (v) profiles: (a) Free jet, (b) impinging jet at H/D=2, and (c) impinging jet at H/D=4.

159

With the above in mind, Figure 5.8 and Figure 5.9 present contour plots for the first two nozzle diameters (x/D=2) at S=0.7 for the two Reynolds numbers (11,600 and 24, 600) where vortex breakdown was detected in free as well as impinging jets (H/D=2, H/D=4). Results show that jets at Re=11,600 exhibit stronger vortex breakdowns, which in all cases appear to end by around x/D=1.0. Additionally, whilst the shear layer in free jets appears to be maintained vertically upwards over x/D=2, impingement plates placed in the near field (H/D=2) cause a more abrupt and earlier widening of the jet. This earlier widening of the jet also leads to the central vortex breakdown bubble to spread radially outwards, compared to free jets and even those impinging at H/D=4. The observed asymme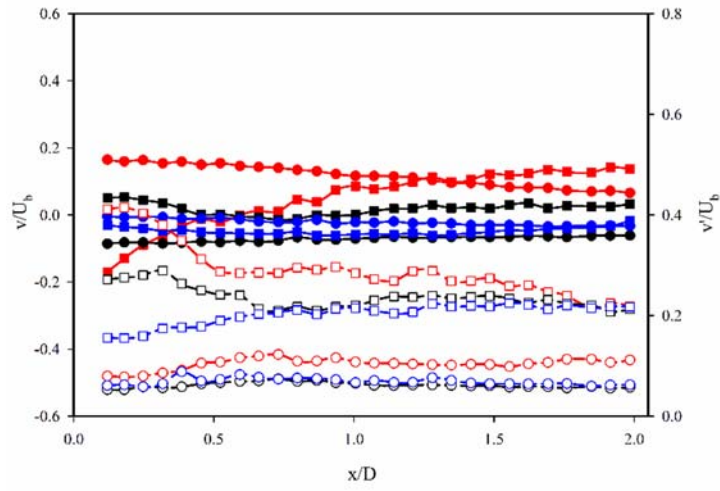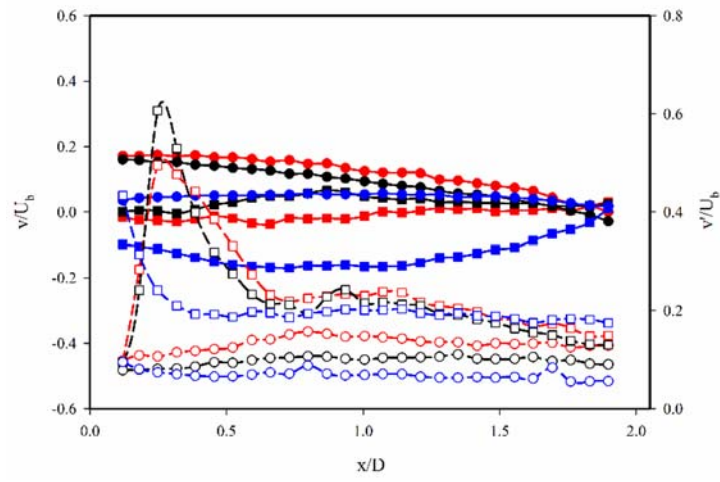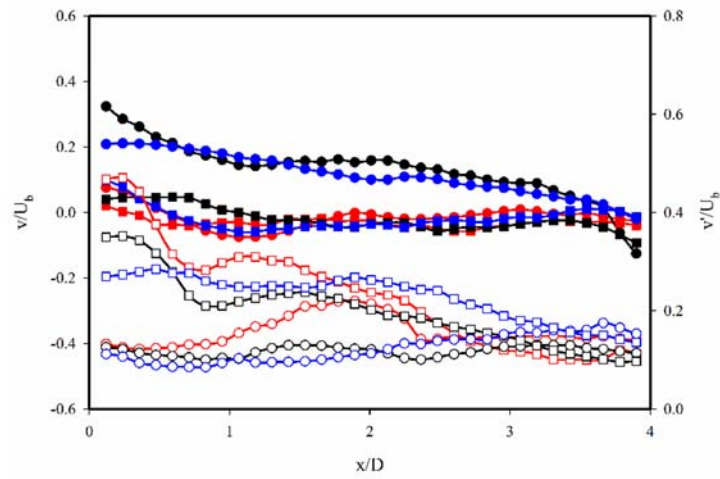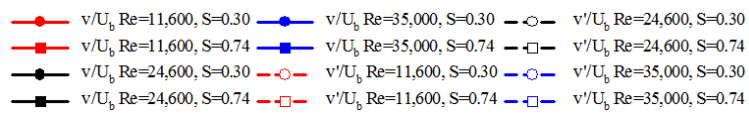try in contour plots could be resulted because of many parameters. For free jet, the vortex breakdown for low Reynolds number (Re=11,600) is stable and symmetrical compared to moderate Reynolds number (Re=24,600). The recirculation bubble at Re=24,600 seems unstable and asymmetrical, the vortex breakdown will vanish with the increase of Reynolds number for the same swirl intensity as observed in the case of Re=35,000.

The radial distribution of axial velocities (u) for these jets over there downstream locations (x/D=0.12, 0.5, and 1.00) is presented in the supplementary materials. Firstly, closer to the exit plane the axial velocities are comparable in free jets (Figure 5-A3) as well as impinging jets at both H/D=2 (Figure 5-A4) and H/D=4 (Figure 5-A6). Secondly, and at the slightly downstream distance of x/D=0.5, the earlier widening of the Re=11,600 and Re=24,600 impinging jets at H/D=2 leads to a broader shear layer, but the shear layer is comparable between free jets and those at H/D=4. For the low swirl, the axial velocity profiles almost look like top hat distribution and the jet width grows with the axial location due to the entrainment phenomenon through the shear layer of the jet. For the location x/D=0.12, the shear layer is positioned between the 0.4 < r/D < 0.5, further downstream the location of the shear layer shifted in the radial direction as the jet spread increases. In the low swirl, the velocity profiles looks like a q-vortex $(w(r)=(1-exp(-r^2))/r)$. Also within the supplementary materials, the radial distributions of radial velocities (v) over X/D=1.0 shows that at S=0.7 at H/D=2 (Figure 5-A5), the radial velocities are much stronger due to the earlier jet widening compared to the free (Figure 5-A3) and impinging jets at H/D=4 (Figure 5-A7). In summary, the effects of impingement are stronger in the lower Reynolds numbers tested at S=0.7, but more adverse for H/D=2 compared to H/D=4, with the latter showing greater resemblance to free jets.

For free jet, the axial component of the velocity is negative from the start (Figure 5.6(a)). For the low Reynolds number, the recirculation bubble sits inside the nozzle exit while for the moderate Reynolds number the axial velocity component becomes negative outside of the nozzle. The negative component of the velocity represents the radially inward flow can be seen from the direction of the vectors in the contour plots (Figure 5.8 and Figure 5.9). This recirculation zone for the free jet is stretched out to almost x/D=1.5. The vortex breakdown for low Reynolds number is much stronger and bigger in size when compared to the moderate Reynolds number when normalized with bulk axial velocity. The asymmetry in the vortex breakdown is less for the low Reynolds number in contrast to Re=24,600. The width of the recirculation zone for Re=11,600 and Re=24,600 spans -0.4 < r/D < 0.4 and -0.2 < r/D < 0.2 respectively. The open type of bubble exists for both boundary conditions [60]. The contour plots show that the recirculation zone for low Reynolds number is stronger and much circular in shape compared to the moderate Reynolds number. For Re=24,600, the recirculation zone is squeezed due to high velocities around it. It can be inferred that further increase in the velocity (Reynolds number) and its corresponding momentum clasped the recirculation zone and push away. This can be seen from the velocity data for Re=35,000 and S=074, no vortex breakdown is observed for the highest tested Reynolds number. The impingement alters the flow field characteristics for both H/D=2 and 4.
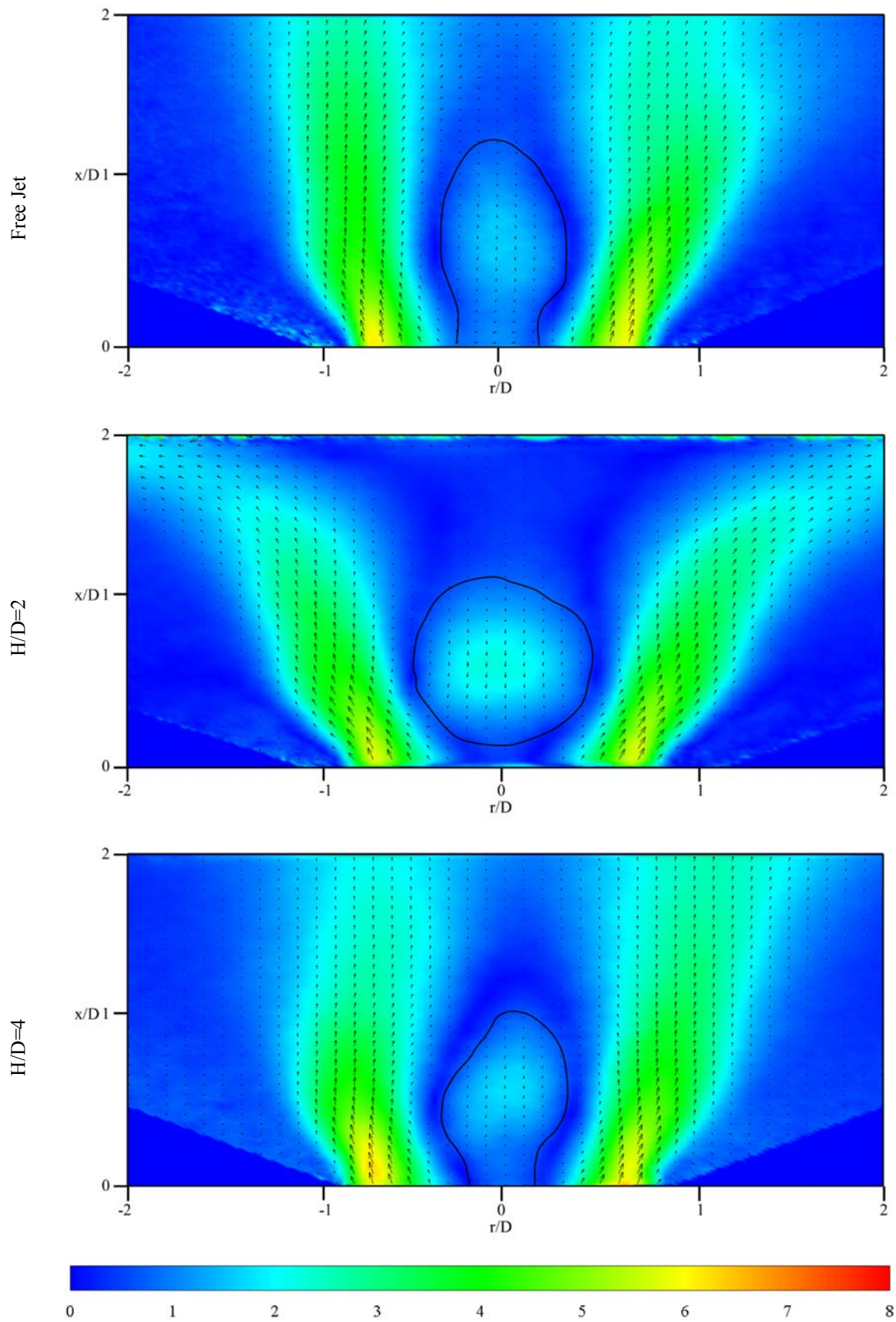
Figure 5.8: Contour plots for velocity magnitude (m/s) with superimposed directional vectors in free and impinging jets (at H/D=2 and H/D=4) for Re=11,600 and S=0.74. The approximate location of the zero velocity envelope in the vortex breakdown bubble is shown.
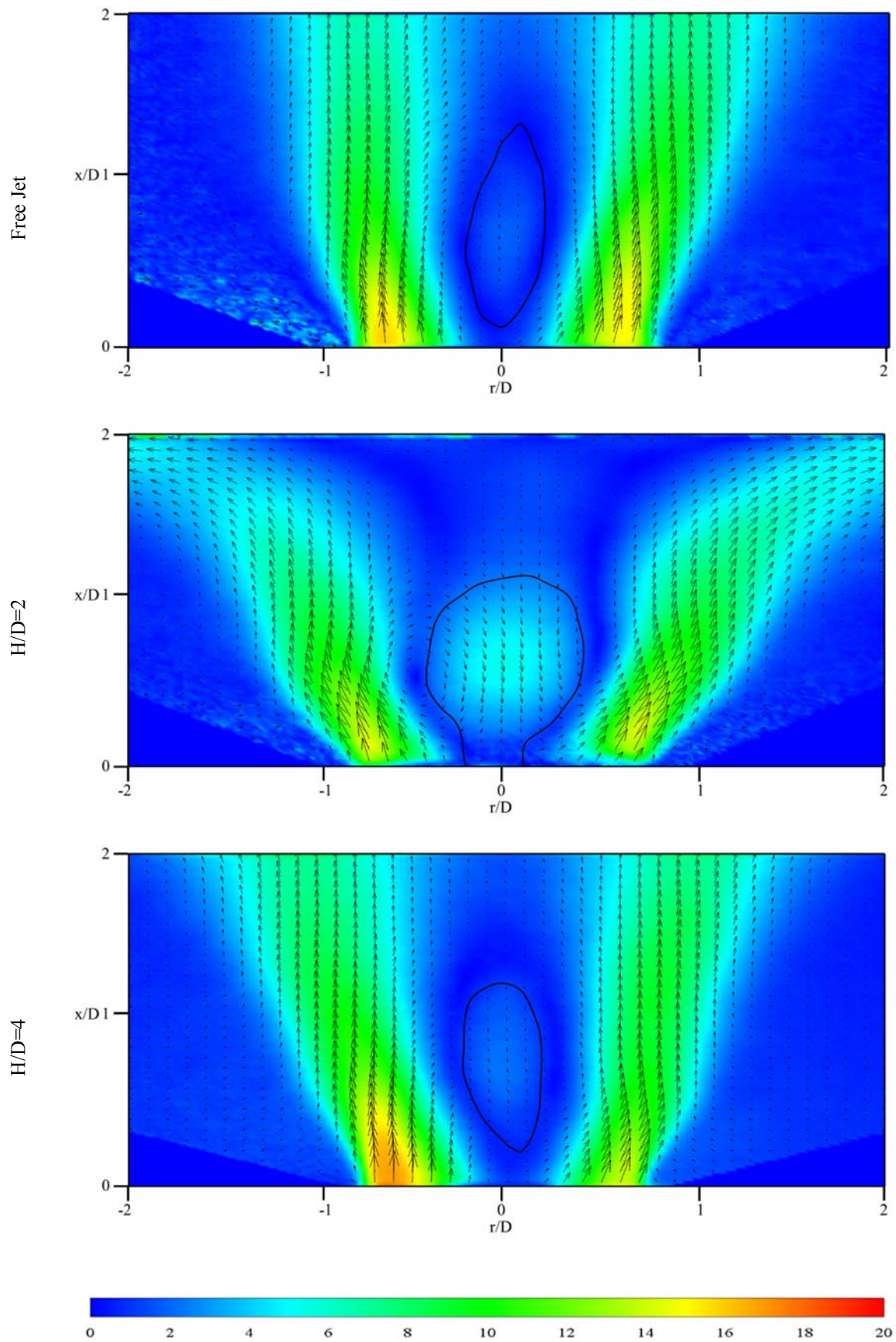
Figure 5.9: Contour plots for velocity magnitude (m/s) with superimposed directional vectors in free and impinging jets (at H/D=2 and H/D=4) for Re=24,600 and S=0.74. The approximate location of the zero velocity envelope in the vortex breakdown bubble is shown.

163

For near-field impingement, the flow around the vortex breakdown is not accelerated due to the bulging of the bubble, and flow around vortex breakdown does not squeeze it, while it moves away and forms the stagnation zone and wall jet region. The widening of the conical shape flow around the recirculation zone (Figure 5.8 and Figure 5.9) a little bit above and due to the low momentum of the flow impingement does not affect the flow dynamics too much at upstream for low Reynolds number. The width of recirculation zone is slightly increased contrary to free jet (-0.5 < x/D < 0.5). Overall asymmetry reduces with the impingement but similar observations can be made with a comparison between two Reynolds numbers. For Re=24,600, due to the high momentum, the bubble is pushed upstream in contrast to Re=11,600. The width of the bubble for the moderate Reynolds number is still thinner than the low Reynolds number. Figure 5.9 shows that for H/D=2, a portion of the recirculation zone is penetrated into the nozzle exit plane. The widening of the jet stream around the recirculation zone allows the bubble to grow in the lateral (radial) direction. For Re 24,600, small negative axial velocity stretches towards the impingement surface and looks like an upside-down toroidal shape. The strength of this toroidal shape is very weak compared to the main recirculation bubble.
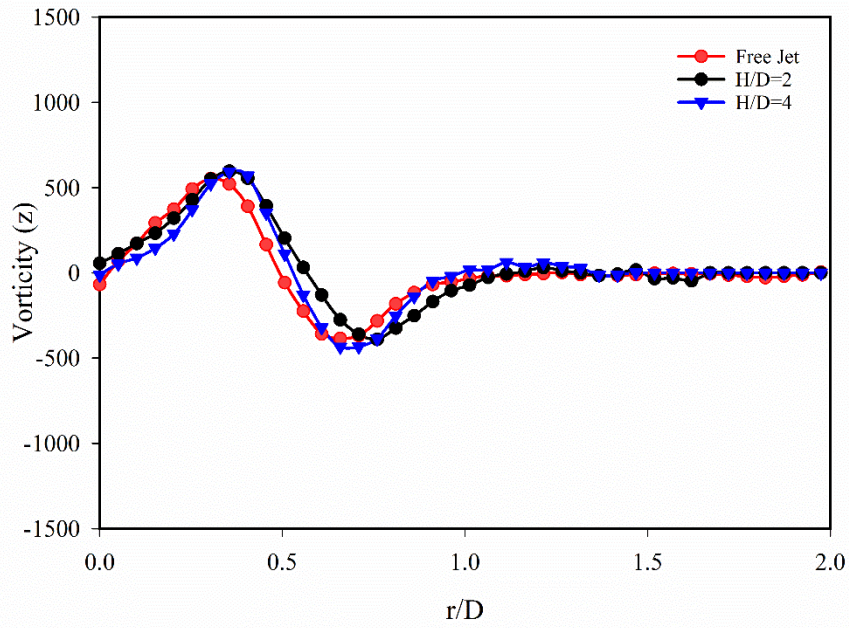
(a)
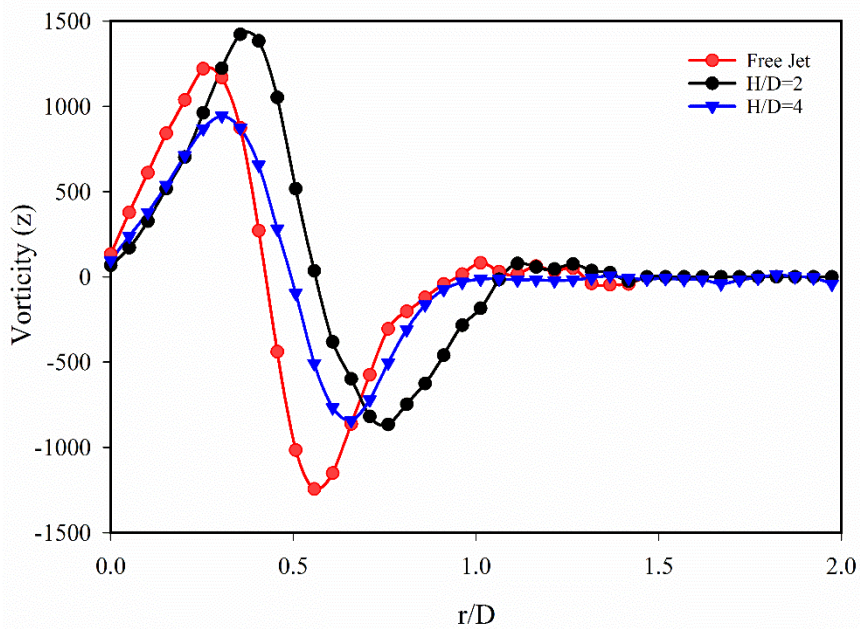
(b)

Figure 5.10: Radial vorticity (z) profile at x/D=1.00 for S=0.74, (a) Re=11,600 and (b) Re=24,600.

The PIV measurements for H/D=4 are taken in two segments. Firstly, the field of view covers the data for $0 \leq x/D \leq 2$ and the second set of measurements spans $2 \leq x/D \leq 4$. The approach is used to keep the constant laser sheet intensity and the same camera pixel pitch throughout the experimental data captured for this study. The contour plots presented in Figure 5.8 and Figure 5.9 for H/D=4 cover the flow field from $0 \leq x/D \leq 2$, near impingement data will be discussed in the later section. For H/D=4, for both Reynolds number, the recirculation bubble tends to achieve the shape similar to free jet. It can be deduced that further increase in the impingement distance, the effect of the impingement will vanish upstream. The width and height of the recirculation bubble are less than the bubble at H/D=2 and free jet respectively. Impingement affects the girth of the vortex breakdown significantly compared to its height. Irrespective of the impingement distance, the height of the recirculation bubble stays within $x/D < 1.5$. A similar observation can be made from Figure 5.10. Figure 5.10 presents the radial plot of vorticity around the z-axis (since 2D-2C PIV data is available). Overall, Re=24,600 has larger velocity gradients compared to Re=11,600, which was expected since the high Reynolds numbers are associated with high momentums. It is also observed that the impingement affects the width of the vortex breakdown for Re=24,600 when compared to Re=11,600. The fluctuations inside the bubble for Re=11,600 are lower than the Re=24,600. It indicates that the bubble at low Reynolds number is very stable and affects the flow like a bluff body at the centre of the nozzle, while at moderate Reynolds number the flow around the bubble is able to affect the size and shape of recirculation zone. For Re=35,000 and S=0.74, no recirculation zone or vortex breakdown is observed, but the axial and radial velocity profiles are different than the other boundary conditions discussed above. It can be surmised that the flow at this operating condition is not as stable as a low swirling flow but it also a pre-vortex breakdown regime. Time-resolved PIV data can reveal the existence of precessing core vortex (which is not in the scope of this study) since the impingement characteristics are similar to flow observed with the vortex breakdown at H/D=4 (will be discussed in section 5.3.2).

5.3.2 Downstream Flow Field and Heat Transfer

Figure 5.11 and Figure 5.13 present the velocity profile data along with heat transfer characteristics at the impingement surface. The axial and radial velocity profiles are extracted near the impingement surface (x/D=1.95 for H/D=2 and x/D=3.95 for H/D=4). Figure 5.12 and Figure 5.14 show the velocity magnitude contour plots for three Reynolds numbers (Re=11,600, 24,600, and 35,000) and two impinging distances (H/D=2 and 4) for S=0.30 and S=0.74 respectively.

166

Figure 5.11 shows that the major contributions of heat transfer distribution especially in the wall jet region are due to the radial velocity component since the axial velocity components are small when compared to its counterpart. For the low swirl, the stagnation zone has high heat transfer because at the impingement the axial velocity reduces drastically instigating a rise in the static pressure which causes the high convective coefficients. The stagnation pressure is the sum of static and dynamic pressure since at the impingement region the velocity is zero the stagnation pressure is equal to static pressure and causes the high heat transfer at the stagnation region. The pressure characteristics were measured previously for swirling impinging jets by Zahir et al. [22]. For the low impingement distance, with the increase in the Reynolds number the peak axial velocity shifts in the radial direction. The radial profile starts increasing as move from the impingement point to the wall jet region. The radial velocity reaches to maximum value corresponding to each Reynolds number and start decreasing as move farther in the radial direction. A similar observation is made by Fairweather and Grant [14], the mean radial wall jet velocity attains its peak at a very short distance from the stagnation zone. In contrast to the axial velocity profiles, the peak in the radial velocity profile shifts towards the stagnation zone. As the impinging distance increases the axial profiles flatten down and peak shifts in the radial direction.

Figure 5.11: Nusselt number at the impingement plane and (axial, radial) velocity profiles (x/D=1.95 for H/D=2, x/D=3.95 for H/D=4) before the impingement plane for S=0.30.
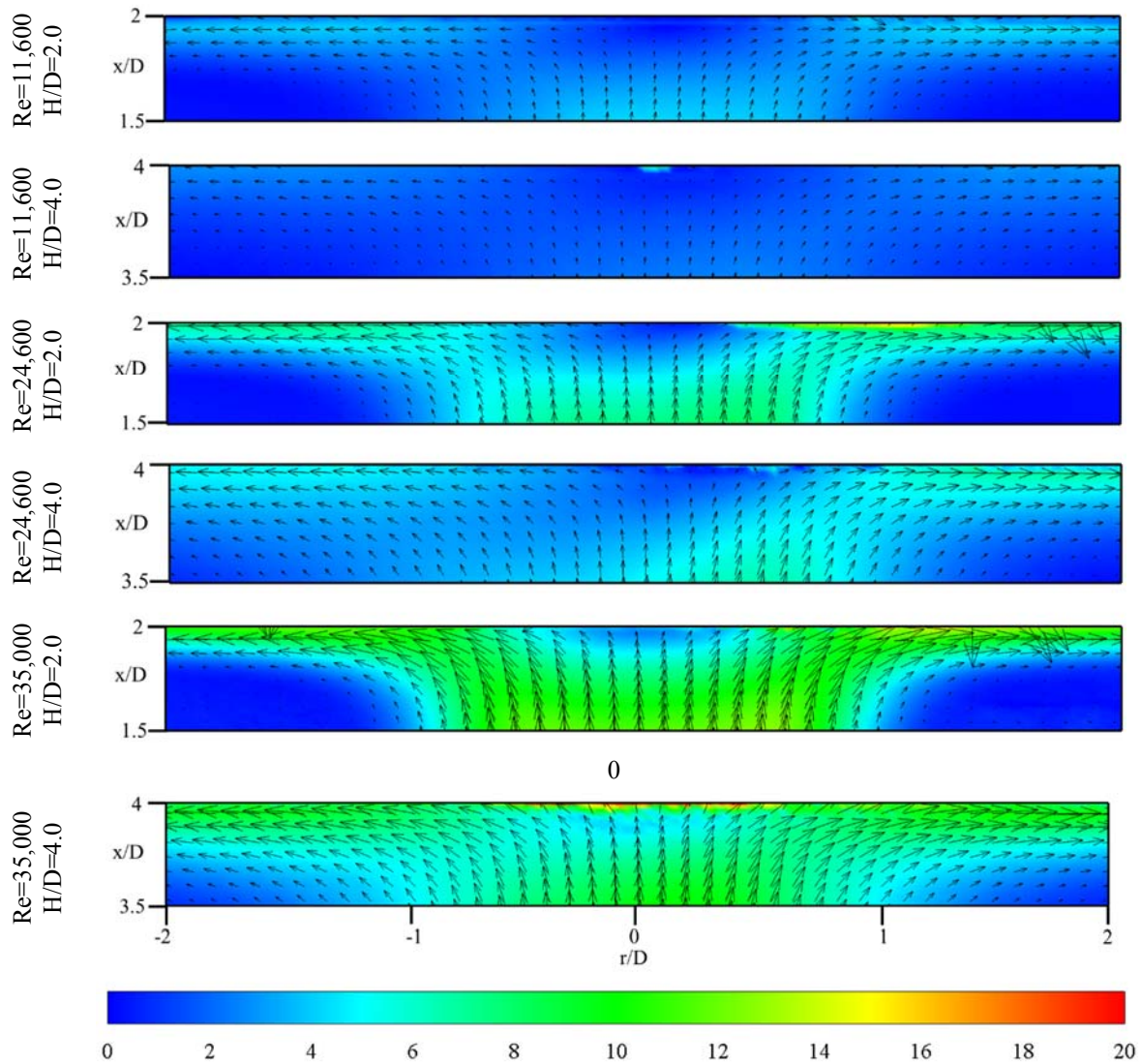
Figure 5.12: Contour plot for velocity magnitude (m/s) near the impingement plane at H/D=2 and 4 for S=0.30. Flow field characteristics in the downstream over the last 0.5x/D are shown.

Figure 5.12 presents the contour plot for velocity magnitude near the impinging plane (for H/D=2, 1.5 < x/D < 2.0 and for H/D=4, 3.5 < x/D < 4.0). As the Reynolds number increases the stagnation zone (zero velocity region) shrinks, smaller stagnation region gives rise to the axial velocity at impingement. The peaks in the heat transfer are off-set with velocity peaks since near the peak velocity, velocity gradients are small, and the location where heat transfer peaks occur, radial velocity gradients are large. For the near field impingement, the wall jet region starts from r/D>0.3 reaching a peak radial velocity depending on impingement distance (r/D≈0.6 for H/D=2 and r/D≈1.0 for H/D=4). For H/D=4, the Nusselt number distribution over the impingement plate flattens out and secondary peaks vanish, similarly, the radial velocity peaks damped out when compared to near-field impingement. The Nusselt number distribution and radial velocity profile also flatten out for the low Reynolds number compared to high Reynolds numbers.
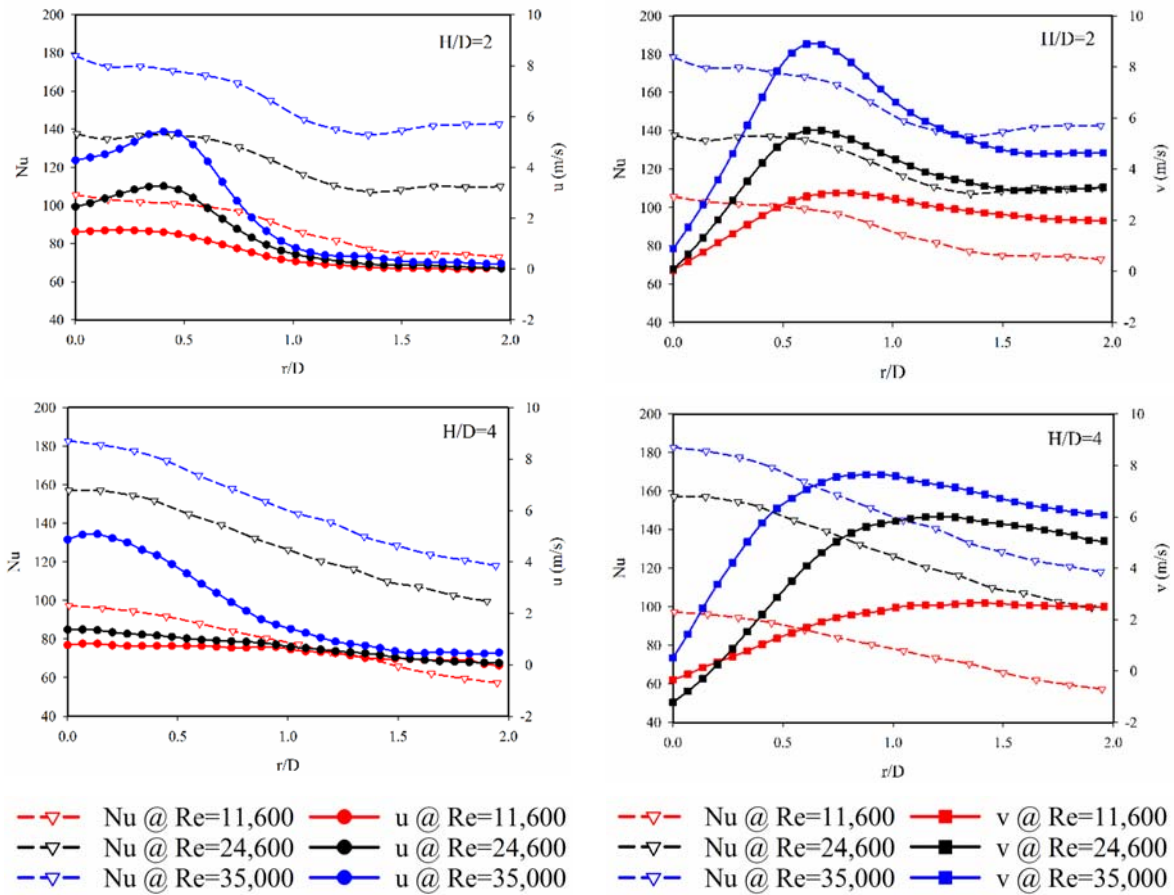
169
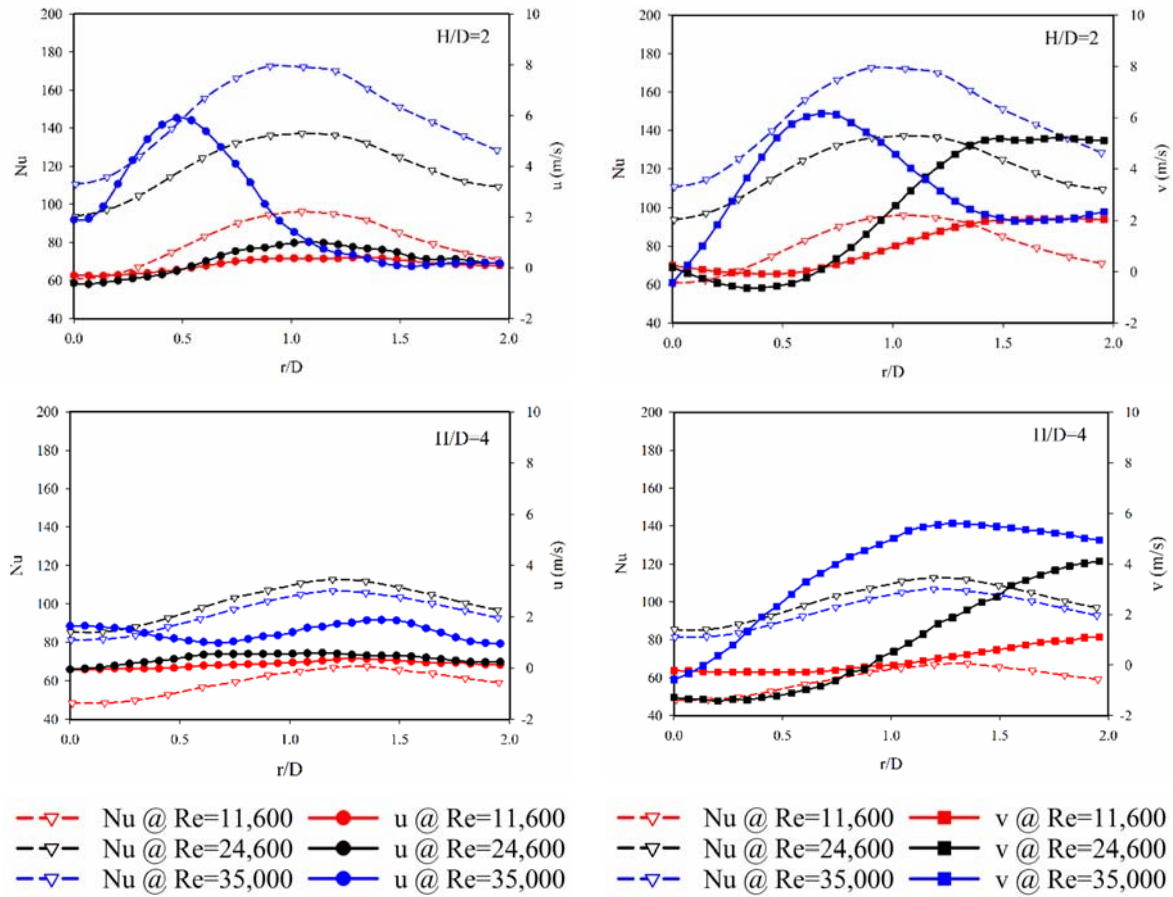
Figure 5.13: Nusselt number at the impingement plane and (axial, radial) velocity profiles (x/D=1.95 for H/D=2, x/D=3.95 for H/D=4) before the impingement plane for S=0.74.

170
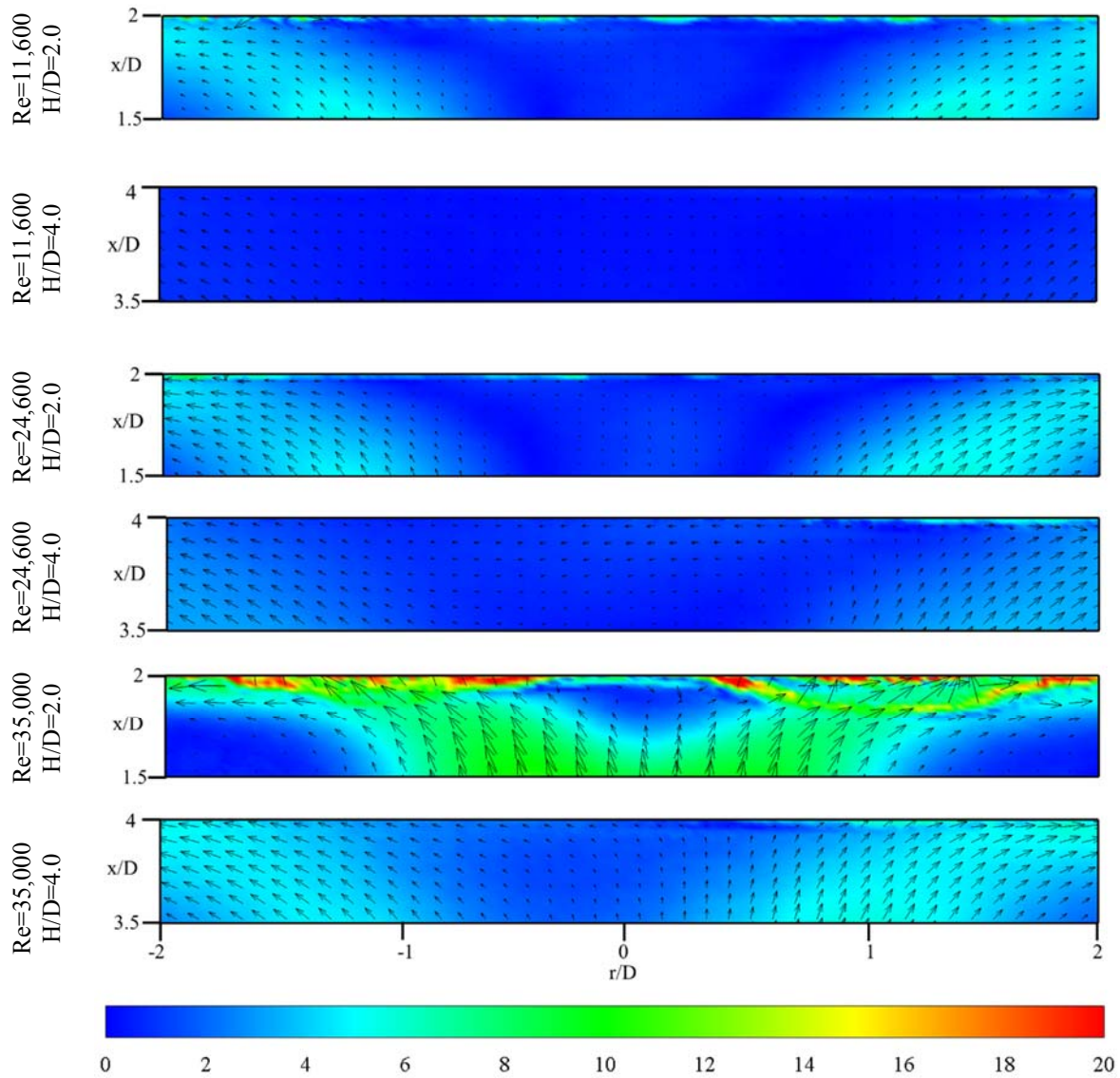
Figure 5.14: Contour plot for velocity magnitude near the impingement plane at H/D=2 and 4 for S=0.74. Flow field characteristics in the downstream over the last 0.5x/D are shown.

For high swirl (S=0.74, Figure 5.13), the axial velocity profiles are almost zero and do not affect the impingement characteristics except for the Re=35,000 at H/D=2. At Re=35,000 and S=74, vortex breakdown does not occur but some flow instabilities are observed through the velocity distributions which are distinct from all other tested boundary conditions. For the high swirl, the velocity and Nusselt number peaks are off-set and the peak heat transfer occurs in the wall jet region compared to low swirl cases. The secondary peaks are absent in the heat transfer data and a more uniform heat transfer distribution is observed for 0.00 < r/D < 2.00. For Re=35,000 and S=0.74, near field impingement (H/D=2) velocity profiles are similar to low swirl impinging jet while for the far-field impingement (H/D=4), the velocity profiles look like the test cases where vortex breakdown occurs. The contour plots (Figure 5.14) also demonstrate that for H/D=2 the stagnation region is small when compared to the region at

171

H/D=4. The heat transfer data also predicts that the flow features for the test case (Re=35,000 and S=0.74) are different from the jet with the low swirl. Time-resolved PIV measurements are needed to comment on flow instabilities for this case and to confirm the presence of precessing core vortex, time-resolved data can also provide in-depth information about the different coherent structure and a correlation can be established with heat transfer characteristics. Alternatively, the FFT (Fast Fourier Transformation) of acoustics data can be used to extract any frequency associated with the flow, phase-locked PIV measurements can be used to visualize different flow structures. The Proportional Orthogonal Decomposition (POD) of the available transient heat transfer data can also provide some in-depth of coherent structure provided the thermal inertia of the heated plate is negligible.

5.4 CONCLUSIONS

Time-averaged flow field characteristics of free and impingement turbulent swirling (incompressible) jets were studied. The nozzle exit boundary conditions were measured using constant temperature anemometry and flow field characteristics were measured by particle image velocimetry. Three different Reynolds numbers (Re=11,600, 24,600, and 35,000) were tested against two Swirl numbers (S=0.30 and 0.74) and two different impingement distances (H/D=2 and 4). Results showed that the impingement affects the upstream flow field significantly. The vortex breakdown's shape and position were also affected by the impingement. Numerous impingement characteristics were affected by different flow features for the low and high swirl. The following results can be summarized in this investigation.

- The low swirling flow (S=0.30) does not experience a vortex breakdown for all Reynolds numbers. For near-field impingement, the centreline velocity decay is similar for all Reynolds numbers in contrast to far impingement distance (H/D=4), low and moderate Reynolds numbers have high centreline decay compared to Re=35,000. The velocity fluctuations for low swirl stay under 20% of its bulk axial velocity.

- For high swirl (S=0.74), low (Re=11,600) and moderate (Re=24,600) Reynolds numbers experience the recirculation bubble into the flow. Impingement and Reynolds number affect the size and position of the recirculation bubble. For Re=11,600, the vortex bubble is bigger and stronger but with an increase of velocity, this recirculation zone is being squeezed by the accelerated flow from its sides. For the free jet, the vortex breakdown girth for Re=11,600 stretches -0.4 < r/D < 0.4 and for Re=24,600 it ranges -0.2 < r/D < 0.2. The impingement also increases the width of the recirculation zone

and the notable difference is being spotted for near-field impingement for Re=24,600. Within the recirculation bubble, the low Reynolds number has lower fluctuations in contrast to moderate Reynolds number. These lower fluctuations indicate that the recirculation bubble at low Reynolds is much more stable and act like a bluff body at the nozzle exit. For Re=35,000 and S=0.74, the flow field is different than the low swirl albeit it is a pre-vortex breakdown regime for high Reynolds number.

- In low swirl impinging jets at S=0.3, due to the high static pressures at the stagnation zone, high heat transfer is observed. The wall jet region starts from r/D>0.3 and reaches peak radial velocity and gradually decreases with a further increase in the radial distance. The location of peak radial velocity depends on impingement distance. For the high swirl, the stagnation region extends and low Nusselt number values are observed near impingement, peak heat transfer occurs in the wall jet region. For Re=35,000 and S=0.74, the impingement characteristics are similar to boundary conditions where vortex breakdown occurs. This attribute strengthens the assumption that there might unstable vortex breakdown or precessing core vortex occurs at this operating condition.

5.5 CHAPTER REFERENCES

[1]   N.A. Chigier, J.M. Beér, J.M. Beér, Velocity and static-pressure distributions in swirling air jets issuing from annular and divergent nozzles, J. Fluids Eng. Trans. ASME. 86 (1964) 788–796. doi:10.1115/1.3655954.

[2]   R. Gardon, J.C. Akfirat, The role of turbulence in determining the heat-transfer characteristics of impinging jets, Int. J. Heat Mass Transf. 8 (1965) 1261–1272. doi:10.1016/0017-9310(65)90054-2.

[3]   N.A. Chigier, A. Chervinsky, Experimental investigation of swirling vortex motion in jets, J. Appl. Mech. 34 (1967) 443. doi:10.1115/1.3607703.

[4]   A.Ü. Tepe, Y. Yetişken, Ü. Uysal, K. Arslan, Experimental and numerical investigation of jet impingement cooling using extended jet holes, Int. J. Heat Mass Transf. 158 (2020) 119945. doi:10.1016/j.ijheatmasstransfer.2020.119945.

[5]   W.C. Lai, P. Yin, Y.H. Liu, Investigation of flow characteristics from an inclined jet on a heated rotating disk, Int. J. Heat Mass Transf. 127 (2018) 943–956. doi:10.1016/j.ijheatmasstransfer.2018.08.028.

[6]   R. Viskanta, Heat Transfer to Impinging Isothermal Gas and Flame Jets, Exp. Therm. Fluid Sci. 6 (1993) 111–134. doi:10.1016/0894-1777(93)90022-B.

[7]   D. Hee Lee, S. Youl Won, Y. Taek Kim, Y. Suk Chung, L.D. Hee, W.S. Youl, K.Y. Taek, C.Y. Suk, D. Hee Lee, S. Youl Won, Y. Taek Kim, Y. Suk Chung, Turbulent heat transfer from a flat surface to a swirling round impinging jet, Int. J. Heat Mass Transf. 45 (2002) 223–227. doi:10.1016/S0017-9310(01)00135-1.

[8]   M.-Y. Wen, K.-J. Jang, An impingement cooling on a flat surface by using circular jet with longitudinal swirling strips, Int. J. Heat Mass Transf. 46 (2003) 4657–4667. doi:10.1016/S0017-9310(03)00302-8.

[9]   Z.X. Yuan, Y.Y. Chen, J.G. Jiang, C.F. Ma, Swirling effect of jet impingement on heat transfer from a flat surface to CO_2 stream, Exp. Therm. Fluid Sci. 31 (2006) 55–60. doi:10.1016/j.expthermflusci.2005.12.007.

[10] A. Ianiro, G. Cardone, Heat transfer rate and uniformity in multichannel swirling

impinging jets, Appl. Therm. Eng. 49 (2012) 89–98. doi:10.1016/j.applthermaleng.2011.10.018.

[11]   J. Ward, M. Mahmood, Heat transfer from a turbulent, swirling, impinging jet, in: Proc. 7th Int. Heat Transf. Conf., Munich, West Germany, 1982: pp. 401–407.

[12]   by W. James Guzlntner, J.N. B Livingood, P. Hrycuk, A.W. Gauntner, Survey of Literature of Flow Characteristics of a Single Turbulent Jet Impinging on a Flat Surface, NASA TN D-5652. (1970). https://ntrs.nasa.gov/archive/nasa/casi.ntrs.nasa.gov/19700009658.pdf (accessed November 22, 2017).

[13]   C. duP. Donaldson, R.S. Snedeker, A study of free jet impingement. Part 1. Mean properties of free and impinging jets, J. Fluid Mech. 45 (1971) 281. doi:10.1017/S0022112071000053.

[14]   N. Zuckerman, N. Lior, I. Summary, Jet impingement heat transfer: Physics, correlations, and numerical modeling, Adv. Heat Transf. 39 (2006) 565–631. doi:10.1016/S0065-2717(06)39006-5.

[15]   J.. W. Baughn, D. Cooper, H. Lacovides, D. Jackson, Instrument for the measurement of heat flux from a surface with uniform temperature, Rev. Sci. Instrum. 57 (1986) 921–925.

[16]   J.W. Baughn, S. Shimizu, Heat transfer measurements from a surface with uniform heat flux and an impinging jet, J. Heat Transf. (Transactions ASME). 111 (1989) 1988–1990. doi:10.1115/1.3250776.

[17]   J.W. Baughn, A.E. Hechanova, X. Yan, An experimental study of entrainment effects on the heat transfer from a flat surface to a heated circular impinging jet, J. Heat Transfer. 113 (1991) 1023–1025. doi:10.1115/1.2911197.

[18]   M.J. Tummers, J. Jacobse, S.G.J. Voorbrood, Turbulent flow in the near field of a round impinging jet, Int. J. Heat Mass Transf. 54 (2011) 4939–4948. doi:10.1016/j.ijheatmasstransfer.2011.07.007.

[19]   K. Bakirci, K. Bilen, Visualization of heat transfer for impinging swirl flow, Exp.

175

Therm. Fluid Sci. 32 (2007) 182–191. doi:10.1016/j.expthermflusci.2007.03.004.

[20] M. Fairweather, G. Hargrave, Experimental investigation of an axisymmetric, impinging turbulent jet. 1. Velocity field, Exp. Fluids. 33 (2002) 464–471. doi:10.1007/s00348-002-0479-7.

[21] H. Yadav, A. Agrawal, Self-similar behavior of turbulent impinging jet based upon outer scaling and dynamics of secondary peak in heat transfer, Int. J. Heat Fluid Flow. 72 (2018) 123–142. doi:10.1016/J.IJHEATFLUIDFLOW.2018.06.001.

[22] Z.U. Ahmed, Y.M. Al-Abdeli, F.G. Guzzomi, Impingement pressure characteristics of swirling and non-swirling turbulent jets, Exp. Therm. Fluid Sci. 68 (2015) 722–732. doi:10.1016/j.expthermflusci.2015.07.017.

[23] Z.U. Ahmed, Y.M. Al-Abdeli, F.G. Guzzomi, Heat transfer characteristics of swirling and non-swirling impinging turbulent jet, Int. J. Heat Mass Transf. 102 (2016) 991–1003. doi:10.1016/j.expthermflusci.2015.07.017.

[24] Z.U. Ahmed, Y.M. Al-Abdeli, F.G. Guzzomi, Flow field and thermal behaviour in swirling and non-swirling turbulent impinging jets, Int. J. Therm. Sci. 114 (2017) 241–256. doi:10.1016/j.ijthermalsci.2016.12.013.

[25] M. Ikhlaq, Y.M. Al-Abdeli, M. Khiadani, Nozzle exit conditions and the heat transfer in non-swirling and weakly swirling turbulent impinging jets, Heat Mass Transf. 56 (2019) 269–290. doi:10.1007/s00231-019-02710-1.

[26] Z.U. Ahmed, Y.M. Al-Abdeli, M.T. Matthews, The effect of inflow conditions on the development of non-swirling versus swirling impinging turbulent jets, Comput. Fluids. 118 (2015) 255–273. doi:10.1016/j.compfluid.2015.06.024.

[27] J. Ortega-Casanova, F.J. Granados-Ortiz, Numerical simulation of the heat transfer from a heated plate with surface variations to an impinging jet, Int. J. Heat Mass Transf. 76 (2014) 128–143. doi:10.1016/j.ijheatmasstransfer.2014.04.022.

[28] Y. Amini, M. Mokhtari, M. Haghshenasfard, M. Barzegar Gerdroodbary, Heat transfer of swirling impinging jets ejected from Nozzles with twisted tapes utilizing CFD technique, Case Stud. Therm. Eng. 6 (2015) 104–115. doi:10.1016/j.csite.2015.08.001.

[29] Z.X. Yuan, Y.Y. Chen, J.G. Jiang, C.F. Ma, Swirling effect of jet impingement on heat transfer from a flat surface to CO2 stream, Exp. Therm. Fluid Sci. 31 (2006) 55–60. doi:10.1016/j.expthermflusci.2005.12.007.

[30] J. Ortega-Casanova, CFD and correlations of the heat transfer from a wall at constant temperature to an impinging swirling jet, Int. J. Heat Mass Transf. 55 (2012) 5836–5845. doi:10.1016/j.ijheatmasstransfer.2012.05.079.

[31] H.Q. Yang, T. Kim, T.J. Lu, K. Ichimiya, Flow structure, wall pressure and heat transfer characteristics of impinging annular jet with/without steady swirling, Int. J. Heat Mass Transf. 53 (2010) 4092–4100. doi:10.1016/j.ijheatmasstransfer.2010.05.029.

[32] L. Huang, M.S.S. El-Genk, Heat transfer and flow visualization experiments of swirling, multi-channel, and conventional impinging jets, Int. J. Heat Mass Transf. 41 (1998) 583–600. doi:10.1016/S0017-9310(97)00123-3.

[33] A. Nozaki, Y. Igarashi, K. Hishida, The Heat Transfer Mechanism of a Swirling Impinging Jet in the Stagnation Region., Trans. Japan Soc. Mech. Eng. Ser. B. 32 (2003) 663–673. doi:10.1299/kikaib.68.2300.

[34] J.K.J. Abrantes, L. Azevedo, L. Fernando, A. Azevedo, Fluid flow characteristics of a swirl jet impinging on a flat plate, in: 13th Int. Symp. Appl. Laser Tech. to Fluid Mech., Lisbon, Portugal, 2006: pp. 26–29. http://ltces.dem.ist.utl.pt/lxlaser/lxlaser2006/downloads/papers/28_3.pdf (accessed September 25, 2017).

[35] A. Ianiro, D. Violato, F. Scarano, G. Cardone, Three dimensional features in swirling impinging jets, in: 15th Int. Symp. Flow Vis., June 25-28, 2012, Minsk, Belarus, 2012.

[36] F. Cozzi, A. Coghe, R. Sharma, Analysis of local entrainment rate in the initial region of isothermal free swirling jets by Stereo PIV, Exp. Therm. Fluid Sci. 94 (2018) 281–294. doi:10.1016/j.expthermflusci.2018.01.013.

[37] F. Cozzi, R. Sharma, G. Solero, Analysis of coherent structures in the near-field region of an isothermal free swirling jet after vortex breakdown, Exp. Therm. Fluid Sci. 109 (2019) 109860. https://www.sciencedirect.com/science/article/pii/S089417771930158X?dgcid=author

(accessed July 25, 2019).

[38]　Y.M. Al-Abdeli, Experiments in turbulent swirling non-premixed flames and isothermal flows, 2004.

[39]　Y.M. Al-Abdeli, A.R. Masri, Recirculation and flowfield regimes of unconfined non-reacting swirling flows, Exp. Therm. Fluid Sci. 27 (2003) 655–665. doi:10.1016/S0894-1777(02)00280-7.

[40]　Y.M. Al-Abdeli, A.R. Masri, & Assaad, R. Masri, A.R. Masri, Precession and recirculation in turbulent swirling isothermal jets, Combust. Sci. Technol. 176 (2004) 645–665. doi:10.1080/00102200490427883.

[41]　A.K. Gupta, D.G. Lilley, N. Syred, Swirl flows, 1984.

[42]　O. Lucca-Negro, T. O'Doherty, O. Lucca-Negro, Vortex breakdown: a review, Prog. Energy Combust. Sci. 27 (2001) 431–481. doi:10.1016/S0360-1285(00)00022-8.

[43]　M.R. Ruith, P. Chen, E. Meiburg, T. Maxworthy, Three-dimensional vortex breakdown in swirling jets and wakes: Direct numerical simulation, J. Fluid Mech. 486 (2003) 331–378. doi:10.1017/S0022112003004749.

[44]　F. Gallaire, M. Ruith, E. Meiburg, J.M. Chomaz, P. Huerre, Spiral vortex breakdown as a global mode, J. Fluid Mech. 549 (2006) 71–80. doi:10.1017/S0022112005007834.

[45]　K. Oberleithner, M. Sieber, C.N. Nayeri, C.O. Paschereit, C. Petz, H.-C.C. Hege, B.R. Noack, I. Wygnanski, Three-dimensional coherent structures in a swirling jet undergoing vortex breakdown: stability analysis and empirical mode construction, J. Fluid Mech. 679 (2011) 383–414. doi:10.1017/jfm.2011.141.

[46]　M. Vanierschot, On the dynamics of the transition to vortex breakdown in axisymmetric inviscid swirling flows, Eur. J. Mech. B/Fluids. 65 (2017) 65–69. doi:10.1016/j.euromechflu.2017.02.009.

[47]　T.B. Benjamin, Theory of the vortex breakdown phenomenon, J. Fluid Mech. 14 (1962) 593–629. doi:10.1017/S0022112062001482.

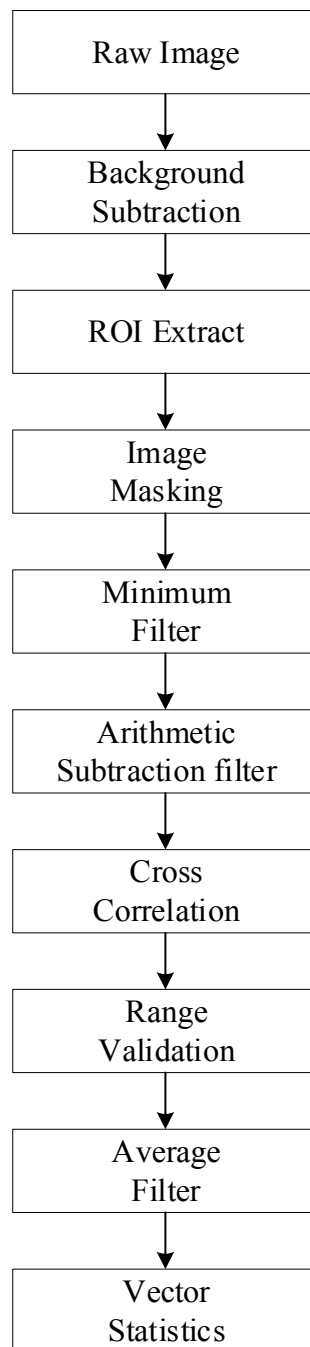[48]　Y.M. Al-Abdeli, A.R. Masri, Turbulent swirling natural gas flames : stability

characteristics, unsteady behavior and vortex breakdown, Combust. Sci. Technol. 179 (2007) 207–225. doi:10.1080/00102200600809092.

[49]   Y.M. Al-Abdeli, A.R. Masri, Review of laboratory swirl burners and experiments for model validation, Exp. Therm. Fluid Sci. 69 (2015) 178–196. doi:10.1016/j.expthermflusci.2015.07.023.

[50]   M. Ikhlaq, Y.M. Al-Abdeli, M. Khiadani, Transient heat transfer characteristics of swirling and non-swirling turbulent impinging jets, Exp. Therm. Fluid Sci. 109 (2019) 109917. doi:10.1016/j.expthermflusci.2019.109917.

[51]   M. Ikhlaq, Y.M. Al-Abdeli, M. Khiadani, Methodology for spatially resolved transient convection processes using infrared thermography, Exp. Heat Transf. (2020) 1–24. doi:10.1080/08916152.2020.1749189.

[52]   F.E. Jorgensen, How to measure turbulence with hot-wire anemometers-A practical guide, Dantec Dyn. Skovlunde, Denmark. (2005).

[53]   Z.U. Ahmed, Y.M. Al-Abdeli, F.G. Guzzomi, Corrections of dual-wire CTA data in turbulent swirling and non-swirling jets, Exp. Therm. Fluid Sci. 70 (2016) 166–175. doi:10.1016/j.expthermflusci.2015.09.007.

[54]   J. Stafford, E. Walsh, V. Egan, A statistical analysis for time-averaged turbulent and fluctuating flow fields using Particle Image Velocimetry, Flow Meas. Instrum. 26 (2012) 1–9. doi:10.1016/j.flowmeasinst.2012.04.013.

[55]   F. Martinelli, A. Olivani, A. Coghe, Experimental analysis of the precessing vortex core in a free swirling jet, Exp. Fluids. 42 (2007) 827–839. doi:10.1007/s00348-006-0230-x.

[56]   M. Raffel, C.E. Willert, F. Scarano, C.J. Kähler, S.T. Wereley, J. Kompenhans, Particle image velocimetry: a practical guide, Springer, 2018.

[57]   I.K. Toh, D. Honnery, J. Soria, Axial plus tangential entry swirling jet, Exp. Fluids. 48 (2010) 309–325. doi:10.1007/s00348-009-0734-2.

[58]   K. Yu, J. Xu, Adaptive PIV algorithm based on seeding density and velocity information, Flow Meas. Instrum. 51 (2016) 21–29. doi:10.1016/j.flowmeasinst.2016.08.004.

[59] K. Jambunathan, E. Lai, M.A.A.A. Moss, B.L.L.L. Button, A review of heat transfer data for single circular jet impingement, Int. J. Heat Fluid Flow. 13 (1992) 106–115. doi:10.1016/0142-727X(92)90017-4.

[60] M. Raizner, V. Rinsky, G. Grossman, R. van Hout, Heat transfer and flow field measurements of a pulsating round jet impinging on a flat heated surface, Int. J. Heat Fluid Flow. 77 (2019) 278–287. doi:10.1016/J.IJHEATFLUIDFLOW.2019.04.010.

5.6 CHAPTER APPENDICES

```
┌─────────────────────┐
│     Raw Image       │
└─────────────────────┘
           │
           ▼
┌─────────────────────┐
│    Background       │
│    Subtraction      │
└─────────────────────┘
           │
           ▼
┌─────────────────────┐
│     ROI Extract     │
└─────────────────────┘
           │
           ▼
┌─────────────────────┐
│      Image          │
│     Masking         │
└─────────────────────┘
           │
           ▼
┌─────────────────────┐
│     Minimum         │
│     Filter          │
└─────────────────────┘
           │
           ▼
┌─────────────────────┐
│    Arithmetic       │
│  Subtraction filter │
└─────────────────────┘
           │
           ▼
┌─────────────────────┐
│      Cross          │
│    Correlation      │
└─────────────────────┘
           │
           ▼
┌─────────────────────┐
│      Range          │
│    Validation       │
└─────────────────────┘
           │
           ▼
┌─────────────────────┐
│     Average         │
│     Filter          │
└─────────────────────┘
           │
           ▼
┌─────────────────────┐
│     Vector          │
│    Statistics       │
└─────────────────────┘
```

Figure 5-A1: PIV post-processing procedures for acquired images.

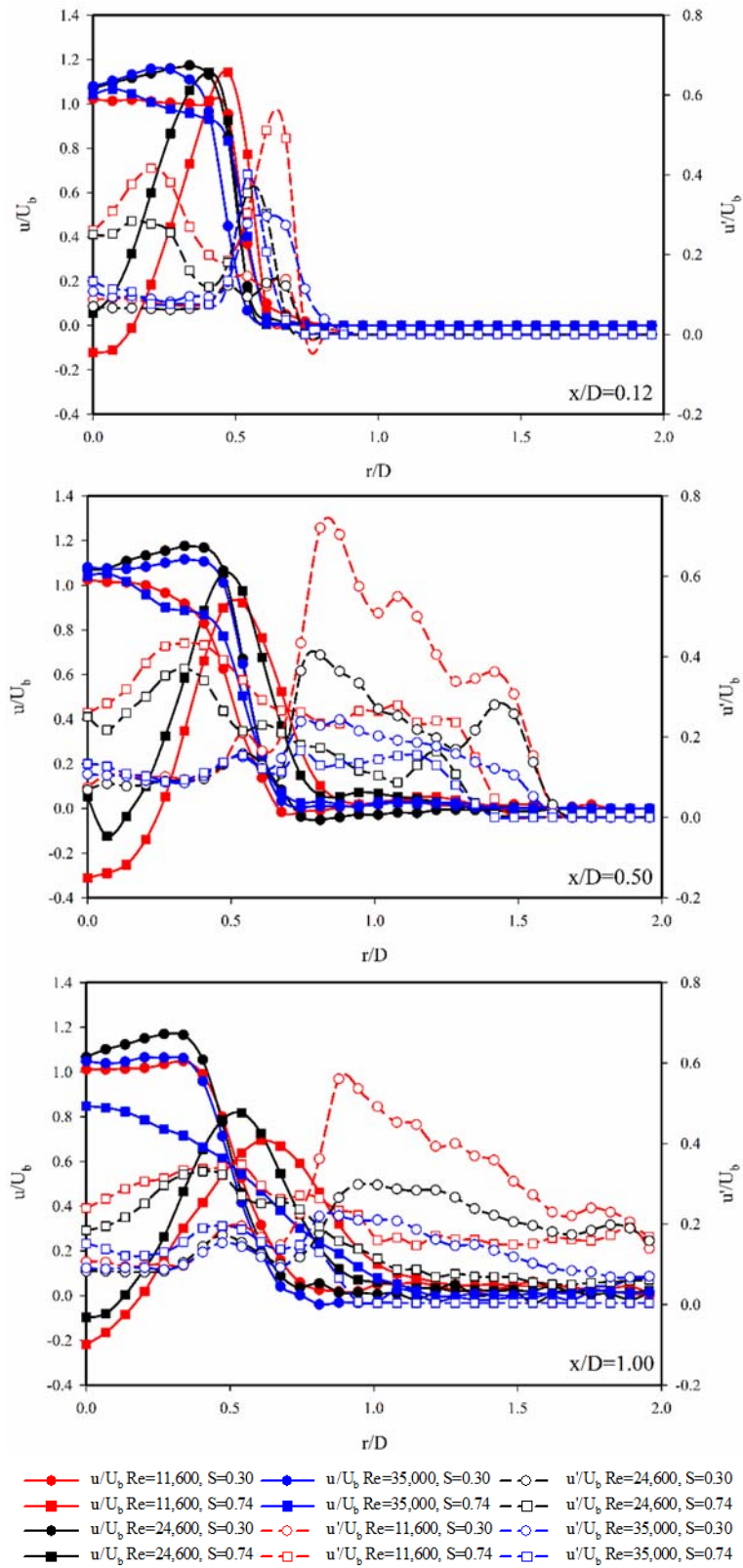**Figure 5-A2: Normalised axial velocity profiles in the radial direction for different axial locations in free jets: (a) x/D=0.12, (b) x/D=0.50, and (c) x/D=1.00.**

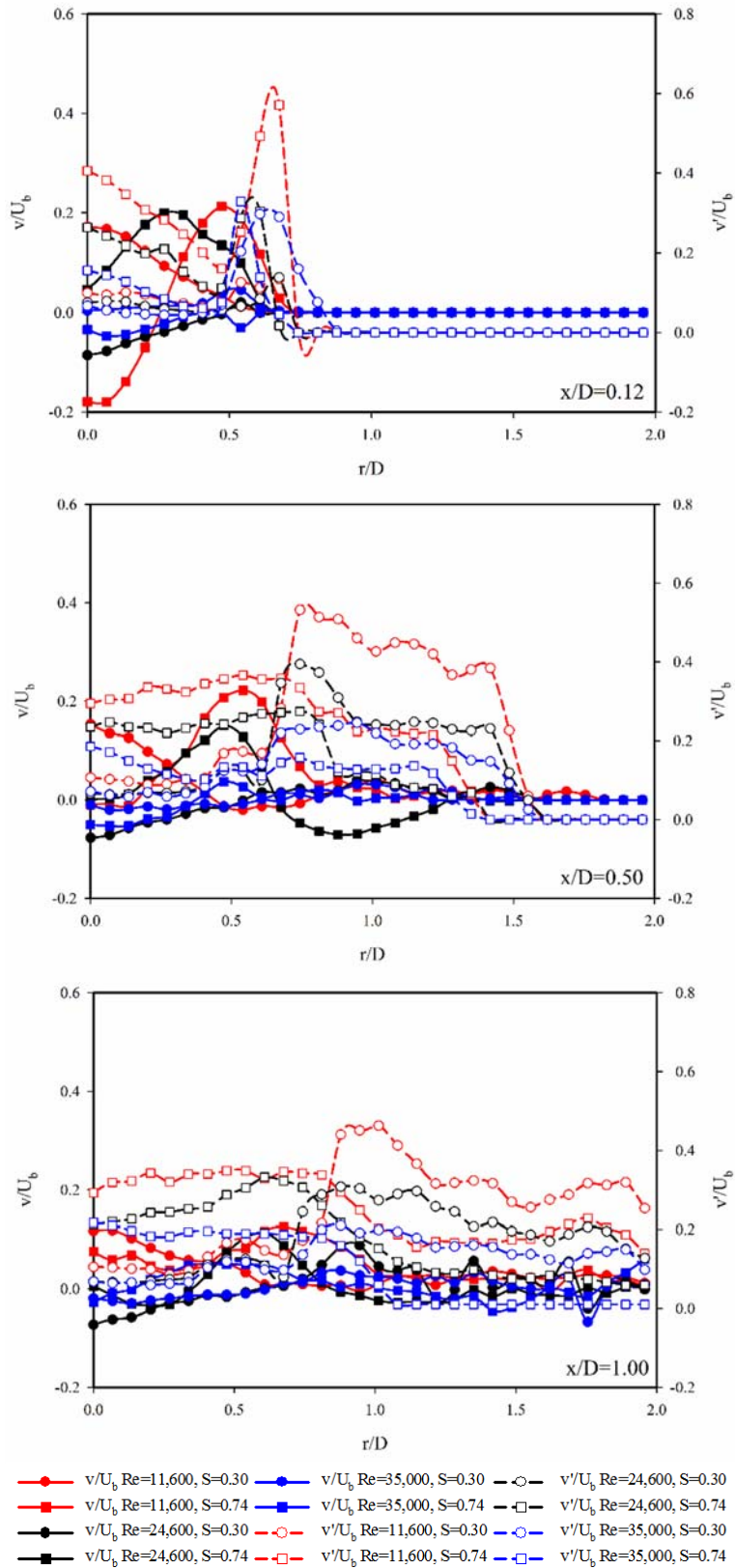**Figure 5-A3: Normalised radial velocity profiles in the radial direction for different axial locations in free jets: (a) x/D=0.12, (b) x/D=0.50, and (c) x/D=1.00.**

Figure 5-A4: Normalised axial velocity profiles in the radial direction for different axial locations in impinging jets at H/D=2: (a) x/D=0.12, (b) x/D=0.50, and (c) x/D=1.00.

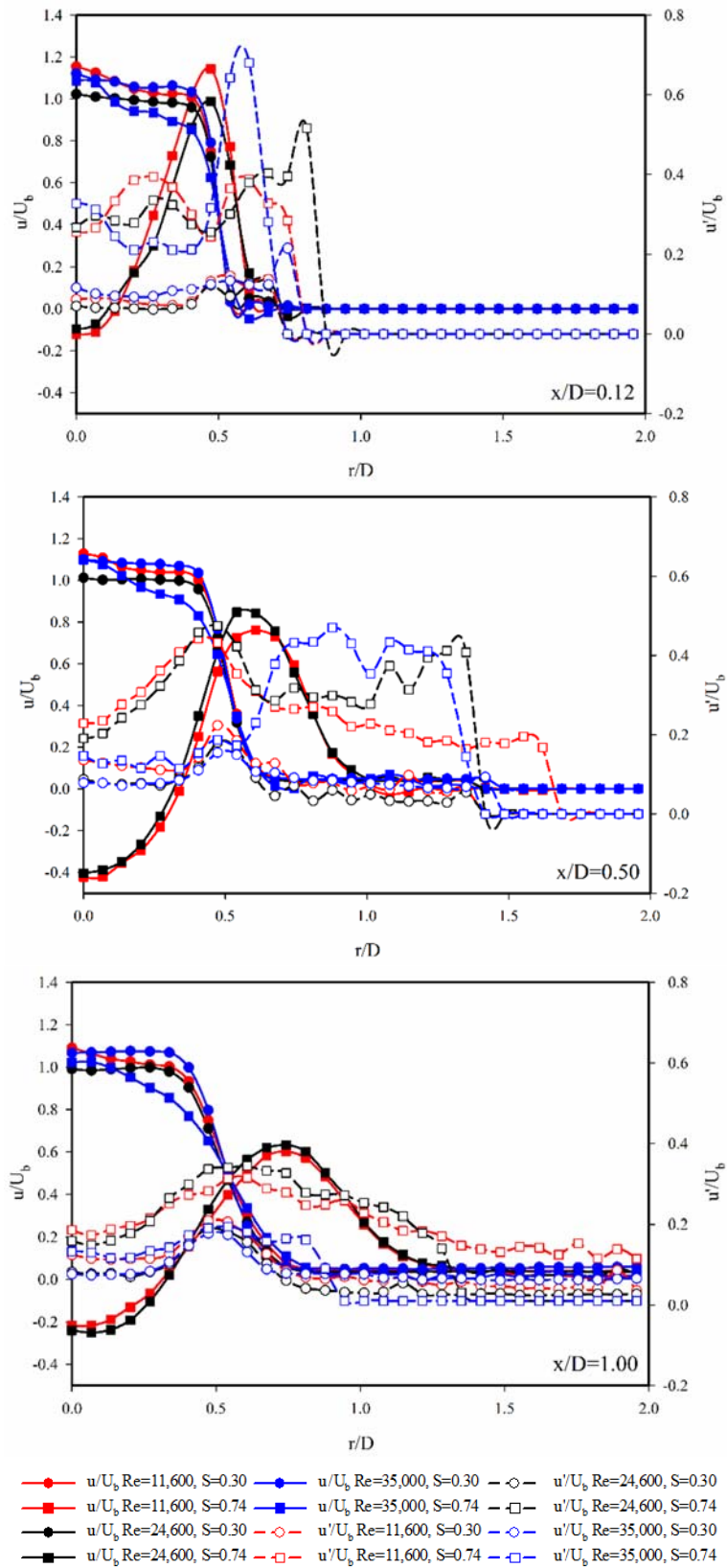**Figure 5-A5: Normalised radial velocity profiles in the radial direction for different axial locations in impinging jets at H/D=2: (a) x/D=0.12, (b) x/D=0.50, and (c) x/D=1.00.**
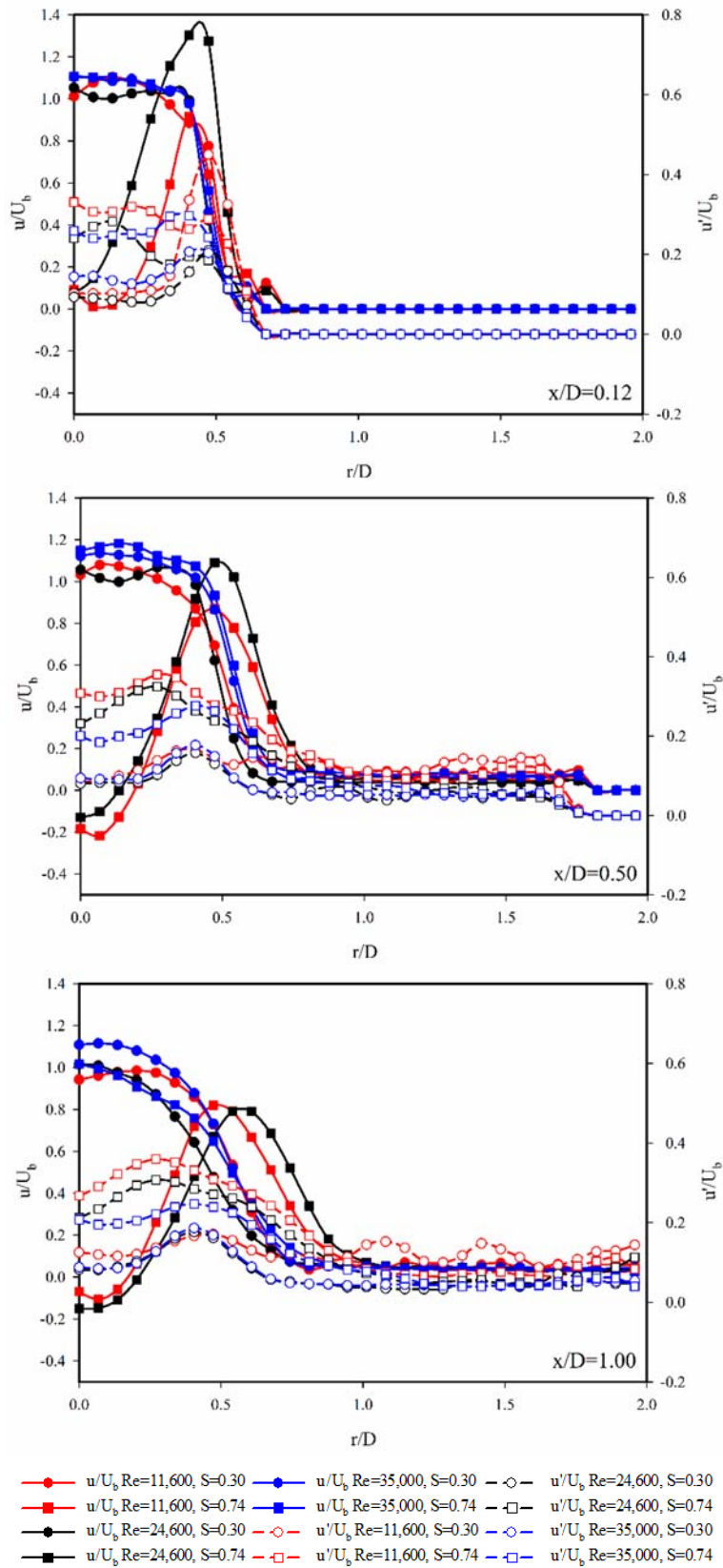
Figure 5-A6: Normalised axial velocity profiles in the radial direction for different axial locations for H/D=4; (a) x/D=0.12, (b) x/D=0.50, and (c) x/D=1.00.

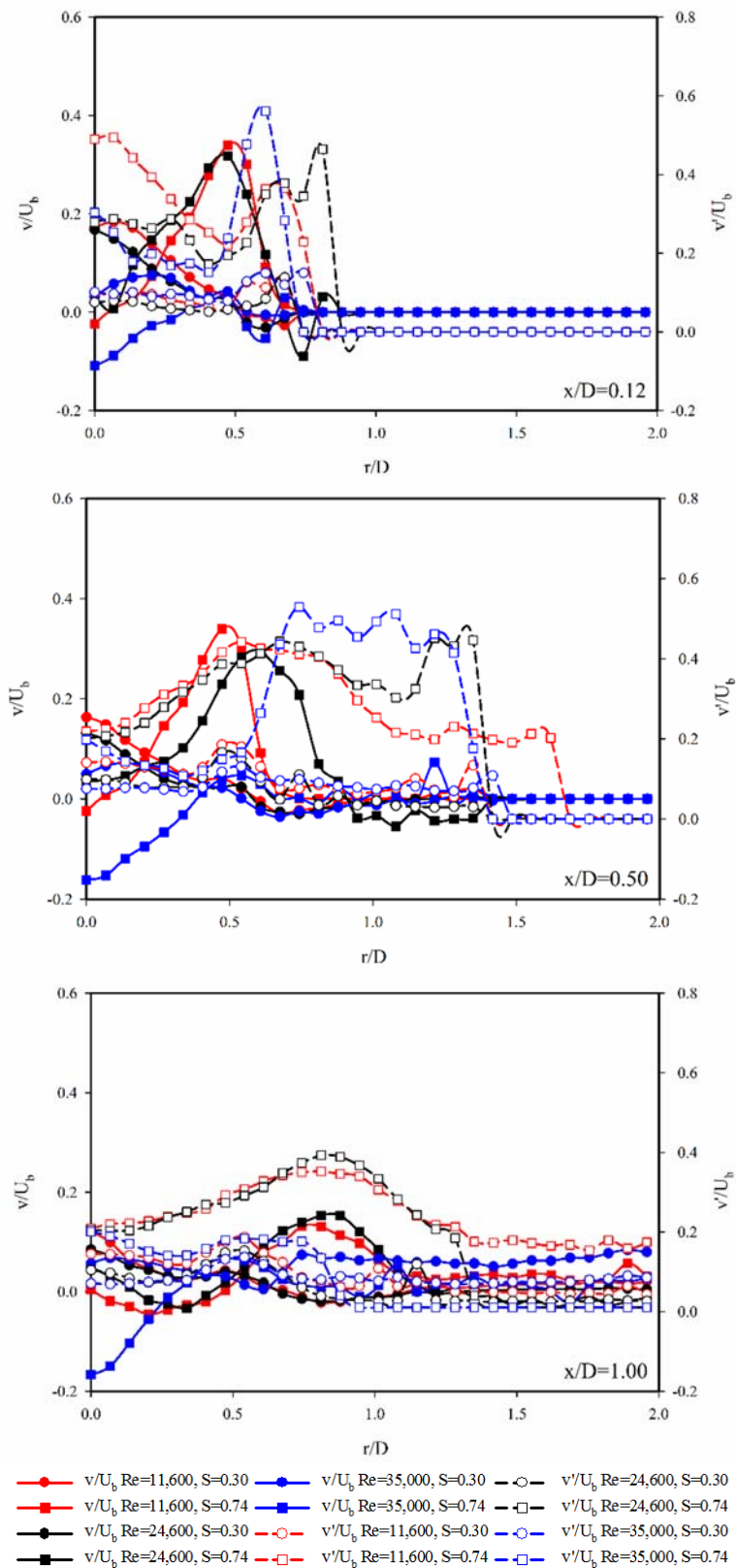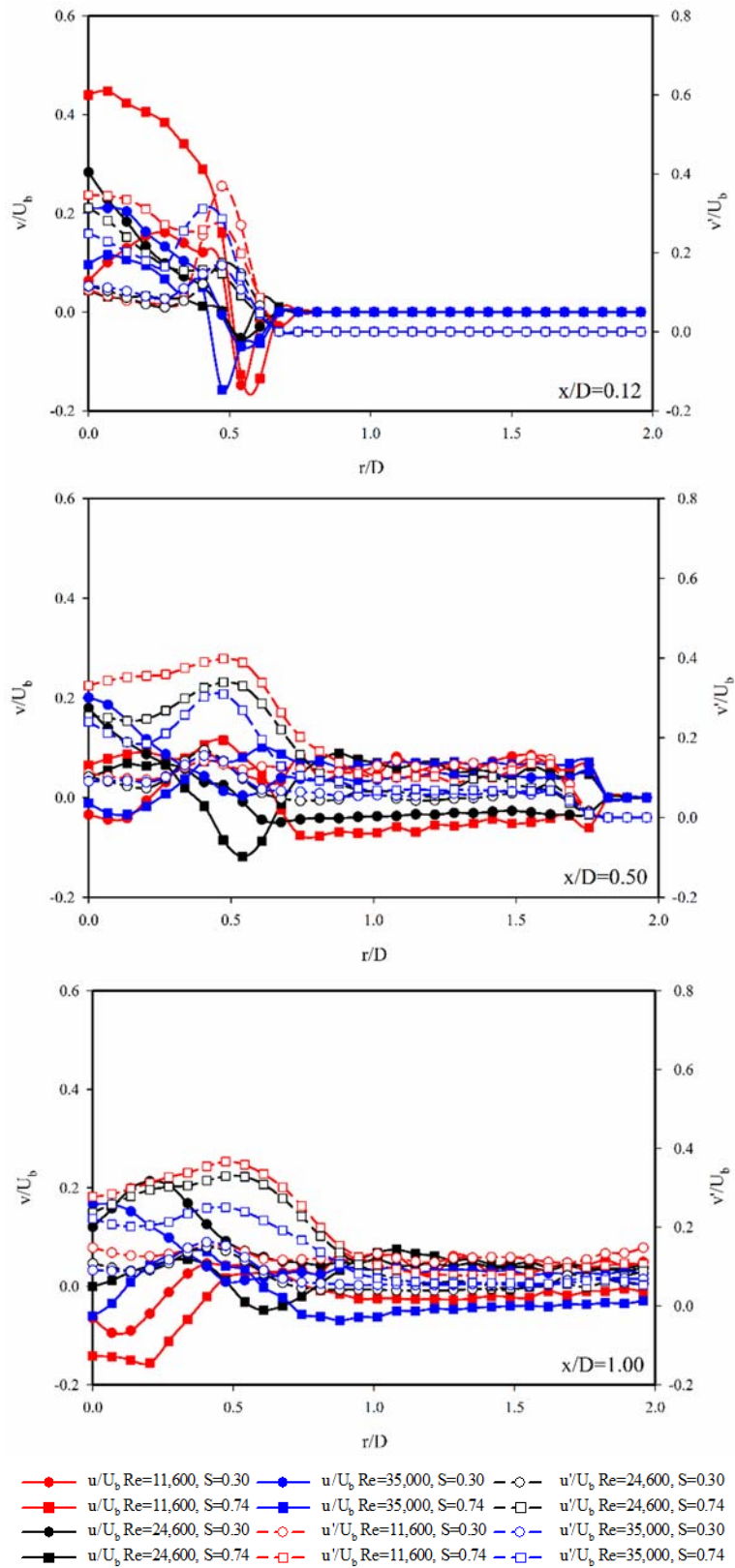**Figure 5-A7: Normalised radial velocity profiles in the radial direction for different axial locations for H/D=4; (a) x/D=0.12, (b) x/D=0.50, and (c) x/D=1.00.**
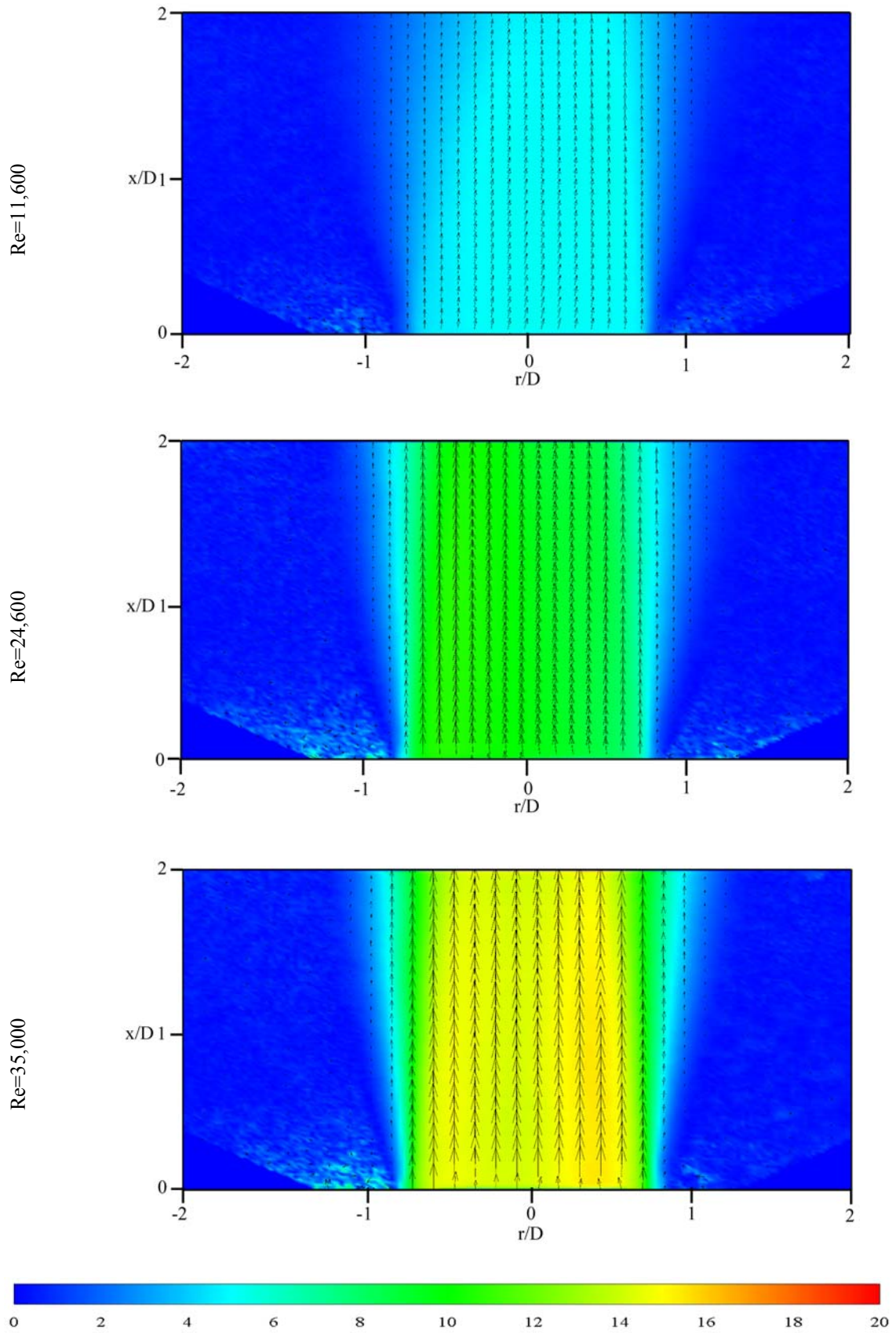
Figure 5-A8: Time-averaged flow field for free jet (0 < x/D < 2) at S=0.3 and Re=11,600, 24,600, and 35,000.
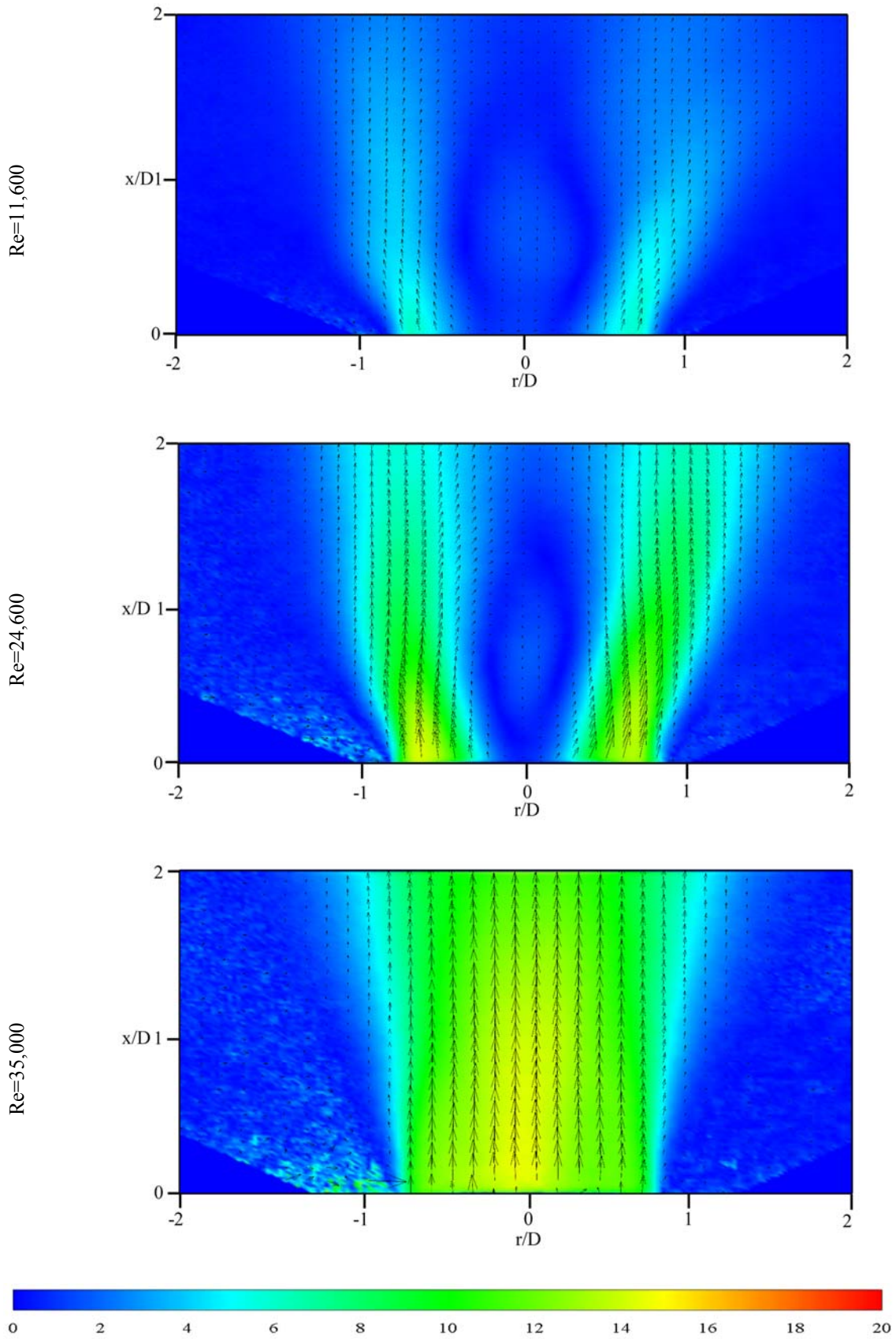
Figure 5-A9: Time-averaged flow field for free jet (0 < x/D < 2) at S=0.74 and Re=11,600, 24,600, and 35,000.
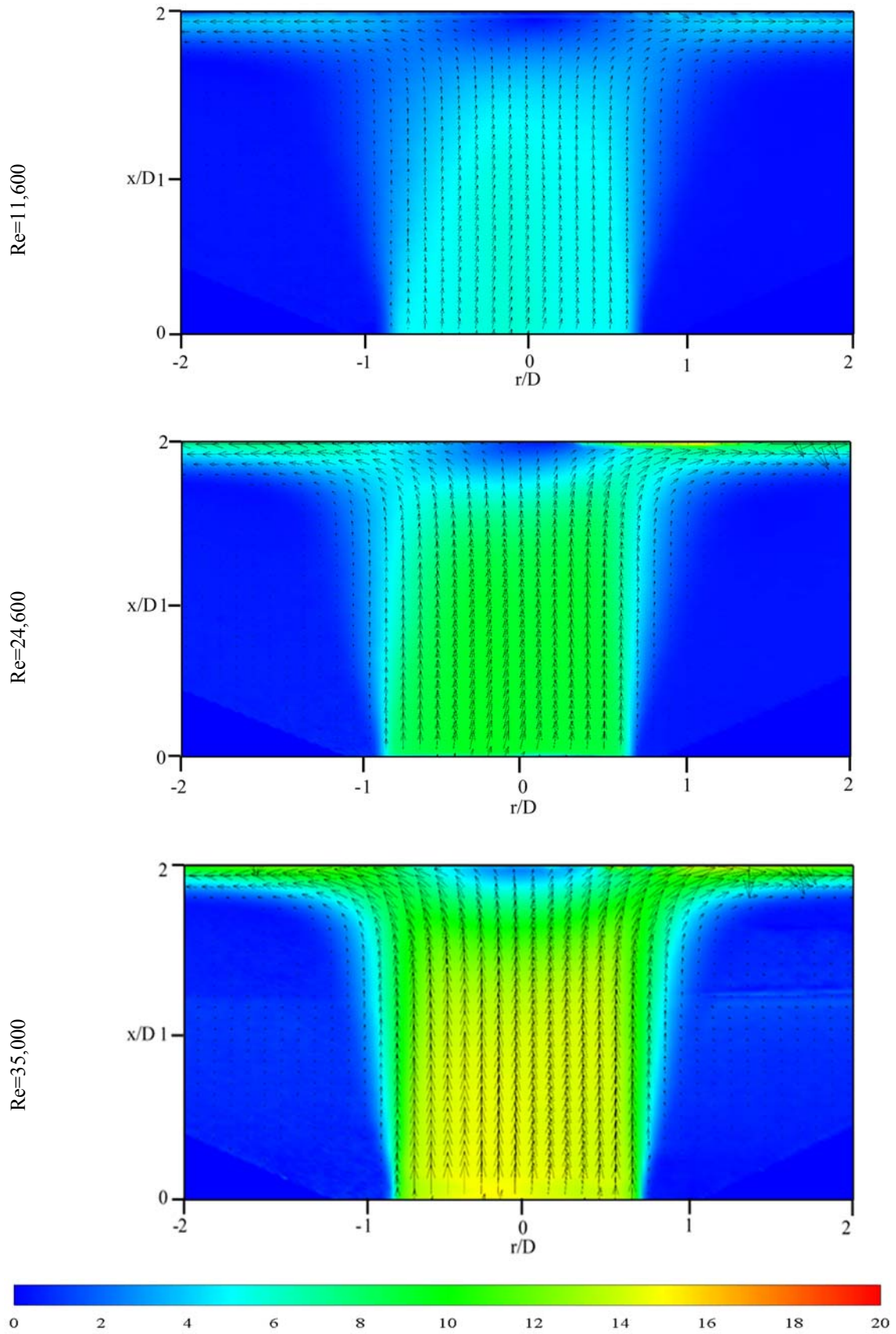
Figure 5-A10: Time-averaged flow field for impinging jet (H/D=2, 0 < x/D < 2) at S=0.3 and Re=11,600, 24,600, and 35,000.
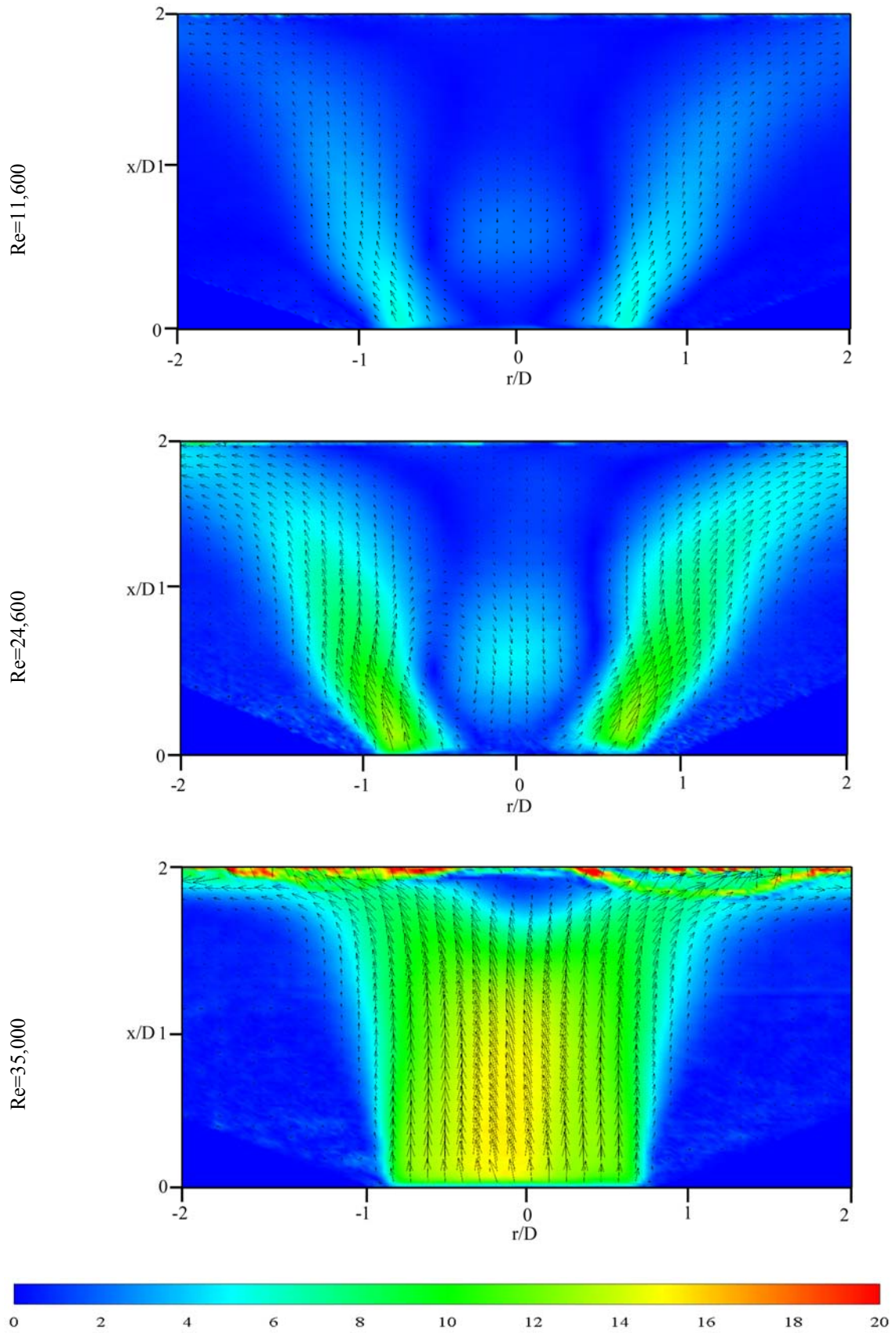
Figure 5-A11: Time-averaged flow field for impinging jet (H/D=2, 0 < x/D < 2) at S=0.74 and Re=11,600, 24,600, and 35,000.
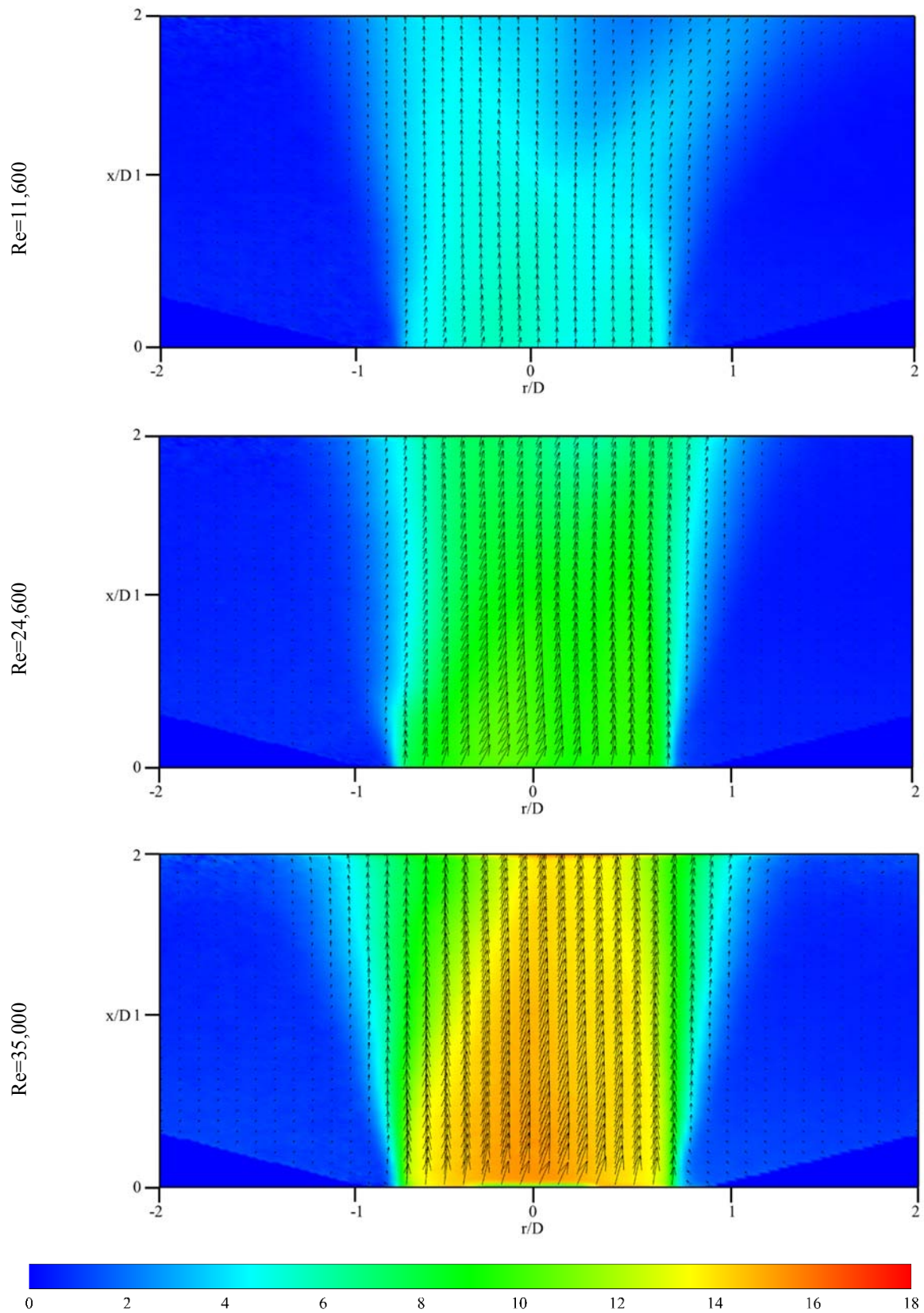
Figure 5-A12: Time-averaged flow field for impinging jet (H/D=4, 0 < x/D < 2) at S=0.30 and Re=11,600, 24,600, and 35,000.

Figure 5-A13: Time-averaged flow field for impinging jet (H/D=4, 0 < x/D < 2) at S=0.74 and Re=11,600, 24,600, and 35,000.
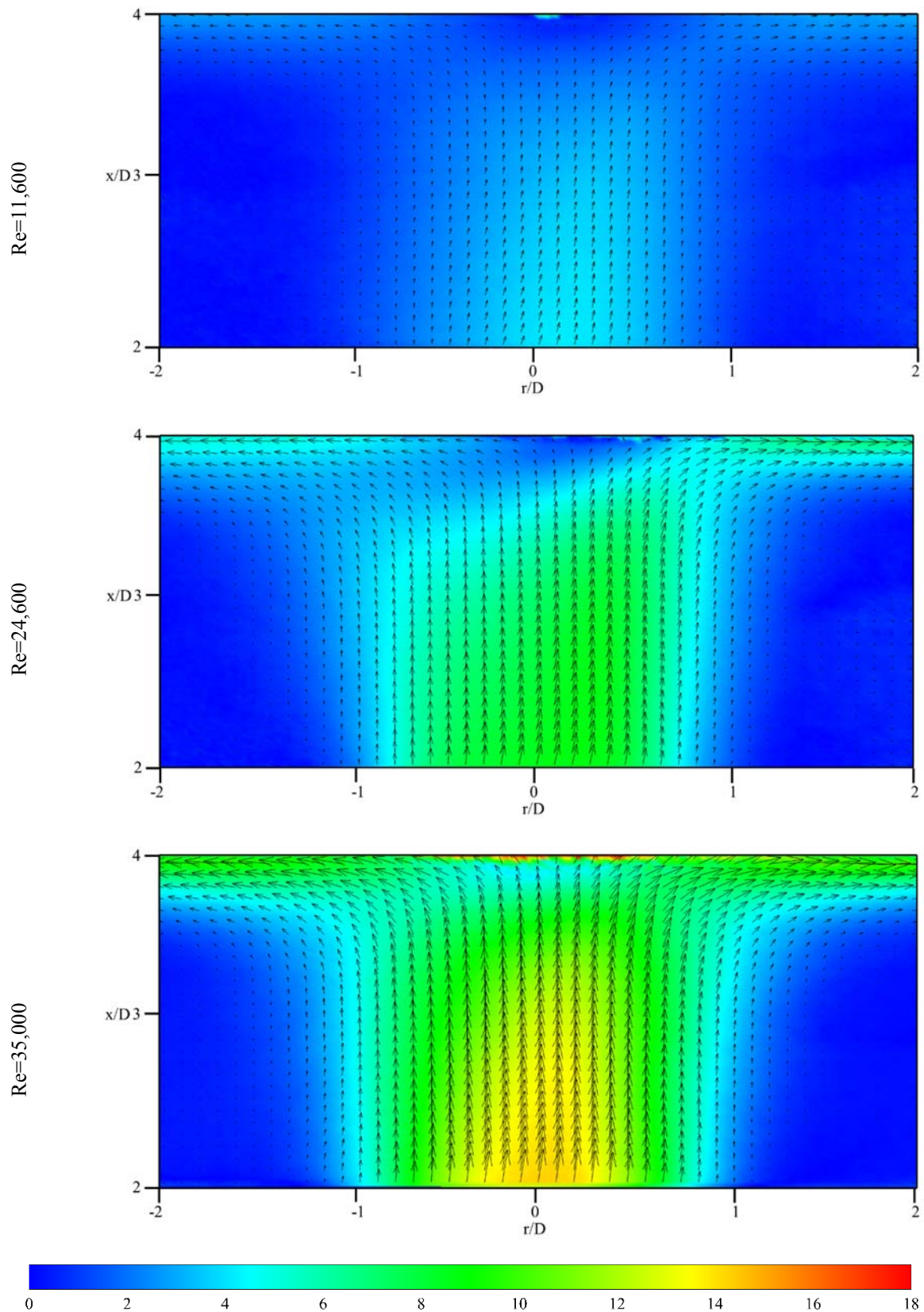
Figure 5-A14: Time-averaged flow field for impinging jet (H/D=4, 2.0 < x/D < 4.0) at S=0.30 and Re=11,600, 24,600, and 35,000. The slight asymmetry observed at Re=24,000 is due to accumulation of illuminating particles.
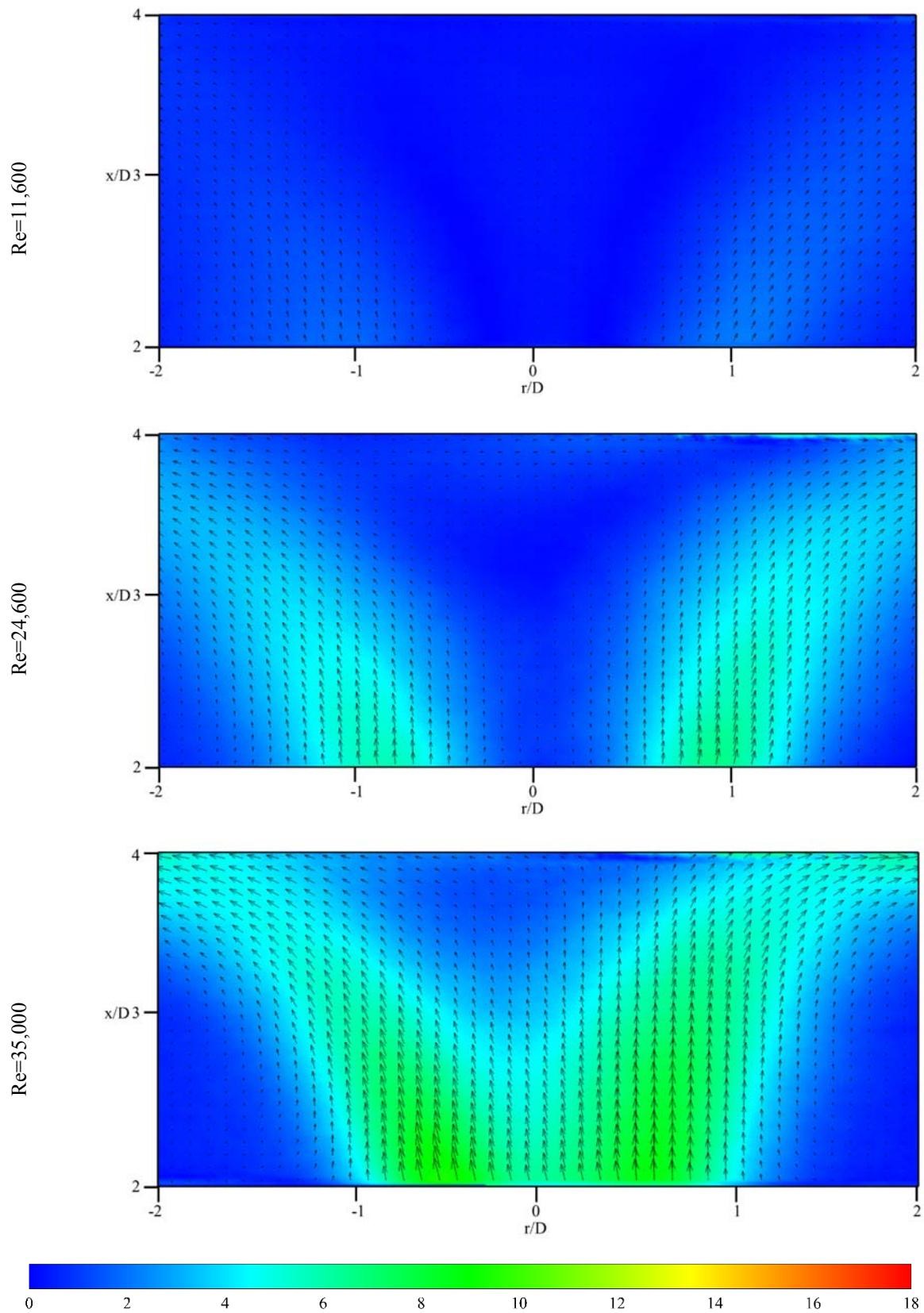
Figure 5-A15: Time-averaged flow field for impinging jet (H/D=4, 2.0 < x/D < 4.0) at S=0.74 and Re=11,600, 24,600, and 35,000.

Chapter 6: General Discussion
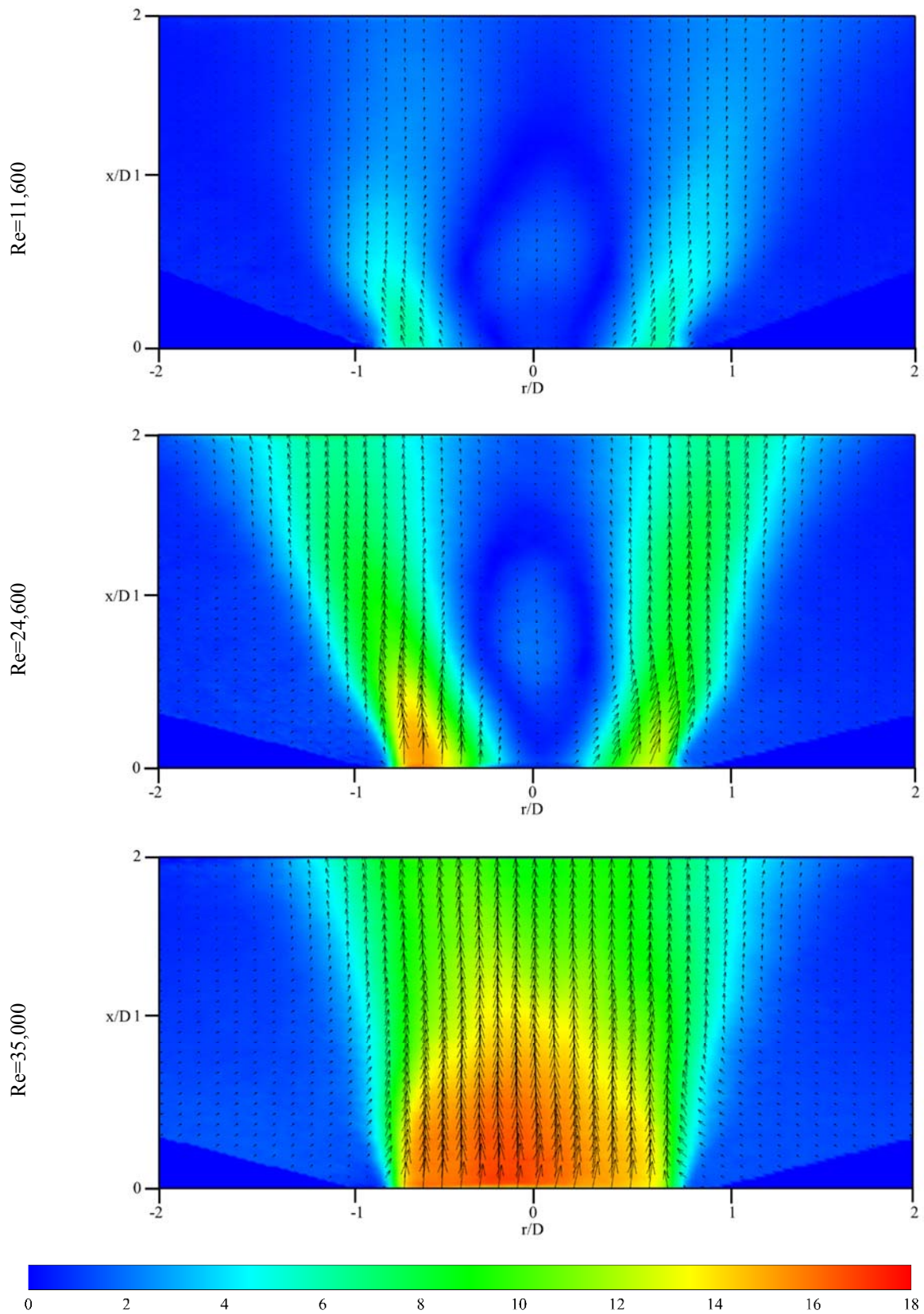
This research has used experiments and numerical analysis to build a deeper understanding of turbulent impinging jets, both swirling and non-swirling, with particular focus on the following:

- Transient behaviour: Development of an image processing methodology to accompany infra-red thermography when applied to resolve transient convection. The role of various operating (Re, S) and geometrical parameters (H/D) on the time to stabilise impingement jet cooling was then studied.

- Steady-state behaviour: Swirl affects the flow field and impingement characteristics but when an insert or vane is inserted into the nozzle it affects the overall operating condition (Reynolds number and swirl intensity) along with nozzle inner shape. This can create ambiguity on understanding the effects of swirl on heat transfer and the role of each parameter, independent from the role of a geometrical insert. The use of aerodynamically generated swirl avoids this. A numerical study looked at the effects of inflow conditions on the flow and heat transfer characteristics for low and weakly swirling impinging jets. Later, experiments were conducted to study the flow field and impingement heat transfer.

Impingement characteristics have been studied under different operating conditions, with special attention with regard to heat transfer rates and their spatial uniformity (heat transfer distribution) for swirling and non-swirling impinging jets. However, literature published to date still lacks to answer research questions relating to understanding how flow features affect impingement characteristics.

Table 6.1: Operating conditions used in thesis chapters.

Thesis Chapter	Re	S	H/D
2 and 3	11,600	0	2
	24,600	0	2
	35,000	0, 0.27, 0.45, 0.77, and 1.05	2, 4, 6
4	24,600	0, 0.31	2,4, 6
5	11,600	0.30, 0.74	2, 4
	24,600	0.30, 0.74	2, 4
	35,000	0.30, 0.74	2, 4

6.1 TRANSIENT HEAT TRANSFER CHARACTERISTICS OF TURBULENT IMPINGING JETS

Firstly, a systematic approach was defined to accurately quantify the transient heat transfer characteristics using infrared thermography. The developed method used heat transfer data acquired in swirling and non-swirling impinging jets and then post-processed this data using MATLAB. The proposed methodology investigated the effect of three different parameters (rate of change of Nu, image resolution, and the spatial discretization) which affects defining the time-period for deciding the system has reached steady-state. Observations revealed that spatial resolution does not affect the time to reach steady-state when compared to other parameters such as defining the rate of change in Nu and spatial discretization. Results also showed that an impinging jet's behaviour evolves over a few seconds (from the start point) before then developing to reach steady-state. The proposed methodology was used to address the RQ1: how does the temporal evolution of heat transfer compare between swirling and non-swirling impinging jets? The tested conditions are stated in Table 6.1.

Secondly, for non-swirling impinging jets, the position of Nusselt number peak remains spatially static over the target surface for the higher Reynolds numbers, but for lower Reynolds numbers its location varies over the time to reach steady-state. The steady-state Nusselt number is directly proportional to the Reynolds number and change in the Reynolds number affects heat transfer substantially in contrast to impingement distance. The time for the impingement plate to reach steady-state heat transfer is around 10s to 20s, because of small transient time the heat transfer rates are high. The heat transfer distributions and magnitudes over the target surface develop concurrently over the time to reach a steady-state. A similar observation is also

made for the swirling impinging jets that stagnation region and wall jet region developed simultaneously over the transient period of heat transfer. For near-field impingement, the peak Nusselt number is at the stagnation for low swirl numbers (S=0.27 and 0.45). As the swirl intensity increases, the location of the peak Nusselt number shifts into the wall jet region. For S=0.77 and S=1.05, the peak Nusselt number is situated at 0.3 < r/D < 0.8 and 0.5 < r/D < 1.0, respectively. For H/D=2 and S=1.05, a distinct region (doughnut-like shape) of high heat transfer is witnessed over the all transient time-period but this effect fades with increases impingement distance and is replaced by more uniform heat transfer distributions.

Although a thin foil heater having small thermal inertia was used in this study, its time constant was calculated and used to normalize the time (to reach steady-state) so results can be extrapolated to conjugate heat transfer where at any instant the temperature in the thickness direction is constant. For non-swirling jets the normalized time to reach steady-state increase as the Reynolds number increases. In contrast to S=0, t/τ decreases with the increase of swirl from S=0 to 0.77. For H/D=2, a further increase in the swirl lengthens the normalised time constant. For H/D=4 and 6, it becomes stable at S=0.45 and 0.77, beyond S=0.77 normalised time to reach steady-state increases for all impingement distances. It was observed that the transient Nusselt number normalized by steady-state Nusselt number (Nu_{st-st}) follows the trend like a negative exponential curve. The rate of change of Nu with time for non-swirling and low swirling impinging jets are similar but are distinct from the moderate and high swirl, hence two different constants were estimated to fit experimental data.

6.2 STEADY-STATE FLOW AND HEAT TRANSFER CHARACTERISTICS OF TURBULENT IMPINGING JETS

Experiments and computations have been conducted to resolve the time-averaged (steady-state) flow field. These have then been correlated to the impingement characteristics of turbulent swirling jets. The following aspects have been studied.

- Non-swirling swirling impinging jets and those with even weak (low) swirl were modelled numerically to gain further insights into the effects of varied inflow conditions (Chapter 4).
- The effect of a central blockage and high turbulent kinetic energy at the centre of the jet (to mimic the use of geometric inserts to impart swirl) was studied with respect to its impact on heat transfer characteristics (Chapter 4).

- Upstream flow features (swirl-induced vortex breakdown) of low and high swirl are studied using Particle Image Velocimetry (PIV) for free and impinging jets. The measurements were conducted against the boundary conditions in Table 6.1 and correspond to chapter 5 in the thesis

- The flow features (downstream surface-stabilised stagnation zones) near impingement with respect to the heat transfer characteristics (Chapter 5).

6.2.1 Upstream Flow Feature of Free and Impinging Turbulent Swirling Jets (PIV)

Two swirl intensities are tested, for low and moderate Reynolds numbers, one in the pre-vortex breakdown regime and the other in the post-vortex breakdown regime. The size and location of the recirculation bubble were determined by the negative axial velocity at the centre of jet. For the higher Reynolds number, greater swirl intensity still lies in the pre-vortex regime but some flow instabilities (distinct impingement characteristics to the low swirling jets) are observed. For low swirl (S=0.30), the potential core for free jet extends to the whole interrogation area (x/D=2), the centreline velocity for the low Reynolds (Re=11,600) number starts to decrease at x/D≈1.00 but stayed with the limitation mentioned by the definition of potential core (95% of jet exit velocity). For impinging jets, the centreline axial velocity starts reducing around x/D=1.00. The centreline axial velocity decay for near and far-impingement (H/D=2 and 4) exhibits different attributes. For near-field impingement, all Reynold numbers showed a similar jet velocity decay when normalized by the bulk axial velocity. For H/D=4, the velocity decay rate for low and moderate Reynolds number is more compared to high Reynolds number away from the target surface.

Vortex breakdown is observed for Re=11,600 and 24,600 at S=0.74 out of all the test cases. When the vortex breakdown occurs the centreline velocity becomes negative and the negative magnitude of the centreline velocity will decide about the strength and size of the recirculation bubble. For free jet, low Reynolds numbers have a much stronger and stable (the shape of VB is not much affected the impingement) recirculation bubble compared to the Re=24,600. The vortex breakdown for Re=24,600 showed some asymmetric behaviour and is clutched by the accelerated flow around it. For the low Reynolds number size and strength of bubble is not much affected rather the position is slightly amended, due to the widening of surrounded fluid it moves downstream compare to free jet. For Re=24,600, the size and position of the vortex bubble are significantly altered due to the near-field impingement. The size and strength of the

recirculation bubble are increased and due to the high-velocity gradients, the bubble moved upstream in contrast to low Reynolds number (Re=11,600).

For far-field impingement (H/D=4), the flow field and recirculation bubble look similar to the free jet, but at this impingement distance still the effect the impinging can be seen from axial velocity profiles. The width of the recirculation bubble is again radially-narrower when compared to near-field impingement. As no vortex breakdown is observed for the Re=35,000 at S=0.74, it can be inferred from the flow field of Re=24,600 that the recirculation bubble is more of an unstable (shape and positions changes) recirculation bubble (impingement affects significantly) and a further increase in the velocity first push the bubble downstream or might be able to vanish it similar to the Re=35,000. The circulation bubble for the low Reynolds number is quite stable and acts like a bluff body at the nozzle exit and flow accelerates around it to maintain the continuity.

6.2.2 Inflow Conditions on Impinging Heat Transfer (CFD/RANS: k-kl-ω)

The flow field characteristics (turbulence and mean velocity components, and its corresponding heat transfer distributions -magnitudes and uniformity) is studied numerically (Ansys Fluent v16.2). The Reynolds Average Navier Stokes (RANS) approach is used to model an impinging jet at Re=24,600. Three different tangential (azimuthal) velocity profiles are tested; Uniform Profile (UP), Solid Body Rotation (SBR), and Parabolic Profile (PP). All these velocity profiles were tested against three impingement distances (H/D=2, 4, and 6). In this study, four commonly used RANS models are implemented but they are not able to capture the secondary peak in the Nusselt number. The secondary peak in the heat transfer distribution for near-field impingement is very common and demonstrated by numerous studies. This secondary peak is typically associated with the transitional region between the laminar flow and turbulent flow starting from the stagnation zone to the wall jet region. A newly proposed turbulence model k-kl-ω is able to predict the heat transfer distribution at the target surface better than the other, it also validates the experimental flow field data as well.

For non-swirling jets, the heat transfer distribution is being affected by the upstream turbulence levels. The region with the high turbulent kinetic energy shows a high influence on heat transfer as well since high shear entrainment is being expected there. For near-field impingement, the first peak of Nusselt number and turbulent kinetic energy matches the start of the wall jet region, but as the impinging distance increases the location shifted in the stagnation zone. For low-swirling impinging jets, similar behaviour is detected for parabolic profile and solid body

rotation but uniform profile showed the peak Nusselt number moves outwards in the radial direction for all tested impingement distances. The uniform profile for the azimuthal velocity component showed a distinct flow feature compared to other modelled boundary conditions. For the UP at H/D=2, a recirculation bubble is sitting near to the impingement which blocks entrainment of air into the stagnation zone and decreases the rate of heat removal from the surface. The recirculation bubble spans $0 < r/D < 0.3$ at stagnation zone, this width of the recirculation bubble matches with the dip in the Nusselt at the target surface.

Geometrically generated swirl is mostly used to generate swirling flows compared to aerodynamically generated swirl. For geometrically generated swirl the central blockage of the nozzle has high turbulent kinetic energy. The geometrically generated swirling jet is mimicked by assuming a very high turbulent kinetic energy near the centre of the nozzle by keeping the overall constant turbulent kinetic energy with the other tested cases. For geometrically generated swirl the azimuthal velocity profile looks like parabolic velocity profile. The central blockage is not considered since flow from inserted tape or vanes is not axisymmetric in its accurate configuration. This case study gives explicit insight into the effect of high turbulence intensity at the centre of the nozzle. It is seen that the impingement characteristics (Nusselt number and turbulent kinetic energy) are being modified and peak Nusselt occurs in the stagnation region. The flow features slightly modified but the turbulent kinetic energy for far-field impingement affected more and this central high shear region affects the out shear and increases outer shear entrainment region especially away from the nozzle exit.

6.2.3 Downstream Flow and Heat Transfer Characteristics (PIV, IR)

Near impingement, velocity profiles have studied with respect to the heat transfer distributions at the target surface. High heat transfer rates are observed near the stagnation zone for low swirling impinging jets due to an increase in the static pressure and deceleration of the axial velocity component at the impingement. For near-field impingement the peak axial velocity tends to shift outward in the radial direction as the Reynolds number increases, the corresponding Nusselt number peak also shifts away in the radial direction with the increase of Reynolds number. At impingement, since the axial velocities are negligible the radial velocities define the heat transfer attributes. For the low and moderate Reynolds numbers at S=0.74 the axial velocity near the impingement is almost zero and the stagnation zone is much bigger and has less heat removal when compared to low swirling imping jets. For high swirling impinging jets, more uniform heat removal is observed at the target surface, small peaks in the

heat transfer are off-set the radial velocity peak since near the velocity peaks the velocity gradients are small. For S=0.74 and Re=35,000, the velocity profiles near impingement are distinct from the other test boundary conditions. For near-field impingement, the stagnation region at the target surface looks like a low swirling jet while for the H/D=4 the size of the stagnation region is in between the low swirl jets and high swirl (where vortex breakdown occurs) jets. There are instabilities associated with this boundary condition and needs further investigations (time-resolved measurements) to reveal more flow features insight.

Chapter 7: Conclusions and Future Work

The chapter summarises the main outcomes from this project and the benefits derived before suggesting several future work recommendations based on identified research gaps in relation to swirling impinging jets.

7.1 CONCLUSIONS

The flow and impingement characteristics of aerodynamically generated turbulent swirling jets were covered across a range of conditions, under both transient and steady-state operation. Results relating to impinging swirl jets were compared to those in non-swirling impinging jets where that relates to either the heat transfer characteristics or flow field. The effects of swirl under impingement conditions on inducing vortex breakdown was also compared to free (unconfined) swirl jets at similar. Velocity field (PIV) data in non-swirling jets (S=0) was not possible due to the fact that the experimental set-up used only permitted seeding through tangential air streams. Non withstanding this, the use of very low swirl conditions as taken as indicative of non-swirl due to earlier experiments on this set-up that showed strong similarity at these conditions based on impingement pressure and heat transfer

Several research questions (mentioned in Chapter 1) were addressed by exploiting experimental and numerical methods. Hotwire anemometry was used to resolve the axial and azimuthal velocity components for each boundary condition at the nozzle exit plane. Infrared thermography was also used to study the temporal evolution of heat transfer characteristics at the impingement surface (in conjunction with the constant flux thin-foil heater). Particle Image Velocimetry was applied to resolve the flow field near the impingement plane, as well as upstream of it, with special consideration given to the occurrence of swirl induced vortex breakdown. Computational Fluid Dynamics modelling (RANS) using Ansys Fluent (version 16.2) was also applied to study were applied to the effect of (upstream) inflow conditions on flow (downstream) flow features near the impingement plane. A range of conditions was used, spanning three Reynolds numbers (Re=11,600, 24,600, and 35,000) over the swirl range (S=0-1.05) were used. A synopsis of results discussed through Chapter 2 to Chapter 5 is listed below.

- **Temporal Heat Transfer Characteristics (experimental):** A method has been developed to enable time-resolved studies of convective processes using infrared imaging. The quantification of time needed to reach system steady-state can be affected by three different parameters; the rate of change of Nusselt number, spatial

discretization, and image resolutions. The image processing technique tested was then used to study the transient heat transfer characteristics of swirling and non-swirling impinging jets. It was found that the peak Nusselt number's position remains constant for all time steps for non-swirling impinging jets. The steady-state Nusselt number is however significantly affected by the Reynolds number, but impingement distance had less of an effect on it. For swirling jets, the wall jet region and stagnation zone simultaneously developed overtime to reach steady-state. The peak Nusselt number for low to moderate swirl occurs at the stagnation region, as the swirl increase this peak shifts in the radial direction, higher the swirl farther the peak from stagnation region (for S=0.77, 0.3 < r/D < 0.8 and for S=1.05, 0.5 < r/D < 1.0). The doughnut-shaped heat transfer region is presented all the time for the highest swirl at near-field impingement, this region has faded with the increase of impingement distance.

- **Flow and Heat Transfer Characteristics (computational):** The newly developed RANS turbulence model (k-kl-ω) performed better than other tested turbulence models. The k-kl-ω was able to predict the secondary peak in the near-field impingement heat transfer. For S=0, the turbulence levels at the inlet affect the heat transfer at the target surface, with the start of the wall jet region identifying the first peak in the Nusselt number. For weakly swirling jets (S=0.31), the nozzle inflow condition significantly affects the flow and heat transfer characteristics. The peak in Nusselt number lies in the wall jet region with a uniform profile (UP) inflow condition, compared to the other two azimuthal velocity profiles (solid-body rotation and parabolic profile) where that peak is closer to the stagnation point. For the uniform profile at H/D=2, there a recirculation zone is predicted to stabilise on the impingement plane and causes significantly deteriorates the heat transfer rates. This pocket of recirculating air is not observed for the other velocity profiles tested.

- **Flow and Heat Transfer Characteristics (experimental):** Two boundary conditions out of six of the tested cases experienced vortex breakdown phenomenon. The impingement characteristics of the flow with the vortex breakdown are distinctive from the other boundary conditions which do not exhibit the vortex breakdown. The strength, the size, and the position of this recirculation bubble depends on the Reynolds number, swirl intensity, and the impingement characteristics (free or impinging jet). For free jets, the recirculation bubble for the low Reynolds number (Re=11,400) is spatially larger and exhibits stronger recirculation velocities when compared with the

boundary condition at Re=24,600. The impingement also affects the recirculation bubble, especially for near-field impingement (H/D=2). Due to the impingement, the vortex breakdown at Re=24,600 becomes more axisymmetric and grows in size in contrast to the free jet. Further increase in the impingement distance pushed the flow features to look like a free jet. For the low swirl, the higher rates of heat transfer occur near the stagnation zone because of higher static pressures as the flow decelerates of the (energy conservation). For higher swirl (S=0.74), the stagnation zone expands for Re=11,600 and 24,600 due to the recirculation bubble which explains why peak in Nusselt number shifts outwards in the radial direction. The stagnation zone for Re=35,000 and S=0.74 is bigger than the low swirling jets and smaller than the one when vortex breakdown occurs. The impingement characteristics at this boundary condition especially for H/D=4 look similar to the heat transfer profile where vortex break occurs, this shows that the flow condition in the pre-vortex breakdown regime but a slight increase in the swirl intensity might lead to the post-vortex breakdown regime.

The study has highlighted that the rates for stabilising the heat transfer characteristics of turbulent impinging jets can be controlled to some extent through the selection of operating parameters. This can lead to improved process control in industrial applications where impinging jets are utilised. An image processing tool has been developed which can also be employed to extract heat transfer characterises under convective heat transfer. The understanding of flow features and their corresponding impingement characteristics has improved.

7.2 FUTURE RECOMMENDATIONS

- Whilst the infrared thermography used in this study utilised a high-resolution camera, the 60Hz limitation on frame rate unable to capture the micro-seconds instabilities and coherent structures at the impingement surface. To overcome this limitation, the use of a high-speed Infrared Camera (up to 100,000 frames per seconds) can enable to study conjugate heat transfer phenomenon can be studied along with time-dependent instabilities in the heat transfer.

- High fidelity CFD simulation is needed to look into the flow structure of the swirling jets. Since RANS modelling is not capable of capturing eddies in the jet shear layer. Initial validation can be done against the available DNS data for the non-swirling free

jet. It might be worth investigating to run the model using a 3D-LES scheme by exploiting a high-performance computing facility.

- PIV system is not capable of resolving the boundary layer at the impinging plane with high resolution due to the reflections from the target surface in impinging jets. Further LES or RANS will help to understand the fresh fluid entrainment into the boundary and its effect on heat transfer from the impingement surface.

- It is established understanding that the coherent structures into the flow affect the surface characteristics (heat and mass transfer, pressure distribution). Time-resolved PIV measurements are needed to evaluate these structures linked with the impinging jets. Proper Orthogonal Decomposition (POD) can be used to estimate different coherent structures associated with different modes of POD analysis.

- The vast majority of research undertaken with impinging jets focusses on heat transfer, but there remains much to be learned about their use for mass transfer (drying of timbers and food products).

- This study has utilized a non-heated jet, for applied research projects, the heat transfer between the heated jet impinges onto the surface of ambient temperature can be studied. The effect of the change of the controlling parameter of swirling jets (Reynolds number, swirl number, and impingement distance) will be examined in accordance with the performance of the heat transfer.

Appendices

APPENDIX A   Permission of copyrighted material

Appendix A is not included in this version of the thesis.

Appendix B   Statement of co-authors contribution

Please refer to the attached DVD (CD-2) for detailed documents of the statement of co-authors contribution for each publication listed.

- B1   Co-authors statement contribution for Chapeter2
- B2   Co-authors statement contribution for Chapeter3
- B3   Co-authors statement contribution for Chapeter4
- B4   Co-authors statement contribution for Chapeter5

Appendix C   Experimental Methods

C-1   Flowmeter Calibration

Three different types of flow meters (LV2S15-AI27 (Make: Influx), LPL1"LH40-AI58 (Make: Influx), and RSF-024V (Make: Dwyer)) were used in this study. Each flow meter had a different flow range and was used together to draw the flow rate for the desired test conditions. The calibration was performed using CTA single sensor (Dantec, model: 55P11) and airflow was measured at the nozzle exit. The upstream pressure of flow meters was kept constant at 400kPa (Gauge). Previously, the uncertainty in the CTA data was checked against the Pitot-static tube and found to be around 2% [1]. Initially, they were checked with previously available calibration data [1] and found that the flow meter LPL1"LH40-AI58 still held the same calibration curve. The calibration curve for the other two flow meters was developed again so that similar boundary conditions could be drawn [1]. The bulk velocity was determined by measuring the velocity profile at the nozzle exit. The bulk velocity was computed using the following equation.

$$U_b = \frac{2}{R^2} \int_0^R <u> r\, dr \qquad \text{(A-1)}$$

Where <u> is the local velocity at a point of nozzle exit measured using CTA. R is the radius of the nozzle exit. The flow rate was calculated using the equation below.

$$Q = U_b A \qquad \text{(A-2)}$$

Where A is the cross-sectional at the nozzle exit. Each experimental reading was repeated for at least three times to assure the consistency and reliability of the data. The following graphs show the calibration curve for the two flow meters (LV2S15-AI27 and RSF-024V).
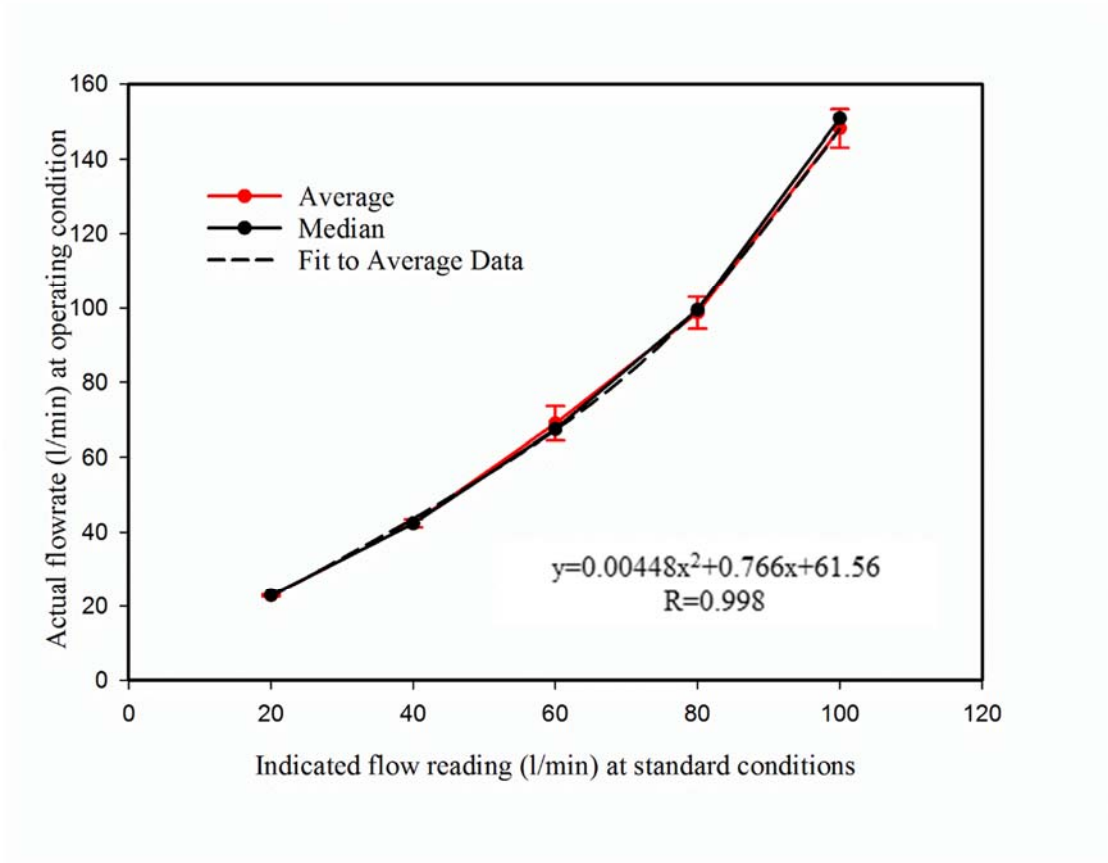
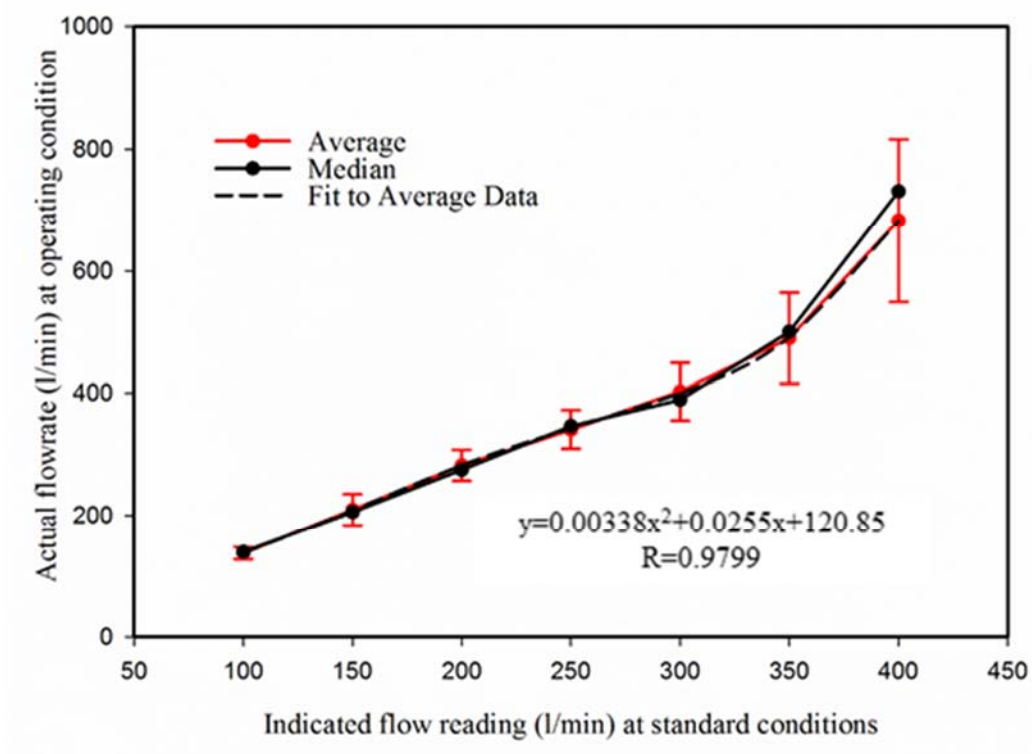Figure C-1-1: Calibration graph for the flowmeter LV2S15-AI 27 (make: Influx).

Figure C-1-2: Calibration graph for the flowmeter RSF025V (make: Dwyer).

C-2   Flowmeters Settings

The number of Boundary conditions were tested for different Reynolds numbers and swirl intensities. The axial and azimuthal velocity components were measured using CTA, and data were validated against previous data [2]. Following boundary conditions are being utilised in this study. The sensor orientation values are used as per the methodology defined previously [3].

Experimental Conditions									
Flow rate								Flowmeter distributions	
Q_a (L/min)	Q_t (L/min)	Q_T (L/min)	Re	Ub	Wb	S	ψ	Q_a	Q_t
1000	0	1000		13.26	0.00	0.00	0	red	
565	435	1000		12.83	3.50	0.28	0	red	green
440	560	1000	35,000	13.52	6.40	0.47	5	green	yellow
360	640	1000		13.52	10.45	0.77	10		yellow
0	1000	1000		17.57	18.38	1.05	25		yellow
703	0	703		9.32	0.00	0.00	0	red	
370	330	700	24,600	9.10	2.81	0.31	0	yellow	green
160	540	700		11.55	8.36	0.72	15	green	yellow
331	0	331		4.39	0.00	0.00	0	yellow	
150	180	330	11,600	5.03	1.63	0.31	0	yellow	green
0	330	330		5.08	3.75	0.74	25		green

Colour Keys:

- red: LPL1H40-AI58
- yellow: RSF-025V
- green: LV2S15-AI24

C-3   Seeder Design

In order to add illuminating particle (Al_2O_3) into the flow to a designated seeder was designed. Three cyclones were used, one for each tangential port. Perspex tubes were utilized as a container for each cyclone, while two cyclone disks with a curved groove were used to mix air and particle. Two thick Perspex plates were used to clamp all three cyclones. Figure C-3-1 shows the overall seeder assembly. Individual seeder is shown in Figure C-3-2. The technical drawings for cyclone and seeder lid are presented in Figure C-3-3 and Figure C-3-4 respectively.
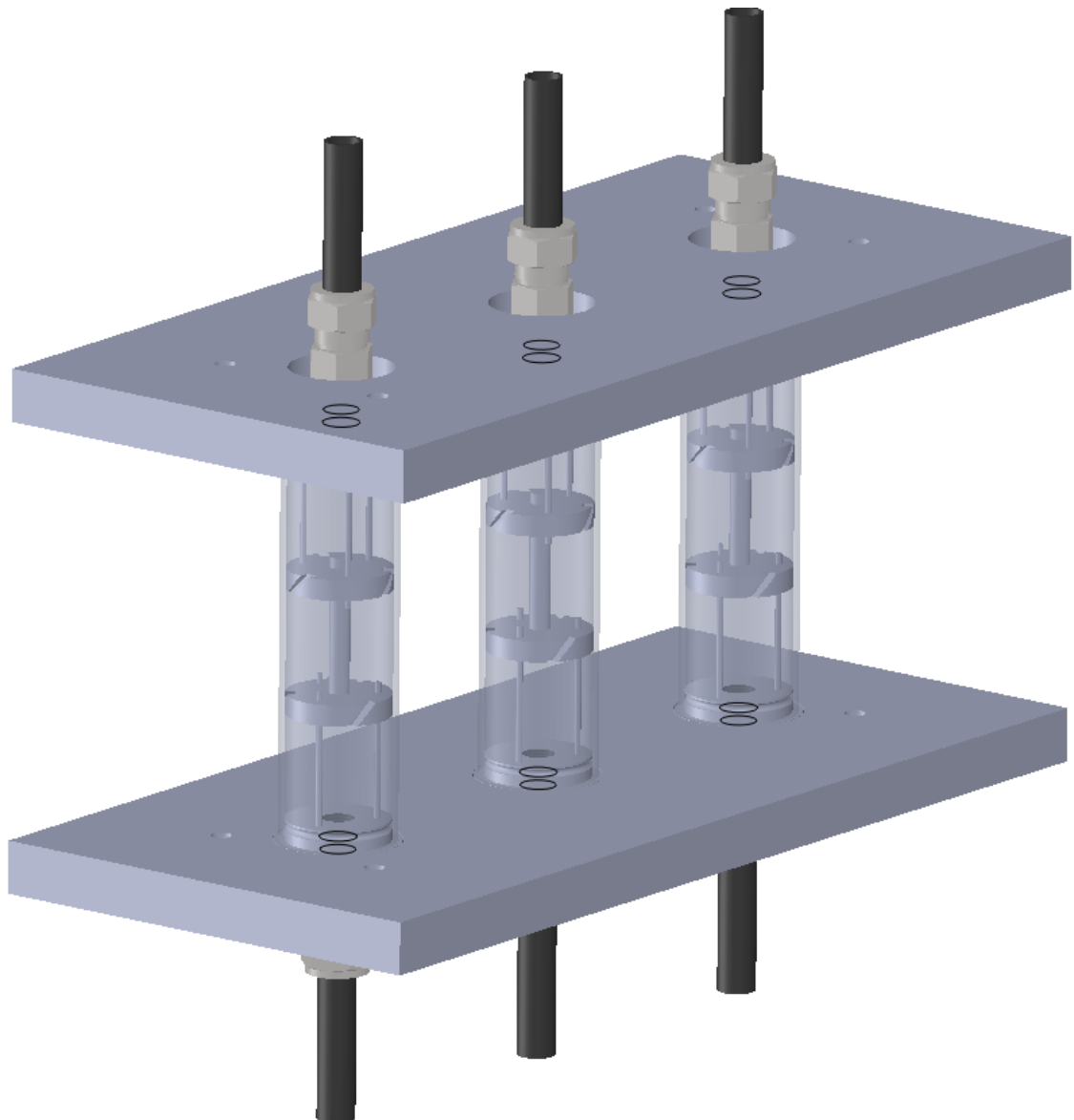
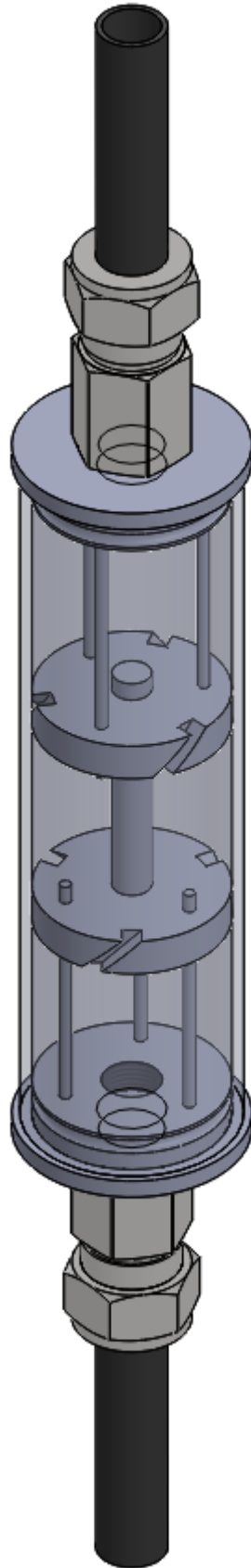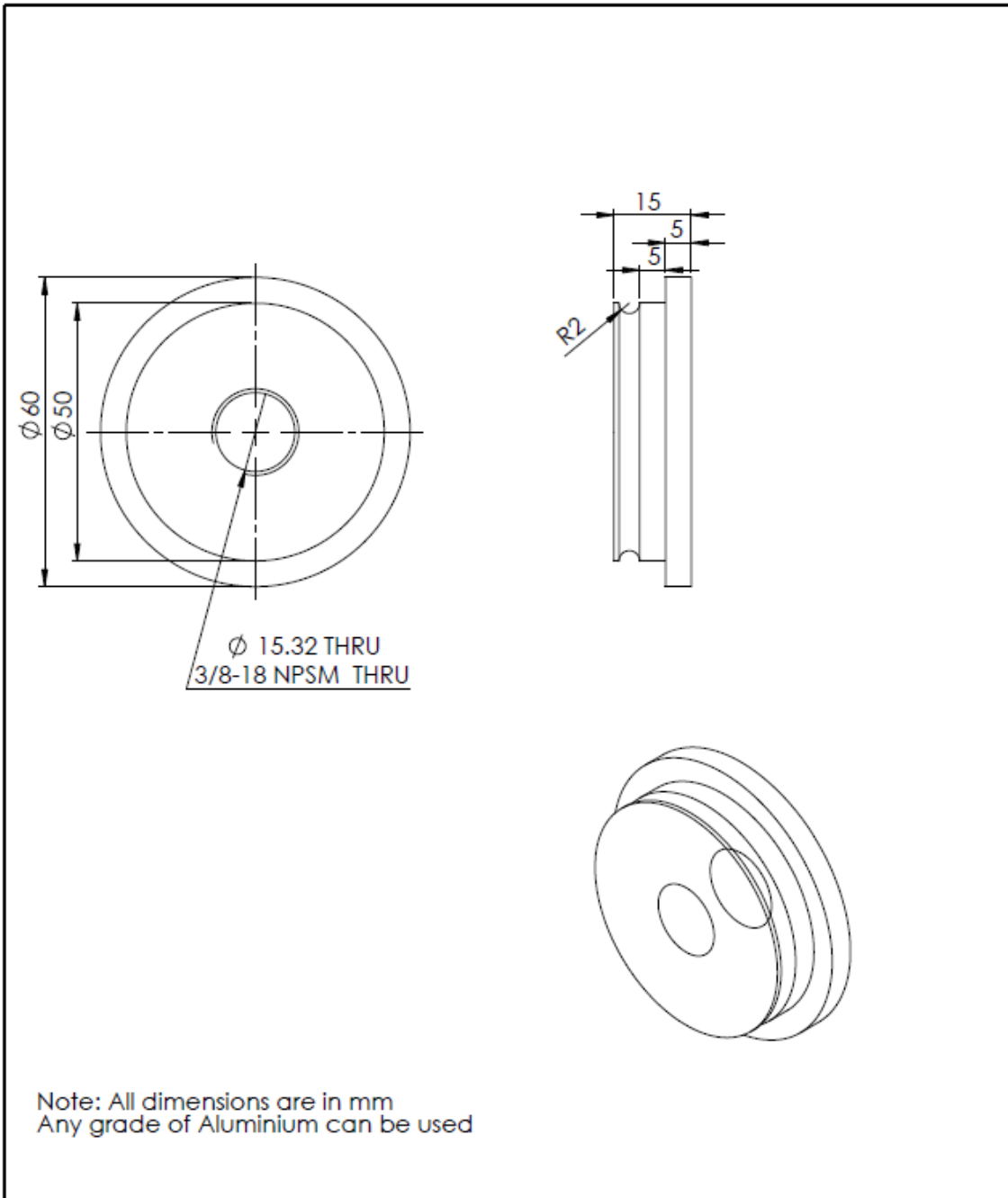

Figure C-3-1: Seeder assembly.

Figure C-3-2: Cyclone for seeder.

15

5

5

R2

Ø 60
Ø 50

Ø 15.32 THRU
3/8-18 NPSM THRU

Note: All dimensions are in mm
Any grade of Aluminium can be used

Figure C-3-3: Technical drawing for cyclone lid.

Ø3(X3) 4.87(X3)

Ø10 5(X3)

10

Ø50

Note: All dimensions are in mm
Any grade of Aluminium can be used

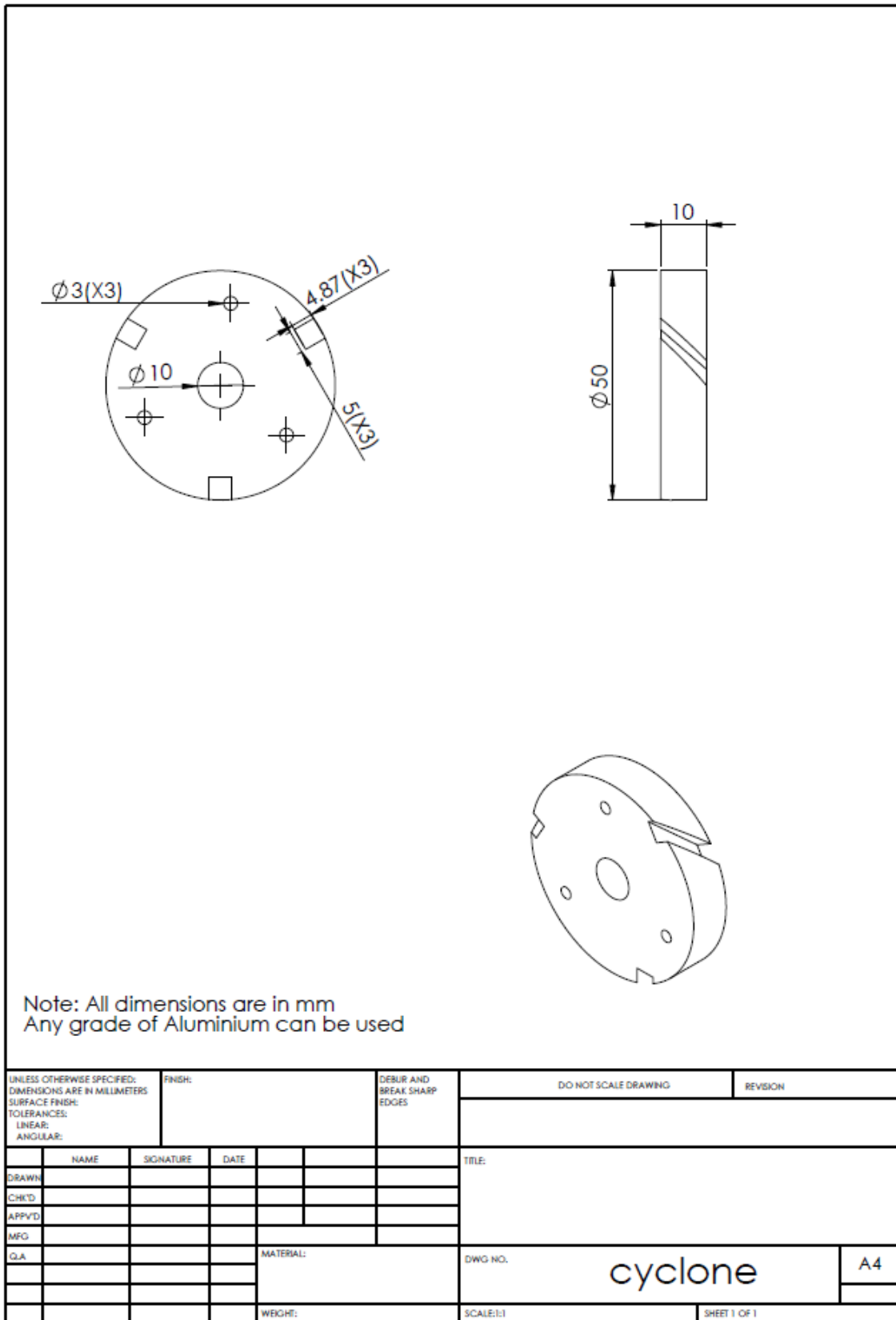| UNLESS OTHERWISE SPECIFIED: DIMENSIONS ARE IN MILLIMETERS SURFACE FINISH: TOLERANCES: LINEAR: ANGULAR:		FINISH:			DEBUR AND BREAK SHARP EDGES		DO NOT SCALE DRAWING		REVISION	
	NAME	SIGNATURE	DATE				TITLE:			
DRAWN										
CHK'D										
APPV'D										
MFG										
Q.A				MATERIAL:			DWG NO.	cyclone		A4
				WEIGHT:			SCALE:1:1		SHEET 1 OF 1	

Figure C-3-4: Technical drawing for cyclone disk.

C-4   Emissivity Measurement

Thin foil constant flux heater is used to quantify the heat transfer characteristics of turbulent swirling impinging jets. The construction of the heater is discussed in detail in Chapter 3. An infrared camera is used to measure the temperature distribution over the surface of the heater. The backside of the thin foil is painted black in order to get a high emissivity camera facing surface. The emissivity of this black paint was previously estimated experimentally [1], similar experiments are repeated to ensure that the surface is still held similar characteristics.

Initially, an AISI316 stainless steel strip 310mm long and 120mm wide was divided into three different portions. One portion was painted black, the second portion was covered with a black electrical insulating tape, the third section was left unpainted. The emissivity for the black insulating tape (0.98) is used as a reference [4]. The metallic strip was placed into the thermostat-controlled water bath. Three different wattages (1000watt, 1200watt, and 1400warr) were applied to the water bath was waited to till the water bath temperature reached steady-state, four k-type thermocouples were used just beneath metallic strip to get the surface temperature near the foil. When the temperatures reached steady-state (the temperature fluctuations were with 0.2°C), the IR image of the foil was taken. The emissivity of all three segments was estimated using the method explained in [5]. The emissivity of the unpainted foil portion and the painted portion was calculated as 0.06 and 0.97 respectively. On contrary the emissivity can also be measured using an Emissometer. Figure C-4-1 presents the picture of thin foil and its corresponding IR image.
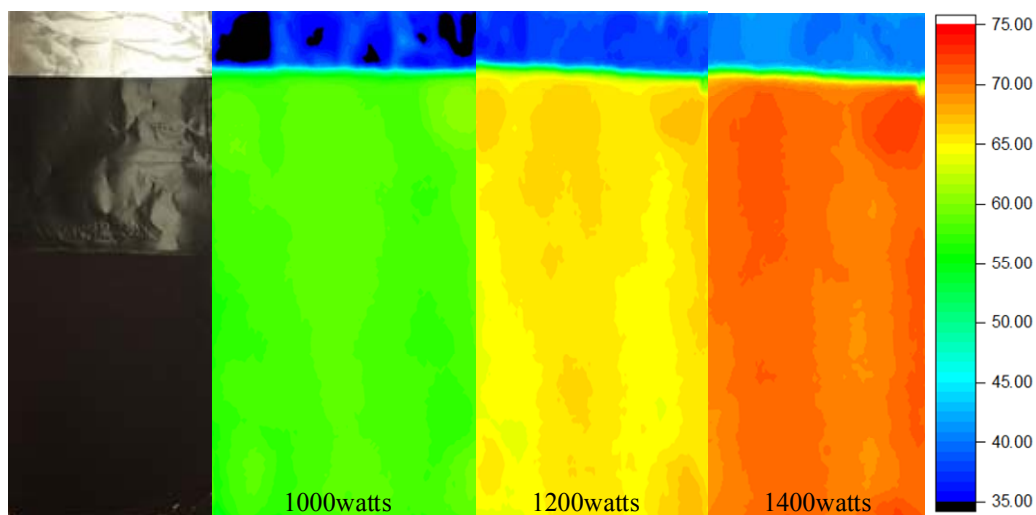

Figure C-4-1: Temperature contour plots for different applied powers.

Appendix D   Experimental Results
## D-1   CTA Boundary Conditions

Constant Temperature Anemometry (CTA) is used to measure velocity profiles at the nozzle exit. The normalised axial and tangential velocities profiles are noted in Chapter 3, Chapter 4, and Chapter 5.

All boundary conditions which are utilized in this study are presented in Figure D-1-1 and Figure D-1-2. The axial and tangential velocity profiles at the exit of the nozzle are presented in Figure D-1-1 and their corresponding fluctuations are shown in Figure D-1-2. Total eleven boundary conditions are mentioned, Re=11,600 and Re=24,600 have three different swirl intensities (S=0, 0.30, and 0.74) while Re=35,000 have five different swirl intensities (S=0, 0.27, 0.45, 0.77, and 1.05).
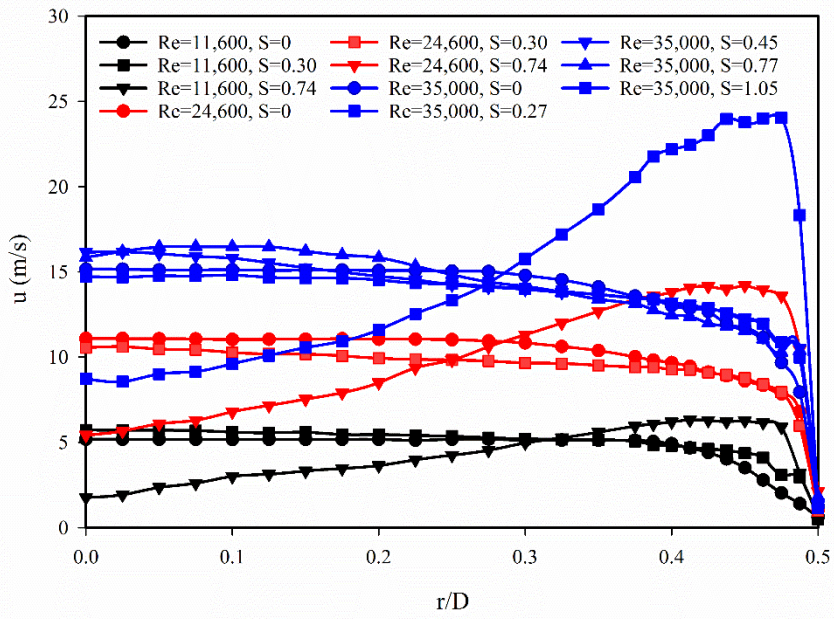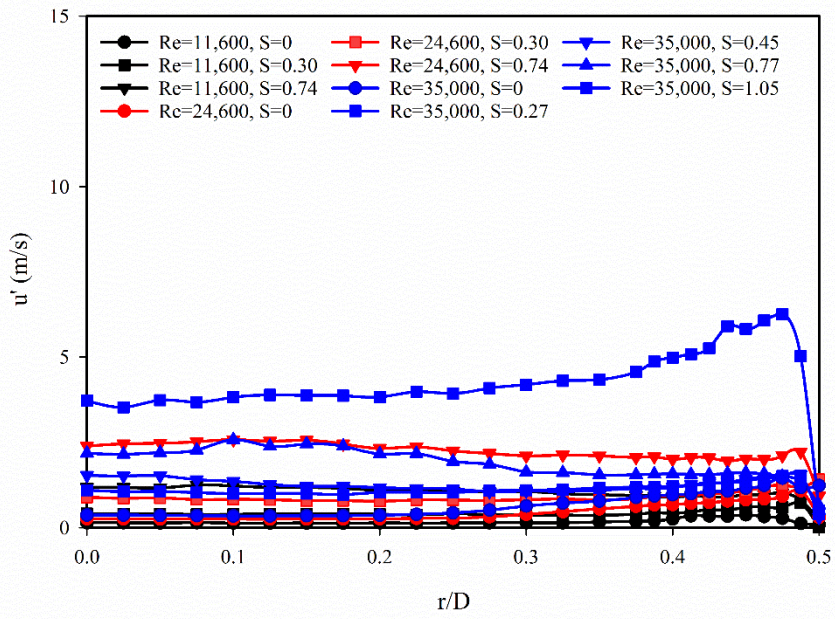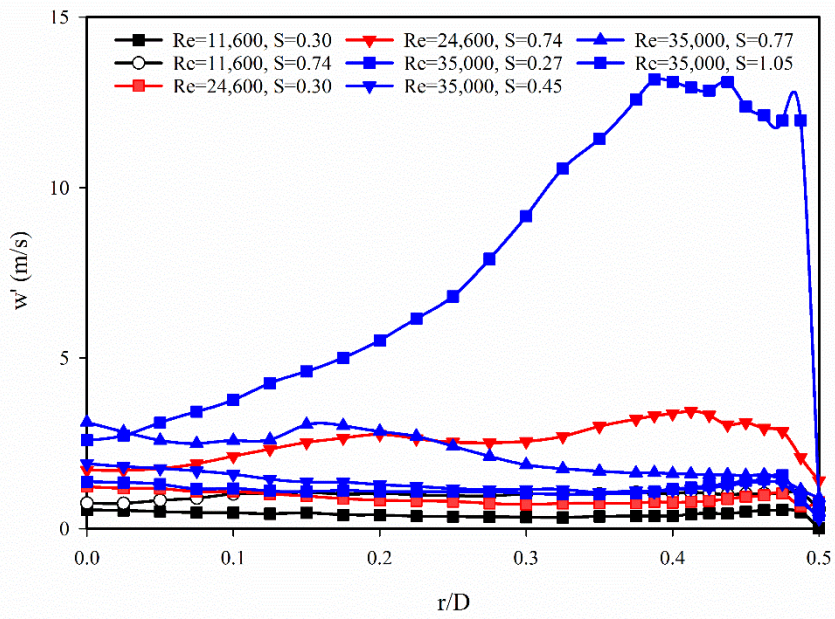
(a)
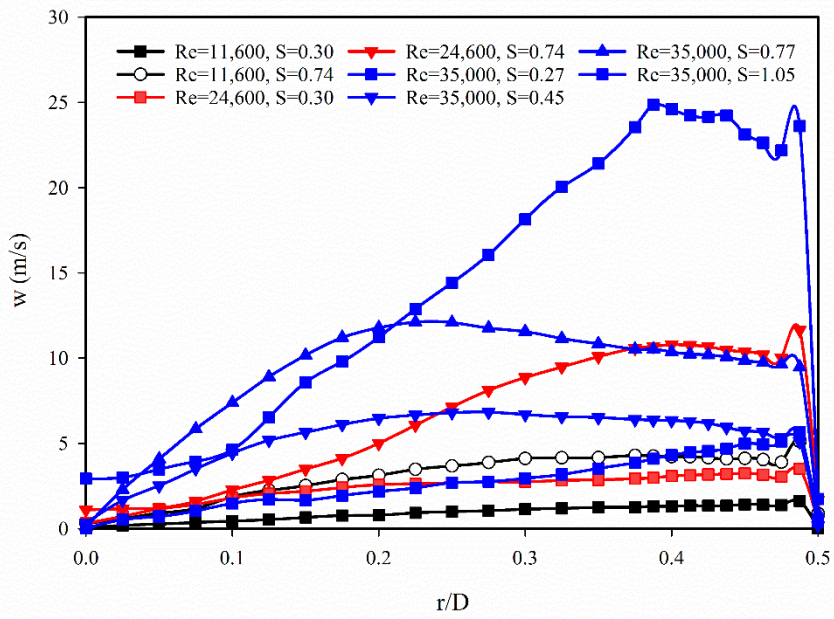
(b)

Figure D-1-1: (a) Axial (u) mean velocity and (b) tangential (w) mean velocity.

(a)

(b)

Figure D-1-2: (a) Axial (u') mean velocity fluctuations and (b) tangential (w') mean velocity fluctuations.

D-2   Swirl Number Definitions and Correlations

There are numerous swirl number definitions and each one of them are defined with respect to some limitation and assumptions. These definitions take the forms of momentum or velocity ratios of azimuthal to the axial component. The definition stated in Equation D-1-1 is used in the present study which is the ratio of bulk tangential velocity to bulk axial velocity resolved via CTA explained by Al-Abdeli [5], this definition is also explained in the earlier chapters as well.

$$S = \frac{W_b}{U_b}$$

(D-1-1)

The definition mentioned in Equation D-1-2 is used by Chigier and Beer [6], Chiger and Chervinsky [7], Farokhi et al. [8] Gilchrist and Naughton [9], Panda and McLaughlin [10], and Sislian and Cusworth [11].

$$S_1 = \frac{G_\theta}{G_x R}$$

(D-1-2)

This above definition of swirl number can be rewritten in several ways. For turbulent incompressible stationary flows, Equation D-1-2 can be rewritten into Equation D-1-3 using boundary-layer approximation.

$$S_1 = \frac{2\pi\rho \int_0^R r^2(uw + \overline{u'w'})dr}{2\pi\rho \left[\int_0^R r\left(u^2 - \frac{1}{2}w^2 + \overline{u'^2} - \frac{1}{2}\left(\overline{w'^2} + \overline{v'^2}\right)\right)dr\right] \times R}$$

(D-1-3)

The experimental techniques used in this study are not able to measure the Reynolds stress component ($\overline{u'w'}$). Usually, it is very small compared to mean flow values [12]. Equation D-1-3 can be simplified as follows.

$$S_{1a} = \frac{2\pi\rho \int_0^R r^2 uw\,dr}{2\pi\rho \left[\int_0^R r\left(u^2 - \frac{1}{2}w^2 + \overline{u'^2} - \frac{1}{2}\left(\overline{w'^2} + \overline{v'^2}\right)\right)dr\right] \times R}$$

(D-1-4)

The Equation D-1-4 can be further simplified as Equation D-1-5 by neglecting the velocity fluctuations. It is observed that the contribution of the fluctuations terms is small as shown in Table D-1-1.

$$S_{1b} = \frac{2\pi\rho \int_0^R r^2 uw\,dr}{2\pi\rho \left[\int_0^R r\left(u^2 - \frac{1}{2}w^2\right)dr\right] \times R}$$

(D-1-5)

Equation D-1-6 can be achieved by further simplification using the initial velocity profiles.

$$S_{1c} = \frac{\frac{1}{2}\left(\frac{W_b}{U_b}\right)}{1 - \frac{1}{4}\left(\frac{W_b}{U_b}\right)}$$

(D-1-6)

The swirl number definition used by Billant et al. [12] and Gallaire and Chomaz [13] is defined in Equation D-1-7.

$$S_2 = \frac{2w\left(\frac{R}{2}, x_0\right)}{u(0, x_0)}$$

(D-1-7)

The swirl numbers (boundary conditions) used in this (Equation D-1-1) study along with correlation to other swirl numbers (Equation D-1-4 through Equation D-1-7) are presented in Table D-1-1 and Figure D-1-3.

Table D-1-1: Experimental conditions.

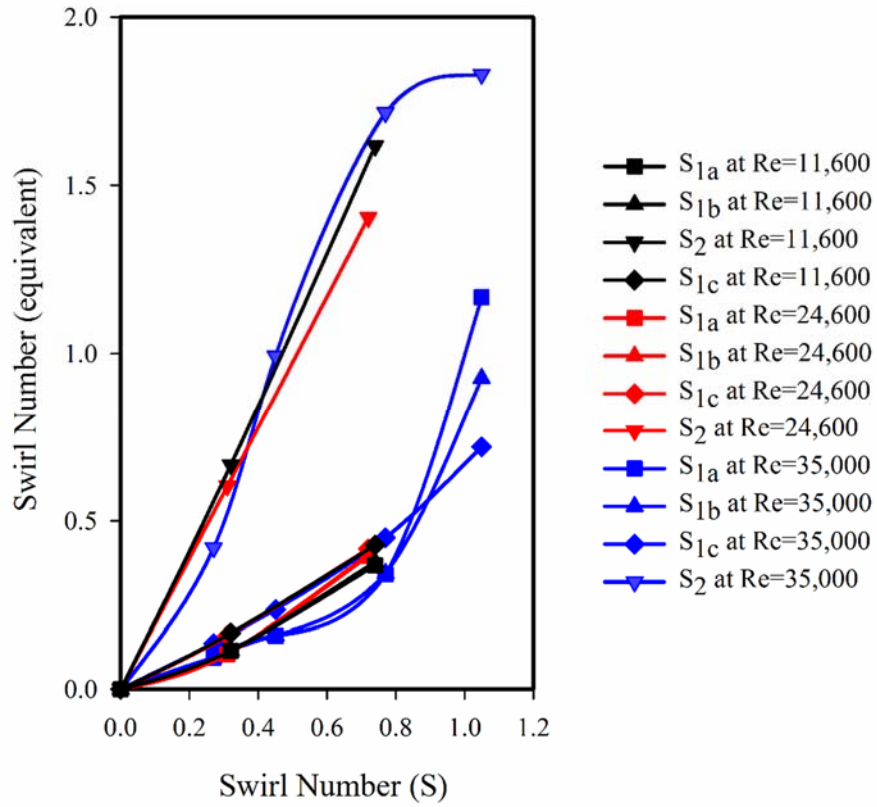| Re	U_b (m/s)	W_b (m/s)	S	S_{1a}	S_{1b}	S_{1c}	S_2
11,600	4.39	0	0	0	0	0	0
	5.03	1.63	0.32	0.114	0.115	0.166	0.666
	5.08	3.75	0.74	0.367	0.377	0.427	1.617
24,600	9.31	0	0	0	0	0	0
	9.10	2.81	0.31	0.104	0.105	0.158	0.603
	11.55	8.36	0.72	0.395	0.399	0.416	1.404
35,000	13.263	0	0	0	0	0	0
	13.14	3.5	0.27	0.094	0.094	0.135	0.419
	13.74	6.18	0.45	0.158	0.159	0.236	0.993
	13.71	10.51	0.77	0.340	0.343	0.449	1.716
	17.57	18.39	1.05	1.168	0.927	0.720	1.830

Figure D-1-3: Equivalent swirl numbers with the swirl number used in this study (S, Equation D-1-1).

APPENDIX E   Digital Archive of Data

Appendix E is not included in this version of the thesis.

Appendix References

[1]   Z. U. Ahmed, "An experimental and numerical study of surface interactions in turbulent swirling jets," Edith Cowan University, 2016.

[2]   Z. U. Ahmed, Y. M. Al-Abdeli, and F. G. Guzzomi, "Heat transfer characteristics of swirling and non-swirling impinging turbulent jet," Int. J. Heat Mass Transf., vol. 102, pp. 991–1003, 2016.

[3]   Z. U. Ahmed, Y. M. Al-Abdeli, and F. G. Guzzomi, "Corrections of dual-wire CTA data in turbulent swirling and non-swirling jets," Exp. Therm. Fluid Sci., vol. 70, pp. 166–175, 2016.

[4]   "FLIR User Manual. 2009, FLIR Systems," .

[5]   M. Vollmer and K.-P. Möllmann, Infrared thermal imaging: fundamentals, research and applications. John Wiley & Sons, 2017.

[5]   Y.M. Al-Abdeli, Experiments in turbulent swirling non-premixed flames and isothermal flows, 2004.

[6]   NA Chigier, JM Beer, Velocity and static pressure distributions in swirling air jets issuing from annular and divergent nozzles. Transactions of the ASME. J Basic Eng 86:788–796, 1964.

[7]   NA Chigier, A Chervinsky, Experimental investigation of swirling vortex motion in jets. J Appl Mech 34:443–451, 1967.

[8]   S Farokhi, R Taghavi, EJ Rice, Effect of initial swirl distribution on the evolution of a turbulent jet. AIAA J 27(6):700–706, 1989.

[9]   RT Gilchrist, JW Naughton, Experimental study of incom- pressible jets with different initial swirl distributions: mean results. AIAA J 43(4):741–751, 2005.

[10]   J Panda, DK McLaughlin, Experiments on the instabilities of a swirling jet. Phys Fluids 6(1):263–276, 1994.

[11]   JP Sislian, RA Cusworth, Measurement of mean velocity and turbulent intensities in a free isothermal swirling jet. AIAA J 24(2):303–309, 1986.

[12]   P Billant, JM Chomaz, P Huerre, Experimental study of vortex breakdown in swirling jets. J Fluid Mech 376:183–219, 1998.

[13]   F Gallaire, JM Chomaz, Mode selection in swirling jet experiment: a linear stability analysis. J Fluid Mech 494:223– 253, 2003.